

UNIVERSITÀ DEGLI STUDI DI PARMA

Dipartimento di Chimica
Ph.D. in Chemical Science
XXV Cycle (2010-2012)

**Silver and Copper complexes with tripodal
ligands: from coordination polymers to
anticancer drug precursors.**

Coordinator: **Prof. Giovanni Predieri**

Supervisor: **Dott. Luciano Marchiò**

PhD candidate: **Irene Bassanetti**

2013

“Simplicity is the ultimate sophistication”

Leonardo da Vinci

To my husband Gianmaria

Contents

1. General introduction on coordination polymer	7
2. Crystal engineering of multidimensional Copper (I) and Silver (I) coordination polymers with flexible ligands.	13
2.1. Introduction	14
2.2. Experimental	16
2.3. Results and discussion	23
3. Rigid vs Flexible N₂S donor ligands: conformational studies on Cu(I) and Ag(I) complexes.	41
3.1. Introduction	42
3.2. Experimental	45
3.3. Results and discussion	50
4. Porous coordination polymers: synthesis and characterization of novel silver(I) supramolecular architectures.	65
4.1. Introduction	66
4.2. Experimental	68
4.3. Results and discussion	73
5. Novel cavity design using pre-organized tripodal ligands: synthesis and solid state characterization.	95
5.1. Introduction	96
5.2. Experimental	98
5.3. Results and discussion	106
6. Pre-organized N₂S₂ donor ligand drives Metal-Organic chain formation.	121
6.1. Introduction	122
6.2. Experimental	124
6.3. Results and discussion	128

7. General introduction on the role of copper in medicine.	145
8. Copper complexes with N₂ and N₂S donor ligands: from caspase inhibition to paraptotic cell death in human cancer cells.	155
8.1. Introduction	156
8.2. Experimental	157
8.3. Results and discussion	169
9. Cytotoxic activity of Copper-dependent cytotoxicity of 8-Hydroxyquinoline derivatives.	189
9.1. Introduction	190
9.2. Experimental	193
9.3. Results and discussion	197
10. Synthesis of Copper(II)complexes with functionalized quinoline derivatives. Study of citotoxic activity on cancer human cells	211
10.1. Introduction	212
10.2. Experimental	217
10.3. Results and discussion	224
11. Bibliography	241
12. Acknowledgment	259
13. Appendix	261

CHAPTER 1

GENERAL INTRODUCTION ON COORDINATION POLYMERS

“One of the continuing scandals in the physical sciences is that it remains in general impossible to predict the structure of even the simplest crystalline solids from a knowledge of their chemical composition”.
J. Maddox (Nature, 1988, 335, 201)¹

Through these twenty years a myriad of successful studies on this complex subject have been conducted and so nowadays this statement has become not completely true. An ever-increasing number of elegant, beautiful and useful functional architectures has been designed and synthesized. Therefore the fast growing interest for molecular design has result in the birth of a new branch of chemistry: crystal engineering^{2,3}. The “golden rule” in crystal engineering is that molecular structure are built on covalent and non covalent intermolecular interactions. Thanks to these we are able to control the rational design of two-(2D) and three-dimensional (3D) architectures⁴.

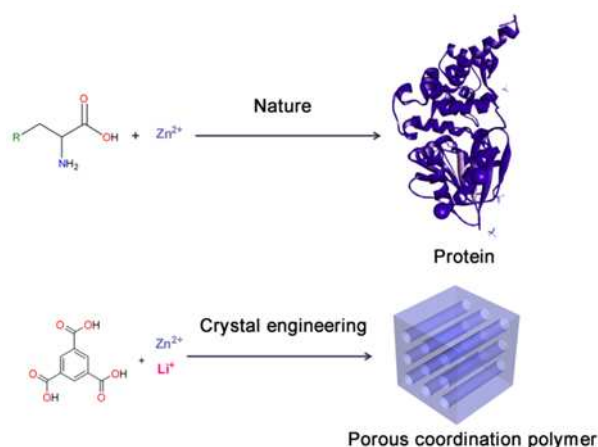


Figure 1. Examples of natural and synthetic self assembly process.

Learning from Nature, crystal engineering studies the way to include specific functionalities in well-defined molecular conformations to drive the packing geometry. Nature can combine simple molecules, to create very complex aggregates with very specific features, such as proteins. This process occurs through the use of, mostly on 3D aggregations, weaker non covalent interactions such as H-bonding, charge-charge, donor-acceptor, π stacking and Van Der Waals forces. In crystal engineering⁵ we use our knowledge to match these interactions in a studied algorithm to build fascinating supramolecular architectures with useful characteristics. Thanks to the extremely large number of possible application much attention has been focused on coordination polymers⁶ (CPs) and in particular on porous coordination polymers (PCPs) or porous coordination networks(PCNs)⁷. The backbone of these coordination polymers consist of metal-ligand coordinative bonds forming polymeric or oligomeric species which extend “infinitely” into one, two or three dimensions via more or less strong non-covalent interactions. The network design but primarily the structure-function relationship are determined by the interplay between the ligand and the metal centre.

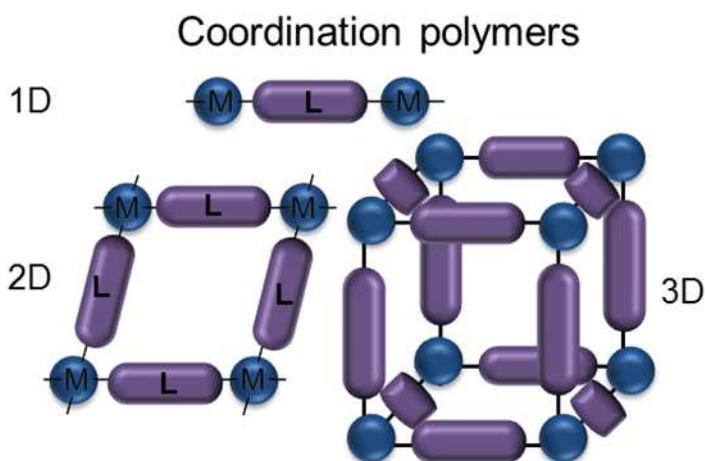


Figure 2. Schematic representation of one, two and three-dimensional coordination polymers.

Transition metal, driven by their preferred coordination geometry can act as acceptor units that can self assemble with the donor ligands into predictable structures. The metals in fact act as nodes into the scaffold and favours the formation of the supramolecular assembly⁸⁻¹⁰.

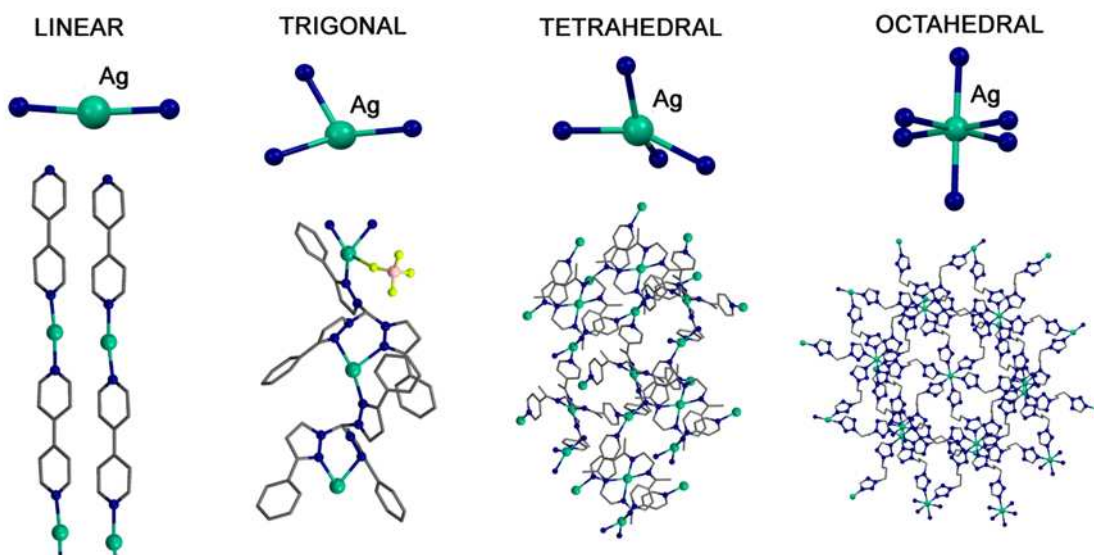


Figure 3. Silver metal ions geometry and the corresponding coordination polymers.

The ligand plays a key role in the control of the architectures. It has to be at least a bridging ligand in order to build network^{11,12}. These ligands are called multitopic depending on the number of donor atoms. Also the mutual orientation of these donor atoms define the ligand geometry and so the coordinative directionality. For example, multicarboxylate ligands are largely used to design coordination polymers¹³⁻¹⁵. They can describe bridges or define angle of 120 degree in the structures. The steric control and the coordination sites orientations are crucial in the design of a porous materials.

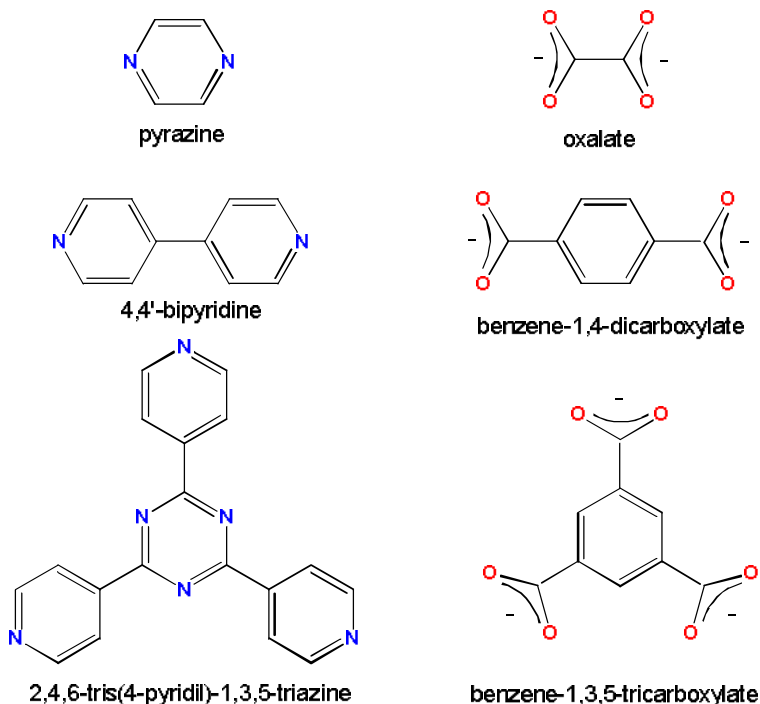


Figure 4. Examples of nitrogen and oxygen donors ligands useful for the construction of coordination polymers.

Ingenious modifications of the organic ligands can control the physical and chemical properties. For example in PCPs the size, the shape and the geometry of the pore are dominated by the length, the shape and the orientation of ligands. The elegant kinetic reversibility between complementary building blocks in the coordination polymers yield a new way to yield a “correct” product that is thermodynamically more stable than the starting components. This is possible thanks to the synergy of metal-ligand bond energies (15-50 kcal/mol) and weak interactions (0.5-10 kcal/mol) which stabilizes a supramolecular isomer with respect to the others. Another main feature of the ligand is the flexibility. Flexible ligand can give rise to flexible architectures useful in the design of porous materials. But on the other hand a rigid ligand can afford robust coordination polymer highly sought because of the foreseeable wide applications. In fact last decade has seen enormous research efforts in the synthesis of materials for reversible exchange of guest molecules. The problem with host/framework stability in the absence of guest molecules is fundamental to design materials for catalysis, gas storage⁵ and gas separation¹⁶⁻¹⁸. The coordination

polymers' applications are not confined in zeolitic behavior but range in luminescence¹⁹, chirality, non linear optics²⁰, magnetism²¹, conductivity, controlled drug release materials²² and many others.

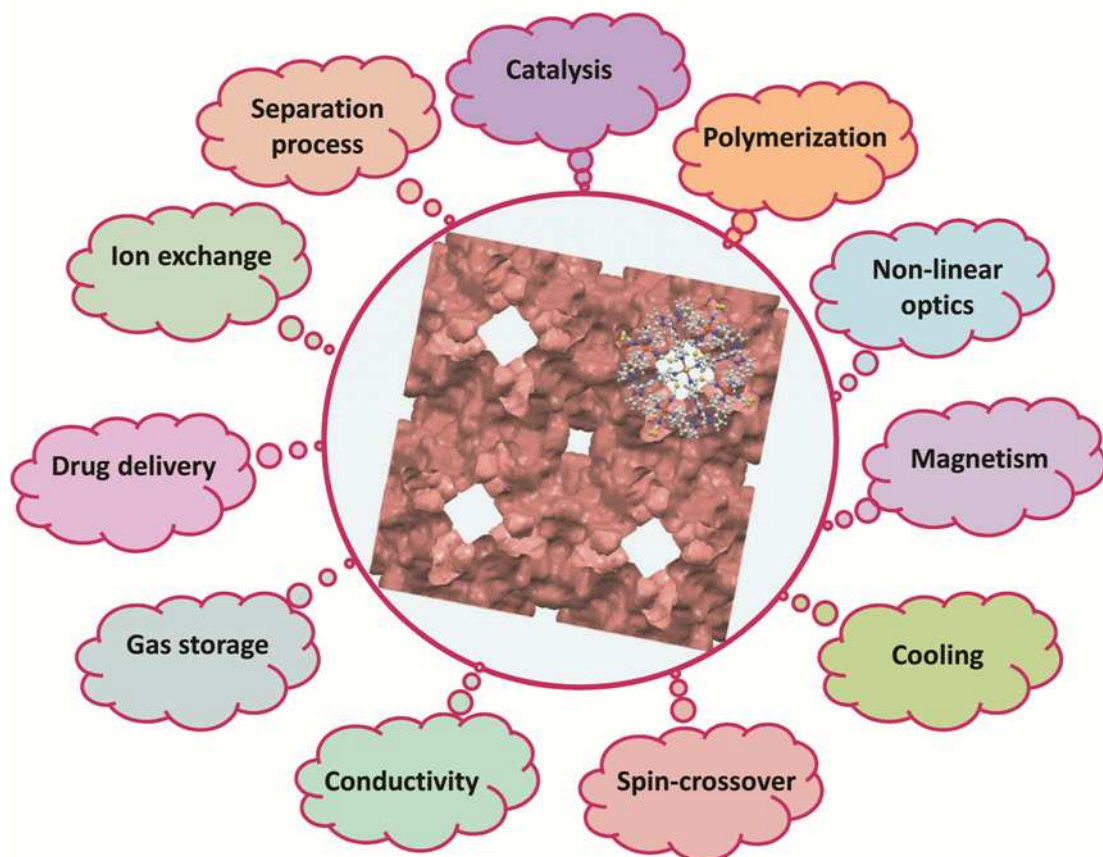
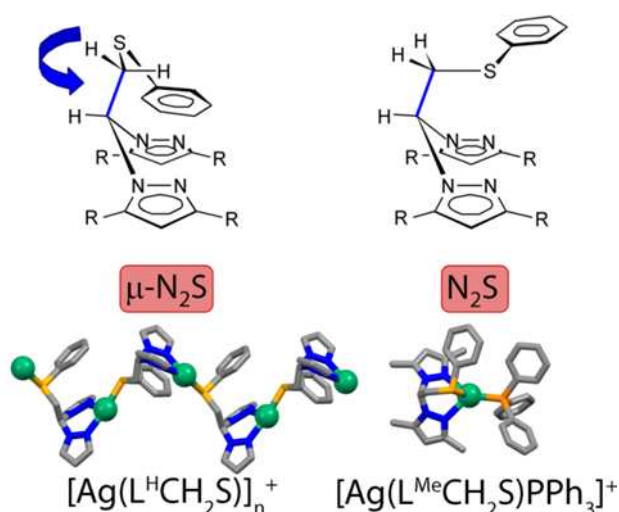


Figure 5. A chart of possible applications of three-dimensional coordination polymers.

For these reason in the following chapters we focus our attention on how ligand conformation and characteristics can influence the molecular structures and what type of interactions are involved in self-assembled porous molecular capsules²³. We studied how slight ligand modifications (steric and electronic) can yield different type of coordination polymers. We have also investigated how weak interactions can influence the porosity in specific coordination polymers.

CHAPTER 2

Crystal engineering of multidimensional Copper (I) and Silver (I) coordination polymers with flexible ligands.



In this chapter²⁴ we present here a new ligand class based on a bispyrazole scaffold functionalized with a flexible ($-\text{CH}_2\text{-S-Ph}$) thioether function: $\text{L}^{\text{R}}\text{CH}_2\text{S}$. The steric and electronic features are varied by changing the substituents on the 3 and 5 positions of the pyrazoles ($\text{R}=\text{H}$, Me, *i*-Pr). The X-ray molecular structures of Ag(I) and Cu(I) binary complexes with $\text{L}^{\text{R}}\text{CH}_2\text{S}$ using different types of counterions (BF_4^- , PF_6^- and CF_3SO_3^-) reveal that the ligands are suitable components for the construction of coordination polymers. In these complexes, the ligands N_2 chelate on a metal center and bridges on a second metal with the thioether group yielding a polymer. On the other hand, when using triphenylphosphine as an ancillary ligand, mononuclear ternary complexes $[\text{M}(\text{L})\text{PPh}_3]^+$ ($\text{M}=\text{Cu}(\text{I})$, $\text{Ag}(\text{I})$; $\text{L}^{\text{R}}\text{CH}_2\text{S}$) are formed. Therefore, from preliminary results, the methylene group acting as spacer in $\text{L}^{\text{H}}\text{CH}_2\text{S}$ imparts an inherent flexibility to this ligands so the conformation responsible of the N_2S chelation is energetically accessible.

2.1. Introduction

Coordination polymers have attracted much attention because of their possible use in the development of new functional material. In fact the possible applications of these various 1- to 3-dimensionality systems can be grouped into diverse fields such as catalysis²⁵, gas adsorption²⁶ (gas separation²⁷ and gas storage^{28,29}), molecular recognition³⁰, luminescence^{31,32}, magnetism^{33,34}, and drug-delivery³⁵. Crucial to the development of coordination architectures is the ability to design multitopic organic ligands that can bind the metal center in a predictable way determined by their preferred conformation. With this respect the ligands may be defined as rigid or flexible according to the high or low energy barrier, respectively, that separates two or more ligand conformers³⁶. The choice of the metal atom as node in the construction of coordination polymers is also of great importance since its stereoelectronic requirements, i.e. coordination numbers and geometry, heavily influence the overall shape of the resulting polymer. Ag(I) is a fashionable metal node for the construction of coordination polymers and it has been used extensively for this purpose. The lack of crystal field effect allows for the occurrence of different coordination geometries, but the most common are the linear, trigonal planar, T-shaped, and tetrahedral geometries. In literature there are many example of Ag(I) coordination polymers in which the nature of the donor ligand may lead to the formation of different frameworks with tailored structures and functions^{37–43}. In this chapter we present a ligand class based on the bis-pyrazole system functionalized with a flexible (–CH₂–S–Ph) thioether function: L^RCH₂S (R=H, Me, iPr), (Figure 6). The molecular structures of Ag(I) and Cu(I) complexes with L^RCH₂S using different types of counterions (BF₄[–], PF₆[–] and CF₃SO₃[–]) are reported and they show how the flexibility of the thioether group influences the formation of polymeric structures. Ternary complexes using triphenylphosphine as ancillary ligand of the type [M(L^RCH₂S)PPh₃] (M=Cu(I) and Ag(I)) are also described and they more clearly show the different conformational behavior of ligands.

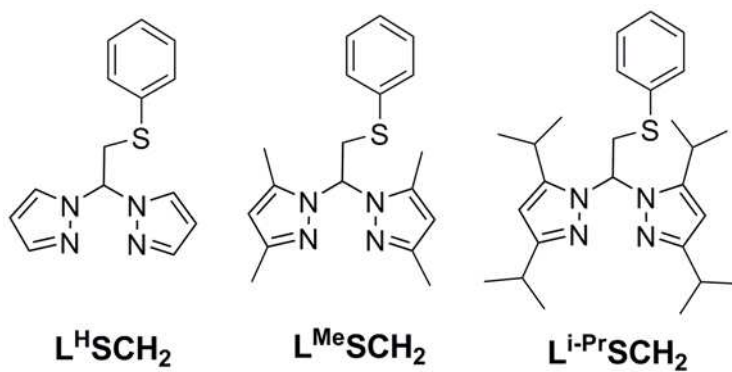


Figure 6. Synthesized ligands $L^R CH_2 S$ with different substituents on 3 and 5 positions of pyrazoles.

2.2. Experimental

2.2.1. Synthesis

General Procedures: All reagents and solvents were commercially available, except for 3,5-dimethylpyrazole, 3,5-diisopropylpyrazole, 2-(phenylthio)acetaldehyde, bis(pyrazolyl)ketone, bis(3,5-dimethylpyrazolyl)ketone, bis(3,5-diisopropylpyrazolyl)ketone, which were prepared as reported elsewhere^{44–46}. Tetrahydrofuran (THF) were distilled over Na/benzophenone. The syntheses of the ligands were performed in inert gas (N₂) using Schlenk techniques. ¹H and ¹³C NMR spectra were recorded on a Bruker Avance 300 spectrometer using standard Bruker pulse sequences. Chemical shifts are reported in parts per million (ppm) referenced to residual solvent protons. Infrared spectra were recorded from 4000 to 700 cm⁻¹ on a Perkin-Elmer FTIR Nexus spectrometer equipped with a Smart Orbit HATR accessory (diamond crystal). Elemental analyses (C, H, and N) were performed with a Carlo Erba EA 1108 automated analyzer.

Synthesis of 1,1'-(2-(phenylthio)ethane-1,1-diyl)bis(1*H*-pyrazole) (**L^HCH₂S**). A mixture of bis(pyrazolyl)ketone (1.90 g, 11.71 mmol), (phenylthio)acetaldehyde (2.00 g, 13.14 mmol) and CoCl₂·6H₂O (5 mg) was heated at 80°C for an hour with stirring. The mixture was then cooled at room temperature and stirred overnight. Dichloromethane (30 mL) was added and the mixture was stirred for 30 minutes. The organic phase was washed with water (50 mL) and brine (20 mL), dried with anhydrous Na₂SO₄ and filtered. The solution was concentrated under vacuum yielding a dark brown oil (yield 2.86 g, 89%). IR (cm⁻¹): 3117w, 3057w, 1747m, 1388m, 1086m, 1035m, 737s, 689s, 618m. ¹H NMR (300 MHz, CDCl₃): δ, 4.01 (d, *J* = 7.5 Hz, 2H, CH₂), 6.27 (t, *J* = 2.1 Hz, 2H, CH Pz), 6.40 (t, *J* = 7.2 Hz, 1H, CH), 7.37 (m, 5H, CH Ph), 7.56 (dd, *J*₁ = 2.1 Hz, *J*₂ = 9.6 Hz, 4H, CH Pz). Anal. Calc. for C₁₄H₁₄N₄S (270.35): C, 62.19; H, 5.22; N, 20.72. Found: C, 61.96; H, 5.07; N, 20.51.

Synthesis of 1,1'-(2-(phenylthio)ethane-1,1-diyl)bis(3,5-dimethyl-1*H*-pyrazole) (**L^{Me}CH₂S**). The procedure used to prepare L^HCH₂S was applied by using a mixture of bis(3,5-dimethylpyrazolyl)ketone (2.18 g, 9.88 mmol), 2-(phenylthio)acetaldehyde (1.50 g, 9.85 mmol) and CoCl₂·6H₂O (5 mg). The solvent was removed under vacuum and a dark green oil was obtained (yield 2.00 g, 62%). IR (cm⁻¹): 2920m, 2865m, 1742m, 1559s, 1438m, 1416s, 1378m, 1312m, 1268w, 1024s, 780m, 739s, 690m. ¹H NMR (300 MHz, CDCl₃): δ, 2.16 (s br, 6H, CH₃), 2.18 (s br, 6H, CH₃), 4.09 (d, *J* = 7.2 Hz, 2H, CH₂), 5.75 (s, 2H, CH Ph), 6.25 (t, *J* = 7.2 Hz, 1H, CH_{central}), 7.27 (m, 5H, CH Ph). Anal.

Calc. for $C_{18}H_{22}N_4S$ (326.46): C, 66.22; H, 6.79; N, 17.16. Found: C, 66.09; H, 6.21; N, 17.01%.

Synthesis of 1,1'-(2-(phenylthio)ethane-1,1-diyl)bis(3,5-diisopropyl-1H-pyrazole) (L^HPrCH_2S). The procedure used to prepare L^HCH_2S was applied by using a mixture of bis(3,5-diisopropylpyrazolyl)ketone (0.77 g, 2.34 mmol), 2-(phenylthio)acetaldehyde (0.36 g, 2.34 mmol) and $CoCl_2 \cdot 6H_2O$ (5 mg). The solvent was removed under vacuum and the crude was purified by silica column chromatography (hexane: ethyl acetate 95:5, r.f. 0.22) and a dark green oil was obtained (yield 0.30 g, 29%). IR (cm^{-1}): 2972m, 2932m, 2868w, 1665w, 1546m, 1473m, 1459w, 1331w, 1315m, 1260w, 1178w, 1064m, 1016m, 931w, 808s, 750m, 701m, 652w, 557w. 1H NMR (300 MHz, $CDCl_3$), δ : 0.86 (d, J = 6.9 Hz, 12 H, CH_3 i-Pr), 1.26 (d, 12 H, CH_3 i-Pr), 2.91 (m, J = 6.9 Hz, CH i-Pr), 3.21 (m, 2H, CH i-Pr), 4.09 (d, J = 7.2 Hz, 2H, CH_2) 5.84 (s, 2H, CH Pz), 6.59 (t, J = 7.2 Hz, 1H, $CH_{central}$), 7.16-7.24 (m, 3H, CH Ph), 7.36 (d, 2H, CH Ph). Anal. Calc. for $C_{26}H_{38}N_4S$ (438.67): C, 71.19; H, 8.73; N, 12.77. Found: C, 70.99; H, 8.66; N, 12.39%.

Synthesis of $[Ag(L^HCH_2S)]_n(BF_4)_n$ (**1**). L^HCH_2S (260 mg, 0.95 mmol) and $AgBF_4$ (186 mg, 0.95 mmol) were mixed in acetone (6 mL), and the colorless solution was stirred for 1 h. The solvent was then removed under vacuum yielding a pale pink solid (180 mg, yield 43%). The compound was recrystallized by stratifying diethyl ether over an acetone solution of the complex, yielding colorless crystals. IR (cm^{-1}): 3117 w, 3008w, 1683m, 1445m, 1400m, 1364w, 1290m, 1227m, 1017s, 971m, 906m, 774m, 745s, 687m, 617m, 485w. 1H NMR (300 MHz, $(CD_3)_2CO$): 4.45 (d, J = 7.5 Hz, 2H, CH_2), 6.52 (t, J = 2.1 Hz, 2H, CH(Pz)), 7.25 (t, J = 7.5 Hz, 1H, $CH_{central}$), 7.34-7.48 (m, 5H, CH(Ph)), 7.81 (d, J = 1.8 Hz 2H, CH(Pz)), 8.25 (d, J = 2.4 Hz 2H, CH(Pz)). Anal. Calc. for $C_{14}H_{14}AgBF_4N_4S$ (464.00): C, 36.21; H, 3.04; N, 12.07. Found: C, 36.45; H, 3.29; N, 12.46%.

Synthesis of $[Cu(L^HCH_2S)]_n(BF_4)_n$ (**2**). In a Schlenk flask under an inert atmosphere (N_2), a solution of $[Cu(MeCN)_4]BF_4$ (240 mg, 0.76 mmol) in 7 mL of dry MeCN was added to a solution of L^HCH_2S (206 mg, 0.76 mmol) in 8 mL of dry MeCN. The colorless solution was stirred for 30 min. The solvent was then concentrated under vacuum, and a white solid was precipitated after addition of diethyl ether. The mixture was filtered under nitrogen to afford a yellow solid (334 mg, yield 97%). The compound was recrystallized by stratifying hexane over a dichloromethane solution of the complex, which yielded colorless crystals. IR (cm^{-1}): 3130w, 1441w, 1403m, 1289m, 1022s, 900m, 747s, 690m, 614m, 520m. 1H NMR (300 MHz, $CDCl_3$): δ 3.80 (s br, 2H, CH_2), 6.22 (s br, 2H, CH(Pz)), 7.15-7.35 (m br, 6H, CH(Ph) and $CH_{central}$), 7.52 (s br, 2H,

CH(Pz)), 8.00 (s br, 2H, CH(Pz)). *Anal.* Calc. for $C_{14}H_{14}CuBF_4N_4S$ (420.02): C, 40.00; H, 3.36; N, 13.33. Found: C, 39.76; H, 3.65; N, 13.05%.

Synthesis of $[Ag(L^{Me}CH_2S)]_n(BF_4)_n$ (3). $L^{Me}CH_2S$ (180 mg, 0.55 mmol) and $AgBF_4$ (107 mg, 0.55 mmol) were mixed in acetone (10 mL). The mixture was stirred for 15 min yielding a white precipitate. The solid was filtered and vacuum dried. (110 mg, 38%). The compound was recrystallized by stratifying diethyl ether over a methanol solution of the complex, yielding colorless crystals. IR (cm^{-1}): 2925w, 1558m, 1466m, 1442m, 1419m, 1393m, 1319m, 1271m, 1232m, 1024s, 920s, 876m, 801m, 753s, 704m, 690w, 667w, 654w. 1H NMR (300 MHz, $(CD_3)_2CO$): δ 2.45 (s, 6H, CH_3), 2.85 (s, 6H, CH_3), 4.37 (d, $J = 7.2$ Hz, 2H, CH_2), 6.10 (s, 2H, CH(Pz)), 6.60 (t, $J = 7.2$ Hz, 1H, CH), 7.40 (m, 5H, CH(Ph)). *Anal.* Calc. for $C_{18}H_{22}AgBF_4N_4S$ (520.06): C, 41.53; H, 4.26; N, 10.77. Found: C, 41.96; H, 4.53; N, 10.55%.

Synthesis of $[Cu(L^{Me}CH_2S)]_n(BF_4)_n$ (4). In a Schlenk flask under an inert atmosphere (N_2), a solution of $[Cu(MeCN)_4]BF_4$ (204 mg, 0.65 mmol) in 7 mL of dry MeCN was added to a solution of $L^{Me}CH_2S$ (212 mg, 0.65 mmol) in 7 mL of dry MeCN. The red solution was stirred for 30 min. The solvent was then concentrated under vacuum and a white solid was precipitated after addition of diethyl ether. The mixture was filtered under nitrogen to afford a white solid (279 mg, yield 93%). The compound was recrystallized by stratifying hexane over a dichloromethane solution of the complex, which yielded colorless crystals. IR (cm^{-1}): 3326w, 3002w, 2920w, 1736w, 1556m, 1419m, 1386m, 1315m, 1265m, 1024s, 739m, 690m, 520m. 1H NMR (300 MHz, $CDCl_3$): δ 1.83 (s br, 6H, CH_3), 2.22 (s br, 6H, CH_3), 3.86 (d, $J = 5.3$ Hz, 2H, CH_2), 5.81 (s br, 2H, CH(Pz)), 6.54 (t, $J = 6.7$ Hz, 1H, CH), 7.08 (m br, 5H, CH(Ph)). Broad peaks are most likely a consequence of the fluxional behaviour of the complex. *Anal.* Calc. for $C_{18}H_{22}BCuF_4N_4S$ (476.09): C, 45.37; H, 4.66; N, 11.77. Found: C, 45.20; H, 4.22; N, 11.52%.

Synthesis of $[Ag(L^{Me}CH_2S)]_n(PF_6)_n$ (5). $L^{Me}CH_2S$ (323 mg, 0.98 mmol) and $AgBF_4$ (249 mg, 0.98 mmol) were mixed in acetone (10 mL). The mixture was stirred for 15 min yielding a white precipitate. The solid was filtered and vacuum dried. (405 mg, 70%). The compound was recrystallized by stratifying diethyl ether over a methanol solution of the complex, yielding colorless crystals. IR (cm^{-1}): 3402w, 2926w, 1736w, 1560m, 1467m, 1420m, 1442m, 1392m, 1319m, 1239m, 1123w, 1037m, 983w, 830s, 750s, 690s, 654m, 555s, 527m. 1H NMR (300 MHz, $(CD_3)_2CO$): δ 2.45(s, 6H, CH_3), 2.94 (s, 6H, CH_3), 4.37 (d, $J = 7.2$ Hz, 2H, CH_2), 6.10 (s, 2H, CH(Pz)), 6.60 (t, $J = 7.2$ Hz, 1H, CH), 7.40 (m, 5H, CH(Ph)). *Anal.* Calc. for $C_{18}H_{22}AgF_6N_4PS$ (578.03): C, 37.37; H, 3.84; N, 9.69. Found: C, 37.56; H, 4.02; N, 9.95%.

Synthesis of $[Ag(L^{iPr}CH_2S)]_n(PF_6)_n$ (6). $L^{iPr}CH_2S$ (78 mg, 0.17 mmol) and $AgPF_6$ (46 mg, 0.17 mmol) were mixed in acetone (10 mL), and stirred for 20 min. The solution was then concentrated and a white solid precipitated after addition of diethyl ether. The solid was filtered, vacuum dried, and recovered. (105 mg, yield 86%). The compound was recrystallized by stratifying diethyl ether over an acetone solution of the complex, yielding colorless crystals. IR (cm^{-1}): 2969m, 2925w, 2865w, 1714w, 1550m, 1462m, 1434m, 1380m, 1287m, 1259w, 1215w, 1177m, 1111w, 1045w, 1012w, 925w, 821s, 749m, 687m, 651m, 552s, 486m. 1H NMR (300 MHz, CD_2Cl_2): δ 1.23 (m, 18H, CH_3), 1.30 (d, $J = 7.2$ Hz, 6H, CH_3), 2.46 (m br, 2H, CH_{iPr}), 2.82 (m, $J = 7.2$ Hz, 2H, CH_{iPr}), 4.09 (s br, 2H, CH_2), 6.11 (s, 2H, $CH(Pz)$), 6.28 (t br, 1H, $CH_{central}$), 7.42 (s br, 5H, $CH(Ph)$). Broad peaks are most likely a consequence of the fluxional behaviour of the complex. *Anal.* Calc. for $C_{26}H_{38}AgF_6N_4PS$ (690.15): C, 45.21; H, 5.55; N, 8.12. Found: C, 44.92; H, 5.93; N, 8.44%.

Synthesis of $[Ag(L^{Me}CH_2S)]_n(CF_3SO_3)_n$ (7). $L^{Me}CH_2S$ (315 mg, 0.96 mmol) and $AgCF_3SO_3$ (247 mg, 0.96 mmol) were mixed in acetone (10 mL), and a white precipitate formed immediately. The mixture was stirred for 15 min. The solid was filtered and vacuum dried. (150 mg, yield 26%). The compound was recrystallized by stratifying diethyl ether over an ethanol solution of the complex, which yielded colorless crystals. IR (cm^{-1}): 3063w, 2953w, 2920w, 1557m, 1462m, 1444m, 1421m, 1391m, 1325w, 1283s, 1239s, 1224s, 1146s, 1027s, 978m, 920m, 871w, 795s, 755w, 691w. 1H NMR (300 MHz, $(CD_3)_2CO$): δ 2.42 (s, 6H, CH_3), 2.88 (s, 6H, CH_3), 4.36 (d, $J = 7.2$ Hz 2H, CH_2), 6.08 (s, 2H, $CH(Pz)$), 6.58 (t, $J = 7.2$ Hz, 1H, $CH_{central}$), 7.40 (m, 5H, $CH(Ph)$). *Anal.* Calc. for $C_{19}H_{22}AgF_3N_4O_3S_2$ (582.01): C, 39.17; H, 3.81; N, 9.62. Found: C, 39.41; H, 3.99; N, 9.32%.

Synthesis of $[Ag(L^{iPr}CH_2S)]_n(CF_3SO_3)_n$ (8). $L^{iPr}CH_2S$ (77 mg, 0.17 mmol) and $AgCF_3SO_3$ (43 mg, 0.17mmol) were mixed in acetone (10 mL), and stirred for 20 min. The solution was then concentrated and a white solid precipitated after addition of diethyl ether. The solid was filtered, vacuum dried, and recovered. (120 mg, yield 97%). The compound was recrystallized by stratifying hexane over a dichloromethane solution of the complex, yielding colorless crystals. IR (cm^{-1}): 2969m, 2925w, 2870w, 1544m, 1465m, 1385m, 1287s, 1232s, 1155s, 1056m, 1023s, 925m, 886w, 843w, 804w, 684m, 634s, 563m, 508m. 1H NMR (300 MHz, CD_2Cl_2): δ 1.25 (m br, 24H, CH_3), 2.83 (m br, 2H, CH_{iPr}), 3.06 (m br, 2H, CH_{iPr}), 4.13 (m br, 2H, CH_2), 6.11 (s, 2H, $CH(Pz)$), 6.28 (m br, 1H, CH), 7.42 (s br, 5H, $CH(Ph)$). Broad peaks are most likely a consequence of the fluxional behaviour of the complex. *Anal.* Calc. for $C_{27}H_{38}AgF_3N_4O_3S_2$ (694.14): C, 46.68; H, 5.52; N, 8.07. Found: C, 46.85; H, 5.25; N, 8.36%.

Synthesis of $[Ag(L^HCH_2S)PPh_3]BF_4$ (9). A solution of $AgBF_4$ (57 mg, 0.29 mmol) in 8 mL of acetone was added to a solution of L^HCH_2S (80 mg, 0.29 mmol) and triphenylphosphine (68 mg, 0.26 mmol) in 10 mL of acetone. The colorless solution was stirred for 15 min. The solvent was then removed under vacuum, the solid was triturated with hexane, and a white product was recovered by filtration (140 mg, yield 73%). Attempts to recrystallize the complex in different solvent mixtures gave hexagonal crystals and a gluey material. IR (cm^{-1}): 3123w, 3047w, 1518w, 1474m, 1430m, 1397m, 1293m, 1047s, 893m, 745s, 690s, 614m, 504s. 1H NMR (300 MHz, CD_2Cl_2): δ 4.08 (t, $J = 5.1$ Hz, 2H, CH_2), 6.46 (t, $J = 2.4$ Hz, 2H, $CH(Pz)$), 6.99 (d, $J = 8$ Hz, 2H, $CH(Ph)$), 7.13-7.28 (m, 3H, $CH_{central}$ and $CH(Ph)$), 7.44-7.66 (m, 18H, $CH(Ph)$ and $CH(Pz)$), 8.23 (d, $J = 2.4$ Hz, 2H, $CH(Pz)$). *Anal.* Calc. for $C_{32}H_{29}AgBF_4N_4PS$ (726.09): C, 52.89; H, 4.03; N, 7.71. Found: C, 52.56; H, 4.17; N, 7.96%.

Synthesis of $[Cu(L^HCH_2S)PPh_3]BF_4$ (10). In a Schlenk flask, and under an inert atmosphere (N_2), a solution of $[Cu(MeCN)_4]BF_4$ (242 mg, 0.77 mmol) in 15 mL of dry MeCN was added to a solution of L^HCH_2S (210 mg, 0.77 mmol) and triphenylphosphine (202 mg, 0.77 mmol) in 10 mL of dry MeCN. The colorless solution was stirred for 1 hour. The solvent was then concentrated under vacuum and a white solid was precipitated after addition of diethyl ether. The mixture was filtered under nitrogen affording a white solid (82 mg, yield 85%). The compound was recrystallized by stratifying diethyl ether over an acetone solution of the complex, yielding colorless crystals. IR (cm^{-1}): 3182w, 3052w, 1556m, 1430m, 1232w, 1094m, 1948s, 996m, 765m, 745s, 696s, 530m, 510m, 493m. 1H NMR (300 MHz, $(CD_3)_2CO$): δ 4.18 (d, $J = 3.6$ Hz, 2H, CH_2), 6.55 (t, $J = 2.4$ Hz, 2H, $CH(Pz)$), 6.63 (d, $J = 8.1$ Hz, 2H, $CH(Ph)$), 7.17 (t, $J = 8.1$ Hz, 2H, $CH(Ph)$), 7.24 (m, 1H, $CH(Ph)$), 7.38-7.58 (m, 15H, $CH(Ph)$), 7.87 (t, $J = 3.6$ Hz, 1H, $CH_{central}$), 8.35 (d, $J = 2.4$ Hz, 2H, $CH(Pz)$). *Anal.* Calc. for $C_{32}H_{29}CuBF_4N_4PS$ (682.12): C, 56.30; H, 4.28; N, 8.21. Found: C, 56.61; H, 4.55; N, 8.36%.

Synthesis of $[Ag(L^{Me}CH_2S)PPh_3]BF_4$ (11). A solution of $AgBF_4$ (49 mg, 0.25 mmol) in 8 mL of acetone was added to a solution of $L^{Me}CH_2S$ (85 mg, 0.25 mmol) and triphenylphosphine (59 mg, 0.22 mmol) in 10 mL of acetone. The colorless solution was stirred for 15 min. The solvent was then removed under vacuum, the solid was triturated with hexane, and a white product was recovered by filtration (135 mg, yield 77%). The compound was recrystallized by stratifying hexane over a THF solution of the complex, which yielded prismatic colorless crystals and hexagonal crystals. IR (cm^{-1}): 3123w, 3052w, 2970w, 1578w, 1545w, 1518w, 1479m, 1430m, 1397m, 1287m, 1047s, 920m, 899m, 740s, 690s, 614m, 499s. 1H NMR (300 MHz, CD_3CN): δ 2.02 (s, 6H, CH_3), 2.36 (s, 6H, CH_3), 4.02 (d, $J = 7.0$ Hz, 2H, CH_2), 5.99 (s, 2H, $CH(Pz)$), 6.36 (t, $J = 7.1$

Hz, 1H, CH_{central}), 7.03 (d, J = 7.3 Hz, 2H, CH(Ph)), 7.13 (t, J = 7.2 Hz, 2H, CH(Ph)), 7.22 (m, 1H, CH(Ph)) 7.50 (m, 15H, CH(Ph)). *Anal.* Calc. for C₃₆H₃₇AgBF₄N₄PS (782.16): C, 55.23; H, 4.77; N, 7.16. Found: C, 55.54; H, 5.02; N, 7.31%.

Synthesis of [Cu(L^{Me}CH₂S)PPh₃]BF₄ (12). In a Schlenk flask, and under an inert atmosphere (N₂), a solution of [Cu(MeCN)₄]BF₄ (257 mg, 0.82 mmol) in 10 mL of dry MeCN was added to a red solution of L^{Me}CH₂S (270 mg, 0.82 mmol) and triphenylphosphine (215 mg, 0.82 mmol) in 10 mL of dry MeCN. The pale orange solution was stirred for 30 min. The solvent was then concentrated under vacuum and a white solid was precipitated after addition of diethyl ether. The mixture was filtered under nitrogen to afford a pale yellow solid (200 mg, yield 40%). The compound was recrystallized by stratifying hexane over a THF solution of the complex, which yielded colorless crystals. IR (cm⁻¹): 3079w, 3057w, 2997w, 2964w, 2915w, 1572w, 1556m, 1473m, 1345m, 1380m, 1320m, 1271m, 1064s, 909m, 805m, 738s, 684s. ¹H NMR (300 MHz, CDCl₃): δ 1.70 (s, 6H, CH₃), 2.62 (s, 6H, CH₃), 4.05 (s br, 2H, CH₂), 5.95 (s, 2H, CH(Pz)), 6.50 (d, J = 7.8 Hz, 2H, CH(Ph)), 7.11 (t, J = 7.5 Hz, 2H, CH(Ph)) 7.19-7.47 (m, 17H, CH_{central} and CH(Ph)). *Anal.* Calc. for C₃₆H₃₇BCuF₄N₄PS (738.18): C, 58.52; H, 5.05; N, 7.59. Found: C, 58.82; H, 5.21; N, 7.89%.

Synthesis of [Ag(L^{iPr}CH₂S)PPh₃]BF₄ (13). A solution of AgBF₄ (28 mg, 0.14 mmol) in 8 mL of acetone was added to a solution of L^{iPr}CH₂S (65 mg, 0.14 mmol) and triphenylphosphine (37 mg, 0.14 mmol) in 10 mL of acetone. The colorless solution was stirred for 15 min. The solvent was then removed under vacuum, the solid was triturated with hexane, and a white product was recovered by filtration (75 mg, yield 57%). The compound was recrystallized by stratifying hexane over a dichloromethane solution of the complex, which yielded prismatic colorless crystals and hexagonal crystals. IR (cm⁻¹): 3129w, 3052w, 2964w, 1584w, 1551w, 1518w, 1474m, 1436m, 1397m, 1293m, 1047s, 893w, 740s, 690s, 619m, 499s. ¹H NMR (300 MHz, CD₃CN): δ 1.02 (m, 12H, CH₃), 1.17 (d, J = 6.8 Hz, 6H, CH₃), 1.25 (d, J = 6.8 Hz, 6H, CH₃), 2.79 (m, J = 6.8 Hz, 2H, CH_{iPr}), 3.10 (m, J = 6.8 Hz, 2H, CH_{iPr}), 4.06 (d, J = 6.6 Hz, 2H, CH), 6.17 (s, 2H, CH(Pz)), 6.55 (t, J = 6.8 Hz, 1H, CH), 7.11 (m, 2H, CH(Ph)), 7.23 (m, 2H, CH(Ph)), 7.31-7.72 (m, 16H, CH(Ph)). *Anal.* Calc. for C₄₄H₅₃AgBF₄N₄PS (894.28): C, 59.04; H, 5.97; N, 6.26. Found: C, 59.27; H, 6.03; N, 6.41%.

Synthesis of [Cu(L^{iPr}CH₂S)PPh₃]BF₄ (14). In a Schlenk flask, and under an inert atmosphere (N₂), a solution of [Cu(MeCN)₄]BF₄ (60 mg, 0.19 mmol) in 8 mL of dry MeCN was added to a solution of L^{iPr}CH₂S (85 mg, 0.19 mmol) and triphenylphosphine (50 mg, 0.19 mmol) in 10 mL of dry MeCN. The colorless solution was stirred for 15

min. The solvent was then removed under vacuum, the solid was triturated with hexane, and a pale pink product was recovered by filtration (135 mg, yield 86%). The compound was recrystallized by stratifying hexane over a THF solution of the complex, which yielded colorless crystals. IR (cm⁻¹): 2966m, 2931w, 2860w, 1545m, 1468m, 1438m, 1384m, 1310m, 1051s, 917m, 742s, 693s, 527s, 444m. ¹H NMR (300 MHz, (CD₃)₂CO): δ 0.82 (m, 12H, CH_{iPr}), 1.40 (d, J = 6.9 Hz, 6H, CH_{iPr}), 1.45 (d, J = 6.6 Hz, 6H, CH_{iPr}), 1.55 (m, 4H, CH₂(THF)), 2.41 (m, J = 6.9 Hz, 2H, CH_{iPr}), 3.35 (m, J = 6.9 Hz, 2H, CH_{iPr}), 3.39 (m, 4H, CH₂(THF)), 3.88 (d, J = 3.3 Hz, 2H, CH₂), 6.23 (s, 2H, CH(Pz)), 6.30 (d, J = 7.5 Hz, 2H, CH(Ph)), 7.04 (t, J = 7.5 Hz, 2H, CH(Ph)), 7.10-7.23 (m, 17H, CH(Ph) and CH_{central}). *Anal.* Calc. for C₄₄H₅₃BCuF₄N₄PS·(C₄H₈O) (922.36): C, 62.45; H, 6.67; N, 6.07. Found: C, 62.04; H, 6.44; N, 5.90%.

2.2.2. X-ray crystallography

Single crystal data were collected with a Bruker Smart 1000 and on a Bruker Smart APEXII area detector diffractometers (Mo Kα; λ = 0.71073 Å). Cell parameters were refined from the observed setting angles and detector positions of selected strong reflections. Intensities were integrated from several series of exposure frames that covered the sphere of reciprocal space⁴⁷. A multiscan absorption correction was applied to the data using the program SADABS⁴⁸. The structures were solved by direct methods (SIR97^{47,48} and SIR2004)⁴⁹ and refined with full-matrix least-squares (SHELXL-97⁵⁰), using the Wingx software package⁵¹. Graphical material was prepared with the Mercury 2.0⁵² program. Crystallographic data are reported in Appendix i-iii.

2.3. Results and Discussion

2.3.1. Synthesis

The ligands 1,1'-(2-(phenylthio)ethane-1,1-diyl)bis(1*H*-pyrazole)) (L^HCH_2S), 1,1'-(2-(phenylthio)ethane-1,1-diyl)bis(3,5-dimethyl-1*H*-pyrazole)) ($L^{Me}CH_2S$), 1,1'-(2-(phenylthio)ethane-1,1-diyl)bis(3,5-diisopropyl-1*H*-pyrazole)) ($L^{i-Pr}CH_2S$), were prepared as described in the Figure 7.

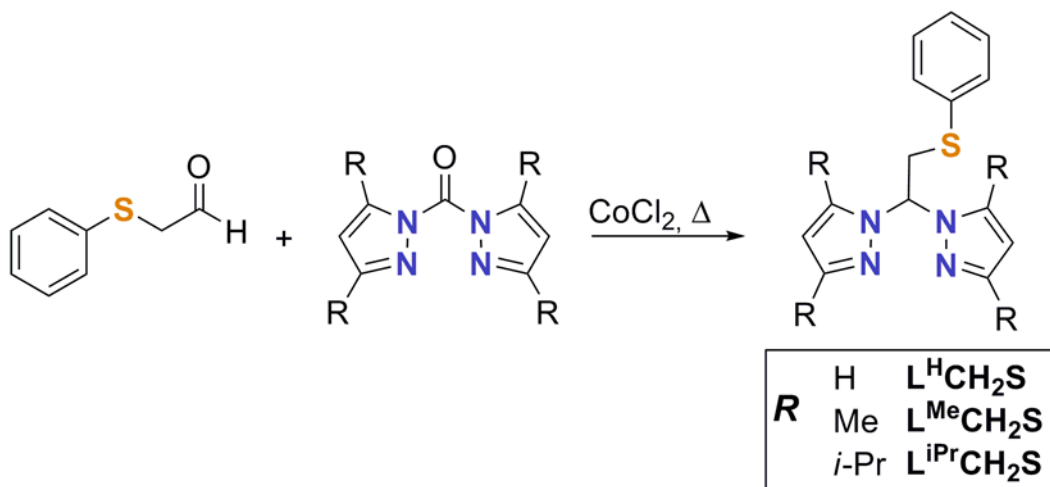


Figure 7. Synthetic path for ligands.

The synthetic route to obtain C-centered functionalized bispyrazole ligands is based on solid state reaction between bis(pyrazolyl)ketones and aldehyde to functionalized the bispyrazole scaffold. The N_2S donor set of the ligand described in this chapter is generated by treating substituted bis(pyrazolyl)ketones with (phenylthio)acetaldehyde using $CoCl_2$ hydrate as catalyst and heating at 110°C overnight. The ligands present a methylene group linking the bis-pyrazole scaffold and the thioether moiety (L^RCH_2S). Moreover, the steric hindrance on the pyrazole ring was increased by substituting the hydrogen atoms in the 3 and 5 positions with methyl or isopropyl groups. To investigate the different coordinative behaviour of the ligands we have employed Ag(I) and Cu(I) cations. The complexes were prepared by treating equimolar amounts (Figure 8) of ligands and $[Cu(MeCN)_4]BF_4$ or Ag(I) salts ($AgBF_4$, $AgPF_6$ and $AgCF_3SO_3$). Different counter anions were employed for the preparation of the Ag(I) complexes in order to study their possible influence in the resulting supramolecular assembly⁵³. The $[M(L)PPh_3]^+$ ternary complexes were prepared by mixing equimolar amounts of metal salts, ligand and PPh_3 . These

syntheses were performed at room temperature and in the air by using acetone or acetonitrile as solvents.

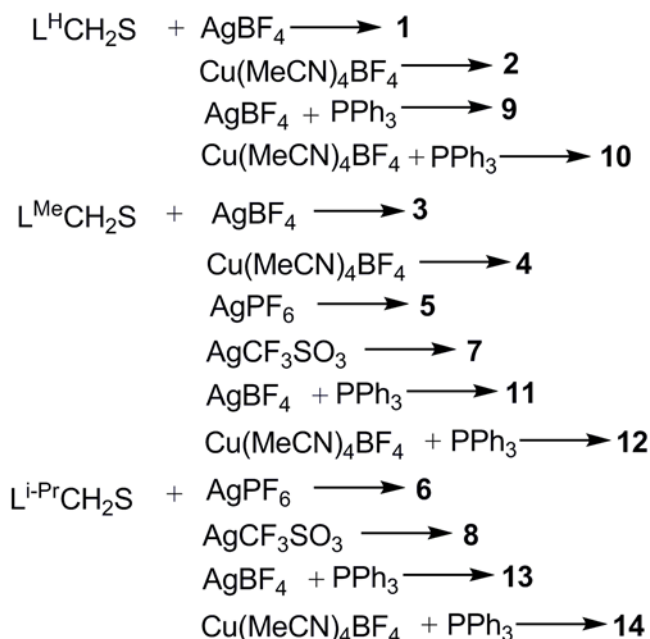


Figure 8. Complexes synthesis.

2.3.2. Solid state structures

The complexes **1**, **2**, **3**, **4**, **5** and **7**, are prepared using the $\text{L}^{\text{H}}\text{CH}_2\text{S}$ or $\text{L}^{\text{Me}}\text{CH}_2\text{S}$ ligands, and they can be described together as they present very similar crystal structures, Figures 9-13. The metal adopts a distorted trigonal planar geometry, with the ligand that N,N chelates on a metal center and bridges with the thioether sulfur atom on a symmetry related metal ion. By inspecting the coordination bond distances, it is evident that in the copper complexes **2**, and **4**, the Cu-N separation varies in the relatively narrow range of 1.958(2)-2.053(2) Å, and the Cu-S bond distance is of 2.17 Å for both compounds.

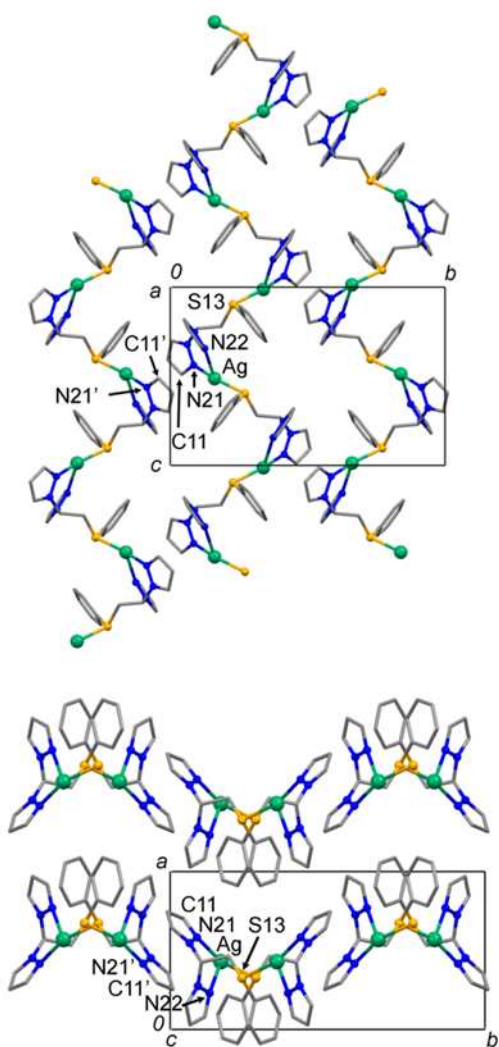


Figure 9. Crystal packing of **1**. The BF_4^- anions and the hydrogen atoms are omitted for clarity. Symmetry code ' = 1-x; -y; 1-z.

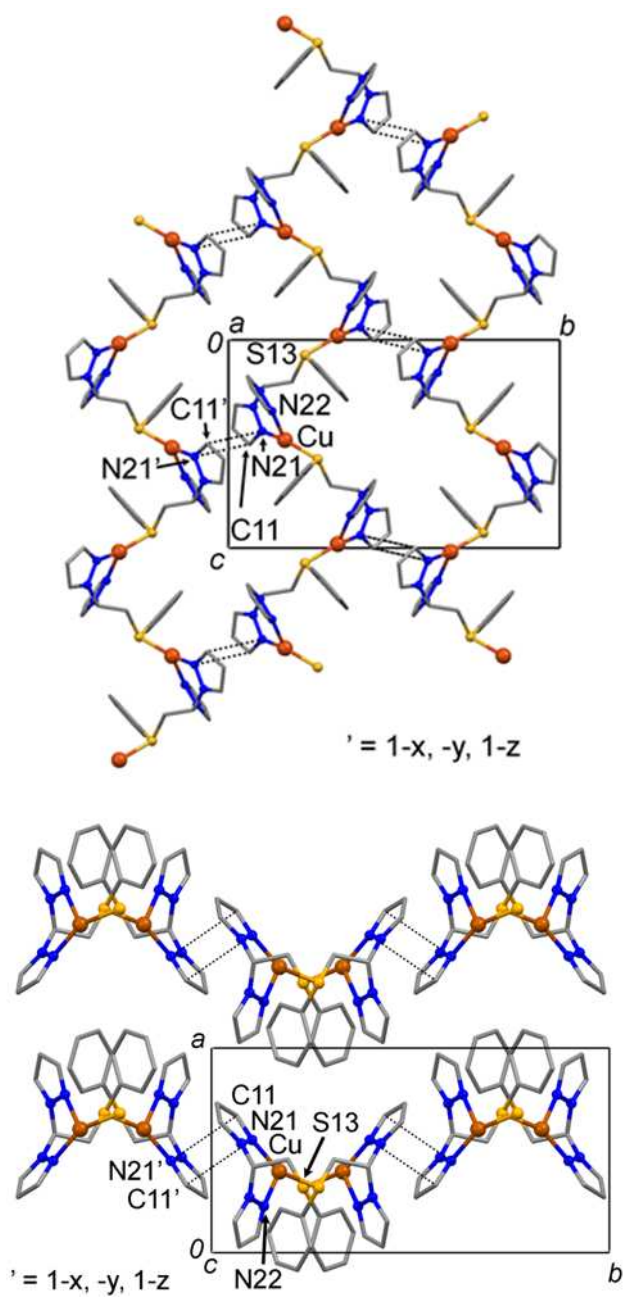


Figure 10. Crystal packing of **2**. The BF_4^- anions and the hydrogen atoms are omitted for clarity.

On the other hand, the silver complexes **1**, **3**, **5**, **7** present a greater variability with respect to the Ag-N bond distances as they are found in the 2.203(2)-2.404(2) Å range. As for the copper complexes, the Ag-S distance is found in a more definite range as it is close to the value of 2.41 Å for all complexes, Tables 1-2.

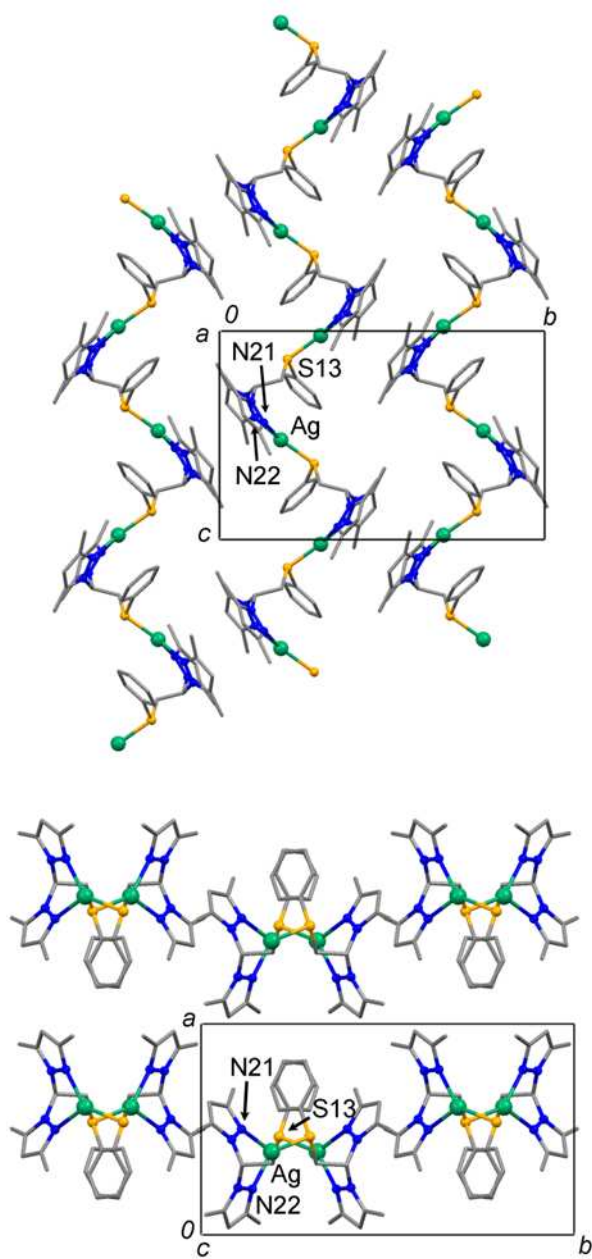


Figure 11. Crystal packing of **3**. The BF_4^- anions and the hydrogen atoms are omitted for clarity.

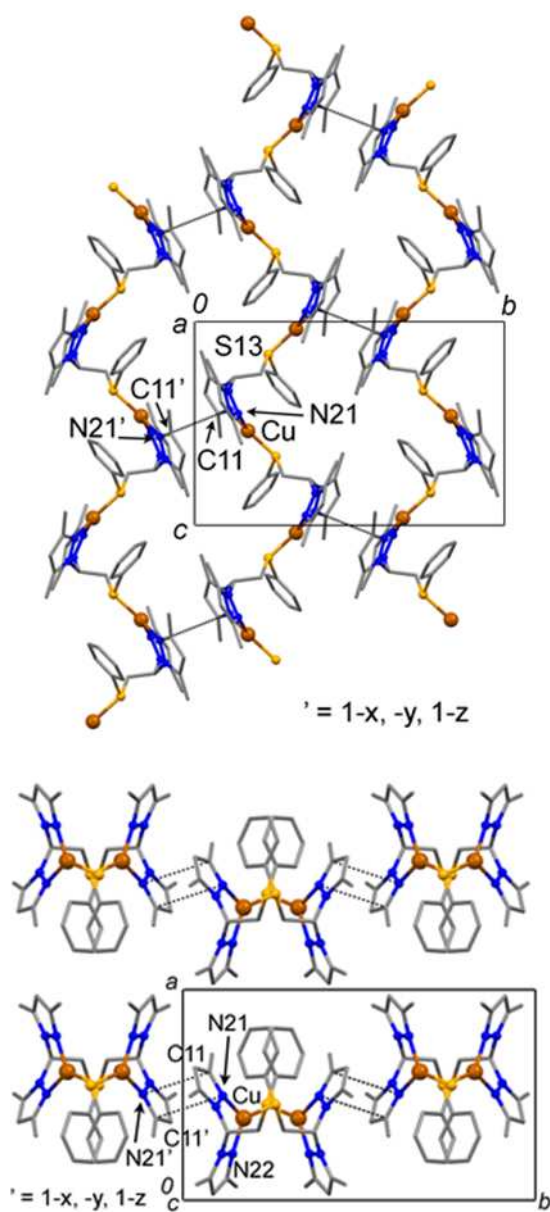


Figure 12. Crystal packing of **4**. The BF_4^- anions and the hydrogen atoms are omitted for clarity.

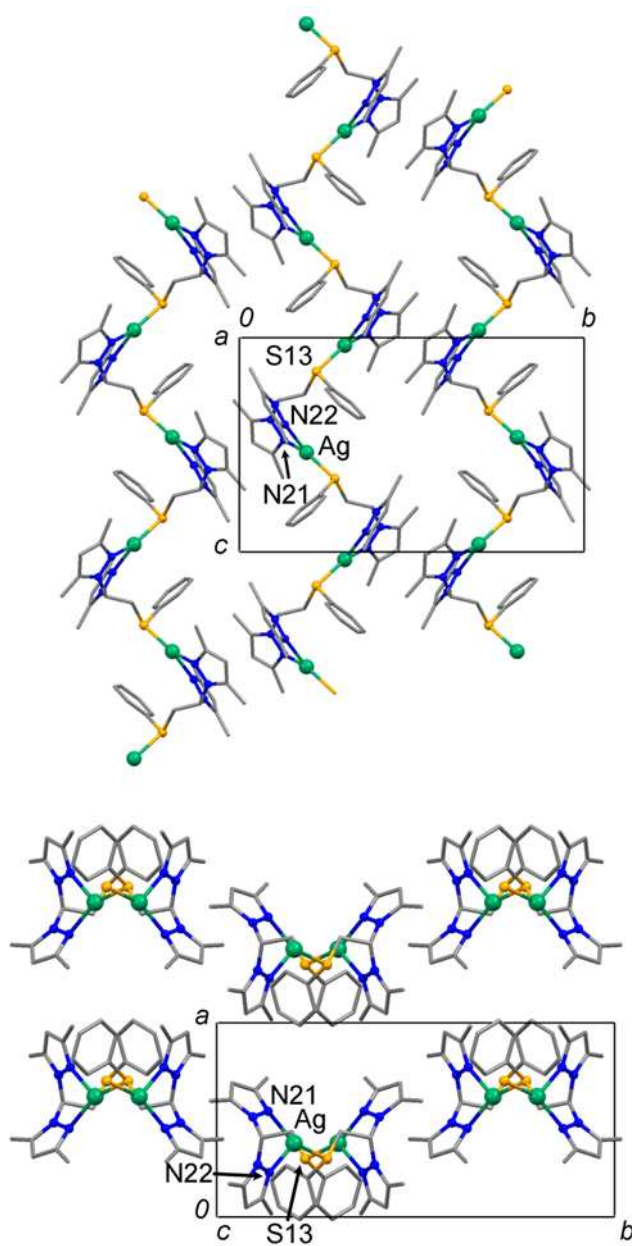


Figure 13. Crystal packing of **5**. The PF_6^- anions and the hydrogen atoms are omitted for clarity

Table 1. Selected bond lengths (Å) and angles (°) for **1**, **3**, **5**, **6**, and **8**

1			
Ag-N(21)	2.203(2)	N(21)-Ag-N(22)	86.43(7)
Ag-N(22)	2.404(2)	N(21)-Ag-S(13)'	162.25(6)
Ag-S(13)'	2.4069(7)	N(22)-Ag-S(13)'	104.43(5)
3			
Ag-N(21)	2.255(3)	N(21)-Ag-N(22)	84.0(1)
Ag-N(22)	2.260(4)	N(21)-Ag-S(13)'	132.1(1)
Ag-S(13)'	2.400(1)	N(22)-Ag-S(13)'	142.9(1)
5			
Ag-N(21)	2.255(3)	N(21)-Ag-N(22)	83.1(1)
Ag-N(22)	2.301(3)	N(21)-Ag-S(13)'	153.50(8)
Ag-S(13)'	2.415(1)	N(22)-Ag-S(13)'	123.07(8)
6			
Ag(1)-N(21)	2.272(3)	N(21)-Ag(1)-N(22)	81.8(1)
Ag(2)-N(22)	2.289(4)	N(21)-Ag(1)-S(16)''	136.19(8)
Ag(1)-S(16)''	2.419(1)	N(22)-Ag(1)-S(16)''	141.85(9)
Ag(2)-N(24)	2.268(3)	N(24)-Ag(2)-N(25)	84.6(1)
Ag(2)-N(25)	2.289(3)	N(24)-Ag(2)-S(13)	135.17(8)
Ag(2)-S(13)	2.429(1)	N(25)-Ag(2)-S(13)	140.24(9)
8			
Ag-N(21)	2.288(3)	N(22)-Ag-N(21)	86.2(1)
Ag-N(22)	2.229(3)	N(22)-Ag-S(13)'''	130.25(9)
Ag-S(13)'''	2.433(1)	N(21)-Ag-S(13)'''	137.90(9)
Ag-O(24)	2.556(3)	N(22)-Ag-O(24)	98.1(1)
		N(21)-Ag-O(24)	105.8(1)
		O(24)-Ag-S(13)'''	90.71(7)

Symmetry codes: ' = x; 1/2-y; 1/2+z, '' = x+1/2; y+1/2; z, ''' = -x+1/2, y+1/2, -z+1/2.

Table 2. Selected bond lengths (Å) and angles (°) for **2**, **4**, and **7**.

2			
Cu-N(21)	1.958(2)	N(21)-Cu-N(22)	94.99(8)
Cu-N(22)	2.053(2)	N(21)-Cu-S(13)'	153.77(6)
Cu-S(13)'	2.1741(7)	N(22)-Cu-S(13)'	110.19(6)
4			
Cu-N(21)	1.990(2)	N(21)-Cu-N(22)	95.50(7)
Cu-N(22)	1.999(2)	N(21)-Cu-S(13)'	127.33(5)
Cu-S(13)'	2.1779(6)	N(22)-Cu-S(13)'	135.22(6)
7			
Ag-N(21)	2.283(3)	N(21)-Ag-N(22)	85.0(1)
Ag-N(22)	2.282(3)	N(21)-Ag-S(13)''	131.64(8)
Ag-S(13)'	2.416(1)	N(22)-Ag-S(13)''	142.50(8)

' = x; 1/2-y; 1/2+z, '' = x; 1/2-y; -1/2+z.

The propensity of the ligand to bridge between two metal centers with the N,N and S donor systems leads to the formation of zig-zag like chains that run parallel to the *c* crystallographic axis, Figures 9-13. To a different degree of strength, the chains interact with each other, or are close to each other, by means of a partial stack of two symmetry related pyrazole rings, in the range of 3.612(4)-3.921(6) Å. This supramolecular interaction between the molecular chains forms a motif that may be described as perpendicular intersecting rectangles, which are occupied by the anions (BF₄⁻, CF₃SO₃⁻ or PF₆⁻). Moreover, by viewing the structure along the *c* crystallographic axis, it can be appreciated how these molecular chains are organized in layers that are parallel to the *bc* crystallographic plane. It may therefore be inferred that the counterion has little influence on the supramolecular aggregation of these complexes. The conformation of the central thioether arm influences the mode of interaction of the chains. The complexes **6** and **8** form zig-zag chains that are analogous to those of the previously described complexes, Figures 14 and 15. Nevertheless, the presence of the *i*Pr groups, in place of the H or Me as substituents on the pyrazole rings, hinders the approach of the pyrazole rings of symmetry related molecules. Hence, the chains do not form the intersecting rectangles found in the previously described complexes.

In **6**, the chains are organized in layers parallel to the *ab* crystallographic plane by interacting through the iPr and phenyl moieties, and the chains belonging to different planes are perpendicular to each other, see Figure 14. At variance with the molecular structures reported so far when using the L^RCH_2S ligands, **8** exhibits the silver atom in a distorted trigonal pyramidal geometry, as a consequence of the coordination of the $CF_3SO_3^-$ anion, $d[Ag-O(24)] = 2.556(3)$ Å, Figure 15.

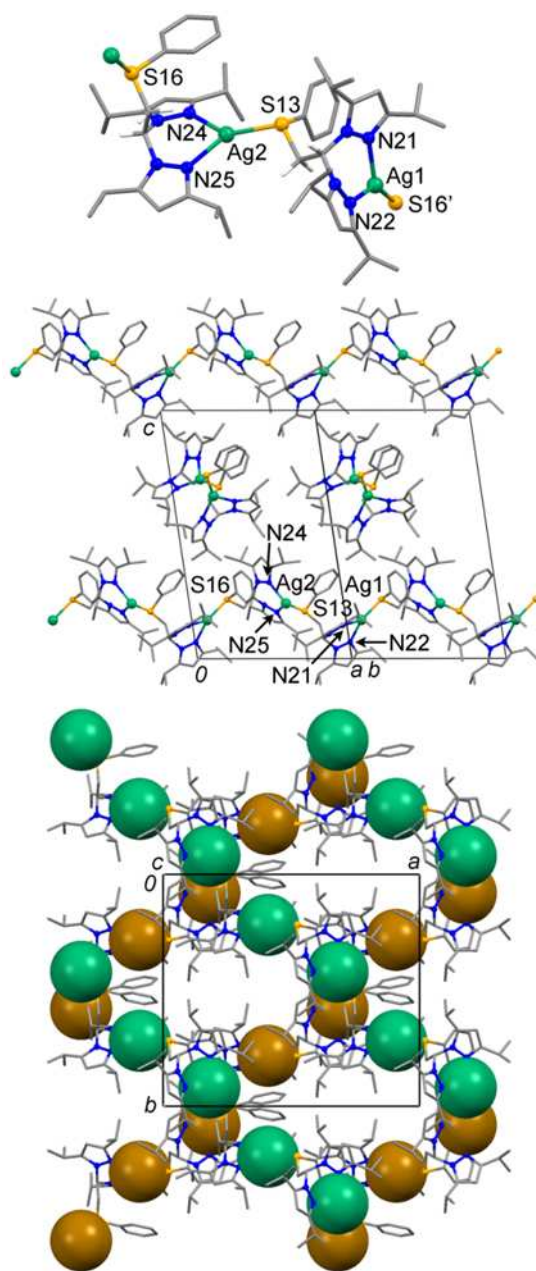


Figure 14. Molecular structure and crystal packing of **6**. The PF_6^- anions, the hydrogen atoms, and the solvent of crystallization are omitted for clarity. Green and brown spheres are the spacefill representations of the silver atoms, which depict the differently oriented molecular chains. Symmetry code $' = \frac{1}{2}+x; \frac{1}{2}+y; z$.

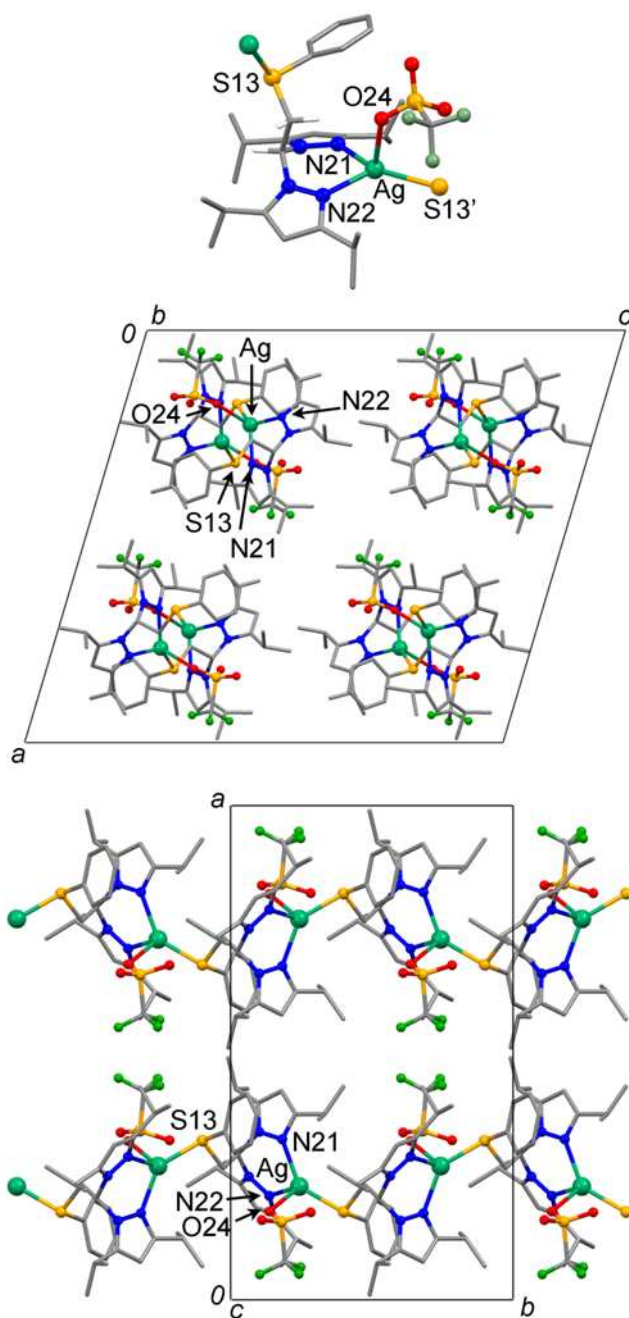


Figure 15. Molecular structure and crystal packing of **8**. The hydrogen atoms and the solvent of crystallization are omitted for clarity. Symmetry code ' = $\frac{1}{2}-x$; $\frac{1}{2}+y$; $\frac{1}{2}-z$.

To further investigate the coordinative behavior of ligands, L^RCH_2S , we have employed triphenylphosphine (PPh_3) as an ancillary ligand for Cu(I) and Ag(I). Mixtures of equimolar amounts L^RCH_2S ligands, PPh_3 , and $AgBF_4$ or $[Cu(CH_3CN)_4]BF_4$ result in the formation of easily recovered $[M(L)PPh_3]BF_4$ ternary complexes from the reaction mixture. The molecular structures of the Cu(I) complexes are reported in Figures 16 and 17. The presence of PPh_3 hinders the formation of coordination polymers so that all of the resulting complexes are mononuclear. **10**, **12** and **14** show the metal in a distorted tetrahedral geometry, and the ligands employ the N_2S donor set. In the present case, the thioether moiety is in a different conformation than that exhibited in the coordination polymers because the sulfur points to the same metal center of the N_2 donor system. In all the complexes, the Cu-N and Cu-P bond distances are in the 1.999(2)-2.065(3) Å and 2.161(6)-2.1863(7) Å ranges, respectively and the Cu-S distance is in the narrow range of 2.4801(8)-2.4860(6) Å (Table 3 and 4). Thus, the increase in the steric hindrance on the pyrazole rings when a hydrogen atom is substituted for an *i*Pr group appears to neither affect the overall geometry of these complexes nor prevent the coordination of a relatively bulky ligand such as PPh_3 . The molecular structures of **11**, and **13** (Figure 18) present the metal in a distorted tetrahedral geometry, and the $L^{Me}CH_2S$ and $L^{iPr}CH_2S$ ligands behave as N_2S tridentate. On average, the coordination bond distances of these silver complexes are more than 0.2 Å longer than those of the copper complexes, which is congruent with the larger size of the silver cation.

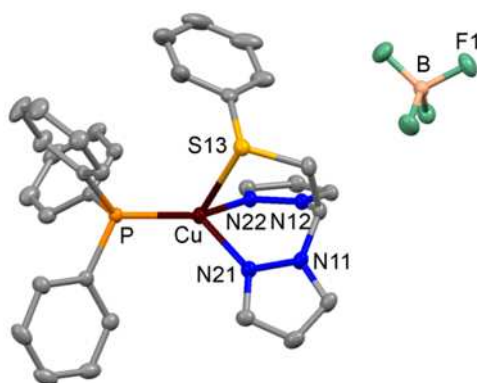


Figure 16. Molecular drawing of **10**. Thermal ellipsoids are drawn at the 30% probability level. The hydrogen atoms are omitted for clarity.

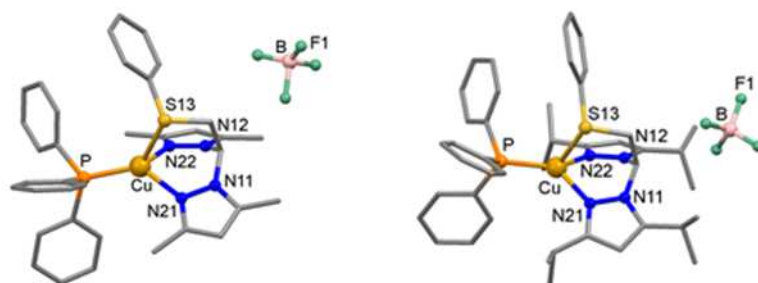


Figure 17. Molecular drawing of **12** and **14**. The hydrogen atoms are omitted for clarity.

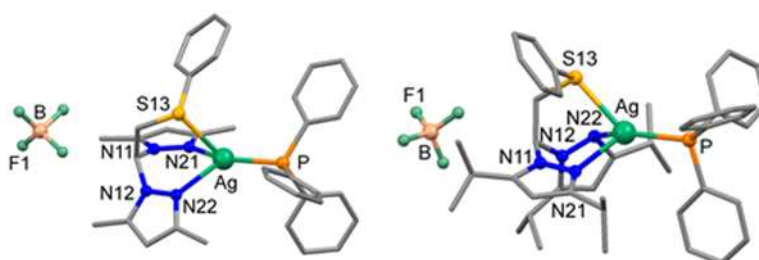


Figure 18. Molecular drawing of **11** and **13**. The hydrogen atoms are omitted for clarity.

In conclusion here we have shown a new class of ligands based on a bispirazolyl scaffold N_2 donors able to chelate a silver ion. The scaffold possess a thioether arm with a S donor function flexible enough to chelate in the N_2S fashion (Figure 19 (B)), but also able to bridge between two metal centers with the N_2 and S donor systems giving rise to coordination polymers (Figure 19 (A)).

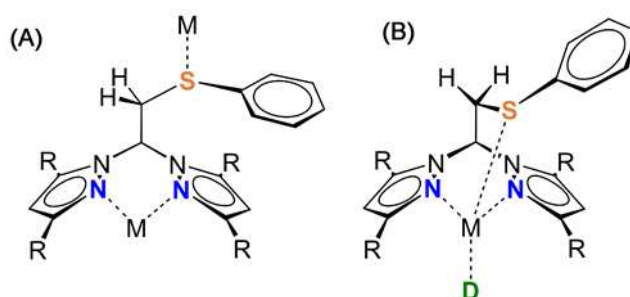


Figure 19. Possible coordination types of L^RCH_2S .

Table 3. Selected bond lengths (Å) and angles (°) for **10**, **12** and **14**.

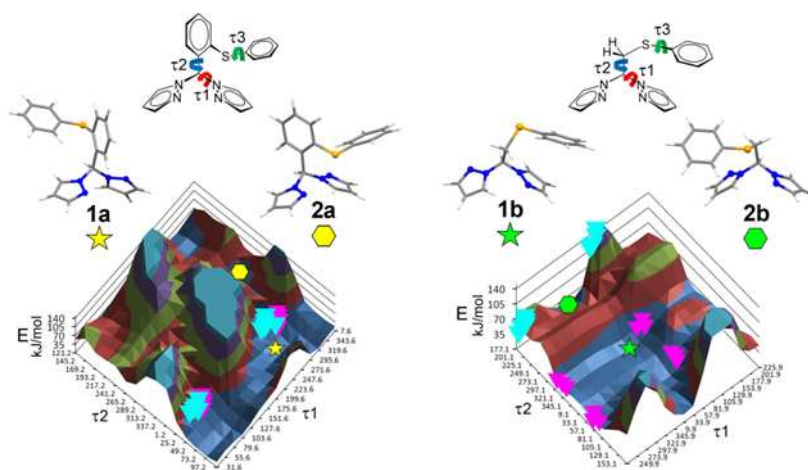
10			
Cu-N(21)	2.030(2)	N(21)-Cu-N(22)	90.55(6)
Cu-N(22)	2.037(2)	N(21)-Cu-P	130.80(5)
Cu-S(13)	2.4860(6)	N(22)-Cu-P	126.13(4)
Cu-P	2.1656(5)	N(21)-Cu-S(13)	90.63(5)
		N(22)-Cu-S(13)	88.81(5)
		P-Cu-S(13)	118.15(2)
12			
Cu-N(21)	2.065(2)	N(21)-Cu-N(22)	92.23(8)
Cu-N(22)	2.028(2)	N(21)-Cu-P	128.98(6)
Cu-S(13)	2.4801(8)	N(22)-Cu-P	126.52(6)
Cu-P	2.1863(7)	N(21)-Cu-S(13)	86.46(6)
		N(22)-Cu-S(13)	89.03(6)
		P-Cu-S(13)	121.25(3)
14			
Cu-N(21)	2.052(2)	N(21)-Cu-N(22)	90.9(1)
Cu-N(22)	2.016(2)	N(21)-Cu-P	133.80(7)
Cu-S(13)	2.4814(9)	N(22)-Cu-P	129.08(7)
Cu-P	2.1804(9)	N(21)-Cu-S(13)	84.95(7)
		N(22)-Cu-S(13)	92.13(8)
		P-Cu-S(13)	111.54(3)

Table 4. Selected bond lengths (Å) and angles (°) for **11** and **13**.

11			
Ag-N(21)	2.277(2)	N(21)-Ag-N(22)	84.55(8)
Ag-N(22)	2.396(2)	N(21)-Ag-P	138.69(6)
Ag-S(13)	2.7345(8)	N(22)-Ag-P	129.73(6)
Ag-P	2.3602(7)	N(21)-Ag-S(13)	81.66(6)
		N(22)-Ag-S(13)	75.67(6)
		P-Ag-S(13)	124.22(3)
13			
Ag-N(21)	2.314(3)	N(21)-Ag-N(22)	83.9(1)
Ag-N(22)	2.497(3)	N(21)-Ag-P	129.93(9)
Ag-S(13)	2.624(1)	N(22)-Ag-P	122.79(9)
Ag-P	2.362(1)	N(21)-Ag-S(13)	86.8(1)
		N(22)-Ag-S(13)	75.25(9)
		P-Ag-S(13)	137.44(4)

CHAPTER 3

Rigid vs Flexible N₂S donor ligands: conformational studies on Cu(I) and Ag(I) complexes.



Here we show²⁴ a new ligands similar to ligands presented in the previous chapter but with a rigid (-Ph-S-Ph) thioether function: L^HPhS. A comparison between Ag(I) and Cu(I) binary complexes built with L^HPhS and L^RCH₂S, respectively, is usefull to demonstrate how the ligand conformation is responsible to the different architectures formed. Several molecular structures of complexes using different types of counterions (BF₄⁻, PF₆⁻) were obtained.. In both cases the ligands are suitable components for the construction of coordination polymers. Also in these complexes, the ligands behaves as N₂ donor on a metal center and bridges on a second metal with the thioether arm. But the steric hindrance due to the phenyl ring used as a linker, instead of a flexible CH₂, determines a completely different behavior of the ligand in presence of ancillary ligands such as thiphenylphosphine. As in chapter 2, mononuclear ternary complexes are formed, but the thioether arm is unable to coordinate the metal center. Throught DFT calculation we demonstrate how the ligand preorganization affects the 3D molecular assembly.

3.1. Introduction

Supramolecular chemistry is an active and ever growing field of investigation where elegant structures are spontaneously generated from smaller building blocks⁵⁴. The components of these assemblies are in many cases represented by an anionic or neutral part in the form of an organic ligand, and by a cationic part represented by a metal center. The ligands can be specifically synthesized in order to incorporate the desired donor atoms in the preferred geometric arrangements. In addition, the different coordination polyhedra, characteristic of opportunely selected metal ions, contribute to the shape of the resulting coordination polymers^{55–57}. Self assembly coordination polymers have attracted attention in recent years especially because of their potential application in material science. The search of new hybrid inorganic-organic materials based on heteroscorpionate ligands is of great interest not only because of their wide variety of amazing molecular structures, but also because of their versatility in metal coordination due to the easy possibility to vary the donor set of the ligand. In the Self-assembly process, thanks to metal-ligand interactions, small molecules aggregate in large species. Other factors interactions play a fundamental role in self-assembled hybrid structures. These factors take into account: 1) the nature of metal center; 2) the type and the geometry of ligand chelation the donor set of ligand; 3) the counterion and last but not least 5) the weak non-covalent As far as the silver and copper complexes are concerned, many other examples can be found in the literature reporting 1D polymeric structures obtained by using nitrogen donor ligands. In some cases, these 1D structures are generated by ligands that act as a bridge between two metal centers thus forming a coordination polymer^{58,59}, whereas in other cases the building blocks are represented by metal complexes that interact with neighboring ones by means of weaker forces such as hydrogen bonds, π - π stacking, or C-H $\cdots\pi$ interactions⁶⁰. By a judicious choice of ligands, these molecular chains can be chiral, either because they form helical structures^{61–64}, or because a chiral ligand has been specifically employed⁶⁵. The choice of metal center results therefore of particular importance: the chemical behavior of silver(I) and copper(I) coordinated through nitrogen pyrazoles of the ligands (for example: bis(pyrazolyl)borates and methane) is well described in the literature. Based on previous reports, most of this monocharged cation complexes are dimeric structures with a ratio M:L 1:2 with the metal center in a distorted tetrahedral geometry without ancillary ligands. More fascinating and less studied from a structural point of view, are the silver complexes based on ditopic heteroscorpionate ligands. Carrano *et al.* studied how silver(I) complexes based on N₂O heteroscorpionate ligand self-

assembled in coordination polymers through hydrogen bonds. In these cases the third arm of the ligand does not take part in to the coordination of the metal center but it is crucial to make hydrogen bonds essential for the building of polymers.

Our approach involved the use of ditopic heteroscorpionate ligand in which a thioether arm is decisive in the construction of the coordination polymers. In the previous chapter we have shown a new class of N_2S ligand in which a bispyrazolyl N_2 scaffold is linked to the thioether arm with a CH_2 , capable of generating coordination polymers with silver(I) and copper(I) molecular. In the present chapter we report a typology of ligand endowed with the same N_2 bispyrazolyl methane moiety, which is functionalized with different substituents linked to the thioether arm with a less flexible linker : a phenyl ring (Figure 20).

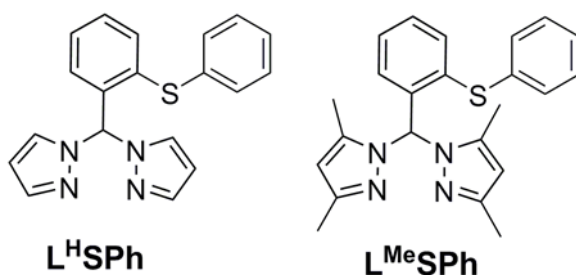


Figure 20. Synthetised ligands.

To estimate again the coordination ability of these heteroscorpionate ligands, Ag(I) and Cu(I) complexes were prepared by treating L^RPhS ($R = H, Me$) with Ag(I) and Cu(I) salts. Here we described the solid state structure of 1D coordination polymers emphasizing the difference between the two ligand classes. The synthesis of ternary complexes using triphenylphosphine as ancillary ligand, as in the previous chapter, are also described to clarify the different conformational behavior of two different ligands L^RPhS and L^RCH_2S .

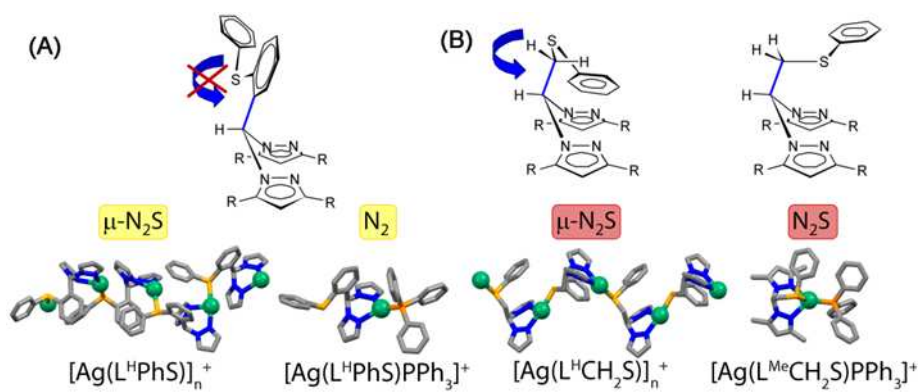


Figure 21 A. Schematic representation of coordination capability of rigid $L^R\text{PhS}$; B. Schematic representation of the coordination abilities for flexible $L^R\text{CH}^2\text{S}$.

3.2 Experimental

3.2.1. Synthesis

General Procedures: All reagents and solvents were commercially available, except for 3,5-dimethylpyrazole, bis(pyrazolyl)ketone and bis(3,5-dimethylpyrazolyl)ketone which were prepared as reported elsewhere^{44–46}. ¹H and ¹³C spectra were recorded on a Bruker Avance 300 spectrometer using standard Bruker pulse sequences. Chemical shifts are reported in parts per million (ppm) referenced to residual solvent protons. Infrared spectra were recorded from 4000 to 700 cm⁻¹ on a Perkin-Elmer FTIR Nexus spectrometer equipped with a Smart Orbit HATR accessory (diamond crystal). Elemental analyses (C, H, and N) were performed with a Carlo Erba EA 1108 automated analyzer.

Synthesis of 1,1'-((2-(phenylthio)phenyl)methylene)bis(1H-pyrazole) (**L^HPhS**). A mixture of bis(pyrazolyl)ketone (0.76 g, 4.68 mmol), 2-(phenylthio)benzaldehyde (1.02 g, 4.76 mmol) and CoCl₂·6H₂O (5 mg) was heated at 80°C for an hour with stirring. The mixture was then cooled at room temperature and stirred overnight. Dichloromethane (30 mL) was added and the mixture was stirred for 30 minutes. The organic phase was washed with water (50 mL) and brine (20 mL), dried with anhydrous Na₂SO₄ and filtered. The solution was concentrated under vacuum and a yellow powder was precipitated with hexane, which was filtered and vacuum dried. The crude was washed with diethyl ether (5 mL) and a white solid was obtained (yield 0.93 g, 60%). IR (cm⁻¹): 3134w, 3095w, 1687w, 1665w, 1440m, 1389m, 1305m, 1083m, 1044m, 795m, 746s, 684s, 624s, 609m, 503m. ¹H NMR (300 MHz, CDCl₃): δ, 6.32 (t, J 2.4 Hz, 2H, CH Pz), 6.94 (m, 1H, CH Ph) 7.20 (m, 8H, CH PhSPh), 7.32 (m, 2H, CH Pz) 7.60 (d, J =1.8 Hz, 2H, CH Pz), 8.21 (s, 1H, CH). Anal.Calc. for C₁₉H₁₆N₄S (332.42): C, 68.65; H, 4.85; N, 16.85. Found: C, 68.54; H, 4.62; N, 16.55%.

Synthesis of 1,1'-((2-(phenylthio)phenyl)methylene)bis(3,5-dimethyl-1H-pyrazole) (**L^{Me}PhS**). The procedure used to prepare **L^HPhS** was applied by using a mixture of bis(3,5-dimethylpyrazolyl)ketone (1.04 g, 4.71 mmol), 2-(phenylthio)benzaldehyde (1.00 g, 4.66 mmol) and CoCl₂·6H₂O (5 mg). A white solid was obtained (yield 1.30 g, 71%). IR (cm⁻¹): 2980w, 2947w, 2920w, 1463m, 1318m, 812m, 797m, 754s, 684m, 619m. ¹H NMR (300 MHz, CDCl₃): δ, 2.08 (s, 6H, CH₃ Pz), 2.20 (s, 6H, CH₃ Pz), 5.85 (s, 2H, CH Pz), 6.90 (t, J =5.7 Hz, 1H, CH Ph), 7.27 (m, 9H, CH PhSPh), 7.99 (s, 1H, CH). Anal. Calc. for C₂₃H₂₄N₄S (388.53): C, 71.10; H, 6.22; N, 14.42. Found: C, 70.93; H, 6.09; N, 14.28%.

*Synthesis of $[Ag(L^HPhS)]_n(BF_4)_n$ (**15**).* L^HPhS (300 mg, 0.90 mmol) and $AgBF_4$ (179 mg, 0.90 mmol) were mixed in acetone (10 mL), and the colorless solution was stirred for 30 min. The solvent was then removed under vacuum, and the white solid was triturated with hexane. The mixture was then filtered to afford a white solid (360 mg, yield 84%). The compound was recrystallized by stratifying diethyl ether over an acetone solution of the complex, which yielded colorless crystals. IR (cm^{-1}): 3128 w, 1693 w, 1589 w, 1512 w, 1441 m, 1397 m, 1287 m, 1024 s, 821 w, 745 s, 690 m, 619 ms, 608 w, 509 m. 1H NMR (300 MHz, $(CD_3)_2CO$): δ , 6.65 (t, J = 2.1 Hz, 1H, CH(Pz)), 7.05 (m, 1H, $CH_{ortho}(Ph)$), 7.28-7.52 (m, 8H, CH(Ph)), 7.84 (d, J = 2.1 Hz, 2H, CH(Pz)), 8.35 (d, J = 2.1 Hz, 2H, CH(Pz)), 8.75 (s, 1H, $CH_{central}$). *Anal.* Calc. for $C_{19}H_{16}AgBF_4N_4S$ (527.09): C, 43.29; H, 3.06; N, 10.63. Found: C, 42.98; H, 3.32; N, 10.40%.

*Synthesis of $[Ag(L^HPhS)]_2(PF_6)_2$ (**16**).* L^HPhS (134 mg, 0.40 mmol) and $AgPF_6$ (100 mg, 0.40 mmol) were mixed in acetone (8 mL), and the colorless solution was stirred for 15 min. The solvent was then concentrated under vacuum and a white solid was precipitated after the addition of diethyl ether. The solid was filtered and vacuum dried (130 mg, yield 56%). The compound was recrystallized by stratifying hexane over a dichloromethane solution of the complex, which yielded colorless crystals. IR (cm^{-1}): 1698 w, 1440 m, 1398 m, 1289 m, 1096 m, 828 s, 747 s, 648 m, 627 m, 607 w, 555 s. 1H NMR (300 MHz, $(CD_3)_2CO$): δ , 6.56 (t, J = 2.4 Hz, 2H, CH(Pz)), 7.17 (m, 1H, CH(Ph)), 7.24-7.52 (m, 8H, CH(Ph)), 7.76 (d, J = 2.4 Hz, 2H, CH(Pz)), 8.35 (d, J = 2.4 Hz, 2H, CH(Pz)), 8.66 (s, 1H, $CH_{central}$). *Anal.* Calc. for $C_{19}H_{16}AgF_6N_4PS$ (585.29): C, 38.99; H, 2.76; N, 9.57. Found: C, 38.76; H, 3.04; N, 10.11%.

*Synthesis of $[Cu(L^HPhS)]_2(BF_4)_2(MeCN)_2$ (**17**).* In a Schlenk flask, under an inert atmosphere (N_2), a solution of $[Cu(MeCN)_4]BF_4$ (147 mg, 0.47 mmol) in 8 mL of dry MeCN was added to a solution of L^HPhS (155 mg, 0.47 mmol) in 10 mL of dry MeCN. The colorless solution was stirred for 15 min. The solvent was then concentrated under vacuum, and a white solid was precipitated after the addition of diethyl ether. The mixture was filtered under nitrogen to afford a white solid (103 mg, yield 88%). The compound was recrystallized by stratifying hexane over a dichloromethane solution of the complex, which yielded colorless crystals. IR (cm^{-1}): 3125 m, 2969 m, 2864 w, 1581 m, 1508 m, 1435 m, 1402 m, 1285 m, 1029 s, 743 m, 690 w, 621 w. 1H NMR (300 MHz, CD_3CN , 235 K): δ 6.46 (t, J = 2.0 Hz, 2H, CH(Pz)), 6.53 (d, J = 8.0 Hz, 1H, $CH_{ortho}(Ph)$), 7.23 (d, J = 7.9 Hz, 1H, CH(Ph)), 7.29-7.37 (m, 7H, CH(Ph)), 7.57 (s br, 1H, CH(Pz)), 7.74 (d, J = 1.6 Hz, 2H, CH(Pz)), 8.26 (s, 1H, $CH_{central}$). *Anal.* Calc. for $C_{42}H_{38}Cu_2B_2F_8N_{10}S_2$ (1047.65): C, 48.15; H, 3.66; N, 13.37. Found: C, 48.38; H, 3.33; N, 13.14%.

Synthesis of [Ag(L^HPhS)PPh₃]BF₄ (18). A solution of AgBF₄ (58 mg, 0.29 mmol) in 8 mL of acetone was added to a solution of L^HPhS (96 mg, 0.29 mmol) and triphenylphosphine (68 mg, 0.26 mmol) in 10 mL of acetone. The colorless solution was stirred for 15 min. The solvent was then removed under vacuum, the solid was triturated with hexane, and a white product was recovered by filtration (170 mg, yield 77%). The compound was recrystallized by stratifying hexane over a dichloromethane solution of the complex, which yielded prismatic colorless crystals and hexagonal crystals. IR (cm⁻¹): 3123w, 3052w, 1512w, 1479m, 1430m, 1403m, 1288m, 1041s, 827w, 740s, 690s, 625m. ¹H NMR (300 MHz, CD₃CN): δ 6.36 (t, J = 1.5 Hz, 2H, CH(Pz)), 6.95 (d, J = 10.8 Hz, 1H, CH(Ph)), 7.20-7.65 (m, 27H, CH(Ph) and CH(Pz)), 8.19 (s, 1H, CH_{central}). *Anal.* Calc. for C₃₇H₃₁AgBF₄N₄PS (788.11): C, 56.34; H, 3.96; N, 7.11. Found: C, 56.24; H, 4.21; N, 7.41%.

Synthesis of [Cu(L^HPhS)PPh₃]BF₄ (19). In a Schlenk flask, under an inert atmosphere (N₂), a solution of [Cu(MeCN)₄]BF₄ (99 mg, 0.32 mmol) in 15 mL of dry MeCN was added to a solution of L^HPhS (106 mg, 0.32 mmol) and triphenylphosphine (86 mg, 0.32 mmol) in 10 mL of dry MeCN. The colorless solution was stirred for 1 h. The solvent was then concentrated under vacuum, and a white solid was precipitated after the addition of diethyl ether. The mixture was filtered under nitrogen to afford a white solid (82 mg, yield 85%). The compound was recrystallized by stratifying hexane over a dichloromethane solution of the complex, which yielded colorless crystals. IR (cm⁻¹): 3117 w, 3041 w, 2975 w, 1726 w, 1435 m, 1047 s, 998 m, 741 s, 691 m, 626 m, 498 m. ¹H NMR (300 MHz, (CD₃)₂CO): δ 6.53 (d, J = 2.1 Hz, 2H, CH(Pz)), 6.91 (t, J = 6 Hz, 1H, CH(Ph)), 7.07 (m, 3H, CH(Ph)), 7.11 (m, 14H, CH(Ph)), 7.52 (m, 6H, CH(Ph)), 8.45 (d, J = 2.1 Hz, 2H, CH(Pz)), 8.79 (s, 1H, CH). *Anal.* Calc. for C₃₇H₃₁CuBF₄N₄PS (745.06): C, 59.65; H, 4.19; N, 7.52. Found: C, 60.32; H, 5.24; N, 7.26%.

Synthesis of [Ag(L^{Me}PhS)PPh₃]BF₄ (20). A solution of AgBF₄ (49 mg, 0.25 mmol) in 8 mL of acetone was added to a solution of L^{Me}PhS (100 mg, 0.25 mmol) and triphenylphosphine (59 mg, 0.22 mmol) in 10 mL of acetone. The colorless solution was stirred for 15 min. The solvent was then removed under vacuum, the solid was triturated with hexane, and a white product was recovered by filtration (160 mg, yield 86%). Attempts to recrystallize the complex in different solvent mixtures gave hexagonal crystals and a gluey material. IR (cm⁻¹): 3118w, 3052w, 2356w, 2159w, 1578w, 1556w, 1474m, 1436m, 1403m, 1288m, 1047s, 827w, 740s, 685s, 630m, 499s. ¹H NMR (300 MHz, CD₃CN): δ 2.11 (s, 6H, CH₃), 2.35 (s, 6H, CH₃), 6.03 (s, 2H, CH(Pz)),

6.79 (m, 2H, CH(Ph)), 7.11 (m, 1H, CH(Ph)), 7.19 (m, 2H, CH(Ph)), 7.27-7.37 (m, 10H, CH(Ph)), 7.44 (m, 6H, CH(Ph)), 7.54 (m, 3H, CH(Ph)), 7.70 (s, 1H, CH_{central}). *Anal.* Calc. for C₄₁H₃₉AgBF₄N₄PS (844.17): C, 58.28; H, 4.66; N, 6.64. Found: C, 58.62; H, 4.42; N, 6.89%.

Synthesis of [Cu(L^{Me}PhS)PPh₃]BF₄ (21). In a Schlenk flask, and under an inert atmosphere (N₂), a solution of [Cu(MeCN)₄]BF₄ (67 mg, 0.21 mmol) in 15 mL of dry MeCN was added to a solution of L^HPhS (101 mg, 0.21 mmol) and triphenylphosphine (55 mg, 0.21 mmol) in 10 mL of dry MeCN. The colorless solution was stirred for 1 hour. The solvent was then concentrated under vacuum and a white solid was precipitated after addition of diethyl ether. The mixture was filtered under nitrogen to afford a white solid (82 mg, yield 85%). The compound was recrystallized by stratifying hexane over a dichloromethane solution of the complex, which yielded colorless crystals. IR (cm⁻¹): 3182w, 3052w, 1556m, 1430m, 1232w, 1094m, 1048s, 996m, 765m, 745s, 696s, 530m, 510m, 493m. ¹H NMR (300 MHz, CDCl₃): δ 1.92 (s, 6H, CH₃), 2.57 (s, 6H, CH₃), 6.05 (s, 2H, CH(Pz)), 6.61 (t, J = 7.5 Hz, 1H, CH(Ph)), 6.80 (d, J = 7.5 Hz, 1H, CH(Ph)), 6.94 (t, J = 7.8 Hz, 1H, CH(Ph)), 7.20 (m, 21H, CH(Ph)), 7.60 (s, 1H, CH_{central}). *Anal.* Calc. for C₄₁H₃₉BCuF₄N₄PS (800.20): C, 61.48; H, 4.91; N, 7.00. Found: C, 61.25; H, 5.21; N, 6.65%.

3.2.2. Single Crystal X-ray Structures

Single crystal data were collected with a Bruker Smart 1000 and on a Bruker Smart APEXII area detector diffractometers (Mo Kα; λ = 0.71073 Å). Cell parameters were refined from the observed setting angles and detector positions of selected strong reflections. Intensities were integrated from several series of exposure frames that covered the sphere of reciprocal space⁴⁷. A multiscan absorption correction was applied to the data using the program SADABS⁴⁸. The structures were solved by direct methods (SIR97^{47,48} and SIR2004⁶⁶) and refined with full-matrix least-squares (SHELXL-97)⁵⁰, using the Wingx software package⁵¹. Graphical material was prepared with the and Mercury 2.0⁵² program. Crystallographic data are reported in Appendix iii-iv.

3.2.3. DFT calculations

Rigid potential-energy surface (PES) scans were performed for the L^HCH₂S and L^HPhS ligands starting from the ligand conformations found in the X-ray structures of complexes **15** and **1**, respectively. The calculations were performed using the gradient-corrected hybrid density functionals B3LYP^{67,68} and the 6-31+G basis set⁶⁹. In particular, the PES scan was performed for L^HCH₂S by rotating three molecular

fragments: 1) one pyrazole ring (360° rotation about the C_{central}-N_{pz} bond: 15 steps, 24°), 2) the CH₂ linker (360° rotation about the C_{central}-CH₂ bond: 15 steps, 24°), and 3) the peripheral phenyl ring (180° rotation about the S-Ph bond: 10 steps, 18°). The PES scan for L^HPhS was performed by the following rotations: 1) one pyrazole ring (360° rotation about the C_{central}-N_{pz} bond: 15 steps, 24°), 2) the phenyl ring linker (360° rotation about the C_{central}-Ph bond: 15 steps, 24°), and 3) the peripheral phenyl ring (180° rotation about the S-Ph bond: 10 steps, 18°). To gain insights on the different binding abilities of the two ligand classes (L^RCH₂S and L^RPhS), we optimized the geometries of two coordination isomers for each model complex, [Ag(L^HCH₂S)PH₃]⁺ and [Ag(L^HPhS)PH₃]⁺. The isomers were differentiated by the presence or absence of the thioether coordination to the metal center. The PH₃ ancillary ligand was used instead of the PPh₃ one, which is present in some reported X-ray structures, to save computational resources. The optimizations of the geometries were performed with the B3LYP density functional, with the 6-31+G(d) basis set for C, H, N, S, and P and with the SDD valence basis set and MWB28 effective core potentials for Ag^{70,71}. Vibrational frequencies were calculated at the same theoretical level to ensure that the stationary points were true minima. All the calculations were performed with the Gaussian 03 software⁷².

3.3. Results and Discussion

3.3.1. Synthesis

The ligands 1,1'-((2-(phenylthio)phenyl)methylene)bis(1H-pyrazole) (**L^HPhS**) and 1,1'-((2-(phenylthio)phenyl)methylene)bis(3,5-dimethyl-1H-pyrazole) (**L^{Me}PhS**) were prepared as described in Figure 22.

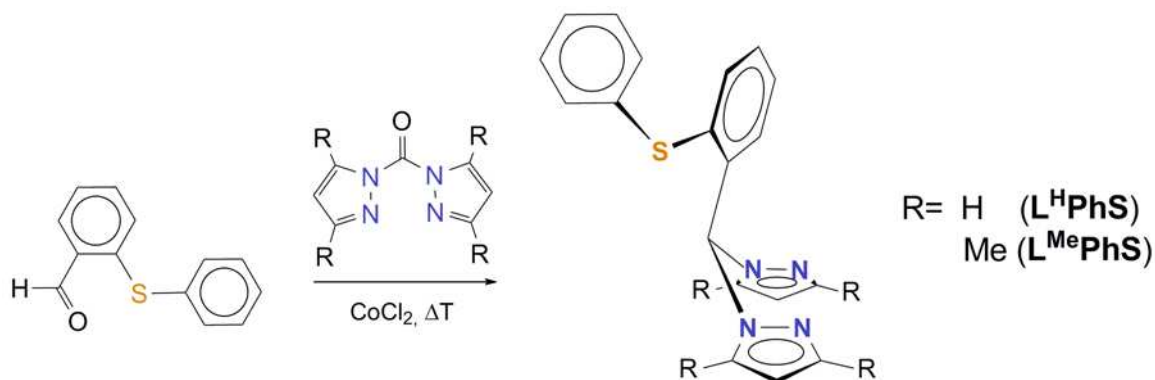


Figure 22. Ligands Synthesis.

The reaction to obtain this synthetic C-centered functionalized ligand class is similar to the synthetic route used for the preparation of the ligands presented in the previous chapter (Chapter 2). These ligands exhibit a phenyl group linking the bis-pyrazole scaffold and the thioether moiety (**L^RPhS**). The steric hindrance on the pyrazole ring was increased by substituting the hydrogen atoms in the 3 and 5 positions with methyl groups. To investigate the different coordinative behaviour of the ligands we have employed Ag(I) and Cu(I) cations. The complexes were prepared by treating equimolar amounts (Figure 23) of the ligand **L^HPhS** and $[\text{Cu}(\text{MeCN})_4]\text{BF}_4$ or Ag(I) salts (AgBF_4 , AgPF_6). The complexes synthesized with **L^{Me}PhS** ligand have given rise to porous coordination polymer with different supramolecular assembly as a function of the counterions. These results will be presented in the forthcoming chapter (Chapter 4). Moreover we have tested the coordinative characteristics of these rigid ligands by introducing an ancillary ligand as triphenylphosphine.

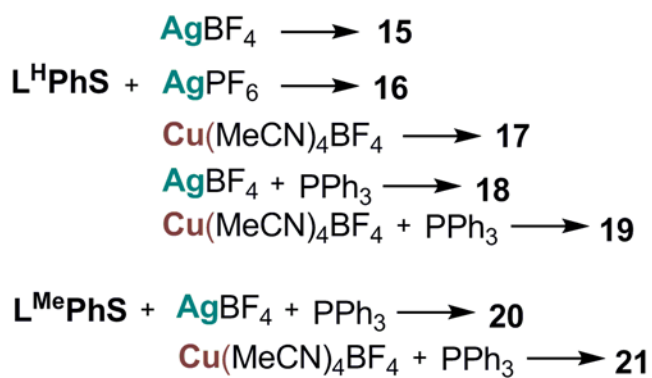


Figure 23. Synthesis of Ag(I) and Cu(I) complexes.

3.3.2. Solid state structures

The reactions between L^HPhS and different cations such as Cu(I) or Ag(I) ($AgBF_4$ and $AgPF_6$) yield very different molecular structures: **16** and **17** are dinuclear while **15** is a polymeric chain. In fact **15** exhibits a chain-like structure that is formed by the N_2 coordination on a metal center and by the bridging of the thioether group on a second metal. Two different types of silver atoms define the asymmetric unit. Both metal atoms are in a distorted T-shaped geometry (this is more pronounced for Ag(1) than for Ag(2)), which is distorted toward the tetrahedral geometry as a consequence of an Ag-C interaction that originates by one pyrazole ring for Ag(2) $\{d[Ag(2)-C(116)] = 2.773(6) \text{ \AA}\}$ and by the peripheral phenyl ring for Ag(1) $\{d[Ag(1)-C(24)] = 2.921(4) \text{ \AA}\}$ (Figure 24). The absence of steric hindrance on the pyrazole rings allows for the approach of the Ag(2) atom over one of the pyrazole rings. The central phenyl ring of the ligand is oriented as previously found for bis(pyrazolyl) functionalized ligands.^{39,40,61-67} This donor-set disposition favors the formation of metal-organic chains, and it is also the preferred conformation adopted by the ligands that exhibit a phenyl ring as a spacer between the bis(pyrazolyl) moiety and the thioether group (*vide infra*). Details of the data-collection parameters and other crystallographic information are given in Appendix iii, whereas experimental bond lengths and angles are provided in Table 5.

The molecular structure of **16** is dinuclear, with the silver atom in a distorted T geometry (Figure 25). The donor atoms are represented by the N_2 chelate system of one ligand and by the S(13) and N(21) atoms of a symmetry-related ligand. Within the N_2 chelate group, the Ag-N(22) bond distance ($2.238(3) \text{ \AA}$) is significantly shorter than that of Ag-N(21) ($2.428(3) \text{ \AA}$). This fact is most likely a consequence of a weak π -interaction that the silver atom exchanges with the symmetry related N(21)' atom ($2.691(3) \text{ \AA}$). The evidence that both nitrogen atoms interact with the metal is derived from the location of the silver atom above the ideal trigonal plane formed by the N(21), N(22), and S(13)' donor atoms and directed toward the N(21)' atom (symmetry code $' = 1-x; 1-y; -z$). As far as the ligand conformation is concerned, the central phenyl ring exhibits a conformation that is very close to that of **15**. The C(11) carbon atom of one pyrazole ring exchanges C-H $\cdots\pi$ interactions with the central phenyl ring of the symmetry-related ligand $d[C(11)-C1t] = 3.622(4) \text{ \AA}$, C1t: phenyl-ring centroid.

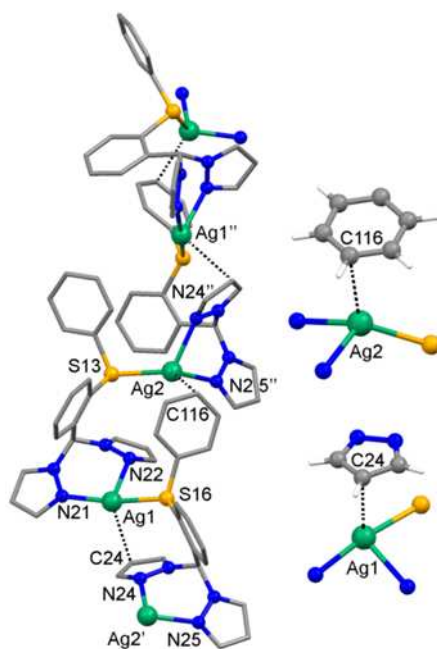


Figure 24. Molecular drawing of **15**. The BF_4^- anions and the hydrogen atoms are omitted for clarity.

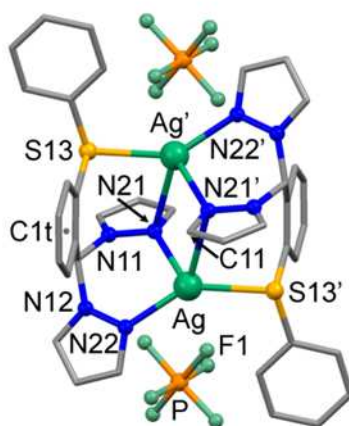


Figure 25. Molecular drawing of **16**. The hydrogen atoms are omitted for clarity. C1t, phenyl ring centroid, symmetry code ' = 1-x; 1-y; -z.

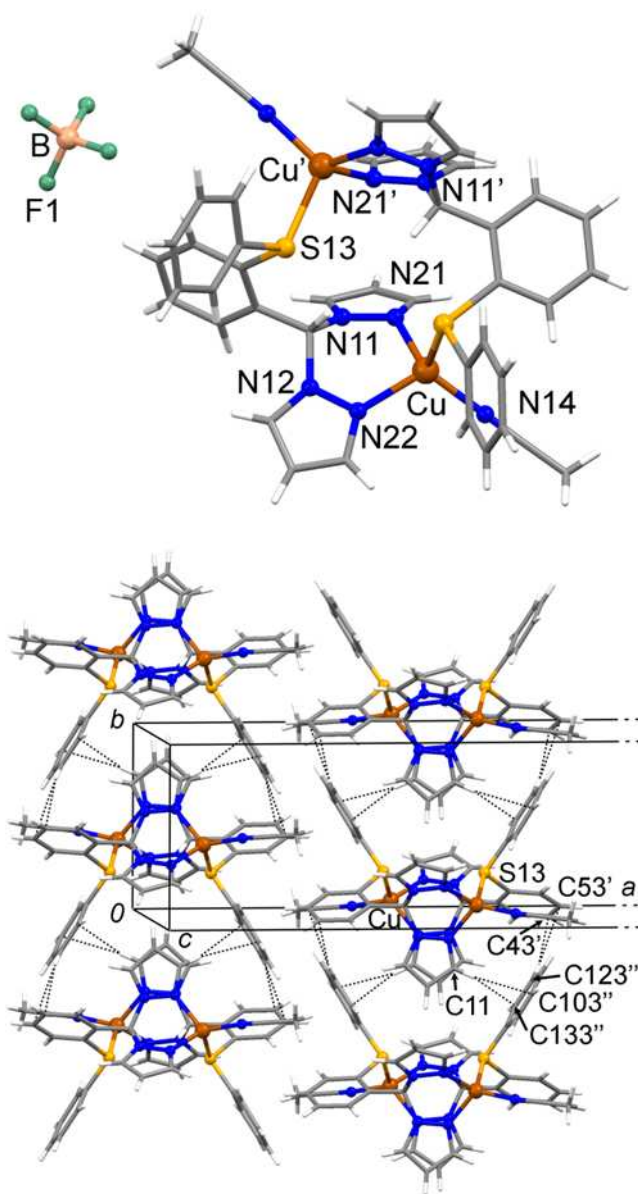


Figure 26. Molecular drawing of **17**, above, and a portion of the crystal packing, below. The BF_4^- anions are omitted for clarity. C-H $\cdots\pi$ interactions are represented by dashed bonds (below). Symmetry codes ' = $1-x; y; \frac{1}{2}-z$, '' = $1-x; y-1; \frac{1}{2}-z$.

The dinuclear complex **17** is obtained from the reaction between $[\text{Cu}(\text{CH}_3\text{CN})_4]\text{BF}_4$ and $\text{L}^{\text{H}}\text{PhS}$. The metal shows a distorted tetrahedral geometry attained by the N_2 chelate system of one ligand, the thioether group of the second ligand, and an acetonitrile molecule (Figure 26). The phenyl ring acting as spacer is rotated approximately 60° with respect to the previous structures. The result of this arrangement is the S atom pointing toward the $\text{C-H}_{\text{central}}$, even though it is located at a non-interacting distance. Moreover, the pyrazole rings also adopt a different conformation from that of **15** and **16** because their nitrogen lone pairs are oriented on the same side of the $\text{C-H}_{\text{central}}$. Obviously, this ligand conformation is unsuitable for the N_2S chelation because the $\text{C-H}_{\text{central}}$ is interposed between the N_2 and S donor atoms. From a pictorial point of view, the overall shape of the molecule resembles that of a cone delimited by alternate pyrazoles (those with N(12) and N(22)) and the peripheral phenyl rings. Two pyrazole rings on the opposite side of the cone face each other at a distance of 3.9 Å (measured from the centroids of the penta-atomic rings) with the minimum distance between symmetry-related N(21) and N(11) atoms (3.782(4) Å). The dinuclear units form pillars in which the stacked pyrazole rings point inside the cone of another molecular unit. These pillars are held together by two types of $\text{C-H}\cdots\pi$ interactions that occur through 1) the C(11) pyrazole carbon atom and the peripheral phenyl ring, $d[\text{C}(11)\cdots\text{C}(103)'] = 3.629(5)$ Å, and $d[\text{C}(11)\cdots\text{C}(133)'] = 3.738(6)$ Å, and 2) through the central and peripheral phenyl rings, $d[\text{C}(123)''\cdots\text{C}(43)'] = 3.773(6)$ Å, and $d[\text{C}(123)''\cdots\text{C}(53)'] = 3.657(6)$ Å, symmetry codes $' = 1-x; y; 1/2-z$, $'' = 1-x; y-1; 1/2-z$. Adjacent pillars are oriented in an antiparallel fashion, and they are aligned along the *b* crystallographic axis (Figure 26).

Table 5. Selected bond lengths (Å) and angles ($^\circ$) for **15**, **16** and **17**.

15			
Ag(1)-N(21)	2.241(4)	Ag(2)-N(24)'	2.398(3)
Ag(1)-N(22)	2.384(4)	Ag(2)-N(25)'	2.316(4)
Ag(1)-S(16)	2.492(1)	Ag(2)-S(13)	2.529(1)
Ag(1)-C(24)	2.921(4)	Ag(2)-C(116)	2.773(6)
N(21)-Ag(1)-N(22)	87.7(1)	N(25)'-Ag(2)-N(24)'	83.0(1)
N(21)-Ag(1)-S(16)	171.1(1)	N(25)'-Ag(2)-S(13)	130.0(1)
N(22)-Ag(1)-S(16)	86.7(1)	N(24)'-Ag(2)-S(13)	117.36(9)

16			
Ag-N(21)	2.428(3)	Ag-S(13)''	2.522(1)
Ag-N(22)	2.238(3)	Ag-N(21)''	2.691(3)
N(21)-Ag-N(22)	82.4(1)	N(22)-Ag-N(21)''	137.8(1)
N(21)-Ag-S(13)''	119.69(7)	N(22)-Ag-S(13)''	143.23(8)
N(21)-Ag-N(21)''	84.1(1)	N(21)''-Ag-S(13)''	75.05(9)
17			
Cu-N(14)	1.944(3)	N(14)-Cu-N(22)	113.0(1)
Cu-N(21)	2.025(3)	N(21)-Cu-N(22)	93.9(1)
Cu-N(22)	2.028(3)	N(14)-Cu-S(13)'''	110.0(1)
Cu-S(13)'''	2.335(1)	N(21)-Cu-S(13)'''	105.4(1)
N(14)-Cu-N(21)	122.3(1)	N(22)-Cu-S(13)'''	111.0(1)

Symmetry codes: ' = $\frac{1}{2}+x$; $\frac{1}{2}-y$; z , '' = $1-x$; $1-y$; $-z$, ''' = $1-x$; y ; $\frac{1}{2}-z$

The Ag(I) and Cu(I) complexes with the L^HPhS ligand show a certain structural diversity when they exhibit dinuclear or polynuclear structures. Nevertheless, the invariant feature appears to be the inability of L^HPhS to chelate in the N₂S fashion. This ligand, in fact, behaves like an N₂ chelate with pyrazole rings and bridges to a different metal ion with the sulfur atom.

To further investigate the coordinative behavior of the two classes of ligands, L^RPhS and L^RCH₂S, we have employed triphenylphosphine (PPh₃) as an ancillary ligand for Cu(I) and Ag(I). Mixtures of equimolar amounts of L^RPhS and L^RCH₂S ligands, PPh₃, and AgBF₄ or [Cu(CH₃CN)₄]BF₄ result in the formation of easily recovered [M(L)PPh₃]BF₄ ternary complexes from the reaction mixture. The molecular structures of the Cu(I) complexes are reported in Figures 27. The presence of PPh₃ hinders the formation of coordination polymers so that all of the resulting complexes are mononuclear. The most striking difference between the complexes exhibiting the two different classes of ligands is the role played by the thioether group.

Table 6. Selected bond lengths (Å) and angles (°) for **18**

18			
Ag-N(21)	2.285(2)	N(21)-Ag-N(22)	82.73(8)
Ag-N(22)	2.291(2)	N(21)-Ag-P	139.88(6)
Ag-P	2.3470(8)	N(22)-Ag-P	137.39(6)
21			
Cu(1)-N(21)	1.999(2)	N(21)-Cu(1)-N(22)	90.76(6)
Cu(1)-N(22)	2.003(2)	N(21)-Cu(1)-P(1)	144.30(5)
Cu(1)-P(1)	2.166(6)	N(22)-Cu(1)-P(1)	124.94(5)
Cu(2)-N(27)	2.014(2)	N(27)-Cu(2)-N(28)	93.84(7)
Cu(2)-N(28)	1.990(2)	N(27)-Cu(2)-P(2)	125.54(5)
Cu(2)-P(2)	2.161(6)	N(28)-Cu(2)-P(2)	140.40(5)

In fact, in complexes **19** and **21**, the metal is in a distorted trigonal-planar geometry and is bound by the N₂ chelate ligand and PPh₃. The thioether group adopts the same conformation already described for the coordination polymers that were constructed with these ligands in the absence of PPh₃. In contrast, **10**, **12** and **14** show the metal in a distorted tetrahedral geometry, and the ligands employ the N₂S donor set. In the complexes (see Figures 16 and 17), the thioether moiety is in a different conformation than that exhibited in the coordination polymers because the sulfur points to the same metal center of the N₂ donor system. In all the complexes, the Cu-N and Cu-P bond distances are in the 1.999(2)-2.065(3) Å and 2.161(6)-2.1863(7) Å ranges, respectively. In the **10**, **12**, and **14** complexes, the Cu-S distance is in the narrow range of 2.4801(8)-2.4860(6) Å (Table 6). Thus, the increase in the steric hindrance on the pyrazole rings when a hydrogen atom is substituted for an i-Pr group appears to neither affect the overall geometry of these complexes nor prevent the coordination of a relatively bulky ligand such as PPh₃.

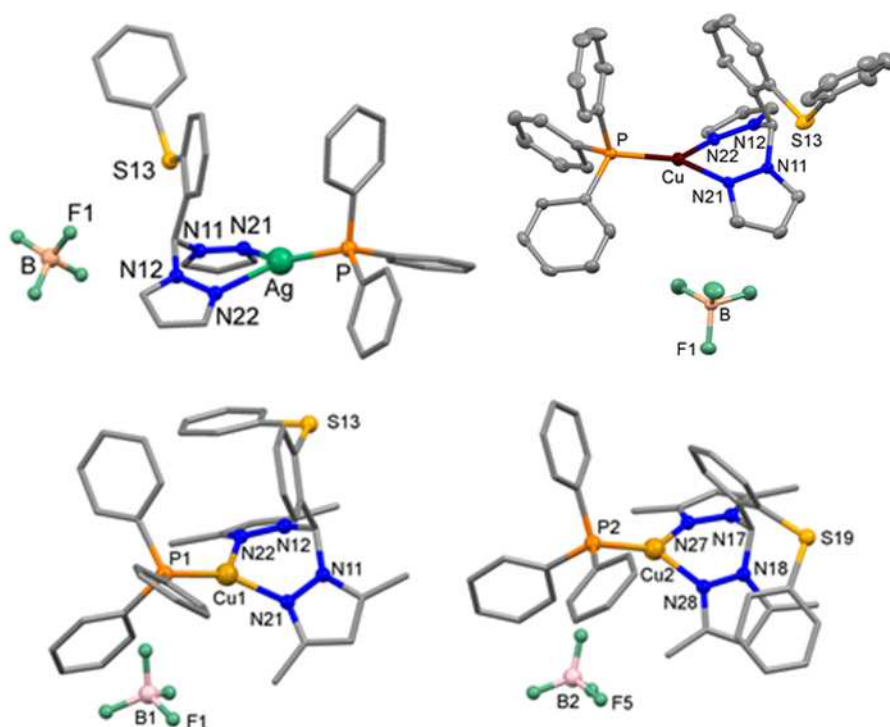


Figure 27. On the top: molecular drawing of **18** and **19**. The hydrogen atoms are omitted for clarity. Down: molecular drawing of **21**: the two molecules comprising the asymmetric unit are reported. The hydrogen atoms are omitted for clarity.

Under nitrogen atmosphere, the crystallization of the Cu(I) complexes reported here always affords colorless crystals of homogeneous shape. In contrast, during the crystallization of the Ag(I) complexes, a considerable number of crystals with hexagonal prismatic shapes are always present among the differently shaped prismatic crystals of the [Ag(L)PPh₃]₂BF₄ ternary complexes. The molecular structure derived from the X-ray diffraction analysis of the hexagonal crystals reveals that the compound is [Ag(PPh₃)₄]₂BF₄ (Figure 28), which is isostructural with the previously reported complex [Ag(PPh₃)₄]₂PF₆.⁶⁸ Given the difficulties encountered during the recrystallization of the Ag(I) complexes, only the molecular structures of **18**, **11**, and **13** could be obtained, and they can be easily related to the corresponding Cu(I) complexes. In fact, in **18**, the metal is in a trigonal-planar geometry achieved by the N₂ chelate ligand and PPh₃, with a thioether group that is not bound to the metal center. In contrast, the molecular structures of **11**, and **13** present the metal in a distorted tetrahedral geometry, and the L^{Me}CH₂S and L^{iPr}CH₂S ligands behave as N₂S tridentate.

On average, the coordination bond distances of these silver complexes are more than 0.2 Å longer than those of the copper complexes, which is congruent with the larger size of the silver cation.

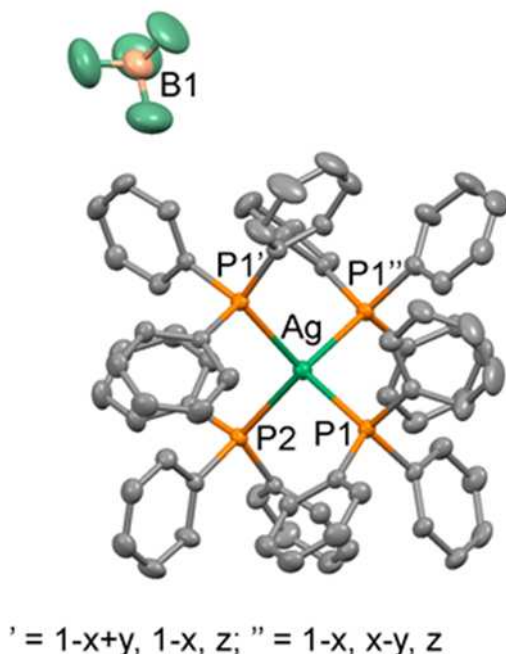


Figure 28. Molecular drawing of $[\text{Ag}(\text{PPh}_3)_4]\text{BF}_4$. Thermal ellipsoids are drawn at the 30% probability level. The hydrogen atoms are omitted for clarity. Selected bond distances (Å): $\text{Ag-P}(1) = 2.681(1)$, $\text{Ag-P}(2) = 2.636(2)$.

The molecular structures of these ternary complexes provide further evidence that the ligands with the methylene group as a spacer are coordinatively flexible and can behave as N_2S chelate or N_2 chelate and S-bridging. In contrast, the ligands with the phenyl ring as a spacer can be considered coordinatively rigid. Accordingly, their predominant conformation in the complexes presented thus far comprises the N_2 and S donor systems that are oriented in nearly opposite directions.

3.3.3. Conformational studies

Conformational studies were performed to investigate the energetics relative to the mobilities of the pyrazole rings and thioether groups of the ligands. The rigid potential-energy surface (PES) scans are performed using the two real systems $\text{L}^{\text{H}}\text{PhS}$ and $\text{L}^{\text{H}}\text{CH}_2\text{S}$ as benchmarks for the investigation of the flexibility of the two ligand classes. The calculations are performed by varying three torsion angles; τ_1 rotates one

of the pyrazole rings, τ_2 rotates the spacer between the thioether and bis-pyrazole moieties (Ph or CH₂), and τ_3 rotates the peripheral phenyl ring. Because the calculations are performed without optimization at every step (rigid PES scan), there are unrealistic conformations in which the phenyl, pyrazole or thioether groups collide with one another. These conformations are characterized by very high energy and will not be discussed further.

The conformation of L^HPhS that exhibits the minimum energy is **1a** reported in Figure 29. This conformation is characterized by the pyrazole ring that orients the nitrogen lone pair on approximately the same side of the molecule ($\tau_1 = 295.6^\circ$) and by the thioether group that points toward the methine proton ($\tau_2 = 49.2^\circ$). Due to the arrangement of the phenyl spacer group, the peripheral phenyl ring does not interact with any other molecular fragment ($\tau_3 = 342.1^\circ$). This lack of interaction has consequences for the energies involved in the free rotation of this group because only 14 kJ/mol are required when $\tau_1 = 295.6^\circ$ and $\tau_2 = 49.2^\circ$. The 360° rotation of the pyrazole ring (τ_1) requires 24 kJ/mol when $\tau_2 = 49.2^\circ$ and $\tau_3 = 342.1^\circ$. In comparison, the rotation of the thioether group requires at least 90 kJ/mol (with $\tau_1 = 295.6^\circ$ and $\tau_2 = 49.2^\circ$). Furthermore, an inspection of all PES scans reported in Figure 29 reveals how the pyrazole rotation is a relatively inexpensive process, whereas the rotation of the phenyl ring acting as a spacer usually implies high energy barriers. In particular, the regions of the PES scans characterized by minor energy are those that are associated with the conformation in which the thioether points toward the central methine proton (τ_2 range of $= 25.2$ - 73.2°). Structure **2a** corresponds to the ligand conformation that would allow the N₂S coordination of this ligand class, and its energy is at least 30 kJ/mol greater than that of **1a**.

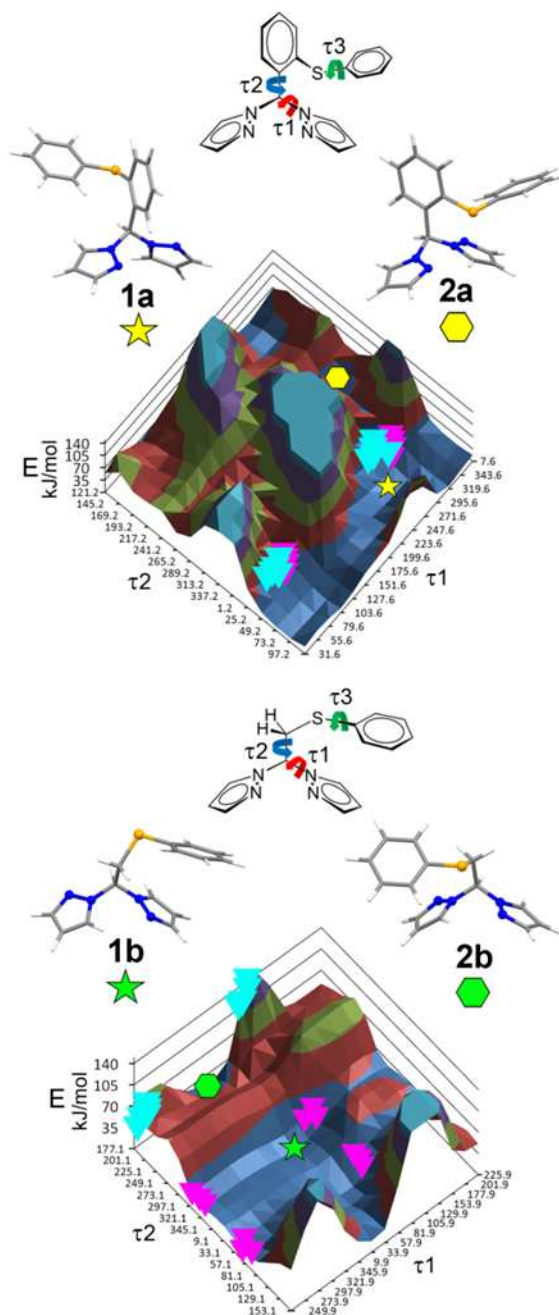


Figure 29. Rigid PES scan of the $L^H\text{PhS}$ and $L^H\text{CH}_2\text{S}$ ligands. For both ligand classes, the conformations corresponding to the potential N_2 and N_2S coordination behavior are indicated by the \star and \bullet symbols, respectively. The conformations adopted by the

ligands in the polynuclear $[M(L)]_n^{n+}$ and mononuclear $[M(L)PPh_3]BF_4$ complexes are indicated with purple and magenta triangles, respectively.

The L^HCH_2S ligand should be characterized by a greater flexibility when compared to the L^RPhS ligand class. This is evident when examining the PES scan of L^HCH_2S , because the regions of low energy are more extensive than those of the L^HPhS PES scan. The conformation of L^HCH_2S that exhibits the minimum energy is **1b** reported in Figure 29. This conformation is characterized by 1) pyrazole rings oriented in an antiparallel fashion ($\tau_1 = 57.9^\circ$), 2) the methylene bridge and the central methine proton in a staggered conformation with the thioether that points toward the methine proton ($\tau_2 = 321.1^\circ$), and 3) the peripheral phenyl ring nearly stacked over one of the pyrazole rings ($\tau_3 = 288.1^\circ$). Based on the analysis of the PES scan, the rotation of the phenyl ring is the least energetically demanding (~ 20 kJ/mol), and the most stable conformation presumably attains a slight stabilization by the partial π -stack of the pyrazole and phenyl rings. Also, the rotation of the pyrazole ring requires a limited expenditure of energy: ~ 33 kJ/mol for a 360° rotation of τ_1 when $\tau_2 = 321.1^\circ$ and $\tau_3 = 288.1^\circ$. The rotation of the thioether group requires slightly more energy, but it is still a relatively inexpensive process: ~ 52 kJ/mol for a 360° rotation of τ_2 when $\tau_1 = 57.9^\circ$ and $\tau_3 = 288.1^\circ$. Furthermore, by a close inspection of the various energy profiles of L^RCH_2S provided in Figure 30, it is evident that there are a number of conformations that are very close in energy; they can be grouped into two main reference structures: one corresponds to the minimum of the PES scan, as previously described (**1b** in Figure 29), whereas the other is still characterized by a staggered conformation of the methylene and methine protons but with the sulfur atoms pointing to the opposite side of the central methine proton (**2b** in Figure 29). This latter conformation, apart from the rotation of one pyrazole ring, is the one adopted by the ligand in the ternary complexes in the presence of PPh_3 .

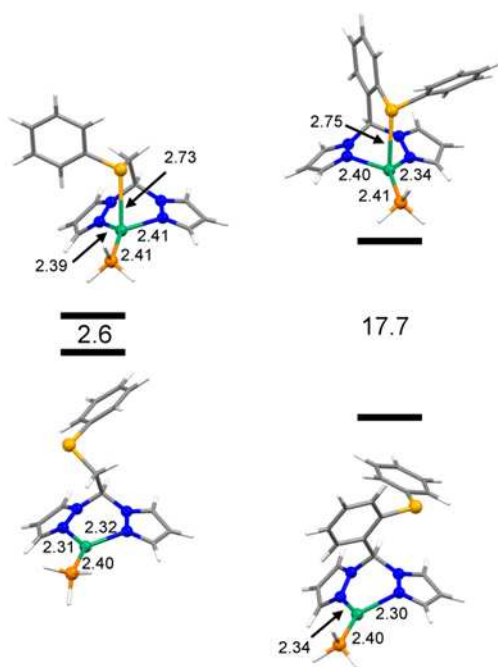


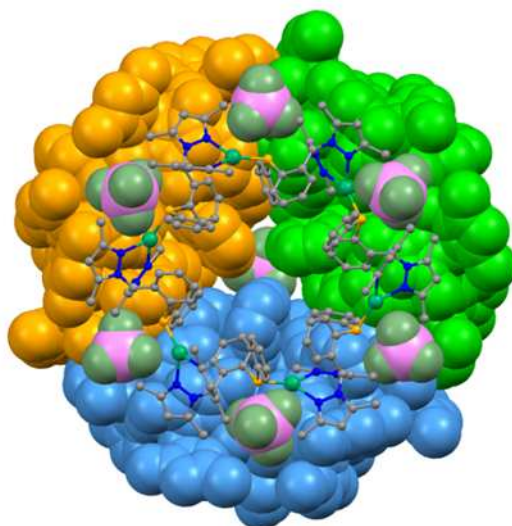
Figure 30. Energy differences (kJ/mol) between the coordination isomers of the two model complexes, $[\text{Ag}(\text{L}^{\text{HPhS}})\text{PH}_3]^+$ and $[\text{Ag}(\text{L}^{\text{HCH}_2\text{S}})\text{PH}_3]^+$ (B3LYP/6-31+G(d)-SDD). Selected coordination bond distances (Å) are reported.

In conclusion, it is evident that the L^{RPhS} ligand class is conformationally more rigid and pre-organized than the $\text{L}^{\text{RCH}_2\text{S}}$ class. In fact, the general and therefore expected behavior of the L^{RPhS} ligands is the N_2 chelation on a metal and possibly the bridging interaction of the thioether group on a second metal. The presence of the phenyl group as a spacer precludes the N_2S chelation mode for this ligand class. In contrast, the $\text{L}^{\text{RCH}_2\text{S}}$ class usually N_2 chelates and bridges with the thioether group on a second metal, but it can also act as a N_2S donor on the same metal ion. The energy expenditure to drive the thioether and the bis-pyrazole systems to chelate the same metal ion is compensated by the metal–sulfur interaction energy, which is evidently not sufficient for the L^{RPhS} system. This compensation is further evidenced by inspecting the energy profiles of the conformational isomers of the two model complexes, $[\text{Ag}(\text{L}^{\text{HPhS}})\text{PH}_3]^+$ and $[\text{Ag}(\text{L}^{\text{HCH}_2\text{S}})\text{PH}_3]^+$ (Figure 30). For $[\text{Ag}(\text{L}^{\text{RCH}_2\text{S}})\text{PH}_3]^+$, the energy difference between the two isomers is only 2.6 kJ/mol, which confirms that there is not a significant energy gain derived by the coordination of the thioether group when a metal ion is present. In contrast, for $[\text{Ag}(\text{L}^{\text{HPhS}})\text{PH}_3]^+$, the isomer with

the N₂S chelate ligand lies 17.7 kJ/mol above that of the isomer with the N₂ bidentate ligand. An inspection of the optimized molecular structure of this complex indicates that the sulfur coordination implies a certain ligand strain. In particular, the sulfur coordination requires a destabilizing approach between the CH_{central} and the CH_{ortho} hydrogen atoms.

CHAPTER 4

Porous coordination polymers: synthesis and characterization of novel silver(I) supramolecular architectures.



As mentioned in the previous chapter we will described here coordination polymers based on the $L^{\text{Me}}\text{PhS}$ ligands. The complexation of a pre-organized thioether-functionalized bis(pyrazolyl)methane ligand ($L^{\text{Me}}\text{PhS}$) with silver precursors produces supramolecular structures organized at two hierarchical levels: $[\text{AgL}]_6(\text{X})_6$ metal-organic cyclic hexamers and their organization in 3D supramolecular architectures⁷³. The cyclic toroidal hexamers of 22-26 Å external diameter are found to be stable already in solution before self-assembly into the crystalline state. In the 3D lattice the hexameric building block are arranged in different highly symmetric space groups as a function of a variety of anions (cubic $Fd\text{-}3$ with PF_6^- or BF_4^- and rhombohedral $R\text{-}3$ with CF_3SO_3^- or NO_3^-) and form cavities with the geometrical shapes of Platonic solids (tetrahedron and octahedron) that can be occupied by a variety of solvent molecules. Upon evacuation, cubic crystals can produce stable frameworks with permanent porosity, which can absorb reversibly several vapors, CO_2 and CH_4 .

4.1 Introduction

Many supramolecular architectures are based on the interaction of opportunely selected ligands and metal ions, and their stereoelectronic complementarity serves to shape notable molecular structure^{74–80}. The stability of the metal-ligand association depends on the affinity between the ligand donor set and the metal ions and this is expressed by the concept of pre-organization. According to that, the more a specific ligand is appropriately constructed with the donor lone pairs properly oriented for metal ion-binding, the more stable the assembly will result⁸¹. Furthermore, the existence of weak non covalent-forces in molecular assemblies determines, in many cases, a reversibility of association so that the final product is in thermodynamic equilibrium with its components, or its partially assembled intermediates. This has led to the formulation of dynamic combinatorial libraries, where a supramolecular structure self-assembles out from a pool of different components when a complementary species is added to the mixture⁸². The application of supramolecular assemblies are as diverse as their molecular structures and they include catalysis^{30,83,84}, the construction of nano-scaled structures for gas storage^{18,22,26,85,86}, the design of molecular sensors⁸⁷ and molecular machines able to execute a mechanical function in presence of an external stimulus^{88,89}. Taking into account the shape of a particular supramolecular entity, much attention has been paid in recent years to self-assembled capsules that provide a confined isolated cavity^{42,90–95}, inside which catalysis^{83,84} and molecular recognition can be efficiently performed. With respect to the latter aspect, the discrimination of enantiomers by means of enantioselective encapsulation has also been reported⁹⁶. In this chapter, self-assembled hexameric complexes having a toroidal shape were synthesized by using an N₂S donor ligand, [M(L^{Me}PhS)]₆⁶⁺ (M = Cu(I) and Ag(I)). The N₂ donor system is derived from the bis(pyrazole)methane moiety and a thioether function attached to its central carbon atom provides the S donor atom of the ligand **L^{Me}SPh** already introduced in chapter 3. This ligand adopts a conformation that makes it suitable to build hexamers when reacted with monovalent metal ions, such as copper or silver, since the N₂ and S donor groups point in nearly opposite directions. The crystallization of [M(L^{Me}PhS)]₆⁶⁺ hexamers in presence of different anions (BF₄⁻, PF₆⁻, CF₃SO₃⁻ and NO₃) yield supramolecular structures whose shape and nuclearity is a function of the counterions.

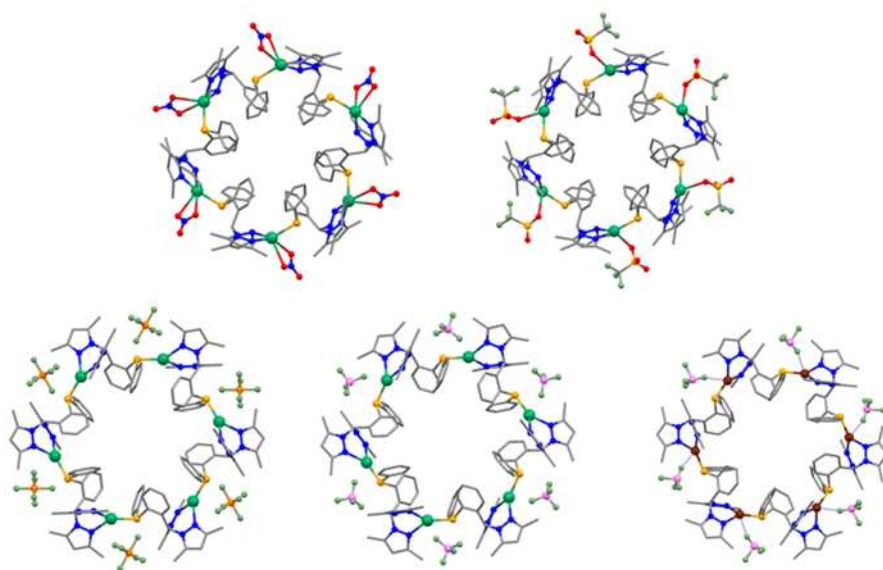


Figure 31. Toroidal hexamers of copper and silver metal ions with different counterions.

4.2 Experimental

4.2.1. Experimental

All reagents and solvents were commercially available. ^1H NMR spectra were recorded on a Bruker Avance 300 spectrometer using standard Bruker pulse sequences. Chemical shifts are reported in ppm referenced to residual solvent protons (CDCl_3 , CD_3CN , $(\text{CD}_3)_2\text{CO}$). Infrared spectra were recorded from 4000 to 700 cm^{-1} on a Perkin-Elmer FT-IR Nexus spectrometer equipped with a Thermo-Nicolet microscope.

Synthesis of **22**. A solution of $[\text{Cu}(\text{MeCN})_4]\text{BF}_4$ (97 mg, 0.31 mmol) in 8 mL of dry MeCN was added to a solution of $\text{L}^{\text{Me}}\text{PhS}$ (101 mg, 0.26 mmol) in 10 mL of dry MeCN in a Schlenk flask under nitrogen. The colorless solution was stirred for 15 min. The solvent was then concentrated under vacuum and a white solid was precipitated after addition of diethyl ether. The mixture was filtered under nitrogen affording a white solid (113 mg, yield 88%). The compound was recrystallized by stratifying diethyl ether over an acetone solution of the complex, yielding colorless crystals. IR (cm^{-1}): 3534w, 3055w, 2963w, 2924w, 1638m, 1558s, 1457s, 1418s, 1394s, 1231m, 1015s, 873m, 762m. ^1H NMR (300 MHz, CD_3CN) δ : 2.25 (s, 6H, $2\text{CH}_3(\text{Pz})$), 2.45 (s, 6H, $2\text{CH}_3(\text{Pz})$), 6.06 (s, 2H, $\text{CH}(\text{Pz})$), 6.61 (m, 1H, $\text{CH}_{\text{orto}}(\text{Ph})$), 7.16 (m, 2H, $\text{CH}(\text{Ph})$), 7.27-7.36 (m, 6H, $\text{C}(\text{Ph})$), 7.57 (s, 1H, $\text{C}_{\text{central}}$). ^{13}C NMR (100 MHz, CD_3CN) δ : 11.67 ($\text{CH}_3(\text{Pz})$), 14.19 ($\text{CH}_3(\text{Pz})$), 68.37 ($\text{CH}_{\text{central}}$), 107.52 ($\text{CH}(\text{Pz})$), 128.27 ($\text{C}(\text{Ph})$), 128.84 ($\text{C}(\text{Ph})$), 130.12 ($\text{C}(\text{Ph})$), 130.43 ($\text{C}(\text{Ph})$), 131.12 ($\text{C}(\text{Ph})$), 131.21 ($\text{C}(\text{Ph})$), 135.05 ($\text{C}(\text{Ph})$), 135.48 ($\text{C}(\text{Ph})$), 136.30 ($\text{C}(\text{Ph})$), 137.75 ($\text{C}(\text{Ph})$), 143.82 ($\text{C}(\text{CH}_3)$), 152.24 ($\text{C}(\text{CH}_3)$). Anal. Calc. for $(\text{C}_{23}\text{H}_{24}\text{N}_4\text{S})_6\text{Cu}_6(\text{BF}_4)_6$ (3233.28): C, 51.26; H, 4.49; N, 10.37. Found: C, 51.05; H, 4.27; N, 10.15%.

Synthesis of **23-BF₄**. $\text{L}^{\text{Me}}\text{PhS}$ (300 mg, 0.76 mmol) and AgBF_4 (150 mg, 0.76 mmol) were mixed in acetone (6 mL), and the colorless solution was stirred for 30 min. The solution was then concentrated under vacuum and a white solid was precipitated after addition of diethyl ether. The solid was filtered and vacuum dried (388 mg, yield 87%). The compound can be recrystallized by stratifying hexane over a dichloromethane solution of the complex yielding colorless crystals. Alternatively, crystals can be obtained by stratifying diethyl ether over an acetone solution of the complex. IR (cm^{-1}): 2975w, 2909w, 1558m, 1463m, 1440m, 1417m, 1315w, 1276w, 1232w, 1049s, 1031s, 874m, 763m, 690m, 745m, 697m, 687m. ^1H NMR (300 MHz, $(\text{CD}_3)_2\text{CO}$) δ : 1.93 (s, br, 6H, $2\text{CH}_3(\text{Pz})$), 2.51 (s, 6H, $2\text{CH}_3(\text{Pz})$), 6.14 (s, 2H, $\text{CH}(\text{Pz})$), 7.19 (d, $J = 1.2\text{ Hz}$, 1H, $\text{CH}_{\text{orto}}(\text{Ph})$), 7.21 (d, $J = 2.1\text{ Hz}$, 2H, $\text{CH}(\text{Pz})$), 7.34-7.44 (m, 5H,

CH(Ph)), 7.85 (s, 1H, CH_{central}). ¹³C NMR (100 MHz, (CD₃CN) δ: 11.51 (CH₃(Pz)), 14.14 (CH₃(Pz)), 68.55 (CH_{central}), 107.63 (CH(Pz)), 128.41 (CH(Ph)), 129.20 (CH(Ph)), 129.28 (CH(Ph)), 130.48 (CH(Ph)), 131.16 (CH(Ph)), 131.42 (CH(Ph)), 135.38 (CH(Ph)), 135.70 (CH(Ph)), 135.79 (CH(Ph)), 137.76 (CH(Ph)), 149.31 (C(CH₃)), 152.39 (C(CH₃)). Anal. Calc. for (C₂₃H₂₄N₄S)₆Ag₆(BF₄)₆ (3499.21): C, 47.37; H, 4.15; N, 9.61. Found: C, 46.95; H, 4.12; N, 9.30%.

Synthesis of **24-PF₆**. L^{Me}PhS (107 mg, 0.27 mmol) and AgPF₆ (73 mg, 0.27 mmol) were mixed in acetone (10 mL), and the colorless solution was stirred for 10 min. The solvent was then concentrated under vacuum and a white solid was precipitated after addition of diethyl ether. The solid was filtered and vacuum dried (152 mg, yield 87%). The compound was recrystallized by stratifying diethyl ether over an acetone solution of the complex, yielding colorless crystals. IR (cm⁻¹): 3057 w, 2909w, 1557m, 1516s, 1464m, 1439m, 1380s, 1315s, 1250m, 1033m, 754s, 692m, 668s, 619m. ¹H NMR (300 MHz, (CD₃)₂CO) δ: 1.95 (s, 6H, 2CH₃(Pz)), 2.65 (s, 6H, 2CH₃(Pz)), 6.15 (s, 2H, CH(Pz)), 7.08 (m, 1H, CH_{orto}(Ph)), 7.22 (m, 2H, CH(Ph)), 7.33-7.41 (m, 6H, CH(Ph)), 7.85 (s, 1H, CH_{central}). ¹³C NMR (100 MHz, (CD₃CN) δ: 11.54 (CH₃(Pz)), 14.10 (CH₃(Pz)), 68.53 (CH_{central}), 107.60 (CH(Pz)), 128.39 (CH(Ph)), 129.23 (CH(Ph)), 129.38 (CH(Ph)), 130.47 (CH(Ph)), 131.12 (CH(Ph)), 131.40 (CH(Ph)), 135.35 (CH(Ph)), 135.66 (CH(Ph)), 135.70 (CH(Ph)), 137.74 (CH(Ph)), 149.29 (C(CH₃)), 152.34 (C(CH₃)). Anal. Calc. for (C₂₃H₂₄N₄S)₆Ag₆(PF₆)₆ (3848.17): C, 43.07; H, 3.77; N, 8.74. Found: C, 43.36; H, 4.01; N, 8.91%.

Synthesis of **25-CF₃SO₃**. L^{Me}PhS (187 mg, 0.48 mmol) and AgCF₃SO₃ (122 mg, 0.48 mmol) were mixed in acetone (5 mL), and the colorless solution was stirred for 20 min. The solvent was then removed under vacuum and the white solid was washed with hexane in an ultrasound bath. The mixture was filtered yielding a white solid (220 mg, yield 71%). The compound was recrystallized by stratifying hexane over a THF solution of the complex, yielding colorless crystals. IR (cm⁻¹): 3052w, 2920w, 1559m, 1485m, 1440m, 1418m, 1277m, 1237s, 1221s, 1153m, 1024s, 876m, 745m, 697m, 634s, 569m, 516w. ¹H NMR (300 MHz, (CD₃)₂CO) δ: 1.94 (s, 6H, 2CH₃(Pz)), 2.55 (s, 6H, 2CH₃(Pz)), 6.14 (s, 2H, CH(Pz)), 7.11 (d, J = 9 Hz, 1H, CH_{orto}(Ph)), 7.32 (m, 2H, CH(Ph)), 7.36-7.44 (m, 6H, CH(Ph)), 7.49 (s, 1H, CH_{central}). ¹³C NMR (100 MHz, (CD₃CN) δ: 11.50 (CH₃(Pz)), 14.12 (CH₃(Pz)), 68.54 (CH_{central}), 107.65 (CH(Pz)), 128.38 (CH(Ph)), 129.19 (CH(Ph)), 129.28 (CH(Ph)), 130.41 (CH(Ph)), 131.13 (CH(Ph)), 131.39 (CH(Ph)), 135.33 (CH(Ph)), 135.68 (CH(Ph)), 135.77 (CH(Ph)), 135.82 (CH(Ph)), 137.80 (CH(Ph)), 149.75(C(CH₃)), 152.33 (C(CH₃)). Anal. Calc. for (C₂₃H₂₄N₄S)₆Ag₆(CF₃SO₃)₆ (3872.81): C, 44.66; H, 3.75; N, 8.68. Found: C, 44.39; H, 3.58; N, 8.53%.

Synthesis of **26-NO₃**. L^{Me}PhS (120 mg, 0.30 mmol) and AgNO₃ (56 mg, 0.30 mmol) were mixed in acetone (5 mL), and the colorless solution was stirred for 10 min. The solvent was then removed under vacuum yielding a white solid that was washed with hexane (150 mg, yield 89%). The compound was recrystallized by stratifying hexane over a dichloromethane solution of the complex, yielding colorless crystals. IR (cm⁻¹): 2920w, 2851w, 1704w, 1557m, 1414s, 1280s, 1027m, 978w, 874w, 845w, 746s, 690s, 616w, 529w. ¹H NMR (300 MHz, (CD₃)₂CO) δ: 2.09 (s, br, 6H, 2CH₃(Pz)), 2.55 (s, 6H, 2CH₃(Pz)), 6.12 (s, 2H, CH(Pz)), 7.14-7.40 (m, 2H, CH(Pz)), 7.88 (s, 1H, CH_{central}). ¹³C NMR (100 MHz, (CD₃CN) δ: 11.49 (CH₃(Pz)), 14.11 (CH₃(Pz)), 68.61 (CH_{central}), 107.61 (CH(Pz)), 128.39 (CH(Ph)), 129.18 (CH(Ph)), 129.30 (CH(Ph)), 130.45 (CH(Ph)), 131.14 (CH(Ph)), 131.41 (CH(Ph)), 135.34 (CH(Ph)), 135.71 (CH(Ph)), 135.80 (CH(Ph)), 137.86 (CH(Ph)), 149.79 (C(CH₃)), 152.33 (C(CH₃)). Anal. Calc. for (C₂₃H₂₄N₄S)₆Ag₆(NO₃)₆ (3350.42): C, 49.47; H, 4.33; N, 12.54. Found: C, 49.22; H, 4.23; N, 12.33%.

4.2.2. Single Crystal X-ray Structures

Single crystal data were collected with a Bruker Smart 1000 and on a Bruker Smart APEXII area detector diffractometers (Mo Kα; λ = 0.71073 Å). Cell parameters were refined from the observed setting angles and detector positions of selected strong reflections. Intensities were integrated from several series of exposure frames that covered the sphere of reciprocal space⁴⁸. A multiscan absorption correction was applied to the data using the program SADABS⁴⁷. The structures were solved by direct methods SIR97^{47,66} and SIR2004⁶⁶ and refined with full-matrix least-squares (SHELXL-97⁵⁰), using the Wingx⁵¹ software package. Graphical material was prepared with the Mercury 2.0⁵² program. Crystallographic data are reported in Appendix v.

4.2.3. Solid State NMR

The ¹³C solid-state NMR spectra were run at 75.5 MHz on a Bruker Avance 300 instrument operating at a static field of 7.04 T equipped with 4 mm double resonance MAS probe. The samples were spun at the magic angle at a spinning speed of 12.5 kHz, and ramped-amplitude cross-polarization (RAMP-CP) transfer of magnetization was applied. The 90° pulse for proton was 2.9 μs. ¹³C cross-polarization (CP) MAS experiments were performed using a recycle delay of 10 s and contact times of 2 ms.

4.2.4. X-ray Powder Diffraction

Powder XRD patterns were collected using a Thermo ARL X'tra powder diffractometer (CuK α radiation) equipped with a Thermo Electron solid state detector. Data collection was performed in Bragg-Brentano configuration by 0.05° steps with counting time ranging from 1 to 5 sec. Temperature-dependent experiments were performed by using an Anton Paar TTK450 chamber connected to a vacuum apparatus.

4.2.5. Thermal analysis

Differential Scanning Calorimetry (DSC) traces were recorded on a Mettler Toledo Stare DSC1 analysis system equipped with N2 low temperature apparatus. The experiments were run under nitrogen atmosphere in a standard 40μl Al pans. The samples were first heated from 25 °C to 125 °C, then cooled to 25 °C and later heated to 300 °C at 10 °C/min. The sample weight were about 5 mg. Standard 70μl alumina pans were used.

4.2.6. PGSE (Pulsed Gradient Spin Echo) ^1H NMR

^1H PGSE NMR measurements were performed for **23-BF $_4$** and **25-CF $_3$ SO $_3$** solutions in CD $_2$ Cl $_2$ and acetone-d $_6$ in the 0.1-0.001 M concentration range (based on the AgL $^+$ unit, 1/6 hexamer). A standard stimulated echo (STE) sequence on a Bruker Avance 300 spectrometer was employed (300 K without spinning). The most intense signals were taken into account during the data processing. The dependence of the resonance intensity (I) on the gradient strength (g) is described by the following equation:

$$I = I_0 \cdot e^{-D \cdot \gamma^2 \cdot g^2 \cdot \delta^2 \cdot (\Delta - \delta/3)}$$

where I = observed intensity (attenuated signal intensity), I $_0$ = reference intensity (unattenuated signal intensity), D = diffusion coefficient, γ = nucleus gyromagnetic ratio, g = gradient strength, δ = gradient duration, and Δ = diffusion delay. The parameters δ and Δ were kept constant during the experiments, whereas g was varied from 2 to 95% in 16 steps. Different values of δ (1-2 ms), Δ (50-100 ms) and number of scans (depending on concentration) were used for different samples. All spectra were acquired using 16K points and processed with a line broadening of 1.0 Hz. PGSE data were treated by applying a procedure reported in the literature,⁹⁷⁻⁹⁹ taking advantage of an internal standard (tetakis(trimethylsilyl)silane, TMSS; r $_H$ ^{TMSS}

(hydrodynamic radius) $\approx r_{\text{vdW}}^{\text{TMSS}}$ (van der Waals radius) = 4.28 Å).¹⁰⁰ A nonlinear regression on I and g^2 data was performed with the SPSS 15.0 software in order to obtain the coefficients $m = D \cdot \gamma^2 \cdot \delta^2 \cdot (\Delta \cdot \delta / 3)$ for both the sample and the corresponding internal standard signals (m^{sample} and m^{TMSS} , respectively). The following expression (based on the Stokes-Einstein equation) was applied and numerically resolved to get the hydrodynamic radius of each sample (r_H^{sample}):

$$\frac{c^{\text{TMSS}} \cdot r_H^{\text{TMSS}}}{c^{\text{sample}} \cdot r_H^{\text{sample}}} = \frac{m^{\text{sample}}}{m^{\text{TMSS}}}$$

The coefficients c^{sample} and c^{TMSS} can be estimated from the semiempirical equation:

$$c^x = \frac{6}{(1 + 0.695 \cdot \frac{r^{\text{solv}}}{r_H^x})^{2.234}}$$

where x = sample or TMSS, and $r^{\text{solv}} \approx$ van der Waals radius of the solvent (2.49 Å for CD₂Cl₂ and acetone-d₆). Uncertainties were obtained by error propagation on m .

The van der Waals radii (r_{vdW})¹⁹ were computed for the two types of hexamers, **23-BF₄** and **25-CF₃SO₃**, using the X-ray geometry and with the software package DS Viewer Pro 5.0 and assuming a spherical molecular shape.

4.3 Results and Discussion

4.3.1. Synthesis

The ligand ((2-(phenylthio)phenyl)methylene)bis(3,5-dimethyl-1H-pyrazole) (L) was prepared as previously reported (chapter 3).

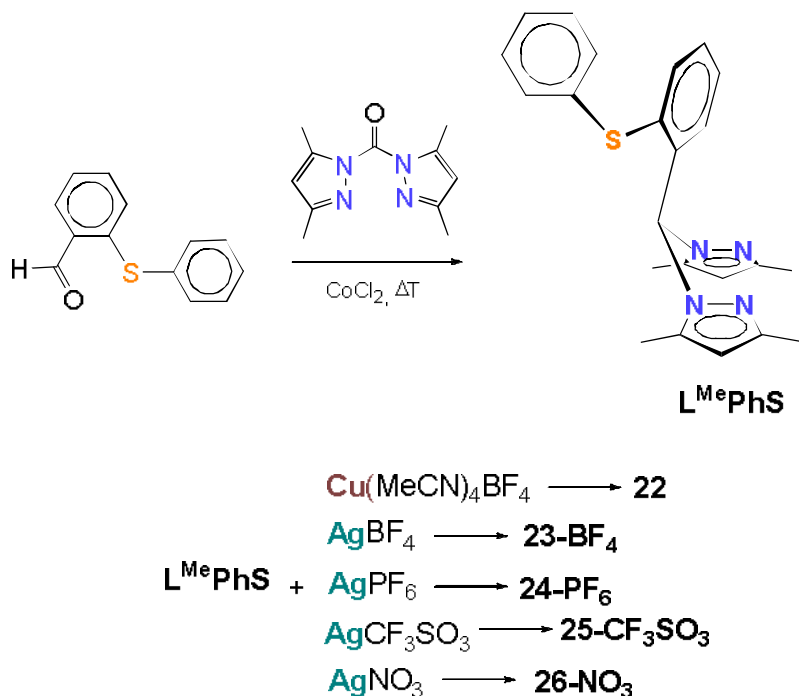


Figure 32. Synthetic path of ligand and complexes

As we have previously described, the synthesis is a solid state reaction in which the aldehyde bearing a thioether group and the bispyrazolylketone react in presence of CoCl_2 as catalyst. The synthesis of silver complexes are performed in the air at room temperature while the copper complexes are produced under inert atmosphere with schlenk techniques.

4.3.2. Solid state structures

By using the L^{MePhS} ligand an invariant hexameric molecular arrangement is achieved either with copper or with silver. In **23-BF₄** the ligand acts as N₂ bidentate on a metal and bridges on another silver atom with the thioether group. The pre-organization of

the ligand was previously described (see chapter 2 and 3) and it determines the coordination properties of this ligand class. More specifically, the presence of the central phenyl ring as spacer implies that the bis(pyrazole) and thioether donor groups are not able to chelate on the same metal center.

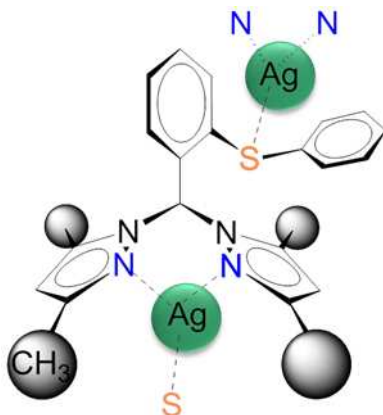


Figure 33. Schematic coordinative way of ligand.

In addition, the peripheral phenyl ring is located above one of the pyrazole ring giving rise to a stabilizing π - π interaction (3.5 Å). The pyrazole rings of six ligands defines the exteriors of the hexamer whereas the phenyl rings are oriented towards the interior, thus shaping an hydrophobic pore of 5.1 Å in diameter (calculated by taking into account the VdW surface of the H oriented towards the interior of the hole). The analysis of the anion influence on the crystal packing is hampered by the fragmentation of the site occupation of the BF_4^- ion within the unit cell. In fact, per each silver cation of the asymmetric unit the BF_4^- anion is distributed in three positions in the unit cell, 1) a 0.1666 fraction lying on a ternary axis and with a halved occupancy, 2) a 0.3333 fraction lying on a ternary axis, and a 3) fraction 0.5 lying on a binary axis.

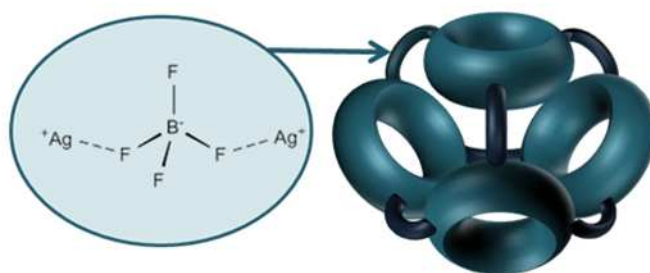


Figure 34. Anion interaction between hexamers which define the capsule formation.

This latter fraction links together two silver atoms of symmetry related hexamers in a way that the centroids of four hexamers occupy the vertex of a tetrahedron thus defining an internal cavity having the shape of a tetrahedron. The distance between the fluorine and the silver atoms is of 2.794(4) Å pointing to the weak nature of this interaction.

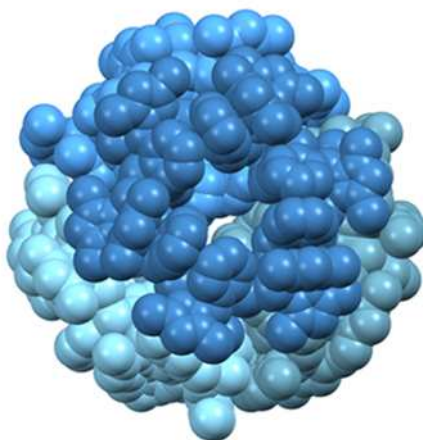


Figure 35. Molecular capsule.

On the other hand, the evidence that plays in favor of an Ag-F weak bond comes by the deviation of the ideal trigonal geometry of the silver atom, which in fact lies out of the plane defined by the N₂S donor system by 0.09 Å and is directed toward the fluorine atom. The ball shaped assembly comprised of four hexameric units, defines the unit cell lattice and forms two types of cavities one that is contained in the sphere (~900 Å³) and the other that is produced by the close packing of the spheres (~1400 Å³). These 3D cavities are filled by highly disordered solvent molecules.

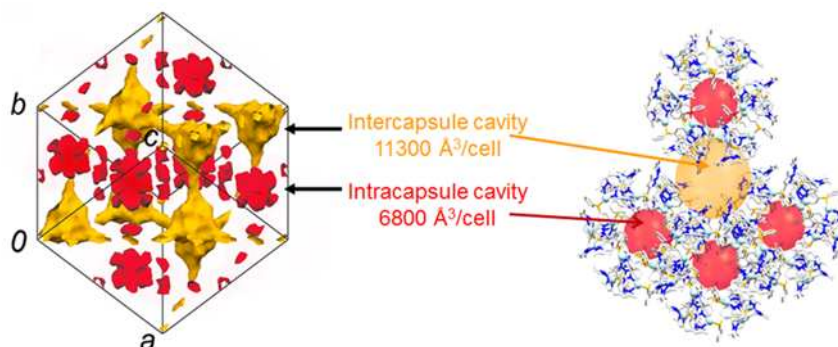


Figure 36. Two interpenetrated cavities frameworks in yellow and in red.

Isostructural crystals could be obtained by crystallizing **23-BF₄** in different solvents such as THF/hexanes, CH₂Cl₂/hexanes, and acetone/diethyl-ether. In all cases the solvent could not be properly located even though the X-ray data collection were performed at 205 K, and it was therefore treated with the PLATON/SQUEEZE program¹⁰¹. The solvent guest can be removed by the cavities without loss of crystallinity. One well defined crystal was evacuated by applying a high vacuum for several hours and then an X-ray data collection was performed. The same crystal was wet with dichloromethane and quickly positioned under the nitrogen cryostream at 205 K, and an X-ray data collection was performed. The same procedure was applied to another crystal that was impregnated with 1,3-dibromopropane and the X-ray data collection was performed at 190 K. In none of the data collection the solvent could be properly located inside the cavities. Also solid NMR on compounds **23-BF₄** and **24-PF₆** confirmed the absence of the solvent molecules (Figure 41).

Table 7. Selected bond lengths (Å) and angles (°) for **23-BF₄**, **24-PF₆**, **25-CF₃SO₃**, **26-NO₃**, **22**.

23-BF₄			
Ag-N(21)	2.282(3)	N(21)-Ag-S(13)'	124.25(7)
Ag-N(22)	2.232(3)	N(22)-Ag-S(13)'	148.59(7)
Ag-S(13)'	2.3934(9)	N(21)-Ag-F(2)	101.1(1)
Ag-F(2)	2.794(4)	N(22)-Ag-F(2)	88.5(1)
N(21)-Ag-N(22)	86.60(9)	S(13)'-Ag-F(2)	90.67(7)
24-PF₆			
Ag-N(21)	2.302(7)	N(21)-Ag-S(13)''	125.2(2)
Ag-N(22)	2.214(6)	N(22)-Ag-S(13)''	149.2(2)
Ag-S(13)''	2.391(2)	N(21)-Ag-F(2)	89.4(2)
Ag-F(2)	2.719(5)	N(22)-Ag-F(2)	91.4(2)
N(21)-Ag-N(22)	85.6(2)	S(13)''-Ag-F(2)	91.3(2)
25-CF₃SO₃			
Ag-N(21)	2.356(3)	N(21)-Ag-S(13)'''	126.5(9)
Ag-N(22)	2.241(3)	N(22)-Ag-S(13)'''	140.43(9)
Ag-S(13)'''	2.464(1)	N(21)-Ag-O(24)	92.9(1)
Ag-O(24)	2.651(4)	N(22)-Ag-O(24)	126.8(1)
N(21)-Ag-N(22)	87.6(1)	S(13)'''-Ag-O(24)	76.4(1)
26-NO₃			
Ag-N(21)	2.365(3)	N(21)-Ag-S(13)'''	123.32(6)
Ag-N(22)	2.251(3)	N(22)-Ag-S(13)'''	131.47(8)
Ag-S(13)'''	2.5046(9)	N(21)-Ag-O(14)	98.4(1)
Ag-O(14)	2.569(3)	N(22)-Ag-O(14)	139.3(1)
Ag-O(24)	2.651(4)	S(13)'''-Ag-O(14)	77.75(7)
N(21)-Ag-N(22)	87.4(1)		

22

Cu-N(21)	2.007(6)	N(21)-Cu-N(22)	94.2(2)
Cu-N(22)	1.997(6)	N(21)-Cu-S(13)'	123.7(2)
Cu-S(13)'	2.164(2)	N(22)-Cu-S(13)'	142.1(2)
Cu-F(2)	2.750(7)		

Symmetry codes: ' = 1-z; $\frac{1}{2}$ -x; $\frac{1}{2}$ -y, '' = 1/2-z; x-1/4; y+1/4. ''' = x-y; x; 1-z.



Figure 37. A picture of **24-PF₆** evacuated crystal and then deep in CH₂Cl₂. From picture it is possible to show the air bubbles derived from the empty cavities.

Nevertheless, the residual electron density in the cavities well correlates with the electronic density of the solvent employed. In particular, as estimated by SQUEEZE-PLATON the dimensions of the cavities and the residual electron density is as follow: 1999 e⁻/cell and 20187 Å³/cell (**23-BF₄**-evacuated, cavity volume: 26 % of total cell volume), 7500 e⁻/cell and 20925 Å³/cell (**23-BF₄**-CH₂Cl₂, cavity volume: 28 % of total cell volume), 9625 e⁻/cell and 21487 Å³/cell (**23-BF₄**-C₃H₆Br₂, cavity volume: 28 % of total cell volume). The same molecular structure is obtained with Cu⁺ in place of Ag⁺, with the major difference represented by the metal-donor atom bond lengths, that in the case of the copper complex are on average 0.2 Å shorter than in the silver one. This has however a minimum effect on the size of the hydrophobic pore, as it now measures 5.0 Å. **24-PF₆** and **23-BF₄** crystallize in the same space group and have nearly the same cell parameters, Tables 7 . The phosphorous atom occupies the same sites of the boron, the only difference is in the different localization of the fluorine atoms. This most likely happens as a favorable match between the spherical symmetry of BF₄⁻ and PF₆⁻ anions and the cavity generated by the close approach of the hexamers. Also for **24-PF₆** the solvent could not be properly located inside the cavities. The residual electron density was estimated by SQUEEZE-PLATON: the dimensions of the cavities and the residual electron density are: 6055 e⁻/cell and 21476 Å³/cell (cavity volume: 27 % of total cell volume).

A different crystal packing is obtained with NO₃⁻ and CF₃SO₃⁻ anions. Both compounds crystallize in the rhombohedral space group *R*-3. Also for these structures, the counterions interact with the metal: in **26-NO₃** the nitrate acts as symmetric O,O bidentate, whereas in **25-CF₃SO₃** the triflate is monodentate, which is the usual behavior of these two anions when bound to a metal center.

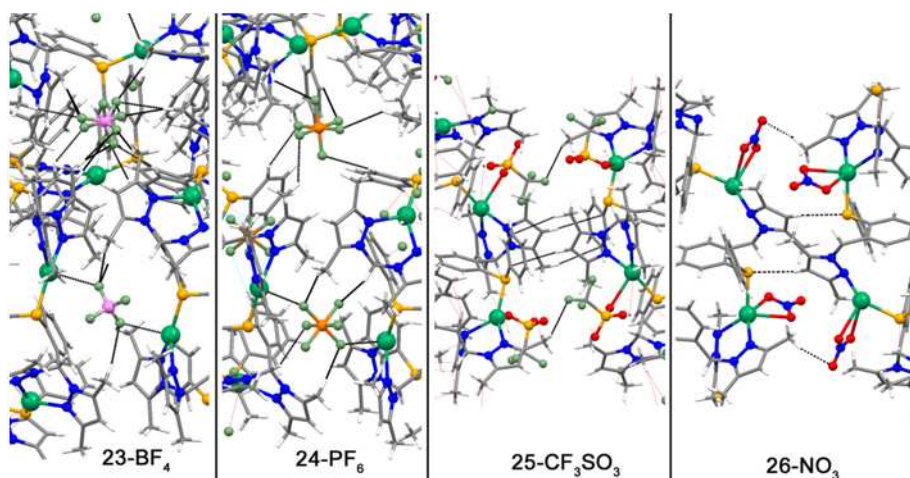


Figure 38. Different anions interaction between hexamers in different compounds.

The metal interacts more strongly with the anions than in the complexes containing BF_4^- or PF_6^- , and this also reflected in the Ag-N and Ag-S bond lengths, which are significantly longer in **26-NO₃** and **25-CF₃SO₃** with respect to **23-BF₄** and **24-PF₆**. Another consequence of the Ag-O interaction, is the more pronounced distortion of the metal trigonal planar geometry, since the metal lies out of the plane of the N₂S donor atoms of 0.3 Å. Another difference is evident in the mutual orientation of the pyrazole rings, as in **24-PF₆** and **23-BF₄** they are symmetrically ligated to the metal, whereas in **26-NO₃** and **25-CF₃SO₃** one of the pyrazole ring is slightly rotated so that there is a considerable mismatch between the directionality of the nitrogen lone pair and the metal center.

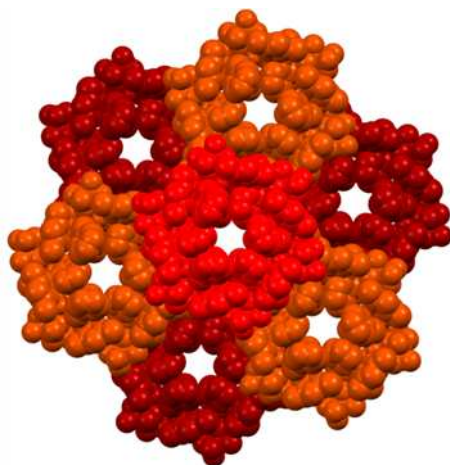


Figure 39. Hexamers assembly for silver compounds with no-symmetrical counteranions such as triflate and nitrate.

Furthermore, as a possible consequence of this pyrazole ring rotation, the peripheral phenyl ring is no longer stacked over the pyrazole ring but it is rotated away from it (the dihedral angle between the pyrazole and phenyl ring planes is of 65°). This has important consequences on the dimension of the hydrophobic pore of the hexamer, as now it has shrunk to 3.4 Å in diameter. The crystal packing of **26-NO₃** and **25-CF₃SO₃** shows other marked differences with that of **24-PF₆**, and **23-BF₄**. In fact, six hexameric units define an octahedral cavity which is in communication with symmetry related cavities aligned along the C3 crystallographic axis by means of the hydrophobic pore. In **26-NO₃** and **25-CF₃SO₃** the volumes of the cavities filled by solvent molecules amounts to ~40% and ~36% of the unit cell volume, respectively: 1825 e⁻/cell and 6287 Å³/cell (**26-NO₃**), and 1901 e⁻/cell and 6113 Å³/cell (**25-CF₃SO₃**). But the loss of solvent molecules implies the collapse of the entire structures.

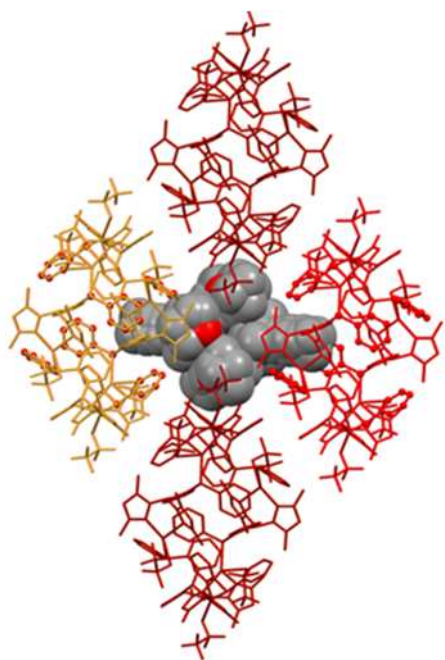


Figure 40. Solvent molecules inside the cavities, determined according to the single crystal x-ray data collection performed at 300K.

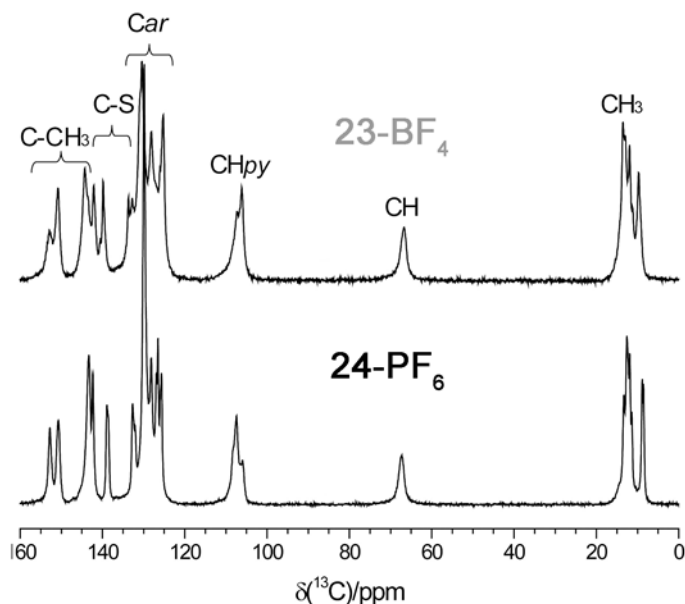


Figure 41. ^{13}C CP MAS NMR of porous **23-BF₄** and **24-PF₆** materials. The samples were crystallized from acetone/diethylether and then subjected to thermal treatment at 60°C under vacuum. No signals of the solvents are detected. Spinning speed of 12500 Hz and contact time of 2 ms were used.

4.3.3. Variable temperature PXRD and thermal analysis

Variable temperature Powder X-ray diffraction was employed to investigate how the crystallinity of the different compounds is affected by temperature. The crystals of **23-BF₄**/**24-PF₆** retain a long range structural order in the 0-160 °C range and this is confirmed also by DSC thermal analysis. Figures 42 and 46. In fact the cristallinity is preserved also at high temperature and the DSC analysis confirmed the presence of a peak of glass transition at 160°C for the compound with the weaker interaction **23-BF₄** and at 200°C, for the compound with the stronger interaction **24-PF₆**. On the other hand the PXRD spectra for **25-CF₃SO₃** and **26-NO₃** show clearly a rapid loss of cristallinity. For **26-NO₃** crystals, the removal from the mother liquor determines the collapse of the entire structure such that in the spectra there is an amourphous profile. The **25-CF₃SO₃** crystals are more robust but the removal of solvent guest molecules (THF) at 100°C determines the collapse of the supramolecular network.

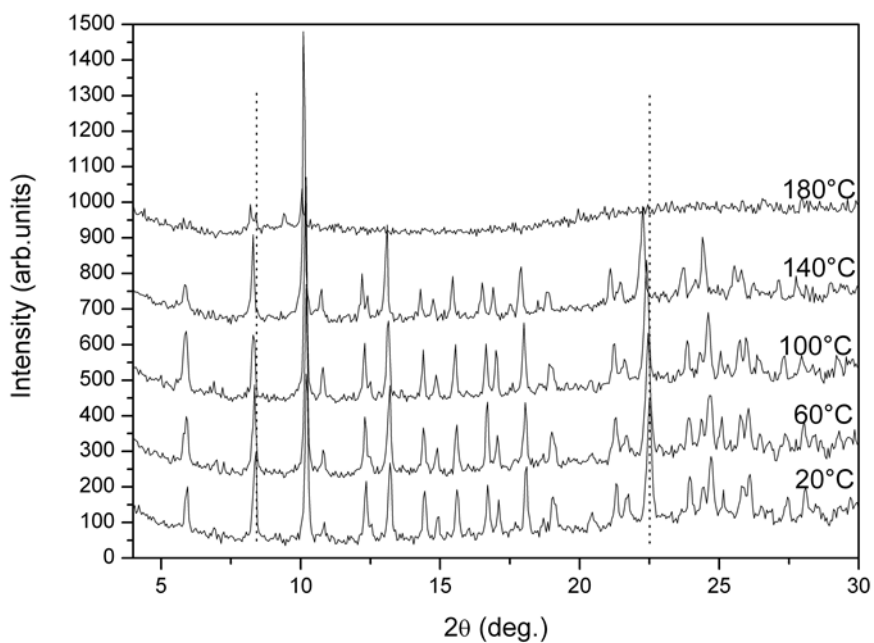


Figure 42. Variable temperature X-ray powder patterns of **23-BF₄** in the 20-180 °C interval.

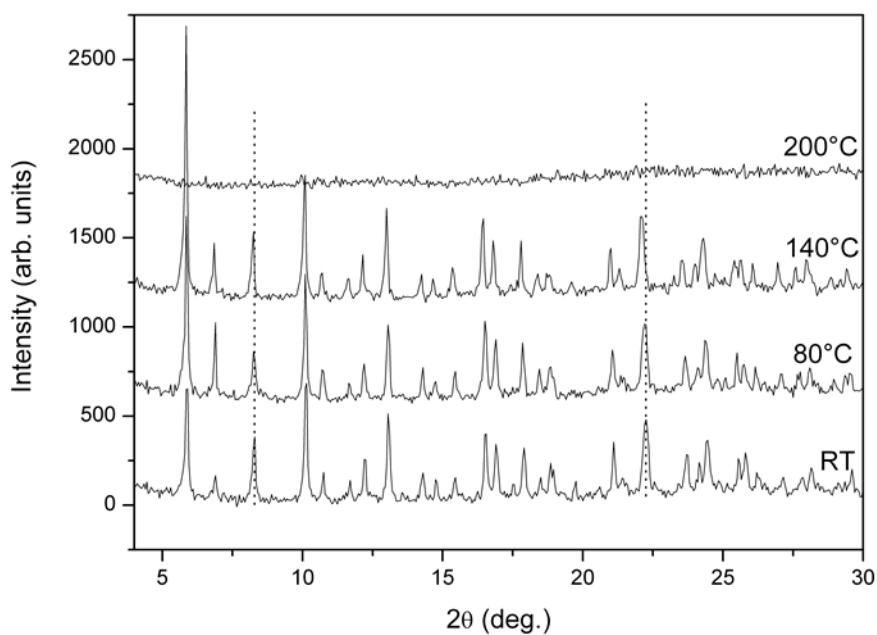


Figure 43. Variable temperature X-ray powder patterns of **24-PF₆** in the 20-200 °C interval.

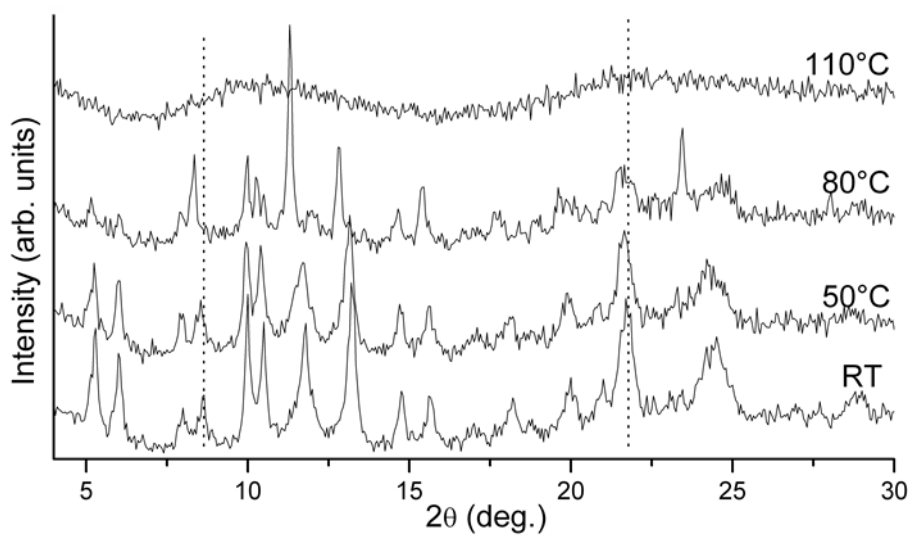


Figure 44. Room temperature X-ray powder pattern of **25-CF₃SO₃** performed on freshly grounded crystals (grown from CH₂Cl₂/Hexanes).

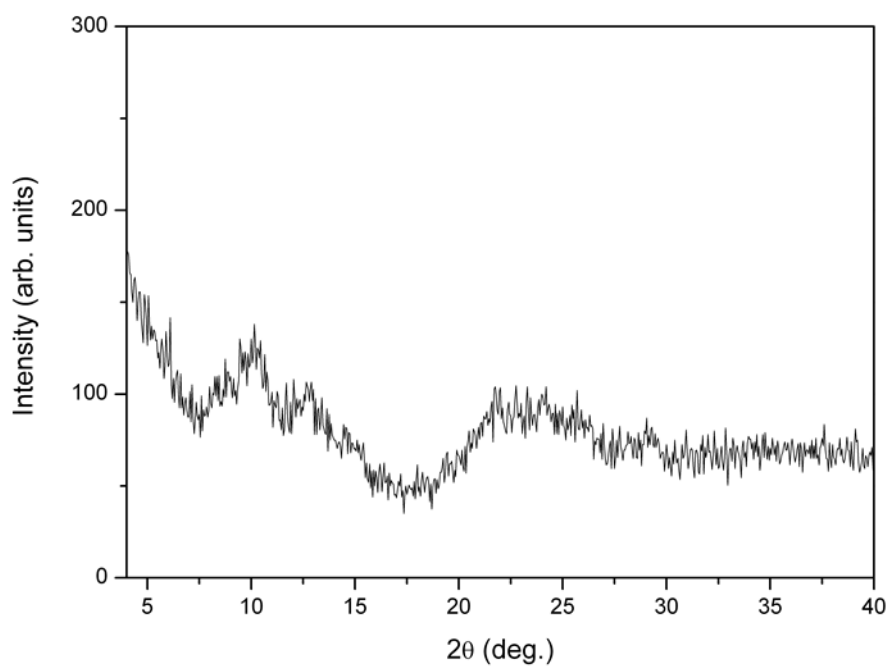


Figure 45. Room temperature X-ray powder pattern of **26-NO₃** performed on freshly grounded crystals (grown from CH₂Cl₂/Hexanes).

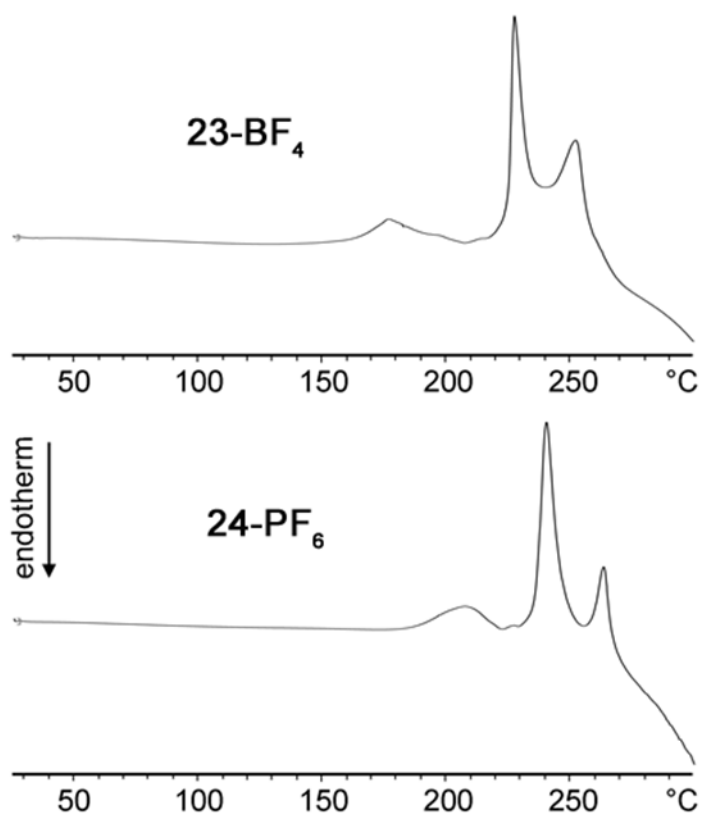


Figure 46. Calorimetric analysis of **23-BF₄** and **24-PF₆** compounds. The heating rate of 10 °C/min was used.

4.3.4. PGSE (Pulse Gradient Spin Echo) ^1H NMR

Pulsed-gradient spin-echo (PGSE) NMR measurements were carried out to investigate how the complexes aggregate in solution. Since the aggregation process and the ion pairing depends on the solvent polarities,³⁶ these experiments were performed in CD_2Cl_2 ($\epsilon = 9.1$) and in acetone- d^6 ($\epsilon = 20.7$) with three different concentrations (0.1–0.001 M), Figures 47 and 48. The measured hydrodynamic radii (r_{H}) for **23-BF₄** and **25-CF₃SO₃** are in the 7.6(3)–6.4(2) Å and 6.2(2)–6.7(3) Å interval, respectively, Table 8. These values reflect the larger size of the **23-BF₄** hexamer when compared to the **26-NO₃** one. The relatively narrow range of the r_{H} values is consistent with the presence of isolated hexameric units in solution, at least in the investigated concentration interval. It is therefore during the crystallization process that the anions intervene in shaping the two different types of crystal lattices, cubic *Fd*-3 with $\text{BF}_4^-/\text{PF}_6^-$ and rhombohedral *R*-3 with $\text{NO}_3^-/\text{CF}_3\text{SO}_3^-$.

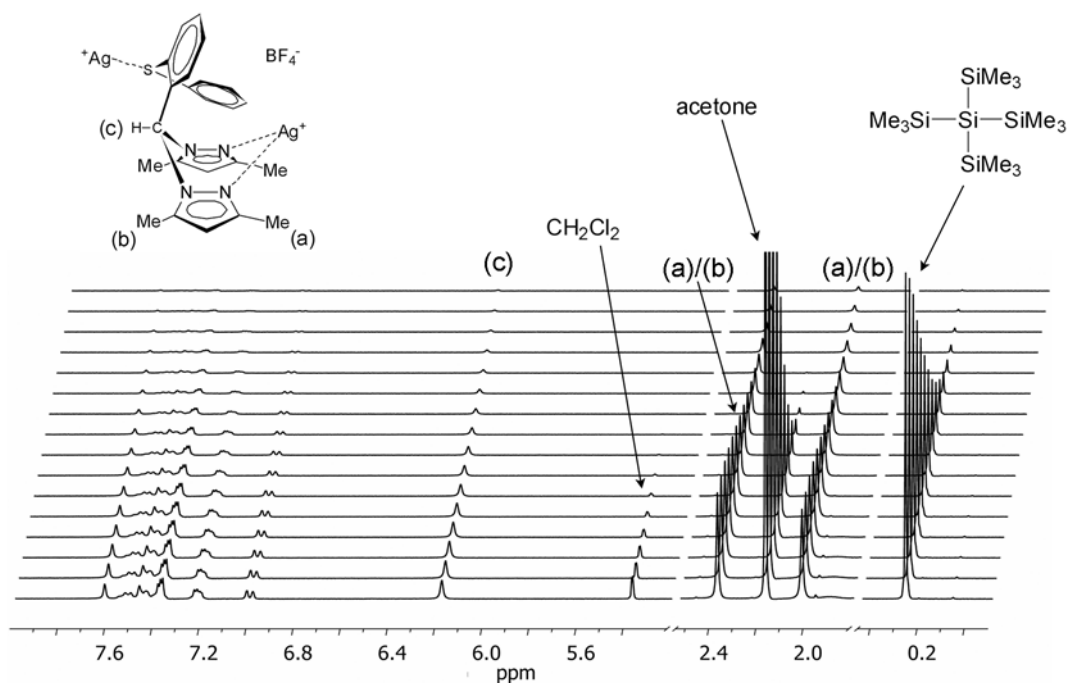


Figure 47. ^1H PGSE NMR of spectrum of **23-BF₄** recorded in CD_2Cl_2 showing the dependence of the resonance intensity on the intensity of the pulsed-field gradient. Conc. = 0.1 M based on 1/6 of the hexameric unit. The decay of the signals is in the following order: $\text{CH}_2\text{Cl}_2 \approx \text{acetone} < \text{TMSS} < \text{23-BF}_4$, according to the increasing

dimensions of the molecules. Internal standard: tetrakis(trimethylsilyl)silane. CH_2Cl_2 and acetone are present as impurities. The crystals were grown from acetone/diethyl-ether.

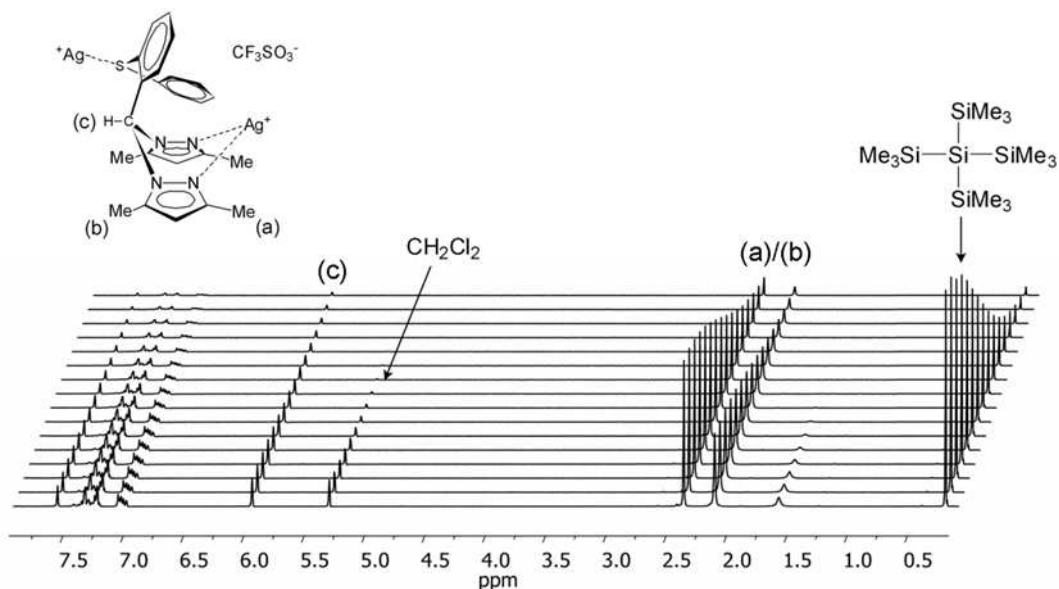


Figure 48. ^1H PGSE NMR of spectrum of **25-CF₃SO₃** recorded in CD_2Cl_2 showing the dependence of the resonance intensity on the intensity of the pulsed-field gradient. Conc. = 0.1 M based on 1/6 of the hexameric unit. The decay of the signals is in the following order: $\text{CH}_2\text{Cl}_2 < \text{TMSS} < \text{23-BF}_4$, according to the increasing dimensions of the molecules. Internal standard: tetrakis(trimethylsilyl)silane. The crystals were grown from CH_2Cl_2 /Hexanes.

Table 8. Experimental Hydrodynamic Radii (r_H , Å) for **23-BF₄**, and **25-CF₃SO₃** in CD₂Cl₂ and acetone-d⁶ at Different Concentrations at 300 K.

Solvent	Conc. (M)	r_H 23-BF₄	r_H 25-CF₃SO₃
CD ₂ Cl ₂	0.001	6.4(0.2)	6.2(0.2)
CD ₂ Cl ₂	0.05	6.6(0.2)	6.3(0.3)
CD ₂ Cl ₂	0.1	7.6(0.3)	6.7(0.3)
acetone-d ⁶	0.001	6.9(0.3)	6.7(0.3)
acetone-d ⁶	0.05	6.7(0.3)	6.6(0.3)
acetone-d ⁶	0.1	7.0(0.4)	6.7(0.2)

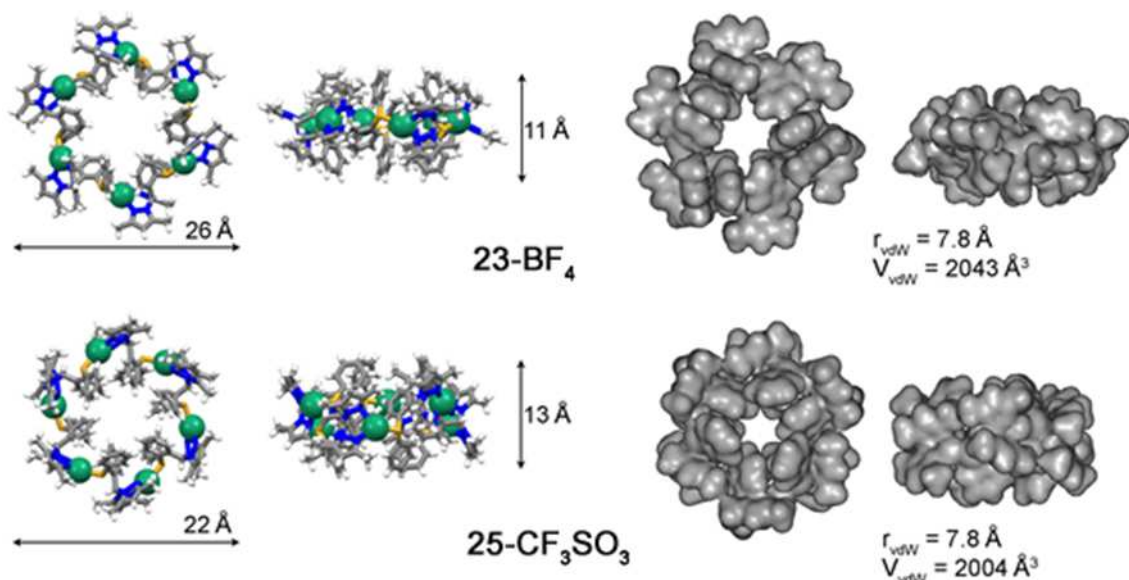


Figure 49. Dimensions and van der Waals radii (r_{vdW}) of **23-BF₄** (above) **25-CF₃SO₃** (below) hexamers as derived from the X-ray crystal structures.

4.3.5. Absorption analysis

The absorption characteristics of these crystal structures were preliminary tested with PXRD analysis: when evacuated crystalline material is placed in a chamber saturated

with solvent vapours, the powder patterns indicate that all peaks are shifted at lower 2θ values, pointing to a 2.7-3.7% increase of the unit cell volume depending on the solvent employed. This data may be interpreted as an enlargement of the structure taking place in order to accommodate the solvent molecules within the empty cavities. This behaviour is observed using dichloromethane, acetone, and methanol, and several cycles of vacuum/solvent-vapors can be applied to the compound without loss of structural order, Figures 50 and 51. As previously reported, a different behaviour is exhibited by the crystals of **25-CF₃SO₃/26-NO₃**, since the crystallinity of the sample is lost very rapidly, Figures 44 and 45. The crystal-to-amorphous transition is accelerated when a high vacuum is applied, suggesting that the stability of the overall crystal structure strongly depends on the occupancy of the cavities. Contrarily to other materials, the crystallinity of the sample is not restored when exposing the amorphous material to solvent vapors. This is most likely the result of different supramolecular arrangement and crystal packing. In fact, a considerable contribution to the stabilization of the 3D structure of **23-BF₄/24-PF₆** is determined by the Ag-F bonds, whereas the crystal packing of **25-CF₃SO₃/26-NO₃** is determined by weaker CH \cdots π /CH \cdots F and CH \cdots S/CH \cdots O interactions, see Figure 38.

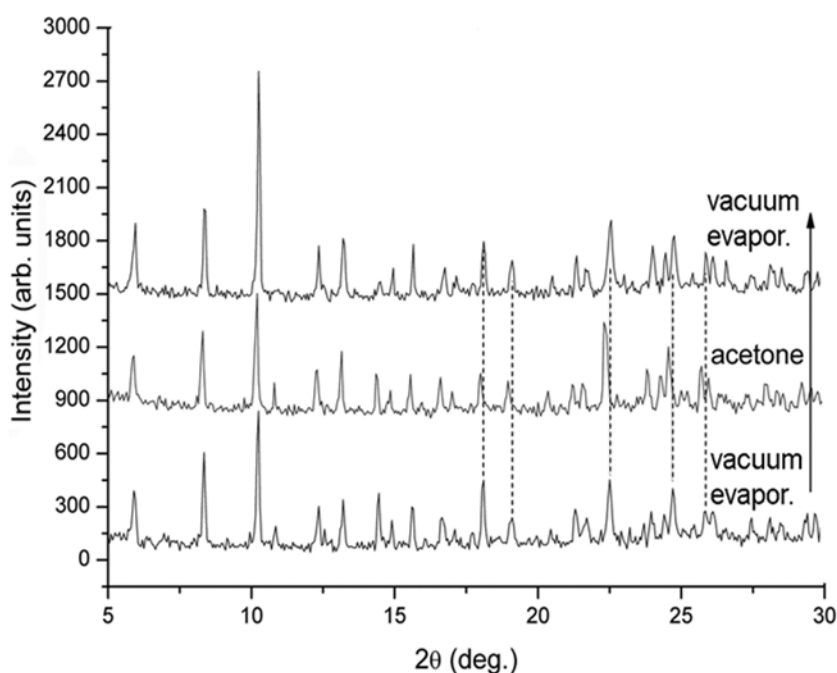


Figure 50. Effect of the solvent absorption on the X-ray powder spectra of **23-BF₄**. Freshly ground crystals (grown from acetone/diethyl ether) were subjected to high

vacuum and $T = 60\text{ }^{\circ}\text{C}$ for 2h. The evacuated crystals were then exposed to acetone vapors in a closed chamber. Crystals were evacuated (high vacuum, $T=60\text{ }^{\circ}\text{C}$, 2 h) before re-exposing them to acetone vapors. Upon contact with solvents, the unit cell volume increases in the 2.7-3.7% range.

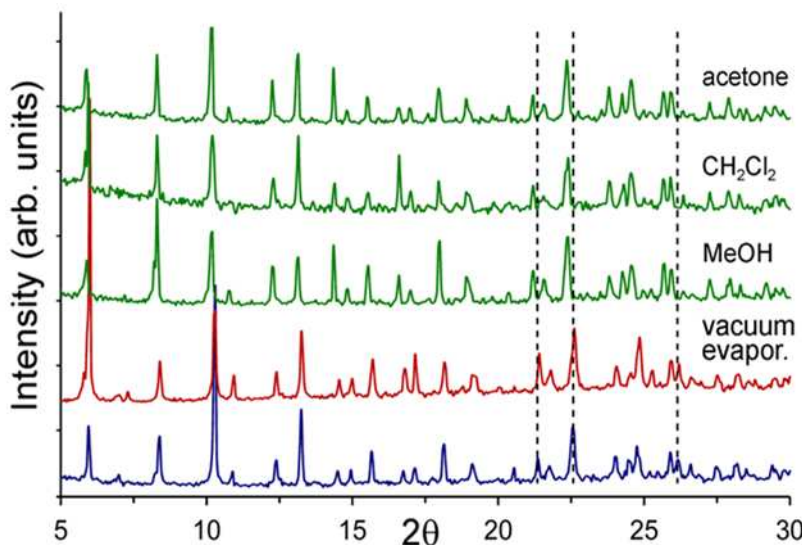


Figure 51. Effect of the solvent absorption on **23-BF₄** crystals. Freshly ground crystals, blue. Crystals subjected to high vacuum and $T = 100\text{ }^{\circ}\text{C}$ for 2h, red. The evacuated crystals were then exposed to saturated solvent vapors (methanol, dichloromethane, or acetone), green.

The permanent porosity of the **23-BF₄**/**24-PF₆** compounds was explored by absorption isotherms of gases. **23-BF₄** can adsorb $77\text{ cm}^3(\text{STP})/\text{g}$ of CO_2 at 195K and 1 atm (15.1wt%) while only $22\text{ cm}^3/\text{g}$ of methane was adsorbed under the same conditions of pressure and temperature (Figure 52). The CO_2 measured capacity, equal to 3.44 mmol/g , corresponds to an occupied volume of 9600 \AA^3 per unit cell ($d_{\text{CO}_2}=1.5\text{ g/cm}^3$ was used) which matches the intercapsule empty space of 11300 \AA^3 per unit cell explored by a sphere with a radius of 1.6 \AA (the kinetic diameter of CO_2 is equal to 3.3 \AA). Thus, this result indicates the virtual complete filling of the intercapsule space which is easily accessible to the gas species diffusing-in while CO_2 molecules are prevented to enter inside the capsules (see Figure 36). Furthermore, the porous material adsorbs selectively CO_2 ($40\text{ cm}^3(\text{STP})/\text{g}$) over CH_4 and N_2 (12 and $6\text{ cm}^3(\text{STP})/\text{g}$, respectively) at room temperature and up to 10 atm. The isosteric heat of

absorption was estimated to be 25 kJ/mol for CO₂ and 19.4 kJ/mol for CH₄ in agreement with the hydrophobic nature of the intercapsule cavity. A foreseeable application of the system is in the gas-separation process where a technological relevant gas is purified out of a gas mixture.

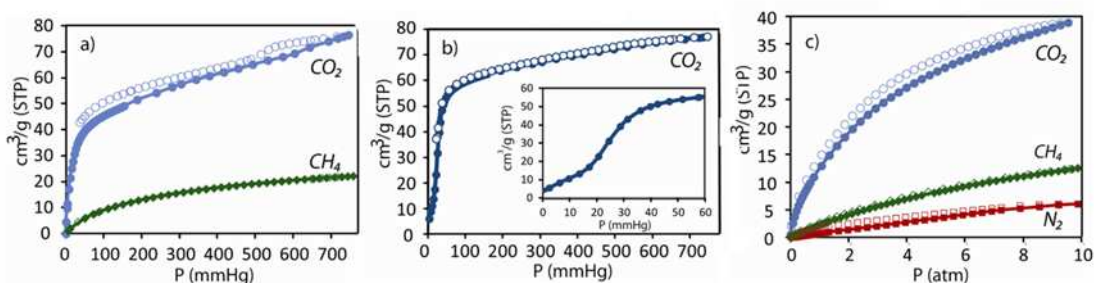
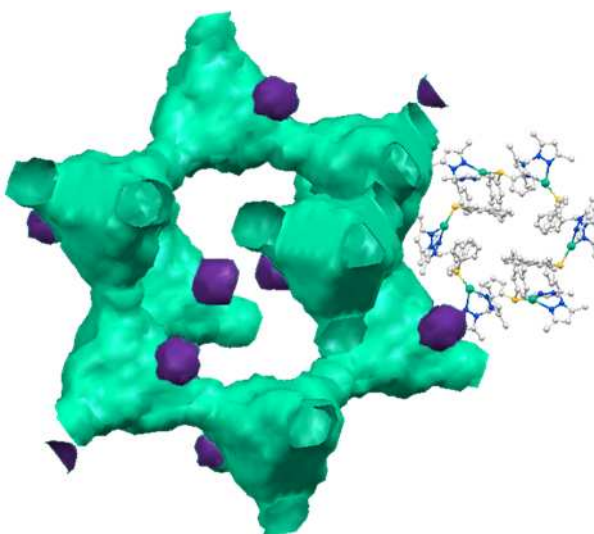


Figure 52. a) Adsorption/desorption isotherms of CO₂ and CH₄ of porous **23-BF₄** compound at 195K. b) CO₂ adsorption/desorption isotherm of porous **24-PF₆** compound at 195K. In the inset enlargement of the low pressure region. c) Adsorption/desorption isotherms of CO₂, CH₄ and N₂ of **23-BF₄** compound at room temperature and up to 10 atm.

CHAPTER 5

Novel cavity design using pre-organized tripodal ligands: synthesis and solid state characterization.



Different porous materials built on the hexameric unit described in the previous chapter were prepared by appropriate modification of the N_2S donor ligands¹⁰². We functionalized the bispyrazolyl scaffold with different thioether arm in order to obtain different cavities. We varied the shape and the size of cavities by introducing substituents on the terminal phenyl ring. We show here that not only the methyl group on the bispyrazolyl scaffold and the phenyl ring are required for the hexamer formation but also the terminal phenyl ring is necessary. Five new ligands were synthesized and fully characterized. Silver complexes were prepared by mixing ligands and $AgPF_6$ and $AgCF_3SO_3$. In most of the cases crystals suitable for X-ray structural analysis were obtained. With the symmetrical counterion PF_6^- ligands and silver ions self assembled in hexamers which form capsules at the supramolecular level. These crystals are isostructural to those described in chapter 4, but the functionalization of the peripheral aromatic group results in the formation of cavities with different volumes.

5.1. Introduction

The use of crystal engineering to design novel porous coordination polymers (PCP's)^{7,9,13,22,25} is a rapid developing area of inorganic coordination chemistry. In fact these porous materials can merge the properties of both porous material and polymers. Above all, the diversity of synthetic routes for these PCP's facilitates the design and construction of numerous framework capable of incorporating multiple chemical functionalities. Crystal engineering enables us to control the dimensions and the electronic characteristics of the pores to obtain suitable materials with defined characteristics. Porous coordination polymers are good candidates due to their synthetic flexibility and structural and functional diversity. In host-guest process, the shape, the geometry and size of cavities play a key role: for that reason the rational design of the pores became particularly important. As we have described in the previous chapters, not only the geometry of metal ions but also the ligand conformation and the coordinative features of the counterions determine the supramolecular architectures^{24,73,103}. For these reasons, various frameworks are capable to incorporate atomic or molecular sized guest inside well-defined cavities. In particular the self assembled architectures of PCP can be used as gas storage, gas separation, controlled released drugs, catalysts and sensors. In literature there are many example of nanoscale design of porous solids. Kitagawa et al. show how the interactive communication between molecules in the framework determines bulk properties starting with a 2D interdigitated structure to obtain porous materials.

In this chapter we present how we modified the steric and electronic features of the cavities in the porous material obtained and described in the previous chapter (Chapter 4). Different structural and porous properties were introduced by changing the thioether arm on the bispyrazolyl scaffold of the N₂S donor ligand. We have utilized two type of anions: symmetrical PF₆⁻ and a non symmetrical CF₃SO₃⁻ to have different supramolecular interaction. Through X-ray on single crystals we determined the molecular structures and the porosity of the complexes.

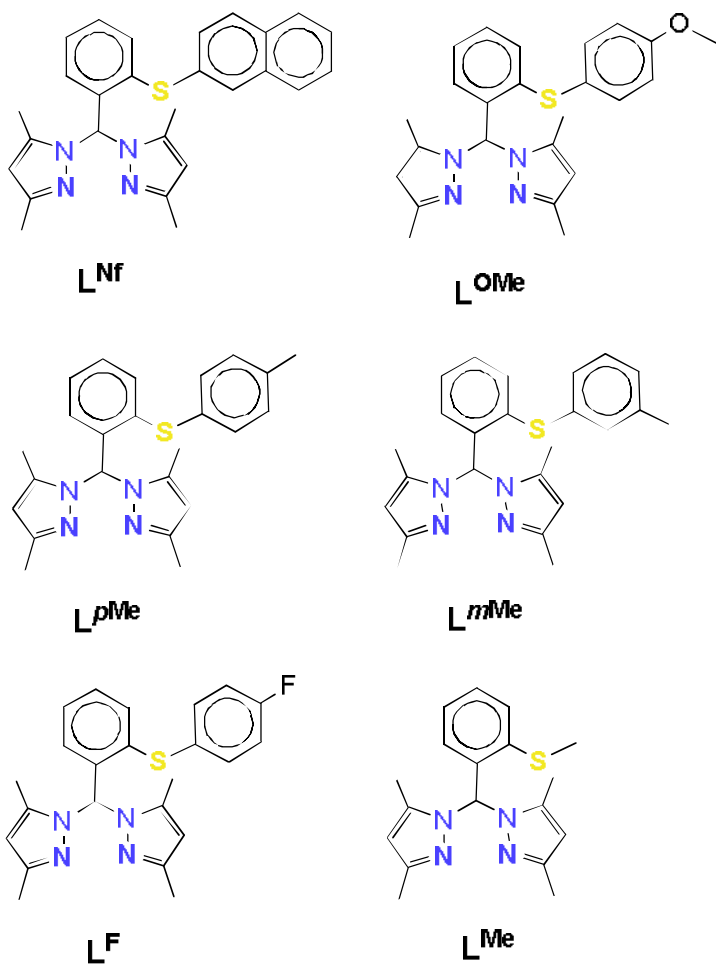


Figure 53. Molecular structure of the ligands modified on the peripheral aromatic moiety.

5.2. Experimental

5.2.1. Synthesis

All reagents and solvents were commercially available, except for bis(3,5-dimethylpyrazolyl)ketone which were prepared as reported elsewhere^{44–46}. The synthesis of aldehydes, except for of 2-(methylthio)benzaldehyde which is commercially available, derive from a synthesis reported in literature¹⁰³. ¹H spectra were recorded on a Bruker Avance 300 spectrometer using standard Bruker pulse sequences. Chemical shifts are reported in parts per million (ppm) referenced to residual solvent protons. Infrared spectra were recorded from 4000 to 700 cm⁻¹ on a Perkin-Elmer FTIR Nexus spectrometer equipped with a Smart Orbit HATR accessory (diamond crystal). Elemental analyses (C, H, and N) were performed with a Carlo Erba EA 1108 automated analyzer.

Synthesis of 2-(naphthalen-1-ylthio)benzaldehyde. To a stirred solution of naphthalene-1-thiol (4.27 g, 26.71 mmol) and anhydrous Na₂CO₃ (3.50 g) in dry DMF (8 mL) under nitrogen at 90 °C, 2-chlorobenzaldehyde (2.40 ml, 21.31 mmol) was slowly added. The mixture was stirred at 90 °C for 3 hours. After cooling, the reaction mixture was poured into water (20 mL) and extracted with diethyl ether (20 mL). The extract was washed with water (2x20 mL), dried with anhydrous Na₂SO₄, and concentrated under vacuum. The resulting oil was triturated with hexane in an ultrasound bath for 20 min, filtered and dried under vacuum to afford a yellow solid (5.03 g, 25.35 mmol, 93%). IR (cm⁻¹): 3356w, 3056w, 2965w, 2860w, 2756w, 1695m, 1591m, 1552w, 1491m, 1447m, 1400m, 300w, 1269m, 1117w, 1060w, 1047w, 939w, 860w, 826m, 808m, 743s, 708m, 630w, 530w, 473s, 430w. ¹H NMR (300 MHz, CDCl₃): δ, 7.13 (d, J = 7.5 Hz, 1H, CH (Ph)), 7.36-7.57 (m, 4H, CH(Ph)), 7.80-7.93 (m, 5H, CH(Ph)), 7.99 (s, 1H, CH(Ph)), 10.45 (s, 1H, CHO). Anal.Calc. for C₁₇H₁₂OS (264.34): C, 77.24; H, 4.58. Found: C, 77.19; H, 4.62%.

Synthesis of 2-(p-tolylthio)benzaldehyde. The procedure used to prepare 2-(naphthalen-1-ylthio)benzaldehyde was applied by using a stirred solution of 4-methylbenzenethiol (2.40 g, 19.32 mmol) and anhydrous Na₂CO₃ (3.01 g) in dry DMF (8 mL) under nitrogen at 90 °C, 2-chlorobenzaldehyde (1.80 ml, 15.98 mmol) and affording a pale yellow solid (2.23 g, 61%). IR (cm⁻¹): 3056w, 3026w, 2917w, 2860w, 1760w, 1686w, 1667m, 1582w, 1552m, 1486w, 1454m, 1440w, 1401m, 1378w, 1300w, 1247w, 1195m, 1124m, 1040w, 1013w, 842m, 810m, 752s, 672m, 656m, 519m, 491w. ¹H NMR (300 MHz, CDCl₃): δ, 2.41 (s, 3H, CH₃), 7.04 (dd, J₁ = 0.9 Hz, J₂ =

7.8 Hz, 1H, CH(Ph)), 7.22-7.40 (m, 6H, CH(Ph)), 7.87 (dd, $J_1=1.8$ Hz, $J_2=9$ Hz, 1H, CH(Ph)), 10.40 (s, 1H, CHO) . Anal.Calc. for $C_{14}H_{12}OS$ (228.31): C, 73.65; H, 5.30. Found: C, 73.54; H, 5.34%.

Synthesis of 2-(4-fluorophenylthio)benzaldehyde. The procedure used to prepare 2-(*naphthalen-1-ylthio*)benzaldehyde was applied by using a stirred solution of 4-fluorobenzenethiol (2.1 ml , 19.32 mmol) and anhydrous Na_2CO_3 (3.01 g) in dry DMF (8 mL) under nitrogen at 90 °C, 2-chlorobenzaldehyde (1.80 ml, 15.98 mmol) and affording a pale yellow solid (1.35 g, 36%). IR (cm^{-1}): 3326w, 3086w, 2856w, 2760w, 1904w, 1673m, 1486s, 1395m, 1186s, 1047m, 830s, 760s, 656m, 521m. 1H NMR (300 MHz, $CDCl_3$): δ , 7.00 (dd, $J=8.1$ Hz, 2H, CH(Ph)), 7.13 (t, $J=8.7$ Hz, 2H, CH(Ph)), 7.29-7.52 (m, 4H, CH(Ph)), 7.87 (dd, $J_1=1.5$ Hz, $J_2=6$ Hz, 1H, CH(Ph)), 10.36 (s, 1H, CHO) . Anal.Calc. for $C_{13}H_9FOS$ (232.27): C, 67.22; H, 3.91. Found: C, 67.30; H, 3.89%.

Synthesis of 2-(4-methoxyphenylthio)benzaldehyde. The procedure used to prepare 2-(*naphthalen-1-ylthio*)benzaldehyde was applied by using a stirred solution of 4-methoxybenzenethiol (2.5 ml , 19.32 mmol) and anhydrous Na_2CO_3 (3.01 g) in dry DMF (8 mL) under nitrogen at 90 °C, 2-chlorobenzaldehyde (1.80 ml, 15.98 mmol) and affording a yellow solid (2.56 g, 66%). IR (cm^{-1}): 2991w, 2939w, 2834w, 2752w, 1669m, 1587m, 1559w, 1491m, 1459w, 1437w, 1405m, 1289m, 1248s, 1197m, 1169m, 1128w, 1101w, 1023s, 1006w, 848w, 821m, 799w, 704w, 678m, 660m, 528m, 499m. 1H NMR (300 MHz, $CDCl_3$): δ , 3.87 (s, 3H, OCH_3), 6.91-6.99 (m, 3H, CH(Ph)), 7.26-7.49 (m, 4H, CH(Ph)), 7.84 (dd, $J_1=1.5$ Hz, $J_2=7.5$ Hz, 1H, CH(Ph)), 10.37 (s, 1H, CHO) . Anal.Calc. for $C_{14}H_{12}O_2S$ (244.31): C, 68.83; H, 4.95. Found: C, 68.88; H, 5.00%.

*Synthesis of 2-(*m*-tolylthio)benzaldehyde.* The procedure used to prepare 2-(*naphthalen-1-ylthio*)benzaldehyde was applied by using a stirred solution of 3-methylbenzenethiol (2.4 ml , 19.32 mmol) and anhydrous Na_2CO_3 (3.98 g) in dry DMF (8 mL) under nitrogen at 90 °C, 2-chlorobenzaldehyde (1.80 ml, 15.98 mmol) and affording a yellow solid (2.63 g, 72%). IR (cm^{-1}): 3056w, 3008w, 2854w, 2760w, 1695w, 1673m, 1588w, 1553m, 1460m, 1439w, 1397m, 1373w, 1304w, 1261w, 1199m, 1166w, 1124m, 1067w, 1041m, 996w, 844m, 784m, 761s, 711w, 694m, 673m, 654m, 553w, 490m, 450w. 1H NMR (300 MHz, $CDCl_3$): δ , 2.37 (s, 3H, CH_3), 7.13 (dd, $J_1=1.8$ Hz, $J_2=7.8$ Hz, 1H, CH(Ph)), 7.20-7.43 (m, 6H, CH(Ph)), 7.90 (dd, $J_1=1.5$ Hz, $J_2=7.5$ Hz, 1H, CH(Ph)), 10.42 (s, 1H, CHO) .Anal.Calc. for $C_{14}H_{12}OS$ (228.31): C, 73.65; H, 5.30. Found: C, 73.54; H, 5.34%.

Synthesis of 1,1'-((2-(naphthalen-1-ylthio)phenyl)methylene)bis(3,5-dimethyl-1H-pyrazole) (**L^{Nf}**). A mixture of bis(pyrazolyl)ketone (0.93 g, 4.21 mmol), 2-(naphthalen-1-ylthio)benzaldehyde (1.07 g, 4.76 mmol) and CoCl₂·6H₂O (5 mg) was heated at 80°C for an hour with stirring. The mixture was then cooled at room temperature and stirred for 2 hours. Dichloromethane (30 mL) was added and the mixture was stirred for 20 minutes. The organic phase was washed with water (50 mL) and brine (20 mL), dried with anhydrous Na₂SO₄ and filtered. The solution was concentrated under vacuum and a white powder was precipitated with hexane, which was filtered and vacuum dried (yield 0.62 g, 34%). IR (cm⁻¹): 3047w, 2952w, 2921w, 1586w, 1552m, 1495w, 1452m, 1417m, 1369w, 1343m, 1321w, 1256m, 1121w, 1034w, 973w, 886w, 813s, 760s, 726m, 700m, 621w. ¹H NMR (300 MHz, CDCl₃): δ, 2.07 (s, 6H, 2CH₃), 2.16 (s, 6H, 2CH₃), 5.79 (s, 2H, CH(Pz)), 6.89-6.92 (m, 1H, CH(Ph)), 7.28-7.35 (m, 4H, CH(Ph)), 7.24-7.36 (m, 2H, CH(Ph)), 7.65-7.70 (m, 3H, CH(Ph)), 7.75-7.78 (m, 1H, CH(Ph)), 7.85 (s, 1H, CH_{central}). Anal.Calc. for C₂₇H₂₆N₄S (438.59): C, 73.94; H, 5.98; N, 12.77. Found: C, 73.99; H, 6.02; N, 12.78%.

Synthesis of 1,1'-((2-(p-tolylthio)phenyl)methylene)bis(3,5-dimethyl-1H-pyrazole) (**L^{PMe}**). The procedure is similar to the synthesis of **L^{Nf}** previous reported with slight modification: a mixture of bis(pyrazolyl)ketone (1.29 g, 5.85 mmol), 2-(p-tolylthio)benzaldehyde (1.32 g, 5.78 mmol) and CoCl₂·6H₂O (5 mg) was heated at 90°C for 3 hour. The product is a white powder (yield 0.97 g, 41%). IR (cm⁻¹): 3430wbr, 3123vw, 3082vw, 3053vw, 3015vw, 2973w, 2944w, 2918w, 2857w, 1589w, 1562m, 1463s, 1443s, 1414s, 1364m, 1319s, 1251m, 1205w, 1032m, 1014m, 864m, 815vs, 789m, 745s, 686m, 621w, 525w. ¹H NMR (300 MHz, CDCl₃): δ, 2.10 (s, 6H, 2CH₃), 2.22 (s, 6H, 2CH₃), 2.34 (s, 3H, CH₃), 5.87 (s, 2H, CH(Pz)), 6.82-6.85 (m, 1H, CH(Ph)), 7.04-7.23 (m, 7H, CH(Ph)), 7.81 (s, 1H, CH_{central}). Anal.Calc. for C₂₄H₂₆N₄S (402.56): C, 71.61; H, 6.51; N, 13.92. Found: C, 71.66; H, 6.52; N, 13.90%.

Synthesis of 1,1'-((2-(4-fluorophenylthio)phenyl)methylene)bis(3,5-dimethyl-1H-pyrazole) (**L^F**). The procedure is similar to the synthesis of **L^{Nf}** previous reported with slight modification: a mixture of bis(pyrazolyl)ketone (1.30 g, 5.90 mmol), 2-(4-fluorophenylthio)benzaldehyde (1.35 g, 5.81 mmol) and CoCl₂·6H₂O (5 mg) was heated at 90°C for 3 hour. The product is a white powder (yield 1.17 g, 40%). IR (cm⁻¹): 3060w, 2921w, 1556m, 1465m, 1321m, 1275s, 1026w, 817m, 756s, 626w, 512w. ¹H NMR (300 MHz, CDCl₃): δ, 2.09 (s, 6H, 2CH₃), 2.21 (s, 6H, 2CH₃), 5.86 (s, 2H, CH(Pz)), 6.84-6.87 (m, 1H, CH(Ph)), 6.93-6.99 (m, 2H, CH(Ph)), 7.21-7.26 (m, 5H, CH(Ph)), 7.81 (s, 1H, CH_{central}). Anal.Calc. for C₂₃H₂₃FN₄S (406.52): C, 67.95; H, 5.70; N, 13.78. Found: C, 68.00; H, 5.71; N, 13.76%.

Synthesis of 1,1'-((2-(4-fluorophenylthio)phenyl)methylene)bis(3,5-dimethyl-1H-pyrazole) (**L^{OMe}**). The procedure is similar to the synthesis of **L^{Nf}** previous reported with slight modification: a mixture of bis(pyrazolyl)ketone (1.18 g, 5.34 mmol), 2-(4-methoxyphenylthio)benzaldehyde (1.29 g, 5.28 mmol) and CoCl₂·6H₂O (5 mg) was heated at 100°C for 3 hour. The product is a white powder (yield 1.08 g, 49%). IR (cm⁻¹) : 3445wbr, 2996w, 2969vw, 2918w, 2832w, 1589s, 1586m, 1561m, 1553m, 1439s, 1458m, 1415m, 1359m, 1342m, 1309m, 1246vs, 1173m, 1181m, 1104w, 1026m, 873m, 834m, 792m, 752m, 717m, 687m. ¹H NMR (300 MHz, CDCl₃): δ, 2.13 (s, 6H, 2CH₃), 2.23 (s, 6H, 2CH₃), 3.83 (s, 3H, OCH₃), 5.89 (s, 2H, CH(Pz)), 6.77 (dd, J₁= 1.5 Hz, J₂= 7.2Hz, 1H, CH(Ph)), 6.84-6.87 (m, 2H, CH(Ph)), 7.08-7.31 (m, 5H, CH(Ph)), 7.81 (s, 1H, CH_{central}). Anal.Calc. for C₂₄H₂₆N₄OS (418.55): C, 68.87; H, 6.26; N, 13.39. Found: C, 68.88; H, 6.30; N, 13.43%.

Synthesis of 1,1'-((2-(m-tolylthio)phenyl)methylene)bis(3,5-dimethyl-1H-pyrazole) (**L^{mMe}**). The procedure is similar to the synthesis of **L^{Nf}** previous reported with slight modification: a mixture of bis(pyrazolyl)ketone (1.27 g, 5.76 mmol), 2-(m-tolylthio)benzaldehyde (1.31 g, 5.74 mmol) and CoCl₂·6H₂O (5 mg) was heated at 100°C for 3 hour. The crude is a yellow oil which was purified through silica column chromatography (hexane:acetate; 70:30; r.f. 0.3), yielding a white powder (yield 0.69 g, 30%) IR (cm⁻¹): 324wbr, 3134vw, 3047vw, 2943w, 2917w, 1591m, 1556s, 1473s, 1443s, 1408s, 1343m, 1260m, 1552w, 1117w, 1078w, 1060m, 1026m, 969w, 878m, 847w, 760vs, 717m, 686s, 626m, 547w, 491w. ¹H NMR (300 MHz, CDCl₃): δ, 2.09 (s, 6H, CH₃), 2.21 (s, 6H, 2CH₃), 2.28 (s, 3H, 2CH₃), 5.86 (s, 2H, CH(Pz)), 6.89-6.92 (m, 1H, CH(Ph)), 7.01-7.06 (m, 3H, CH(Ph)), 7.12-7.17 (m, 1H, CH(Ph)), 7.26-7.33 (m, 3H, CH(Ph)), 7.78 (s, 1H, CH_{central}). Anal.Calc. for C₂₄H₂₆N₄S (402.56): C, 71.61; H, 6.51; N, 13.92. Found: C, 71.58; H, 6.55; N, 13.88%.

Synthesis of 1,1'-((2-(methylthio)phenyl)methylene)bis(3,5-dimethyl-1H-pyrazole) (**L^{SMe}**). The procedure is similar to the synthesis of **L^{Nf}** previous reported with slight modification: a mixture of bis(pyrazolyl)ketone (2.00 g, 9.06 mmol), 2-(methylthio)benzaldehyde (1.30 ml, 10.00 mmol) and CoCl₂·6H₂O (5 mg) was heated at 80°C for an hour. The product is a white powder (yield 1.30 g, 44%). IR (cm⁻¹): 3121w, 3091w, 3060w, 2982w, 2913m, 2860w, 1691m, 1678m, 1586m, 1551m, 1560m, 1463m, 1442m, 1415m, 1361m, 1373m, 1384m, 1322s, 1257m, 1216m, 1147m, 1124m, 1666m, 1023m, 889m, 895m, 825s, 794m, 755vs, 689s, 625m. ¹H NMR (300 MHz, CDCl₃): δ, 2.12 (s, 6H, 2CH₃), 2.22 (s, 6H, 2CH₃), 2.38 (s, 3H, SCH₃), 5.88 (s, 2H, CH(Pz)), 6.70 (d, J= 7.5 Hz, 1H, CH(Ph)), 7.12-7.18 (m, 1H, CH(Ph)), 7.34 (d,

$J = 3.9\text{ Hz}$, 2H, CH(Ph)), 7.66 (s, 1H, CH_{central}). Anal. Calc. for C₁₈H₂₂N₄S (326.46): C, 66.22; H, 6.79; N, 17.16. Found: C, 66.19; H, 6.76; N, 17.15%.

Synthesis of $[Ag(L^{Nf})]_6(PF_6)_6$ (**27-PF₆**). L^{Nf} (200 mg, 0.46 mmol) and AgPF₆ (118 mg, 0.46 mmol) were mixed in acetone (12 mL), and the colorless solution was stirred for 15 min. The solvent was then removed under vacuum and the crude was triturated with hexane in an ultrasound bath, yielding a white solid. The solid was filtered and vacuum dried (185 mg, yield 60%). The compound can be recrystallized by stratifying diethylether over an acetone solution of the complex yielding colorless crystals. IR (cm⁻¹): 3035w, 2984w, 2928w, 1735w, 1566w, 1466w, 1418w, 1385w, 1307w, 1277w, 1274w, 1035w, 836s, 754m, 689m, 616w, 555m, 469m. ¹H NMR (300 MHz, (CD₃)₂CO): δ 1.90 (s, 6H, 2CH₃), 2.55 (s, 6H, 2CH₃), 6.10 (s, 2H, CH (Pz)), 7.08-7.92 (m, 12H, CH(Ph) + CH_{central}) Anal. Calc. for (C₂₇H₂₆N₄S)₆Ag₆(PF₆)₆ (4148.52): C, 46.90; H, 3.79; N, 8.10. Found: C, 46.92; H, 3.76; N, 8.58%.

Synthesis of $[Ag(L^{PMe})]_n(PF_6)_n$ (**28-PF₆**). L^{PMe} (217 mg, 0.54 mmol) and AgPF₆ (136 mg, 0.54 mmol) were mixed in acetone (10 mL), and the colorless solution was stirred for 15 min. The solution was then concentrated under vacuum and a white solid was precipitated after addition of diethyl ether. The solid was filtered and vacuum dried (195 mg, yield 55%). The compound can be recrystallized by stratifying diethylether over an acetone solution of the complex yielding colorless crystals. IR (cm⁻¹): 3673w, 2921w, 1552w, 1413w, 1313w, 1243w, 1039w, 830s, 695m, 552m. ¹H NMR (300 MHz, (CD₃)₂CO) : δ 2.08 (s br, 6H, 2CH₃), 2.36 (s, 3H, CH₃), 2.58 (s, 6H, 2CH₃), 6.17 (s, 2H, CH(Pz)), 7.00 (d, $J = 7.8\text{ Hz}$, 1H, CH(PH)), 7.16-7.46 (m, 7H, CH(Ph)), 7.83 (s 1H, CH_{central}). Anal. Calc. for (C₂₄H₂₆N₄S)₆Ag₆(PF₆)₆ (3932.34): C, 43.98; H, 4.00; N, 8.55. Found: C, 43.96; H, 3.99; N, 8.60%.

Synthesis of $[Ag(L^F)]_6(PF_6)_6$ (**29-PF₆**). L^F (150 mg, 0.37 mmol) and AgPF₆ (93 mg, 0.37 mmol) were mixed in acetone (10 mL), and the colorless solution was stirred for 15 min. The solvent was then removed under vacuum obtaining a yellow oil which was triturated with hexane in an ultrasound bath, yielding a white solid. The solid was filtered and vacuum dried (185 mg, yield 60%). The solution was then concentrated under vacuum and a white solid was precipitated after addition of diethyl ether. The solid was filtered and vacuum dried (120 mg, yield 50%). The compound can be recrystallized by stratifying diethylether over an acetone solution of the complex yielding colorless crystals. IR (cm⁻¹): 2017w, 1560w, 1495w, 1417w, 1234w, 1160w, 1034w, 830s, 695w, 617w, 552m, 500w. ¹H NMR (300 MHz, (CD₃)₂CO): 1.99 (s, 6H, 2CH₃), 2.60 (s, 6H, 2CH₃), 6.17 (s, 2H, CH(Pz)), 7.02-7.49 (m, 8H, CH(Ph)), 7.89 (s, 2H,

CH_{central}). Anal. Calc. for (C₂₃H₂₃N₄SF)₆Ag₆(PF₆)₆ (3956.10): C, 41.90; H, 3.52; N, 8.50. Found: C, 41.92; H, 3.46; N, 8.56%.

Synthesis of [Ag(L^{OMe})]₆(PF₆)₆ (**30-PF₆**) . L^{OMe} (164 mg, 0.39 mmol) and AgPF₆ (99 mg, 0.39 mmol) were mixed in acetone (10 mL), and the colorless solution was stirred for 15 min. The solvent was then removed under vacuum and the crude was triturated with hexane in an ultrasound bath, yielding a white solid. The solid was filtered and vacuum dried (130 mg, yield 50%). The compound can be recrystallized by stratifying hexane over an dichloromethane solution of the complex yielding colorless crystals. IR (cm⁻¹): 2926w, 1700w, 1586m, 1565m, 1500m, 1447m, 1360m, 1291m, 1243m, 1178m, 1121w, 1026m, 826s, 756m, 695m, 613m, 552s, 530m. ¹H NMR (300 MHz, (CD₃)₂CO): δ 1.98 (s, 6H, 2CH₃), 2.62 (s, 6H, 2CH₃), 3.87 (s, 3H, OCH₃), 6.21 (s, 2H, CH(Pz)), 6.89-7.42 (m, 8H, CH(Ph)), 7.83 (s, 2H, CH_{central}). Anal. Calc. for (C₂₄H₂₆N₄SO)₆Ag₆(PF₆)₆ (4028.34): C, 42.93; H, 3.90; N, 8.34. Found: C, 42.92; H, 3.97; N, 8.33%.

Synthesis of [Ag(L^{mMe})]₆(PF₆)₆ (**31-PF₆**) . L^{pMe} (330 mg, 0.82 mmol) and AgPF₆ (206 mg, 0.82 mmol) were mixed in acetone (10 mL), and the colorless solution was stirred for 15 min. The solvent was then removed under vacuum and the crude was triturated with hexane in an ultrasound bath, yielding a white solid. The solid was filtered and vacuum dried (383 mg, yield 71%). The compound can be recrystallized by stratifying hexane over an dichloromethane solution of the complex yielding colorless crystals. IR (cm⁻¹): 3743w, 2017w, 1560w, 1421w, 1239m, 1152m, 1026s, 756m, 634s, 521m. ¹H NMR (300 MHz, CD₃Cl) : δ 1.82 (s br, 3H, CH₃), 2.19 (s, 3H, CH₃), 2.30 (s, 3H, CH₃), 2.38 (s, 6H, CH₃), 6.03 (s br, 2H, CH(Pz)), 6.89-7.42 (m, 8H, CH(Ph)), 7.56 (s 1H, CH_{central}). Anal. Calc. for (C₂₄H₂₆N₄S)₆Ag₆(PF₆)₆ (3932.34): C, 43.98; H, 4.00; N, 8.55. Found: C, 43.88; H, 4.05; N, 8.50%.

Synthesis of [Ag(L^{SMe})]_n(BF₄)_n (**32**) . L^{SMe} (212 mg, 0.65 mmol) and AgBF₄ (126 mg, 0.82 mmol) were mixed in acetone (20 mL), and the colorless solution was stirred for 15 min. The solution was then concentrated under vacuum and a white precipitated. The solid was filtered and vacuum dried (265 mg, yield 78%). IR (cm⁻¹): 3147w, 2921w, 1560m, 1465m, 1443m, 1417m, 1391w, 1313w, 1278w, 1052vs, 1026vs, 873m, 847w, 760s, 700m, 621w, 517m. ¹H NMR (300 MHz, CD₃CN) δ: 2.29 (s, 6H, 2CH₃(Pz)), 2.54 (s, 3H, SCH₃), 2.59 (s, 6H, 2CH₃(Pz)), 6.25 (s, 2H, CH(Pz)), 6.80 (d, J = 7.8 Hz, 1H, CH_{orto}(Ph)), 7.31-7.35 (m, 1H, CH(Ph)), 7.56-7.59 (s, 3H, CH(Ph)+ CH_{central}). Anal. Calc. for (C₁₈H₂₂N₄S)₆Ag₆(PF₆)₆ (3475.74): C, 37.32; H, 3.83; N, 9.67. Found: C, 37.37; H, 3.92; N, 9.69%.

Synthesis of $[Ag(L^{Nf})]_n(CF_3SO_3)_n$ (**27-CF₃SO₃**). L^{Nf} (84 mg, 0.20 mmol) and $AgCF_3SO_3$ (52 mg, 0.20 mmol) were mixed in acetone (12 mL), and the colorless solution was stirred for 15 min. The solvent was then removed under vacuum and the crude was triturated with hexane in an ultrasound bath, yielding a white solid. The solid was filtered and vacuum dried (60 mg, yield 44%). The compound can be recrystallized by stratifying hexane over a dichloromethane solution of the complex yielding colorless crystals. IR (cm^{-1}): 2969w, 2926w, 1552m, 1460w, 1421w, 1386w, 1278s, 1239s, 1152m, 1021s, 869m, 817m, 756m, 691m, 634s, 687m. 1H NMR (300 MHz, CD_3Cl): δ 2.22 (s, 3H, CH_3 (Pz)), 2.45 (s, 3H, CH_3 (Pz)), 5.98 (s, 2H, CH (Pz)), 6.98-7.33 (m, 8H, CH (Ph)), 7.56 (s 1H, $CH_{central}$). Anal. Calc. for $C_{28}H_{26}N_4S_2O_3AgF_3$ (695.52): C, 48.35; H, 3.77; N, 8.06. Found: C, 48.42; H, 3.76; N, 8.10%.

Synthesis of $[Ag(L^{pMe})]_n(CF_3SO_3)_n$ (**28-CF₃SO₃**). L^{pMe} (193 mg, 0.48 mmol) and $AgCF_3SO_3$ (122 mg, 0.48 mmol) were mixed in acetone (10 mL), and the colorless solution was stirred for 15 min. The solution was then concentrated under vacuum and a white solid was precipitated after addition of diethyl ether. The solid was filtered and vacuum dried (292 mg, yield 92%). The compound can be recrystallized by stratifying hexane over a dichloromethane solution of the complex yielding colorless crystals. IR (cm^{-1}): 2978w, 2921w, 2865w, 1717w, 1560w, 1473w, 1413w, 1278m, 1234s, 1152s, 1026s, 878m, 808m, 756m, 695m, 639s, 569m, 521m. 1H NMR (300 MHz, CD_3Cl): δ 2.20 (s, 3H, CH_3 (Pz)), 2.35 (s, 3H, CH_3 (Ph)), 2.43 (s, 3H, CH_3 (Pz)), 5.97 (s, 2H, CH (Pz)), 6.90 (d, $J = 7.2$ Hz, 1H, CH (Ph)), 7.01-7.24 (m, 7H, CH (Ph)), 7.58 (s 1H, $CH_{central}$). Anal. Calc. for $C_{25}H_{26}N_4S_2AgF_3O_3$ (659.49): C, 45.53; H, 3.97; N, 8.50. Found: C, 45.96; H, 3.99; N, 8.60%.

Synthesis of $[Ag(L^F)]_n(CF_3SO_3)_n$ (**29-CF₃SO₃**). L^F (138 mg, 0.34 mmol) and $AgCF_3SO_3$ (87 mg, 0.34 mmol) were mixed in acetone (10 mL), and the colorless solution was stirred for 15 min. The solvent was then removed under vacuum obtaining a yellow oil which was triturated with hexane in an ultrasound bath, yielding a white solid. The solid was filtered and vacuum dried (89 mg, yield 40%). The compound can be recrystallized by stratifying hexane over a dichloromethane solution of the complex yielding colorless crystals. IR (cm^{-1}): 3469wbr, 3234wbr, 3147w, 3091w, 3055w, 2973w, 2917w, 1591m, 1560m, 1419s, 1460m, 1421m, 1382m, 1282s, 1239vs, 1217vs, 1156m, 1026s, 873w, 834w, 756m, 695w, 634vs, 573w, 517m. 1H NMR (300 MHz, CD_3Cl): δ 2.22 (s, 3H, CH_3 (Pz)), 2.45 (s, 3H, CH_3 (Pz)), 5.98 (s, 2H, CH (Pz)), 6.98-7.33 (m, 8H, CH (Ph)), 7.56 (s 1H, $CH_{central}$). Anal. Calc. for $C_{24}H_{23}N_4S_2AgF_3O_3$ (663.46): C, 43.45; H, 3.49; N, 8.44. Found: C, 43.42; H, 3.46; N, 8.49%.

Synthesis of $[Ag(L^{OMe})]_n(CF_3SO_3)_n$ (**30-CF₃SO₃**) . L^{OMe} (178 mg, 0.42 mmol) and $AgCF_3SO_3$ (109 mg, 0.42 mmol) were mixed in acetone (10 mL), and the colorless solution was stirred for 15 min. The solvent was then removed under vacuum and the crude was triturated with hexane in an ultrasound bath, yielding a white solid. The solid was filtered and vacuum dried (160 mg, yield 56%). The compound can be recrystallized by stratifying diethylether over an acetone solution of the complex yielding colorless crystals. IR (cm^{-1}): 2839w, 1699w, 1565m, 1491m, 1456m, 1247vs, 1156s, 1021vs, 839m, 756s, 643vs, 517s. 1H NMR (300 MHz, CD_3Cl) : δ 2.61 (s, 3H, CH_3 (Pz)), 2.48 (s, 3H, CH_3 (Pz)), 3.83 (s, 3H, OCH_3 (Ph)), 6.01 (s, 2H, CH (Pz)), 6.79 (d, J = 7.8 Hz, 1H, CH (Ph)), 6.84-7.50 (m, 7H, CH (Ph)), 7.64 (s 1H, $CH_{central}$). Anal. Calc. for $C_{25}H_{26}N_4S_2AgF_3O_4$ (675.49): C, 44.45; H, 3.88; N, 8.29. Found: C, 44.46; H, 3.90; N, 8.30%.

Synthesis of $[Ag(L^{mMe})]_n(CF_3SO_3)_n$ (**31-CF₃SO₃**) . L^{mMe} (353 mg, 0.87 mmol) and $AgCF_3SO_3$ (224 mg, 0.87 mmol) were mixed in acetone (10 mL), and the colorless solution was stirred for 15 min. The solvent was then removed under vacuum and the crude was triturated with hexane in an ultrasound bath, yielding a white solid. The solid was filtered and vacuum dried (467 mg, yield 81%). The compound can be recrystallized by stratifying hexane over a THF solution of the complex yielding colorless crystals. IR (cm^{-1}): 3743w, 2017w, 1560w, 1421w, 1239m, 1152w, 1026m, 756w, 634s, 521w. 1H NMR (300 MHz, CD_3Cl) : δ 2.17 (s, 3H, CH_3 (Pz)), 2.29 (s, 3H, CH_3 (Ph)), 2.42 (s, 3H, CH_3 (Pz)), 5.94 (s, 2H, CH (Pz)), 6.83-7.31 (m, 8H, CH (Ph)), 7.61 (s 1H, $CH_{central}$). Anal. Calc. for $C_{25}H_{26}N_4S_2AgF_3O_6$ (659.49): C, 43.98; H, 4.00; N, 8.55. Found: C, 43.90; H, 3.97; N, 8.51%.

5.2.2. Single Crystal X-ray Structures

Single crystal data were collected with a Bruker Smart 1000 and on a Bruker Smart APEXII area detector diffractometers (Mo $K\alpha$; λ = 0.71073 Å). Cell parameters were refined from the observed setting angles and detector positions of selected strong reflections. Intensities were integrated from several series of exposure frames that covered the sphere of reciprocal space⁴⁸. A multiscan absorption correction was applied to the data using the program SADABS⁴⁷. The structures were solved by direct methods SIR97¹⁰⁴ and SIR2004⁶⁶ and refined with full-matrix least-squares (SHELXL-97⁵⁰), using the Wingx software package⁵¹. Graphical material was prepared with the Mercury 2.0⁵² program. Crystallographic data are reported in Appendix vi-vii.

5.3. Results and discussion

5.3.1. Synthesis

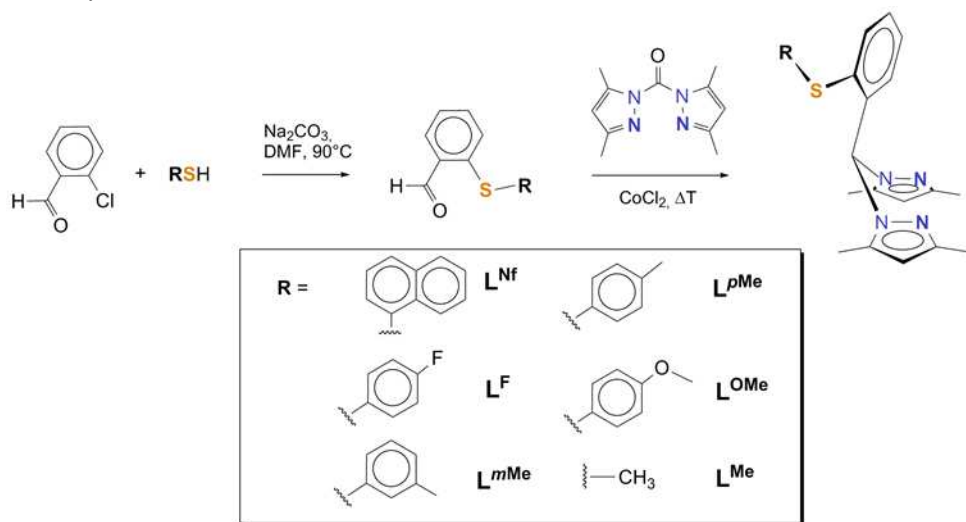


Figure 54. Synthetic route for the preparation of the heteroscorpionate N_2S ligands.

The ligands were prepared according to a slight modification of synthesis previously reported in chapter 3. The ligands synthesis derived from a slight modification of the synthetic route reported in the previous chapter (chapter 3). The different steric hindrance on the thioether arm determines a certain difficulties on the nucleophilic attack of the aldehydic carbonyl carbon so it is necessary to increase the time and the temperature of the solid state reaction. Silver(I) complexes were synthesized in the air at room temperature using $AgPF_6$ and $AgCF_3SO_3$ as silver precursors.

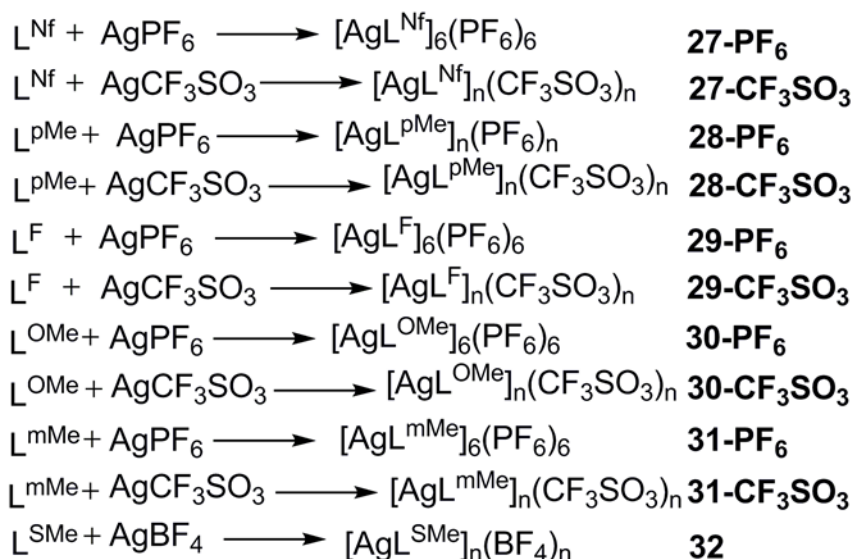


Figure 55. Complexes synthesized

5.3.2. Molecular structures

When using the PF_6^- anion, hexameric molecular structures $[\text{Ag}(\text{L})]_6(\text{PF}_6)_6$ are preferentially obtained, Figures 56-57. The only exception is represented by the system with the $\text{L}^{\text{p-Me}}$ ligand that form a molecular chain analogous to that found for the complexes with the triflate anion (Figure 58) and that will be therefore described in the section dedicated to the $[\text{Ag}(\text{L})]_n(\text{CF}_3\text{SO}_3)_n$ complexes (see below). Since the complexes **27-PF₆**, **29-PF₆**, **30-PF₆**, and **31-PF₆** are iso-structural, their general structural features will be described together. The difference among the four hexameric complexes is determined by the different substituents on the peripheral aromatic rings, that however has little influence on the overall structural arrangement. In all complexes the ligand acts as N_2 bidentate on a metal and bridges on another silver atom with the thioether group, and central phenyl ring adopts a particularly fixed geometry. This can be appreciated by inspecting the torsion angle τ that defines the orientation of the phenyl ring with respect to one of the pyrazole groups. In fact, τ varies in the very narrow range of 0.8-1.4°. The peripheral phenyl ring is located above one of the pyrazole ring giving rise to a weak π - π interaction. The pyrazole rings of six ligands defines the exteriors of the hexamer whereas the peripheral aromatic rings are oriented towards the interior. As a function of the substituents (naphthyl, methoxy, m-Me, and F) that are present on the aromatic

ring, a pore of different size can be obtained. The diameter of this pore is 1.6, 2.6 and 3.0 Å for the **27-PF₆**, **29-PF₆** and **31-PF₆** complexes, respectively. In **30-PF₆** the methoxy groups occlude completely the intra-ring space, Figure 57. The size of the pore was calculated in an approximate way by taking into account the vdW surface of the H oriented towards the interior of the hole.

The PF₆⁻ anion exhibits a fragmented site occupation within the unit cell. In fact, per each silver cation of the asymmetric unit the PF₆⁻ anion is distributed in three positions in the unit cell, 1) a 0.1666 fraction lying on a ternary axis and on an inversion center 2) a 0.3333 fraction lying on a ternary axis, and 3) a 0.5 fraction lying on a binary axis. This latter fraction links together two silver atoms of symmetry related hexamers in a way that the centroids of four hexamers occupy the vertex of a tetrahedron thus defining an internal cavity having the shape of a tetrahedron. The distance between the fluorine and the silver atoms varies in the range 2.749(3)-2.818(9) Å suggesting the weak nature of this interaction. The PF₆⁻ anion that acts as a linker between the metals is also held in place by a C-H...F interaction with one of the methyl groups of the pyrazole ring. The capsular shaped assembly comprised of four hexameric units, defines the unit cell lattice and forms two types of cavities: one that is contained in the sphere and the other that is produced by the close packing of the spheres, Figure 57. The size of the cavities diminishes as the bulkiness of the substituent of the aromatic ring increases, and the following order of cavity size is observed: **27-PF₆** (15338 Å³/cell) < **30-PF₆** (19284 Å³/cell), **31-PF₆** (20792 Å³/cell) ≈ **29-PF₆** (20520 Å³/cell). In addition if we express the cavities volumes as a percentage of the unit cells volumes we have: **27-PF₆** (19.3 %) < **30-PF₆** (24.3 %), **31-PF₆** (25.6 %) ≈ **29-PF₆** (25.7 %). According to the fact that two types of cavities are present, the substituents on the peripheral phenyl ring affect the size of only the intra-capsular space, and the increasing bulkiness that is present on going from F, *m*-Me, OMe, and Nf, determines the shrinkage of this cavity type. On the opposite, the cavity size of the inter-capsular space is lined with methyl groups of the pyrazole rings and is almost invariant in the four structures.

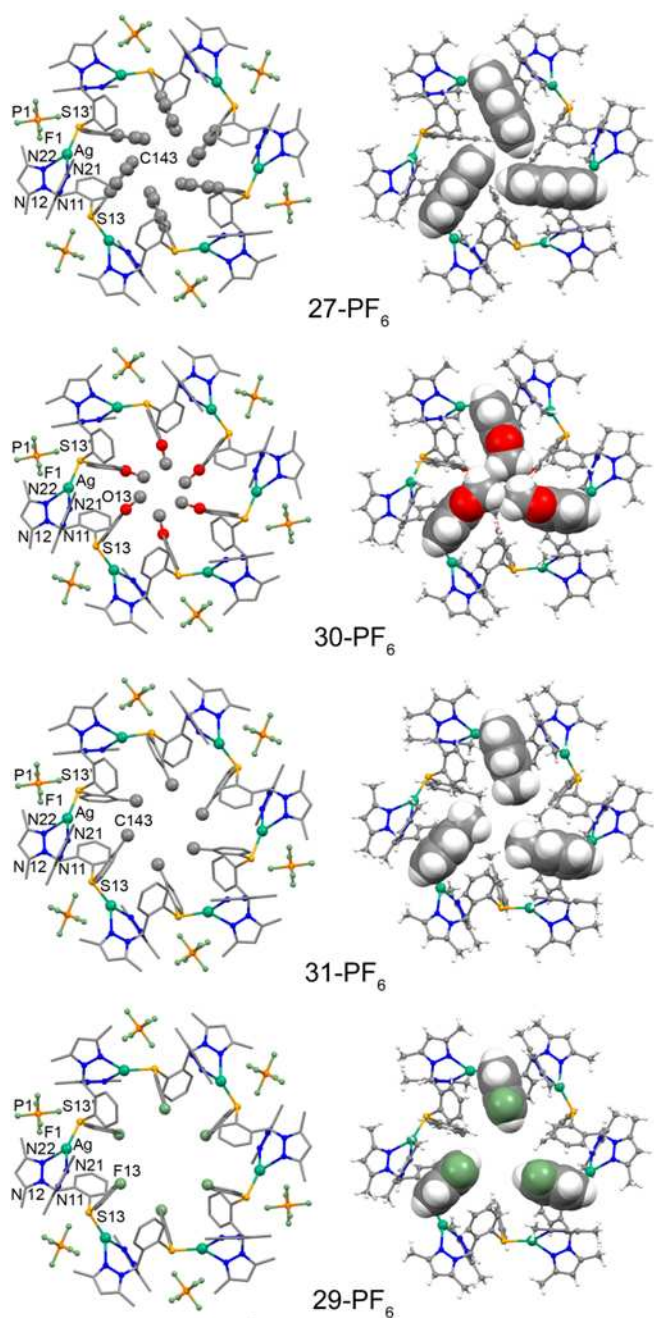


Figure 56. Left, molecular drawing of the hexameric unit of $[\text{Ag}(\text{L}^{\text{SNf}})]_6(\text{PF}_6)_6$, $[\text{Ag}(\text{L}^{\text{SPhOMe}})]_6(\text{PF}_6)_6$, $[\text{Ag}(\text{L}^{\text{SPhm-Me}})]_6(\text{PF}_6)_6$, and $[\text{Ag}(\text{L}^{\text{SPhF}})]_6(\text{PF}_6)_6$. Hydrogen atoms are omitted for clarity. The ' symbol denotes symmetry related atoms. Right, representation of the different sizes of the pores for the hexameric complexes. The

peripheral aromatic groups were depicted with van der Waals atomic radii. Colors: Ag, green; S, yellow; N, blue; C, gray; O, red; F, light green, P, orange.

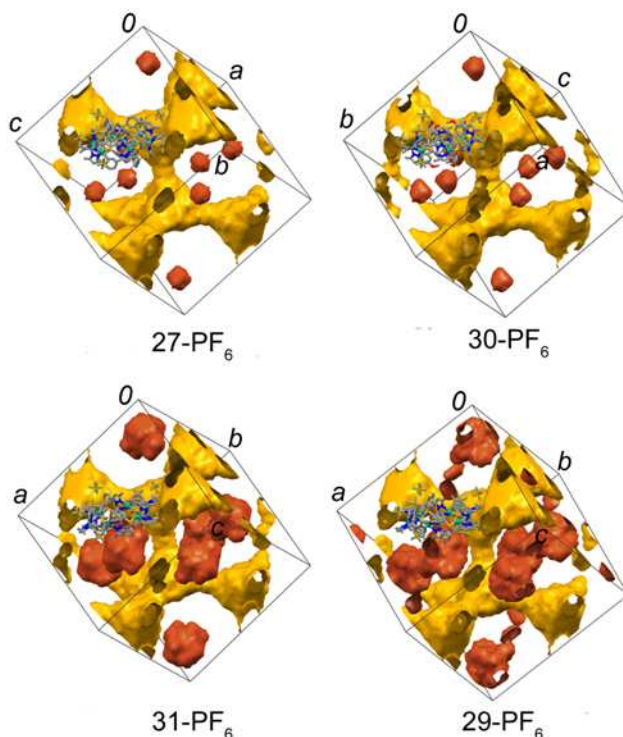


Figure 57. Depiction of the two types of cavities that are present in the hexameric complexes. Yellow: inter-capsular space; red: intra-capsular space. The cavities were generated by rolling a probe sphere of 1.6 Å diameter over the molecular surface.

When employing the triflate anion, the silver complexes crystallize in the form of molecular chains, and the general formula is $[\text{Ag}(\text{L})]_n(\text{CF}_3\text{SO}_3)_n$, Figure 58. As stated above, when mixing AgPF_6 with the ligand $\text{L}^{\text{p-Me}}$, the molecular structure of the complex presents structural features analogous to those obtained with the triflate anion. The molecular arrangement in **27-CF₃SO₃**, **28-CF₃SO₃**, **29-CF₃SO₃**, **30-CF₃SO₃**, and **31-CF₃SO₃** are very similar despite the fact that these complexes crystallize in different space groups, and therefore their structures will be described together. The complex **29-CF₃SO₃** crystallizes as a molecular chain but the structural features are slightly different from those of the other complexes, Figure 59. For all of these compounds the ligand acts as N₂ bidentate on a metal and bridges on another silver

atom with the thioether group, with the central phenyl ring in a rigid geometry, since the π angle is in narrow range of 0.6-6.7°. At variance with the structures of the haexameric complexes, the peripheral phenyl ring exhibits a higher degree of conformational flexibility, since it is not always stacked above one of the pyrazole rings, as it happened for the hexameric complexes. In fact, the dihedral angle between the pyrazole and peripheral aromatic rings (β is in the range of 9.7-42.3° for the molecular chains and 10.8-15.4° in the hexameric complexes. When viewing the molecular chains of **27-CF₃SO₃**, **28-CF₃SO₃**, **29-CF₃SO₃**, **30-CF₃SO₃**, and **31-CF₃SO₃** along their direction of propagation (Figure 59) it can be appreciated how their projection has a square section with sides in the 18.9-14.4 Å range. The larger size is for **27-CF₃SO₃** that present the most cumbersome substituent. These molecular chains exhibit a helical arrangements with a pitch in the range 20.46-22.96 Å and that comprises four AgL units. The exterior of the chains is defined by alternate anions and pyrazole rings, whereas in the interior are located the peripheral aromatic moieties. This is a structural feature that also characterizes the hexameric complexes, even though in the molecular chains there is a the less defined orientation of the anions that surrounds the molecular chains. In fact, in the hexameric complexes, the PF₆⁻ moiety occupies precise and invariant structural sites for all of the complexes, whereas in the chains, the anions are interacting with the metals, but are somehow free to rotate around the Ag-O bond. From an aesthetical point of view the hexameric species can be imagined as derived by a slight twisting reorientation of fraction of the chains comprising six AgL units.

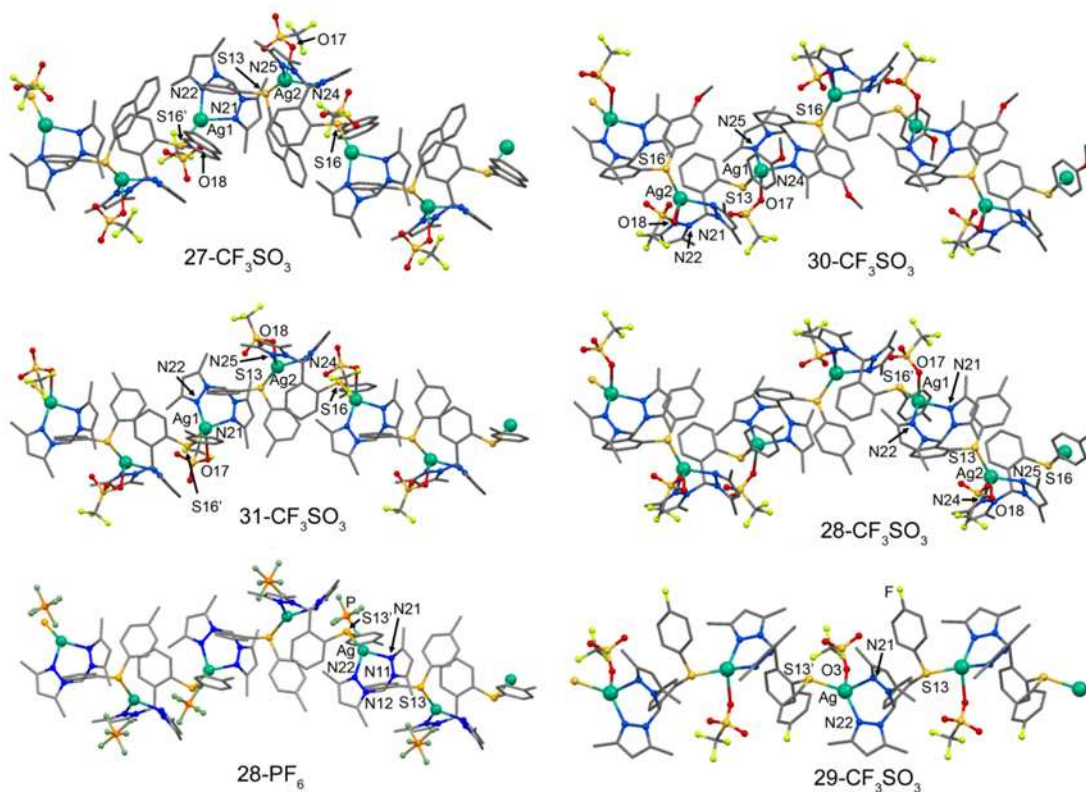


Figure 58. Portion of the molecular chains of **27-CF₃SO₃**, **28-CF₃SO₃**, **29-CF₃SO₃**, **30-CF₃SO₃**, **31-CF₃SO₃** and **28-PF₆**. The ' symbol denotes symmetry related atoms. Colors: Ag, green; S, yellow; N, blue; C, gray; O, red; F, light green, P, orange.

The molecular chain of **29-CF₃SO₃** is different from the previously described structures, in fact the silver atoms are organized in a zig-zag fashion and the polymer does not form a helix. In addition, by inspecting its projection along the propagation of the molecule, it can be observed that the-PhF group and one of the pyrazole rings are oriented on one side whereas the central phenyl ring and the triflate anion are located on the other side.

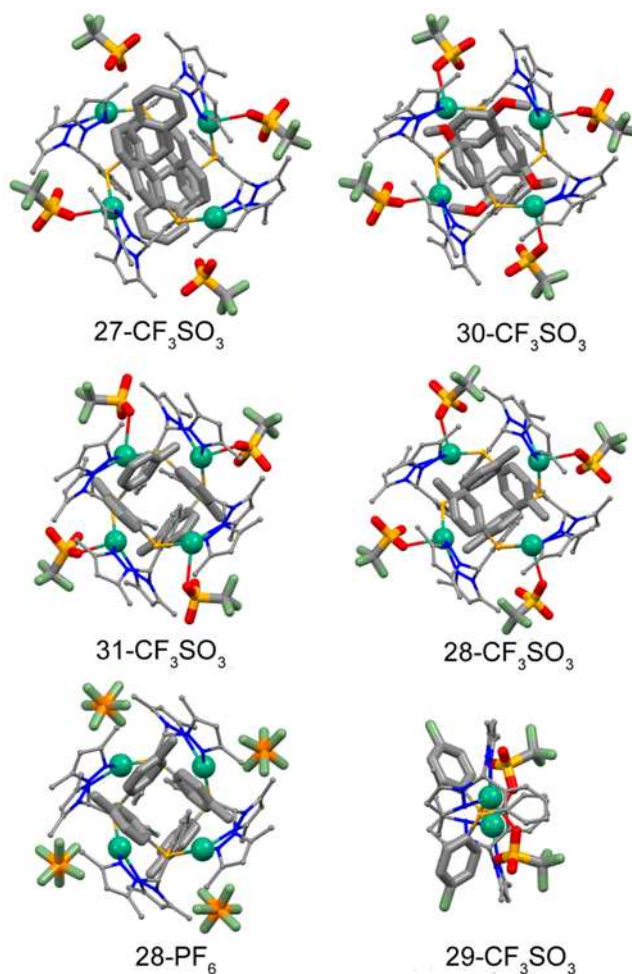


Figure 59. Depiction of the molecular chains viewed along the direction of propagation of the helix. Colors: Ag, green; S, yellow; N, blue; C, gray; O, red; F, light green, P, orange. Thick stick representation highlight anions and the peripheral aromatic moieties.

In chapter 2, 3 and 4 we have evaluated the importance of the steric hindrance of the methyl groups on the bispyrazolyl scaffold and also the importance of the phenyl linker to obtain hexameric species. Now we can add that the presence of terminal ring is also fundamental for the building of the spheres (Figure 60).

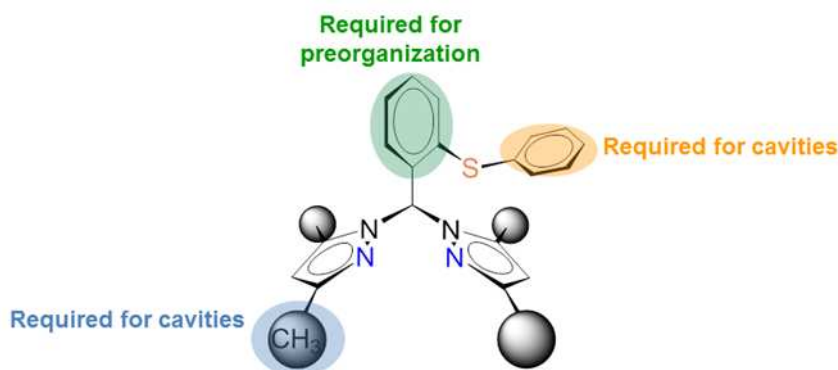


Figure 60. Schematic representation of ligands: in orange and blu the groups required for cavities and in green the ring required for preorganization.

5.3.3. X-ray powder diffraction.

To investigate the adsorption properties of the new porous compounds, substantial amounts of crystalline materials are required (ca 0,5 g). the growth of a considerable amount of these crystalline materials presented some practical problems for some of these systems. At present only a sufficient amount of crystals could be grown for **27-PF₆** and **31-PF₆**. X-ray powder diffraction was performed on the samples in order to verify the purity of the crystalline materials. In Figure 61 and 62 are reported the experimental and simulated X-ray powder pattern. The latter is derived by the single crystal x-ray analysis.

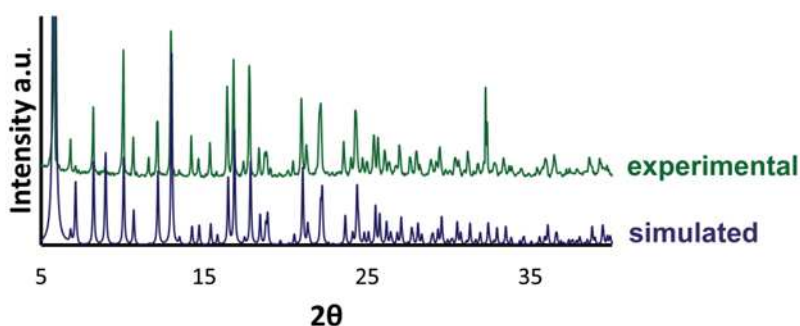


Figure 61. In blue experimental X-ray powder pattern of **27-PF₆**; in green the simulated pattern from single crystal.

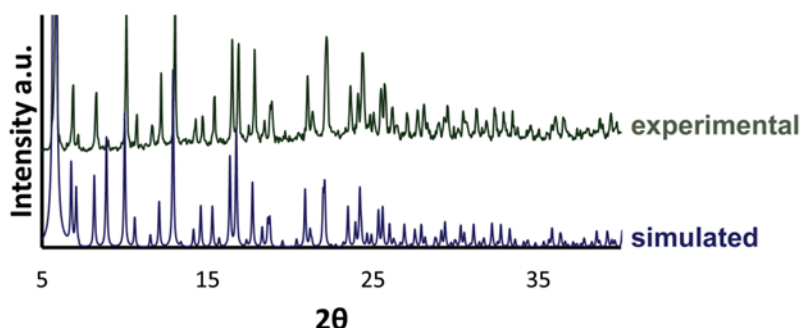


Figure 62. In blue experimental X-ray powder pattern of **27-PF₆**; in green the simulated pattern from single crystal.

The ability of **27-PF₆** and **31-PF₆** to absorb volatile material was preliminary investigated by recording PXRD spectra under vacuum and in presence of saturated solvent vapours. In Figure 63 and 64 it is shown that when the evacuated powder is exposed to vapours there is an enlargement of the unit cell in agreement with the porous properties of the materials. Adsorption experiments will be performed to prove the thesis which concerned the filling of only the intercapsules cavities as previously hypothesized in chapter 4. In fact if the same gas volume present in the **23-PF₆** cavities will be adsorbed, only the intercapsule volume will be occupied and the volume of intracapsule cavity will be irrelevant. Future work will improve, increase and functionalize the intermolecular cavities modifying the bispyrazolyl scaffold.

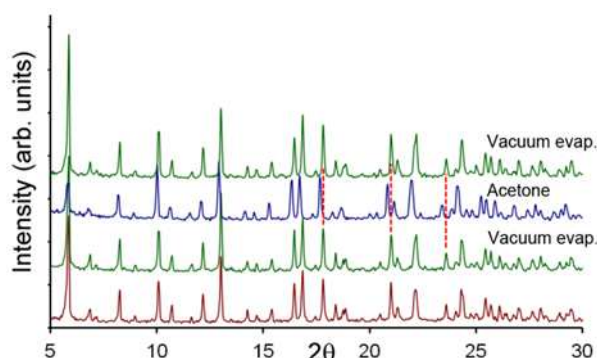


Figure 63. Effect of the solvent absorption on **27- PF₆** crystals. Freshly ground crystals, red. Crystals subjected to high vacuum and T = 100°C for 2 h, green. The evacuated crystals were then exposed to saturated solvent vapors (acetone), blue.

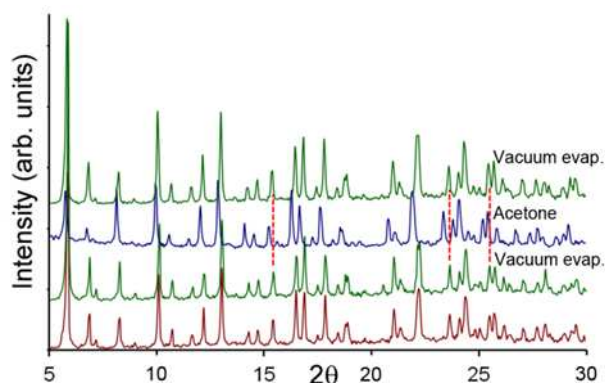


Figure 64. Effect of the solvent absorption on **31- PF₆** crystals. Freshly ground crystals, red. Crystals subjected to high vacuum and T = 100°C for 2 h, green. The evacuated crystals were then exposed to saturated solvent vapors (acetone), blue.

Table 9. Selected bond lengths (Å) and angles (°) for **27-PF₆**, **28-PF₆**, **29-PF₆**, **30-PF₆**, **31-PF₆**

27-PF₆			
Ag-N(21)	2.222(3)	N(21)-Ag-N(22)	84.90(9)
Ag-N(22)	2.331(3)	N(21)-Ag-S(13)'	148.10(7)
Ag-S(13)'	2.378(8)	N(22)-Ag-S(13)'	126.88(7)
Ag-F(1)	2.754(3)		
28-PF₆			
Ag-N(21)	2.250(3)	N(21)-Ag-N(22)	84.6(1)
Ag-N(22)	2.321(3)	N(21)-Ag-S(13) [‡]	142.60(9)
Ag-S(13) [‡]	2.4367(9)	N(22)-Ag-S(13) [‡]	130.68(8)
29-PF₆			
Ag-N(21)	2.225(4)	N(21)-Ag-N(22)	84.4(2)

Ag-N(22)	2.285(5)	N(21)-Ag-S(13) [#]	147.0(1)
Ag-S(13) [#]	2.386(2)	N(22)-Ag-S(13) [#]	127.5(1)
Ag-F(1)	2.801(4)		
30-PF₆			
Ag-N(21)	2.229(8)	N(21)-Ag-N(22)	84.7(3)
Ag-N(22)	2.315(9)	N(21)-Ag-S(13)''	146.5(2)
Ag-S(13)''	2.377(3)	N(22)-Ag-S(13)''	128.8(2)
Ag-F(1)	2.818(9)		
31-PF₆			
Ag-N(21)	2.232(3)	N(21)-Ag-N(22)	84.5(1)
Ag-N(22)	2.322(4)	N(21)-Ag-S(13)'''	151.59(9)
Ag-S(13)'''	2.400(1)	N(22)-Ag-S(13)'''	123.85(9)
Ag-F(1)	2.749(3)		

Symmetry codes: ' = $\frac{1}{2}-z$; $\frac{1}{2}-x$; $1-y$, '' = $z-1/4$; $1-x$; $y-1/4$, ''' = $\frac{1}{2}-y$; $\frac{1}{2}-z$; $1-x+1$, [‡] = $3/4-y$; $x-3/4$; $\frac{1}{4}+z$, [#] = $\frac{1}{2}-y$; $\frac{1}{2}-z$; $1-x$.

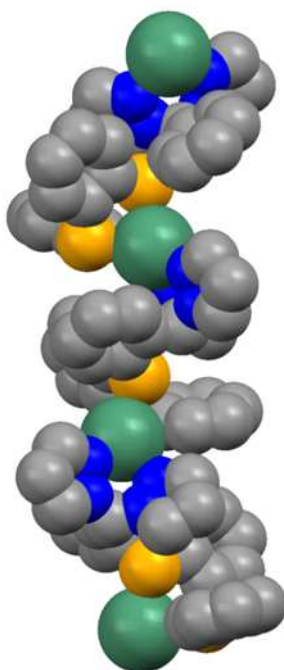
Table 10. Selected bond lengths (Å) and angles (°) for **27-CF₃SO₃**, **28-CF₃SO₃**, **29-CF₃SO₃**, **30-CF₃SO₃**, **31-CF₃SO₃**.

27-CF₃SO₃			
Ag(1)-N(21)	2.338(4)	Ag(2)-N(24)	2.277(5)
Ag(1)-N(22)	2.231(5)	Ag(2)-N(25)	2.285(5)
Ag(1)-S(16)'	2.430(2)	Ag(2)-S(13)	2.432(2)
Ag(1)-O(19) [§]	2.58(2)	Ag(2)-O(17)	2.518(4)
Ag(1)-O(210) [§]	2.53(2)	N(24)-Ag(2)-N(25)	84.2(2)
N(21)-Ag(1)-N(22)	86.4(2)	N(24)-Ag(2)-S(13)	129.5(1)
N(21)-Ag(1)-S(16)'	119.6(1)	N(25)-Ag(2)-S(13)	144.5(1)
N(22)-Ag(1)-S(16)'	147.1(1)		
28-CF₃SO₃			
Ag(1)-N(21)	2.263(5)	Ag(2)-N(24)	2.296(4)
Ag(1)-N(22)	2.312(4)	Ag(2)-N(25)	2.299(5)
Ag(1)-S(16) [‡]	2.435(1)	Ag(2)-S(13)	2.465(1)
Ag(1)-O(17)	2.523(4)	Ag(2)-O(18)	2.573(5)
N(21)-Ag(1)-N(22)	84.8(2)	N(24)-Ag(2)-N(25)	85.7(2)
N(21)-Ag(1)-S(16) [‡]	136.9(1)	N(24)-Ag(2)-S(13)	129.7(1)
N(22)-Ag(1)-S(16) [‡]	135.0(1)	N(25)-Ag(2)-S(13)	136.7(1)
29-CF₃SO₃			
Ag-N(21)	2.345(3)	Ag-S(13) [#]	2.526(1)
Ag-N(22)	2.283(3)	Ag-O(14)	2.398(4)
N(21)-Ag-N(22)	83.8(1)	N(22)-Ag-O(14)	133.1(1)
N(21)-Ag-S(13) [#]	120.86(8)	N(21)-Ag-O(14)	98.5(2)
N(22)-Ag-S(13) [#]	128.06(8)	O(14)-Ag-S(13) [#]	90.9(1)
30-CF₃SO₃			
Ag(1)-N(24)	2.273(3)	Ag(2)-N(21)	2.302(4)
Ag(1)-N(25)	2.327(4)	Ag(2)-N(22)	2.297(4)

Ag(1)-S(13)	2.434(1)	Ag(2)-S(16)''	2.446(1)
Ag(1)-O(17)	2.498(3)	Ag(2)-O(18)	2.566(5)
N(24)-Ag(1)-N(25)	84.9(1)	N(21)-Ag(2)-N(22)	84.9(1)
N(24)-Ag(1)-S(13)	135.39(9)	N(21)-Ag(2)-S(16)''	126.8(1)
N(25)-Ag(1)-S(13)	138.45(9)	N(22)-Ag(2)-S(16)''	144.2(1)
31-CF₃SO₃			
Ag(1)-N(21)	2.283(5)	Ag(2)-N(24)	2.290(4)
Ag(1)-N(22)	2.318(6)	Ag(2)-N(25)	2.303(4)
Ag(1)-S(16)'''	2.500(2)	Ag(2)-S(13)	2.454(1)
Ag(1)-O(17)	2.701(4)	Ag(2)-O(18)	2.423(2)
N(21)-Ag(1)-N(22)	84.1(2)	N(24)-Ag(2)-N(25)	85.2(2)
N(21)-Ag(1)-S(16)'''	144.3(2)	N(24)-Ag(2)-S(13)	139.0(1)
N(22)-Ag(1)-S(16)'''	126.8(1)	N(25)-Ag(2)-S(13)	132.1(1)

[§] O(19) and O(210) are two disordered fragments of the same atom. Symmetry codes: ' = ½+x; -y; ½-z, '' = 1-x; ½+y; 1-z, ''' = -x+½; y-½; -z+3/2; [‡] = -x; y-½; -z-½. [#] = 3/2-x; ½+y; z.

Pre-organized N₂S₂ donor ligand drives Metal-Organic chain formation.



Three new N₂S₂ donor ligands 1,1'-((2-(2-(phenylthio)phenylthio)phenyl)methylene)bis(3,5-R-1*H*-pyrazole), R = H (**L^HPhSPhSPh**), R = Me (**L^{Me}PhSPhSPh**), R = *i*-Pr (**L^{iPr}PhSPhSPh**)¹⁰³ were prepared and characterized. These bifunctional ligands incorporate two distinct chelate donor systems, by virtue of the presence of bispyrazole and bisthioether functions. The preferred conformation of these ligands is such that the N₂ and S₂ donor moieties are usually oriented in opposite directions, thus favouring the formation of molecular chains when reacted with AgBF₄. The X-ray structures of Ag(I) complexes show that depending on the steric hindrance present on the pyrazole rings, these ligands behave as κ⁴-SSNN-μ bridging tetradentate (when R = H), κ³-SNN-μ bridging tridentate (when R = Me, *i*-Pr). Interestingly, [Ag(**L^HPhSPhSPh**)]BF₄ crystallizes in the chiral space group *P*4₁, with the molecular chain that is folded around the 4₁ screw axis.

6.1 Introduction

The stability of supramolecular architectures depends on the affinity between the ligand donor set and the metal ions, and more specifically it is crucially dependent on the capacity that the binding sites of the ligand are suitable for satisfying the stereochemical requirement of the metal center. There is in fact a net thermodynamic advantage during the generation of the supramolecular structure when the ligands display a pre-organized donor set in which the metal ion can easily settle^{81,105}. In this chapter, three different N₂S₂ donor ligands were synthesised, L^HPhSPhSPh, L^{Me}PhSPhSPh, and L^{iPr}PhSPhSPh. They ideally represent a modification of the ligands described in chapter 4 and 5 since an additional thioether group was attached to the bispirazole scaffold. The N₂ donor system derives by a bis(pyrazole)methane moiety, and attached to its central carbon a atom is located a bithioether function that provide the S₂ donor system. These ditopic ligands adopt a conformation that makes them suitable to build molecular chains when reacted with metal ions since the N₂ and S₂ donor groups point in nearly opposite directions as found for L^{Me}SPh class. Furthermore, the three ligands differ by the steric hindrance positioned on the pyrazole ring in the form of H, Me or *i*-Pr groups, and this has structural consequences on the overall polynuclear structure. To investigate the suitability of these ligands in the construction of molecular chains, Ag(I) complexes were prepared by reacting AgBF₄ with L^HPhSPhSPh, L^{Me}PhSPhSPh or L^{iPr}PhSPhSPh. The molecular structures of the ligand L^{iPr}PhSPhSPh and of the complexes [Ag(L^HPhSPhSPh)]BF₄ (**33**) , [Ag(L^{Me}PhSPhSPh)(Me₂CO)]BF₄·Me₂CO (**34**), and [Ag(L^{iPr}PhSPhSPh)(Me₂CO)]BF₄ (**35**) are described. Interestingly the complex **33** crystallizes in the chiral space group *P*4₁ due to the formation of a homochiral molecular chain having the shape of a right-handed helix. As far as the silver complexes are concerned, many other examples can be found in the literature reporting 1D polymeric structures obtained by using nitrogen donor ligands. In some cases these 1D structures are generated by ligands that act as a bridge between two metal centers thus forming a coordination polymer^{58,59}, whereas in other cases the building blocks are represented by metal complexes that are interacting with neighbor ones by means of weaker forces such as hydrogen bonds, π-π stack, or C-H...π interactions⁶⁰. By a judicious choice of ligands, these molecular chains can be chiral either because they form helical structures^{61–64} or because a chiral ligand has been specifically employed⁶⁵.

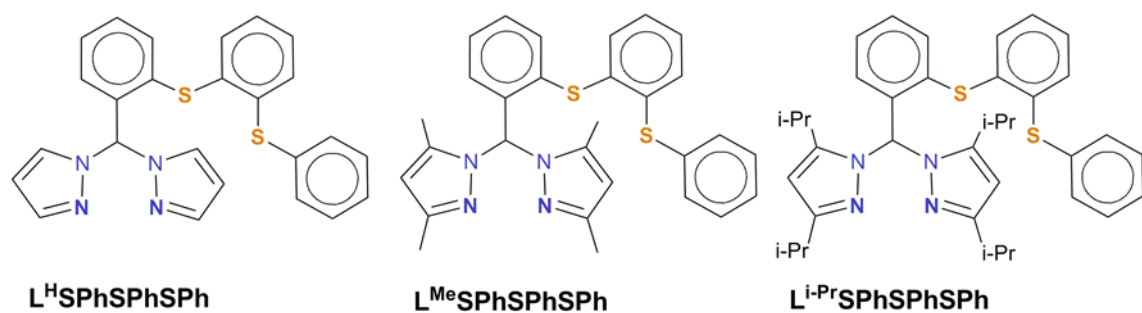


Figure 65. Molecular structures of the ligands described in this chapter.

6.2. Experimental

6.2.1. Synthesis

Bis(pyrazolyl)ketones^{44–46} were prepared as reported in the literature. 2-(phenylthio)benzenethiol⁷⁵ and 2-(2-(phenylthio)phenylthio)benzaldehyde¹⁰³ were prepared by slight modifications of reported procedures. All reagents and solvents were commercially available. Solvents were dried and distilled before use. ¹H NMR spectra were recorded on a Bruker Avance 300 spectrometer using standard Bruker pulse sequences. Chemical shifts are reported in ppm referenced to residual solvent protons (CDCl₃, CD₂Cl₂, CD₃CN, (CD₃)₂CO). Infrared spectra were recorded from 4000 to 700 cm⁻¹ on a Perkin-Elmer FT-IR Nexus spectrometer equipped with a Thermo-Nicolet microscope. Elemental analyses (C, H, N) were performed with a Carlo Erba EA 1108 automated analyzer.

Synthesis of 2-(phenylthio)benzenethiol. A solution of thiophenol (4 ml, 39.0 mmol) in cyclohexane (10 ml) was added to a solution of *n*-BuLi (1.6 M in hexane, 54 ml, 86.4 mmol) and N,N,N',N'-tetramethylethylenediamine (TMEDA, 13 ml, 86.7 mmol) in cyclohexane (60 ml) at 0 °C under nitrogen. The reaction was stirred for 30 min at 0 °C and for 6 h at room temperature. A solution of diphenyl disulfide (9.5 g, 43.6 mmol) in cyclohexane (90 ml) was added at 0 °C. After being stirred for 30 min at 0 °C, the mixture was stirred overnight at room temperature and quenched with 15% HCl(aq) (175 ml). The organic and water layers were separated and the latter was extracted with diethyl ether (3x 50 ml). The organic phases were mixed and dried with anhydrous Na₂SO₄. Solvents were removed under vacuum. The solid was recrystallized from a CH₂Cl₂:EtOH mixture, yielding a colorless crystalline solid (4 g, 18.4 mmol, 47%). ¹H NMR (300 MHz, CDCl₃): δ, 4.29 (s, 1H, SH), 7.1–7.6 (m, 9H, CH). Anal. calcd for C₁₂H₁₀S₂ (218.02): C, 66.01; H, 4.62. Found: C, 66.10; H, 4.44.

Synthesis of 2-(2-(phenylthio)phenylthio)benzaldehyde. To a stirred solution of 2-(phenylthio)benzenethiol (2 g, 9.2 mmol) and anhydrous Na₂CO₃ (1.3 g) in dry DMF (5 ml) under nitrogen at 90 °C, 2-chlorobenzaldehyde (0.9 ml, 7.99 mmol) was slowly added. The mixture was stirred at 90 °C overnight. After cooling, the reaction mixture was poured into water (50 ml) and extracted with diethyl ether (50 ml). The extract was washed with water (2x50 ml), dried with anhydrous Na₂SO₄, and concentrated under vacuum. The resulting oil was triturated with hexane in an ultrasound bath for 20 min, filtered and dried under vacuum to afford a pale white solid (1.85 g, 5.7 mmol, 72%). ¹H NMR (300 MHz, CDCl₃): δ, 7.11–7.51 (m, 12H, CH Ph), 7.94 (d, J = 7.5

Hz, 1H, CH Ph), 10.39 (s, 1H, CHO). Anal. calcd for C₁₉H₁₄OS₂ (322.05): C, 70.77; H, 4.38. Found: C, 70.53; H, 4.51.

Synthesis of 1,1'-((2-(2-(phenylthio)phenylthio)phenyl)methylene)bis(1H-pyrazole) (L^HPhSPhSPh). 2-(2-(phenylthio)phenylthio)benzaldehyde (875 mg, 2.71 mmol) and CoCl₂·6H₂O (5 mg, 0.021 mmol) were added to bis(1H-pyrazol-1-yl)ketone (565 mg, 3.48 mmol) in a Schlenk flask under nitrogen. The mixture was heated at 130 °C and vigorously stirred. After 1 h, the green mixture was cooled to room temperature. Diethyl ether (50 ml) and water (50 ml) were then added, the organic phase was separated and washed with brine (2 x 50 ml), dried with anhydrous Na₂SO₄ and filtered. The volatiles were removed under vacuum yielding a pale oil. The compound was recrystallized in hot methanol (5 ml) and leaving the solution to rest at 0°. Colorless micro-crystals were isolated and vacuum dried (L^{Me}, 907 mg, 2.06 mmol, 76%). ¹H NMR (300 MHz, CDCl₃): δ, 6.26 (t, J = 2.0 Hz, 2H, CH pz), 6.86 (dd, J = 7.5 Hz, J = 1.6 Hz, 1H CH Ph), 6.99-7.40 (m, 14H, CH Ph, CH pz), 7.62 (d, J = 1.7 Hz, CH pz), 8.20 (s, 1H, CH bridge). Anal. calcd for C₂₅H₂₀N₄S₂ (440.59): C, 68.15; H, 4.58; N, 12.72. Found: C, 67.86; H, 4.21; N, 12.41.

Synthesis of 1,1'-((2-(2-(phenylthio)phenylthio)phenyl)methylene)bis(3,5-dimethyl-1H-pyrazole) (L^{Me}PhSPhSPh). 2-(2-(phenylthio)phenylthio)benzaldehyde (900 mg, 2.79 mmol) and CoCl₂·6H₂O (5 mg, 0.021 mmol) were added to bis(3,5-dimethyl-1H-pyrazol-1-yl)ketone (670 mg, 3.07 mmol) in a Schlenk flask under nitrogen. The mixture was heated at 90 °C and vigorously stirred. After 2 h, the dark blue mixture was cooled to room temperature. CHCl₃ (50 ml) and water (50 ml) were then added. The organic layer was separated and washed with water (2 x 50 ml), dried with anhydrous Na₂SO₄ and concentrated under vacuum yielding a pale oil, which was purified by column chromatography (Silica gel, gradient of elution from hexane/ethyl acetate 18:1 to pure ethyl acetate). The oil was then triturated with hexane in an ultrasound bath, filtered and dried under vacuum, affording a white powder (L^{Me}, 790 mg, 1.59 mmol, 57%). ¹H NMR (300 MHz, CDCl₃): δ, 2.11 (s, 6H, CH₃), 2.20 (s, 6H, CH₃), 5.82 (s, 2H, CH pz), 6.99-7.14 (m, 5H, CH Ph), 7.31 (m, 8H, CH Ph), 7.86 (s, 1H, CH bridge). Anal. calcd for C₂₉H₂₈N₄S₂ (496.69): C, 70.13; H, 5.68; N, 11.28. Found: C, 69.96; H, 5.79; N, 11.36.

Synthesis of 1,1'-((2-(2-(phenylthio)phenylthio)phenyl)methylene)bis(3,5-diisopropyl-1H-pyrazole) (L^{iPr}PhSPhSPh). 2-(2-(phenylthio)phenylthio)benzaldehyde (770 mg, 2.39

mmol) and $\text{CoCl}_2 \cdot 6\text{H}_2\text{O}$ (4 mg, 0.017 mmol) were added to bis(3,5-diisopropyl-1H-pyrazol-1-yl)ketone (910 mg, 2.75 mmol) in a Schlenk flask under nitrogen. The mixture was heated at 150 °C and vigorously stirred. After 4 h, the dark green mixture was cooled to room temperature. CHCl_3 (50 ml) and water (50 ml) were then added, and the organic layer was separated and washed with water (2 x 50 ml), dried with anhydrous Na_2SO_4 and concentrated under vacuum yielding a dark oil, which was purified by column chromatography (Silica gel, hexane:ethyl acetate 9:1). The resulting oil was recrystallized from hexane (2-3 ml) at room temperature, yielding a crystalline white solid (L^{Pr} , 640 mg, 1.05 mmol, 44%). ^1H NMR (300 MHz, CDCl_3): δ , 0.92 (d, J = 6.9 Hz, 6H, CH_3), 0.99 (d, J = 6.9 Hz, 6H, CH_3), 1.20 (d, J = 6.9 Hz, 12H, CH_3), 2.91 (hept, J = 6.9 Hz, 2H, CH *i*-Pr), 3.15 (hept, J = 6.9 Hz, 2H, CH *i*-Pr), 5.91 (s, 2H, CH pz), 6.95 (m, 1H, CH Ph), 7.08 (m, 4H, CH Ph), 7.19-7.32 (m, 8H, CH Ph), 8.00 (s, 1H, CH bridge). Anal. calcd for $\text{C}_{37}\text{H}_{44}\text{N}_4\text{S}_2$ (608.90): C, 72.98; H, 7.28; N, 9.20. Found: C, 73.07; H, 7.11; N, 9.12.

Synthesis of $[\text{Ag}(\text{L}^{\text{H}}\text{PhSPhSPh})]\text{BF}_4$ (33). $\text{L}^{\text{H}}\text{PhSPhSPh}$ (100 mg, 0.227 mmol) and AgBF_4 (44 mg, 0.227 mmol) were mixed in acetone (20 ml), and the colorless solution was stirred for 1 h. The solvent was then removed under vacuum and the white solid was washed with diethyl ether in an ultrasound bath. The mixture was filtered affording a white solid (45 mg, 0.091 mmol, 40%). The compound was recrystallized by stratifying pentane over an acetone solution of the complex, yielding colorless crystals. IR (cm^{-1}): 3133 w, 3051w, 2969w, 1689w, 1621w, 1566w, 1511w, 1434m, 1396m, 1287m, 1052s, 1021s, 746s, 690m, 626m, 520m. ^1H NMR (300 MHz, $(\text{CD}_3)_2\text{CO}$): δ , 6.47 (t, J = 2.4 Hz, 1H, CH pz), 6.98 (d, J = 8.1 Hz, 1H, CH Ph), 7.21 (m, 4H, CH Ph), 7.46 (m, 8H, CH Ph), 7.68 (d, J = 1.8 Hz, 2H, CH pz), 8.10 (d, J = 2.7 Hz, 2H, CH pz), 8.69 (s, 1H, CH). Anal. calcd for $\text{C}_{25}\text{H}_{20}\text{AgBF}_4\text{N}_4\text{S}_2$ (635.26): C, 47.27; H, 3.17; N, 8.82. Found: C, 47.76; H, 3.02; N, 8.45.

Synthesis of $[\text{Ag}(\text{L}^{\text{Me}}\text{PhSPhSPh}^e)(\text{Me}_2\text{CO})]\text{BF}_4 \cdot \text{Me}_2\text{CO}$ (34). $\text{L}^{\text{Me}}\text{PhSPhSPh}$ (100 mg, 0.201 mmol) and AgBF_4 (40 mg, 0.205 mmol) were mixed in acetone (15 ml), and the colourless solution was stirred for 1 h. The solvent was then concentrated under vacuum and a white solid was precipitated after addition of pentane. The solid was filtered and vacuum dried. (138 mg, 0.187 mmol, 93%). The compound was recrystallized by stratifying pentane over an acetone solution of the complex, yielding colorless crystals. IR (cm^{-1}): 3062w, 2985w, 2914w, 1708w, 1692m, 1577m, 1442m, 1419m, 1248w, 1051s, 1030s, 876m, 753s, 689m, 521m. ^1H NMR (300 MHz, CD_3CN): δ , 1.95 (s, 6H, CH_3), 2.37 (s, 6H, CH_3), 6.03 (s, 2H, CH pz), 6.88 (d, J = 7.2 Hz, 1H, CH

Ph), 7.22 (m, 12H, CH Ph), 7.72 (s, H, CH_{central}). Anal. calcd for C₃₅H₄₀AgBF₄N₄O₂S₂ (807.52): C, 52.06; H, 4.99; N, 6.94. Found: C, 51.67; H, 4.52; N, 6.68.

*Synthesis of [Ag(L^{iPr}PhSPhSPh)(Me₂CO)]BF₄ (**35**).* L^{iPr}PhSPhSPh (123 mg, 0.202 mmol) and AgBF₄ (40 mg, 0.205 mmol) were mixed in acetone (15 ml), and the colorless solution was stirred for 1 h. The solvent was then concentrated under vacuum and a white solid was precipitated after addition of pentane. The solid was filtered and vacuum dried. (147 mg, 0.164 mmol, 81%). The compound was recrystallized by stratifying pentane over an acetone solution of the complex, yielding colorless crystals. IR (cm⁻¹): 2963w, 2876w, 1693m, 1544w, 1462m, 1441m, 1380w, 1363w, 1303w, 1276w, 1226m, 1048s, 821m, 758s, 648m, 528m. ¹H NMR (300 MHz, CD₃CN): δ, 1.11 (m, 24H, 8CH₃), 2.65 (s br, 2H, CH *i*-Pr), 3.24 (m, J = 6.9 Hz, 2H, CH *i*-Pr), 6.24 (s, 2H, CH pz), 6.56 (s br, 1H, CH Ph), 7.13 (m, 2H, CH Ph), 7.28 (m, 10H, CH Ph), 7.91 (s, 1H, CH). Anal. calcd for C₄₀H₅₀AgBF₄N₄OS₂ (861.66): C, 55.76; H, 5.85; N, 6.50. Found: C, 55.34; H, 5.39; N, 6.17.

6.2.2. X-ray crystallography

A summary of data collection and structure refinement for L^{iPr}PhSPhSPh, **33-35** are reported in Appendix viii. Single crystal data was collected with a *Bruker AXS Smart 1000*, Mo Kα: λ = 0.71073 Å. The intensity data were integrated from several series of exposures frames (0.3° width) covering the sphere of reciprocal space⁴⁸. An absorption correction was applied using the program SADABS with min. and max. transmission factors of: 0.777-1.000 (L^{iPr}PhSPhSPh), 0.506-1.000 (**33**), 0.828-1.000 (**34**), 0.808-1.000 (**35**), and 0.834-1.000 (**35**). The structures were solved by direct methods (SIR97⁶⁶) and refined on F² with full-matrix least squares (SHELXL-97⁵⁰), using the Wingx software package⁵¹. Non hydrogen atoms were refined anisotropically for all compounds, and the hydrogen atoms were placed at their calculated positions. The BF₄⁻ anion in **34** and **35** was statically disordered in two positions with site occupancy factors of 0.56/0.44 (**34**), and 0.67/0.33 (**35**). Graphical material was prepared with Mercury 2.0⁵² programs.

6.3. Results and Discussion

6.3.1. Synthesis

There are two main synthetic routes that lead to C-centered heteroscorpionate tripodal ligands based on the bispyrazole scaffold. The first method consists in the deprotonation of methylene bridge of bis(pyrazolyl)methane with a strong base. The generated carbanion can then be reacted with specific electrophiles. This procedure has been developed for the production of various tripodal ligands among which are the bis(pyrazolyl)carboxylate/bis(pyrazolyl)thiocarboxylate¹⁰⁶, and the hybrid bis(pyrazolyl)cyclopentadienyl¹⁰⁷ ligands. In the second synthetic route, as we have already described in previous chapters, bis(pyrazolyl)ketones are reacted with aldehydes or ketones bearing the desired donor groups that are to be attached to the bispyrazole platform^{108,109}.

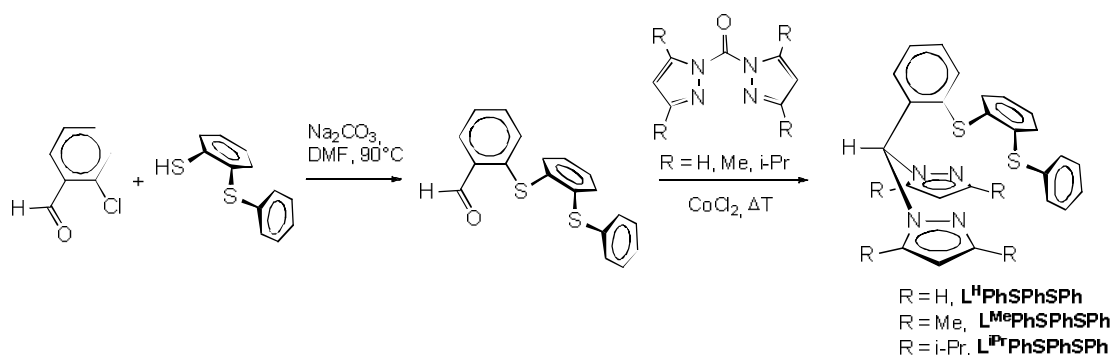


Figure 66. Synthesis of the ligands described in this chapter.

The ligands reported were prepared according to the second procedure, by reacting bis(pyrazolyl)ketones with 2-(2-(phenylthio)phenylthio)benzaldehyde, Figure 66. These ligands exhibit a N₂S₂ donor set and they could provide the geometric environment for the encapsulation of a metal center in a distorted tetrahedral arrangement. To test this hypothesis two models based on the L^{Me}PhSPhSPh ligand and Cu(I) or Ag(I) were taken as benchmark, and their geometry were optimized⁷². The ligand can accommodate both metals, but by doing so it faces a certain degree of distortion of the aromatic ring attached to the bispyrazole moiety. In addition, this ligand conformation would bring the CH_{central} and the aromatic CH_{ortho} in close

proximity, and this could possibly constitute an additional destabilizing factor. In order to investigate the coordinative behaviour of these ligands, Ag(I) complexes were prepared by reacting equimolar amounts of ligands and AgBF₄. The complexes could be crystallized by stratifying pentane over an acetone solution of each complex.

6.3.2. Molecular structures

The molecular structure of **L^{iPr}PhSPhSPh** ligand is reported in Figure 67. The two pyrazole rings are in an *anti* conformation, and this arrangement is probably adopted to avoid the electronic repulsion between the nitrogen lone pairs. This is a common feature of ligands based on the bis(pyrazolyl)methane scaffold [38]. In addition, a weak CH...N interaction between N(21) and the C(72) of an *i*-Pr group (3.196(5) Å) contributes to the stabilization of this pyrazoles arrangement. Another feature worth of mentioning is represented by the conformation of the thioether arm with respect to the pyrazole rings that can be better described by introducing the torsion angle $\tau(1)$ (Figure 73), which is -121.9(3)° in the present case. Furthermore, the steric repulsion between the C(33)-H and C(13)-H forces away these two groups, and may be an additional factor contributing to the resulting ligand arrangement. This has important consequences on the structures of the metal complexes prepared with these ligands, since the pre-organization of the free ligand favours the preorientation of the N₂ and S₂ donor system in different directions. This is responsible of the polymeric molecular structures of the Ag(I) complexes described below.

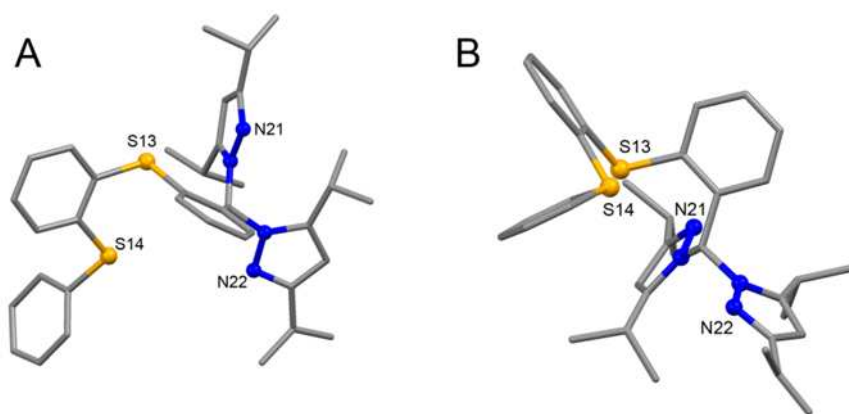


Figure 67. Stereochemical descriptors (a), and torsion angles varied during the conformational studies (b).

It is worth of note that the asymmetry of the bisthioether group and the present ligand conformation implies that $L^{iPr}PhSPhSPh$ is chiral, though we may speak of a conformational chirality, and as stereodescriptor we can use the $\tau(1)$ angle defined above. With this respect, in the unit cell are present both conformational enantiomers, one with $\tau(1) = -121.9(3)^\circ$ and the other one with $\tau(1) = 121.9(3)^\circ$, Figure 68.

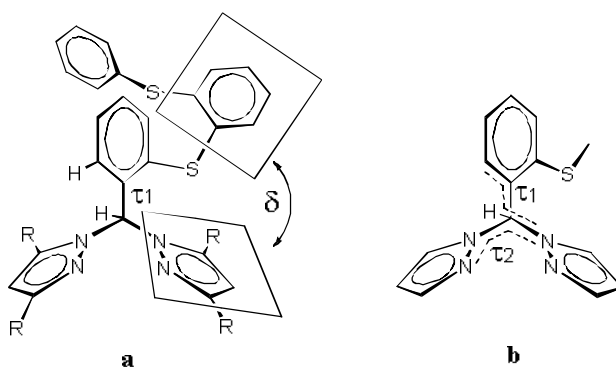


Figure 68. Stereochemical descriptors (a), and torsion angles varied during the conformational studies (b).

Selected bond lengths and angles for complex **33** are reported in Table 9, whereas the molecular structure and crystal packing are depicted in Figures 69-70. The ligand behaves as κ^4 -SSNN- μ bridging tetradentate, being N_2 chelated on a metal center and linking a second metal with the bisthioether functions that are pointing approximately in opposite direction with respect to the N_2 donor system. The metal adopts a severely distorted tetrahedral geometry and the distortion from the ideal geometry is a consequence of the small bite angles of the N_2 (85°) and S_2 (75°) chelate groups. The Ag-N bond distances (2.297(6) and 2.355(7) Å) are considerably smaller than the Ag-S ones (2.607(2) and 2.625(2) Å). The ligand adopts the same conformation of the thioether arm found for $L^{iPr}PhSPhSPh$ with the torsion angle $\tau(1)$ -[C(33)-C(23)-C(13)-N(11)] of $-130.3(7)^\circ$. This preferred conformation of the thioether moiety with respect to the bispyrazole scaffold leads to the formation of molecular chains that are parallel to the c crystallographic axis. Furthermore, since the compound crystallizes in the chiral space group $P4_1$, only one ligand conformation is present in the structure, with the molecular chains that are homochiral. These chains have the shape of a right-handed helix folded around the c axis, and the helix pitch corresponds to the length of

the c axis ($\sim 30.5 \text{ \AA}$), whereas the displacement of the silver atoms from the helix center is $\sim 1 \text{ \AA}$. It is likely that during the crystallization process, a racemic conglomerate¹¹⁰ formed and that both enantiomorphic space groups were present ($P4_1$ and $P4_3$). However, the inspection of the morphology of the crystals did not permit to individuate the enantiomorphic pairs as the complex gave rise to long needle-like crystals with poorly defined faces¹¹¹. Similar examples of racemic conglomerate formed when using an achiral pyridine-thioether ligand were reported. Also in those cases, the formation of the helical structures depends on the conformation adopted by the ligand when bound to the metal^{62,112}.

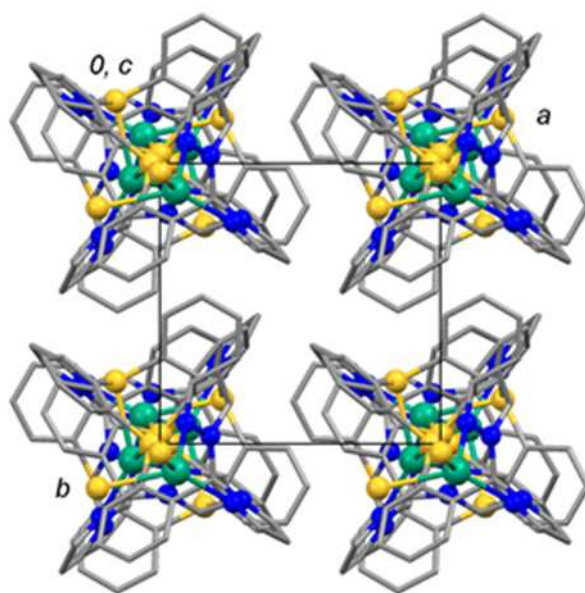


Figure 69. Crystal packing of **33** projected along the c axis. The hydrogen atoms and the BF_4^- counterion were removed for clarity

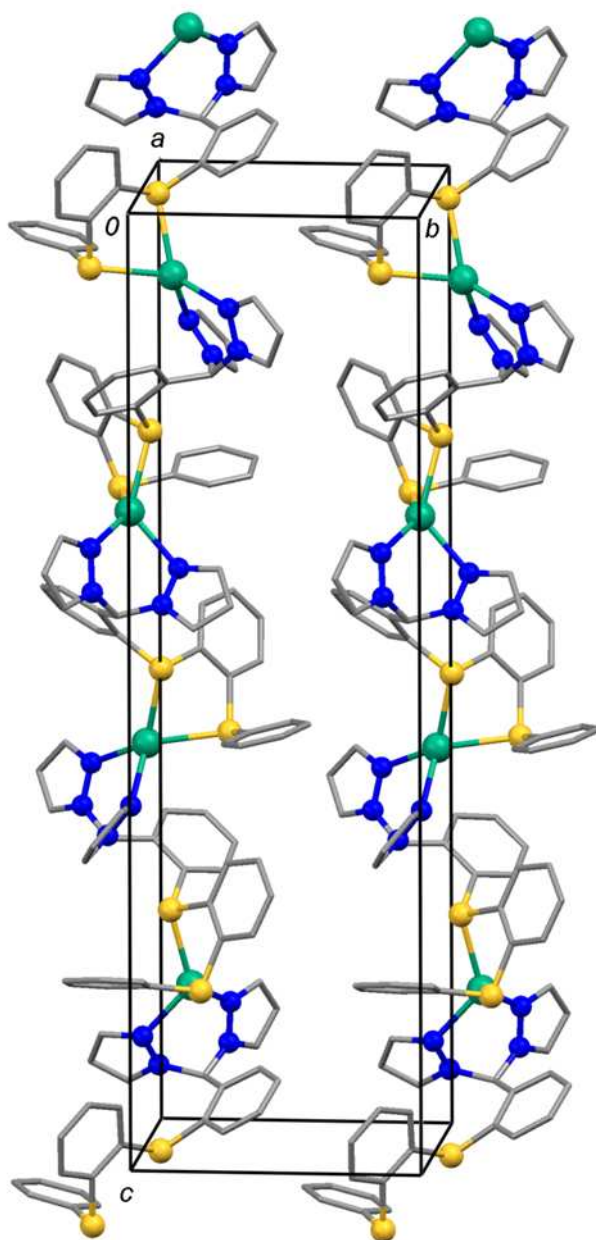


Figure 70. Crystal packing of **33** projected along the *a* axis. The hydrogen atoms and the BF_4^- counterion were removed for clarity.

Selected bond lengths and angles for complex **34** are reported in Table 9, whereas the molecular structure and crystal packing are depicted in Figures 71-72. Differently from **33**, in the present complex the ligand acts as $\kappa^3\text{-SNN-}\mu$ bridging tridentate,

bound to a metal center with the bis(pyrazole)moiety and bridging another metal center with the S(14) sulfur atom. The S(13) atom does not take part to the metal coordination. The metal is in a trigonal planar geometry that is distorted toward the tetrahedral one according to the presence of the acetone molecule ligated to the metal ($d[\text{Ag-O}(1\text{s})] = 2.550(2) \text{ \AA}$). The metal-nitrogen and metal-sulfur bond distances are significantly smaller than the metal-oxygen one, attesting the weak nature of the latter interaction. The presence of a certain steric hindrance in the form of methyl groups on the pyrazole rings causes the second phenyl ring (**II**) of the thioether arm to adopt a conformation that prevents the coordination of the S(13) atom to the metal center, Figure 73. The conformation of ring **I** is analogous to that of the previous structures, and since the space group is a non chiral one, both conformers are present with $\tau(1)-[\text{C}(33)-\text{C}(23)-\text{C}(13)-\text{N}(11)]$ of $\pm 121.6(2)^\circ$. The pyrazole ring and **II** form an angle of 82° , whereas in **33**, where there are no bulky groups on the pyrazoles, this angle is of 51° . The formation of molecular chains is determined by the coordination of the S(14) atom to a second metal. These chains present the phenyl residues oriented on the opposite side with respect to the coordinated acetone molecules, and the pyrazole rings are interposed between these two donor groups. The chains are homochiral, built by ligands of the same conformations, and chains of opposite chirality are present in the unit cell.

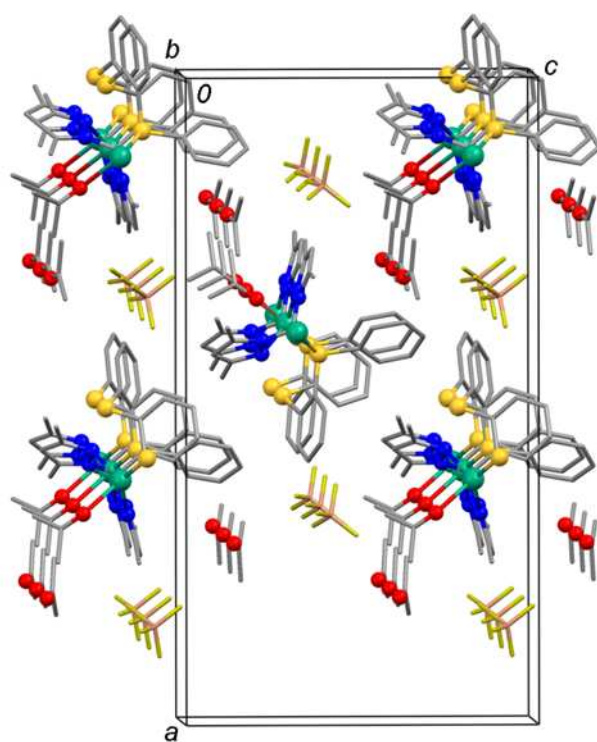


Figure 71. Portion of the crystal packing of **34**, projected along the *b* axis. The hydrogen atoms were removed for clarity.

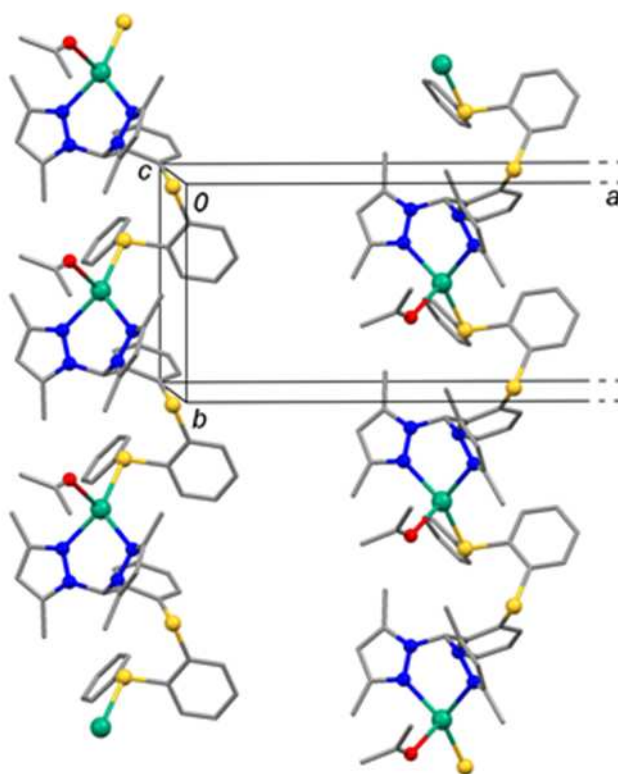


Figure 72. Portion of the crystal packing of **34** projected along the *c* axis. The hydrogen atoms, the BF_4^- counterion, and the solvate acetone molecules were removed for clarity.

The molecular structure of the asymmetric unit of complex **35** is essentially analogous to that of **34**, Figures 73-74. The metal presents a trigonal planar geometry achieved by the bis(pyrazole) moiety and by a bridging sulfur atom (S(14)). Also for this complex, a weak Ag-O interaction deriving from an acetone molecule distorts the trigonal geometry towards the tetrahedral one. However, the Ag-O1s distance in the present complex is ~ 0.2 Å longer than that found in **34**, Table 9. The conformation of the **I** phenyl ring of thioether arm is analogous to that of the previous complexes, with $\tau(1)\text{-}[\text{C}(33)\text{-C}(23)\text{-C}(13)\text{-N}(11)]$ of $-130.0(5)^\circ$. The steric hindrance on the pyrazole rings is determined by *i*-Pr residues and this reproduces an effect similar to the methyl groups in **34** to the overall structure. In fact, the S(13) atom is not bound to the metal and the **II** phenyl ring of the thioether arm is nearly perpendicular to the

pyrazole plane, Figure 75. Differently from the previously described complexes, the molecular chains contain alternating ligands of opposite chirality. The crystal packing is also similar to that of **34**, even though in the present complex there are no additional acetone molecules of crystallization.

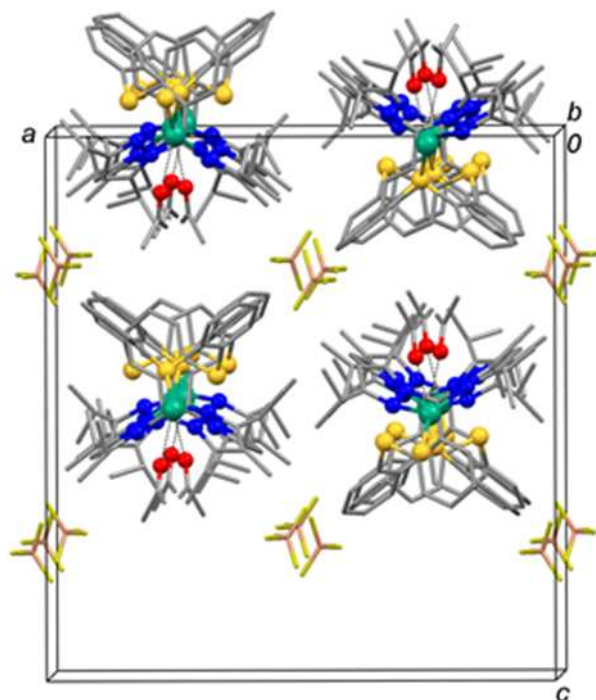


Figure 73. Portion of the the crystal packing of **35** projected along the *b* axis. The hydrogen atoms were removed for clarity.

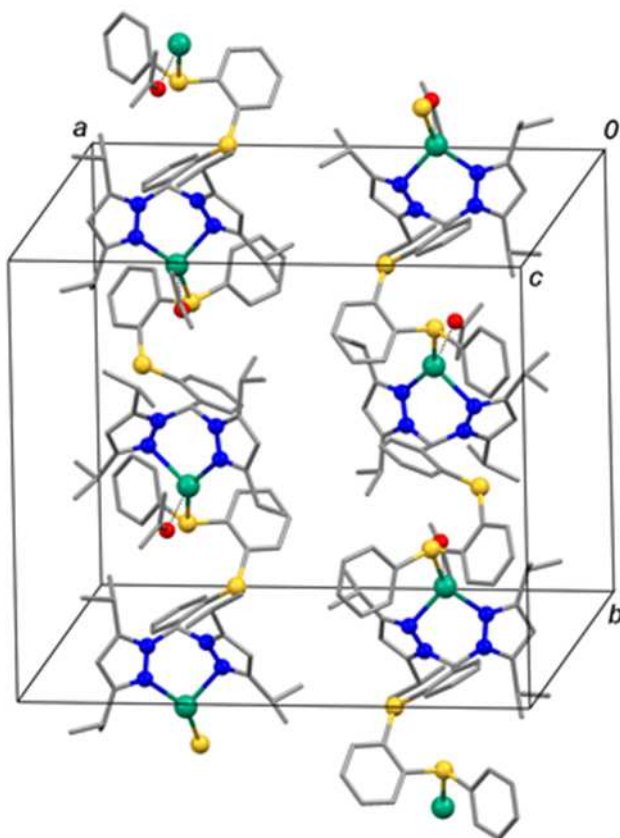


Figure 74. Portion of the crystal packing of **35** projected along the *c* axis. The hydrogen atoms and the BF_4^- counterion were removed for clarity. The chains are composed of alternating ligand conformers.

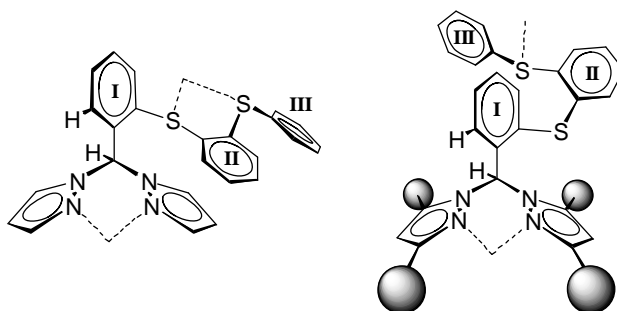


Figure 75. Different pyrazole substituents determines different ligand conformation and modes of coordination.

Table 9. Selected bond lengths (Å) and angles (°) for **33**, **34** and **35**.

33			
Ag-N(21)	2.355(7)	N(21)-Ag-N(22)	84.9(2)
Ag-N(22)	2.297(6)	N(21)-Ag-S(13)'	125.2(2)
Ag-S(13)'	2.607(2)	N(21)-Ag-S(14)'	111.2(2)
Ag-S(14)'	2.625(2)	N(22)-Ag-S(13)'	128.4(2)
		N(22)-Ag-S(14)'	137.0(2)
		S(13)'-Ag-S(14)'	75.52(6)
34			
Ag-N(21)	2.307(2)	N(21)-Ag-N(22)	86.74(6)
Ag-N(22)	2.253(2)	N(21)-Ag-O1s	107.34(7)
Ag-S(14)''	2.4324(6)	N(21)-Ag-S(14)''	123.96(5)
Ag-O1s	2.550(2)	N(22)-Ag-O1s	94.55(7)
		N(22)-Ag-S(14)''	142.99(5)
		O1s-Ag-S(14)''	94.82(5)
35			
Ag-N(21)	2.252(4)	N(21)-Ag-N(22)	86.6(2)
Ag-N(22)	2.321(4)	N(21)-Ag-O1s	96.7(1)
Ag-S(14)'''	2.427(1)	N(21)-Ag-S(14)'''	124.2(1)
Ag-O1s	2.737(4)	N(22)-Ag-O1s	91.3(2)
		N(22)-Ag-S(14)'''	146.1(1)
		O1s-Ag-S(14)'''	98.1(1)

' = y; -x; z-1/4, '' = x; y+1; z, ''' = -x+1/2, y+1/2, z

6.3.3. Conformational studies.

Conformational studies were performed in order to investigate the energetics relative to the mobility of the pyrazole rings and of the thioether group of the ligands. For this purpose, a model complex was used in which the **-II-S-III** fragment was replaced by a

methyl group, Figure 73. The calculations were performed by varying two torsion angles, one that rotates the thioether group with respect to the pyrazole rings (τ_1), and the other one that rotates one of the pyrazole rings (τ_2). A picture describing this rigid potential energy surface scan is depicted in Figure 76. It can be noted that there are very high energy peaks, and these correspond to unrealistic conformations where C-H and $-S-CH_3$ groups are in very close proximity. This occurs because at every calculation step the molecular geometry was not optimized (rigid scan). For all of the other regions the maximum energy difference is approximately 80 kJ/mol, and there appear preferential pathways for the conformational mobility. In particular, the trajectory that connects the 1-3 conformations is characterized by the rotation of the pyrazole ring (τ_2), but with the sulphur atom that points towards the CH_{central} . The conformation 1 is similar to that observed for the structure of $L^{\text{ipr}}\text{PhSPhSPh}$, with the pyrazole rings in *anti* disposition, whereas in 3 one of the pyrazoles exchanges an interaction with the CH_{phenyl} in ortho position. The normalized energy profile of this conformational change is depicted in Figure 13. The saddle point (structure 2) lies approximately 30 kJ/mol above the 1 and 3 minima. On the other hand, the trajectory that connects the 4 and 5 conformations lies 80 kJ/mol above the one that connects the 1-3 conformations. Along this 4-5 path, the molecule rotates the pyrazole ring, but a destabilizing factor is represented by the repulsive interaction between the sulphur atom and one of the nitrogen atoms. Two other structural modifications can be envisaged by inspection of Figure 77, and are those linking 1-4 and 3-5 conformations. These correspond to the rotation of the thioether group with respect to the bis(pyrazole) moiety. The normalized energy profile of the 1-4 trajectory shows that the saddle point 4 is ~ 80 kJ/mol above the minima, and ~ 50 kJ/mol higher than the saddle point 2.

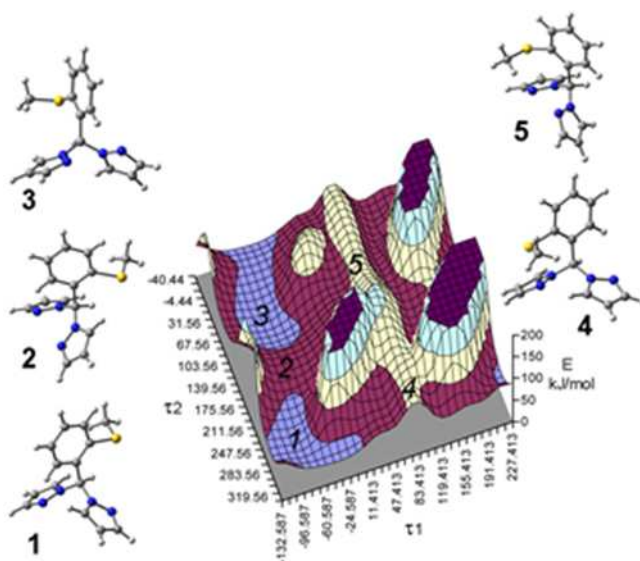


Figure 76. Rigid potential energy surface scan obtained by varying $\tau(1)$ and $\tau(2)$ torsion angles as defined in Scheme 2b. Molecular structures of relevant conformations are also reported

From this calculations, it is evident that the thioether group is preferentially oriented towards the hydrogen atom of $\text{CH}_{\text{central}}$, hence on the opposite direction with respect to the N_2 donor atoms, whereas the rotation of the pyrazole ring is a more viable scenario as it requires a minor energetic expenditure. Extending these results to the $\text{L}^{\text{H}}\text{PhSPhSPh}$, $\text{L}^{\text{Me}}\text{PhSPhSPh}$ and $\text{L}^{\text{iPr}}\text{PhSPhSPh}$ ligands, it can be then proposed that, prior to their interaction with a metal center, they are in either one of the 1-3 conformations. When a metal center approaches the ligands, it becomes chelated by the pyrazole rings and the sulphur atom(s) is(are) available for bridging on a second metal center on the opposite side. The results here presented are to be taken as a qualitative picture of the possible conformations occurring in solution for the real ligand systems $\text{L}^{\text{H}}\text{PhSPhSPh}$, $\text{L}^{\text{Me}}\text{PhSPhSPh}$, and $\text{L}^{\text{iPr}}\text{PhSPhSPh}$. Besides, these results are in agreement with the similar results obtained for the simpler system $\text{L}^{\text{R}}\text{PhS}$ already studied in chapter 3.

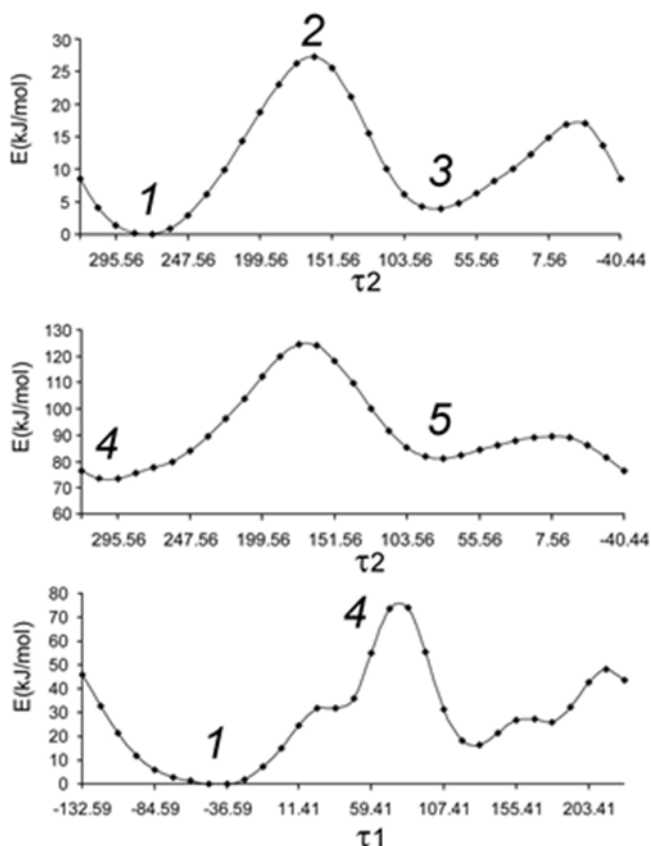


Figure 77. Energy profile of selected trajectories of the potential energy surface. The energy values were normalized by taking the conformation 1 as reference (PES minimum).

As far as the silver complexes are concerned, the ^1H NMR spectra recorded in CD_3CN or $(\text{CD}_3)_2\text{CO}$ at variable temperature suggest that a dynamic behaviour involves at least one of the two pyrazole rings. In fact the substituents of $\text{L}^{\text{Me}}\text{PhSPHSPH}$ and $\text{L}^{\text{iPr}}\text{PhSPHSPH}$ of one pyrazole group exhibit coalescence at approximately 250 K for $\text{L}^{\text{Me}}\text{PhSPHSPH}$ and 280 K for $\text{L}^{\text{iPr}}\text{PhSPHSPH}$, Figure 78.

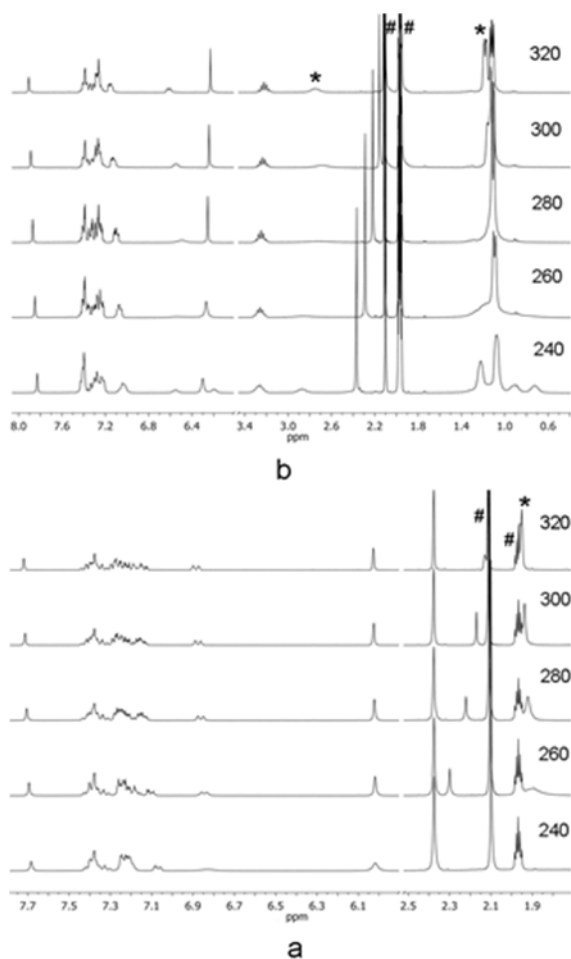


Figure 78. Variable temperature ^1H NMR spectra of **34** (a) and **35** (b) recorded in CD_3CN . The asterisks denote fluxional Me or *i*-Pr protons. # = impurities (CD_2HCN and acetone).

The reason for this behavior is not easily interpretable but it may be related to the rotation of pyrazole ring along the $\text{C}_{\text{central}}\text{-N}$ vector. This process determines the rupture of the Ag-N bond and consequently a modification of the silver geometry. In support of this hypothesis are the molecular structures of **33-35**, where it is evident that one of the Ag-N bond distances is significantly longer than the other one by 0.05 Å (**33** and **34**) and 0.07 Å (**35**). Furthermore the longest Ag-N distance is associated to the pyrazole on the same side of the sulfur atom and for which there is a mismatch between the directionality of the nitrogen lone pair and the silver atom.

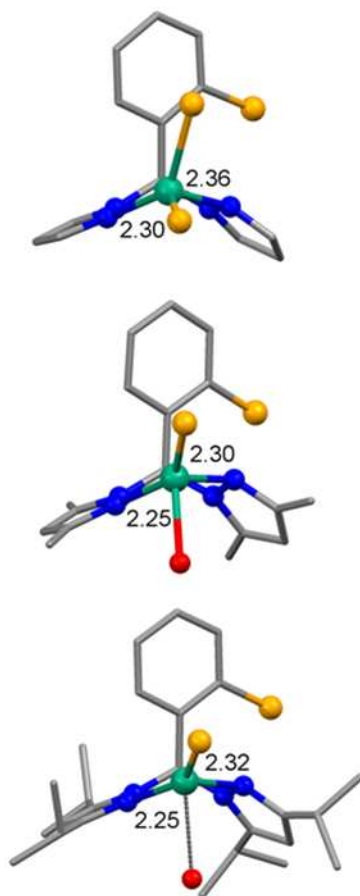


Figure 79. Comparison of the Ag environment and Ag-N bond distances in **33-35**.

At the same time, the N-Ag-S bond angle opposite to fluxional Ag-N bond tends towards the linearity (128° in **33**, 143° in **34** and 146° in **35**) further supporting the lability of the Ag-N bond^{113–115}. Assuming this fluxional behaviour, the silver coordination varies between the distorted tetrahedral and distorted T-shaped

CHAPTER 7

GENERAL INTRODUCTION ON THE ROLE OF COPPER IN MEDICINE

“The adult body contains between 1.4 and 2.1 mg of copper per kilogramme of body weight. Hence a healthy human weighing 60 kilogrammes contains approximately a tenth of one gramme of copper. However, this small amount is essential to the overall human well-being.”

Copper is a trace element essential for every living species. The key role plays by copper was found out in the early 30's when rats fed with a copper-deficient diet developed anemia. Also in humans, copper deficiency is primarily associated with the occurrence of anemia, bone abnormalities and altered immune system¹¹⁶. Copper is found in the active site of many proteins and enzymes, from microorganisms to human beings. The standard potential associated to its redox reactions $\text{Cu(I)}/\text{Cu(II)}$ is accessible even inside a biological system, where the pH must stay close to 7. This gives copper the ability to cycle between its two redox states, +1 and +2, and makes it an important redox active metal, like iron, commonly used in the redox centre of proteins. Consequently it is generally not used for structural functions, which are carried out mainly by zinc, a metal that shows only one available redox state (+2). The principal metalloproteins and metalloenzymes containing copper are cytochrome c oxidase, blue copper proteins, superoxide dismutase, catechol oxidase (tyrosinase), amine oxidase, ceruloplasmin, metallothionein and albumine. Cytochrome c oxidase is the last enzyme of the mitochondrial electron transfer cascade, where each O_2 molecule is reduced to H_2O by means of the oxidation of four cytochrome cs.

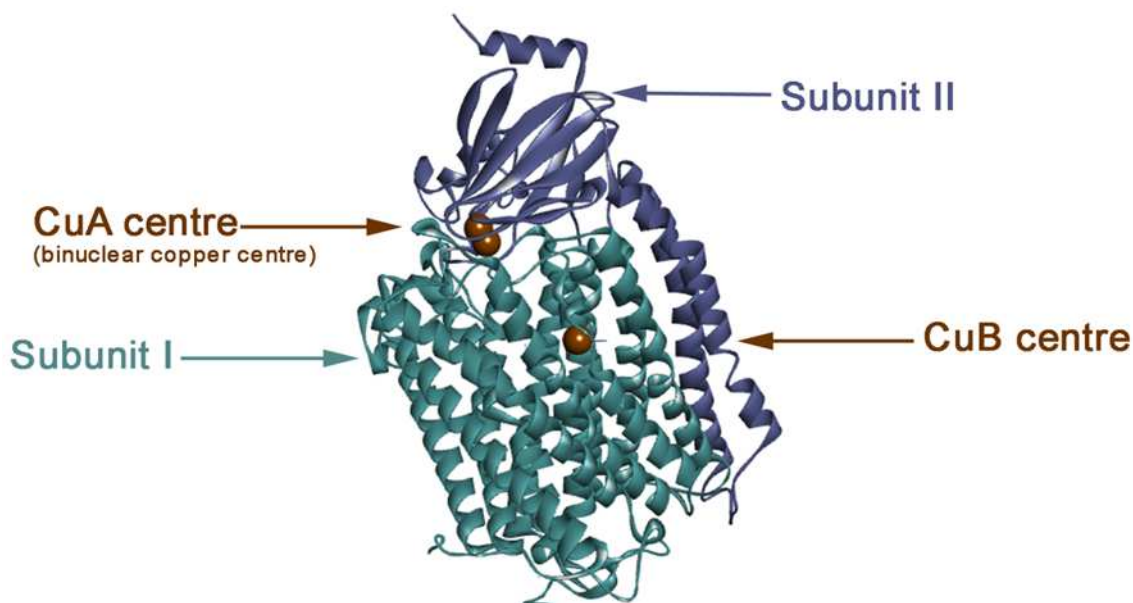


Figure 80. Catalytic core subunits I and II of cytochrome c oxidase from *Rhodobacter sphaeroides*². Copper atoms are represented as Wan der Waals spheres.

Blue copper proteins are a family of electron transfer proteins characterized by an intense blue color that are used for cellular respiration and photosynthesis by bacteria and plants.

The Cu/Zn superoxide dismutase (SOD) is the enzyme responsible of lowering the toxicity of the superoxide radical $\bullet\text{O}_2^-$ by promoting its disproportion into H_2O_2 and O_2 . The diffusion limited reaction occurs so quickly that SOD is the most efficient enzyme known. The active site of the enzyme consists in one Cu atom, which is the catalytic core, and in one Zn atom, which plays a structural role. The mechanism is a cycle in which the copper atom interacts with superoxide O_2^- both in the oxidized form Cu(II) and in the reduced form Cu(I) yielding O_2 and H_2O_2 ¹¹⁷.

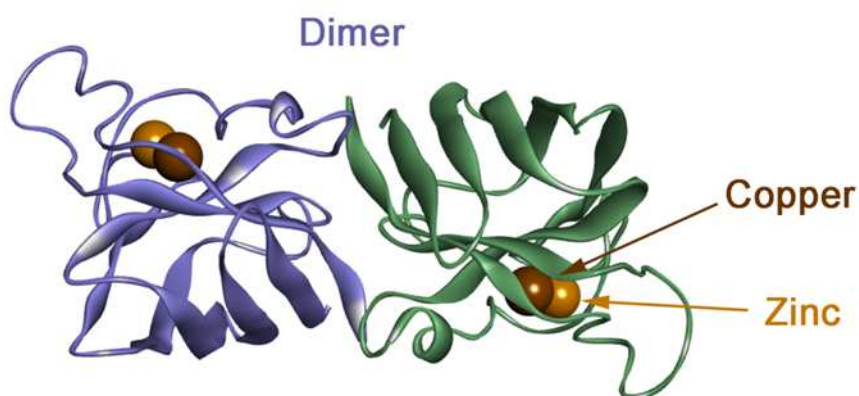


Figure 81. Crystal structure of homo sapiens Cu/Zn SOD¹¹⁸. Copper atoms are colored in brown and zinc atoms in grey.

After its absorption in the small intestine, copper is immediately bound to different plasmatic proteins (albumine and transcuprein) through which it reaches the liver. Albumine is a common transporter of spare copper atoms, since it holds high-affinity binding sites for Cu(II), with a total $\log\beta$ of 11-13, and it is contained in the plasma in concentration close to 0.6 mM. Albumin can carry up to 35% of the total copper present in the blood. Once inside the liver, copper is used for the synthesis of ceruloplasmin, a blue copper oxidase implicated in the oxidation of Fe(II) to Fe(III), which keeps copper tightly bound and brings it to other tissues. Ceruloplasmin holds about 65% of the plasma copper and it is fundamental for delivering copper to tissues. Whereas albumin and transcuprein provide labile bonds with copper and can exchange it anytime in the plasma, ceruloplasmin holds it irreversibly until specific receptors on the cell surface bind the holo-ceruloplasmin, inducing conformational changes that release copper. In order to cross the cellular membrane Cu(II) must be reduced to Cu(I), which is achieved through cuprioreductase. The specific transport protein that delivers copper into the cytoplasm is Ctr1. Here at least three different paths for copper exist¹: each of them is mediated by a specific transporter, the chaperon, that transport the metal to specific copper proteins. Cox17 transports copper to the mitochondria, CCs transports copper to SOD and Atox1 transfers copper to the Golgi network, where it can be involved in the synthesis of other cuproproteins or expelles from the cell. The latter task is fulfilled by two ATPases:

Atp7A, known as MNK for humans, and the other is the Atp7B, WND for humans. Atp7B is located only in hepatic cells and delivers copper to apo-ceruloplasmin¹¹⁹.

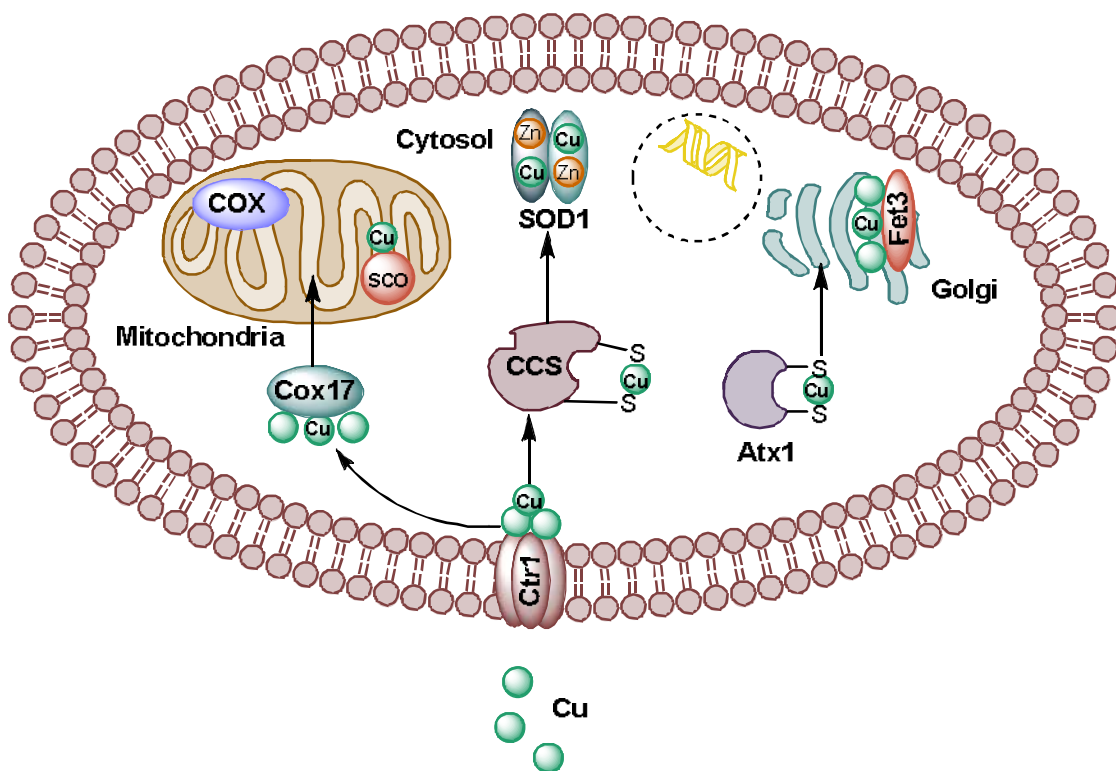
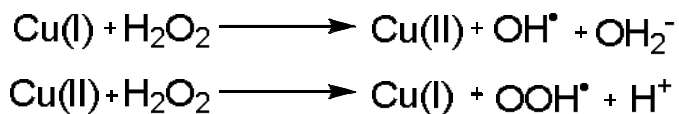


Figure 82. Known copper chaperons for mammalian cells¹²⁰.

Given the huge importance that copper shows into biological systems, its quantity inside organisms is strictly since copper, as iron, can promote formation of ROS (Reactive Oxygen Species) such as $\bullet\text{O}_2^-$, $\bullet\text{OH}$, $\bullet\text{OOH}$ and H_2O_2 , through the cycling between Cu(I)/Cu(II). This happens through the Fenton reaction¹²¹:



These radical species are toxic because they generate an oxidative stress that can damage proteins, nucleic acids and lipids. For this reason every aerobic organism is supplied with proteins like SOD and ceruloplasmin that can lower the concentration of ROS. The homeostasis of copper inside the cell is maintained by modulating its expulsion through transporters Atp7A and Atp7B or by higher expression of metallothioneins, a family of cystein-rich proteins associated with metal detoxification.

Two genetic diseases are correlated with incorrect copper homeostasis: Wilson disease and Menkes syndrome¹¹⁷. The first one comes from excessive quantities of the metal, due to disfunction of Atp7B (WND), which cannot export copper efficiently, leading to its over accumulation in the liver, brain and eyes, where it becomes noticeable in the irises. Consequences can be chronicle hepatitis, cirrhosis and neurological disturbs. On the other hand Menkes syndrome is determined by a severe deficiency in copper, derived from defects of the Atp7A (MNK), which lead to a poor absorption of the metal in the organism. A copper deficiency is correlated with a reduced activity of Cu-enzymes, which is fatal for brain development. Main effects are mental disorders and neurological degeneration.

The altered metabolism of cancer cells and the differential response between normal and tumor cell to copper load may open the way to the success of copper-based anticancer strategies. For this reason, copper complexes are the main source of putative copper anticancer drugs and the organic framework of these compounds (the ligand, L) is of crucial importance since it can modulate the targeting and the properties of the metal toxicity: as an example sulphur and phosphorous donor ligands stabilize Cu(I), whereas nitrogen and oxygen donor ligands stabilize preferentially Cu(II). Additionally, L greatly influence the lipophilic/hydrophilic nature of the resulting complex and it can determine its solubility in extracellular fluids as well as the ability to permeate the bilayer lipid membrane. Copper is an essential cofactor for tumor growth dynamics, because it is known to be associated to angiogenesis. Angiogenesis is the process by which new blood vessels are generated. Any kind of tissue requires copper to grow, but this is especially true for tumoral tissues, because of their fast rate of expansion. Owing to the accelerated and defective metabolism of cancer cells, a state of hypoxia is typical for them. The construction of more blood vessels in order to keep up with oxygen demand makes cancer cells richer in copper than normal cells This point is a valuable weapon against

tumor cells, making them more sensitive to any variation in copper concentration. There are mainly three ways of attacking cancer cells with copper complexes that have been investigated:

- formation of ROS species *in situ*, damaging the DNA;
- chelation and reduction of the copper content in the cell;
- inhibition of the 20S proteasome activity.

The first strategy is intended to bring copper complexes inside the cell that can induce oxidative damages to DNA, lipids or proteins of the unwanted cell. Due to the fast vital cycle of these cells, they can be less resistant to modifications and damages rather than normal cells; this weakness is already exploited by other antitumoral agents, one among all being cisplatin¹²² which is able to strongly interact with DNA and irreversibly alter its structure and function.

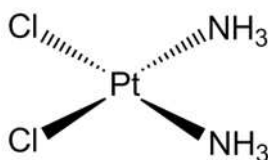


Figure 83: Molecular structure of *cis*-diamminedichloroplatinum(II), known as Cisplatin

Cytotoxicity of ROS producing complexes is usually decreased by introduction of antioxidants like vitamin C or E, and might be also related to an increased oxidation of endogeneous glutathione (GSH), leading to its deficiency in the cell. GSH is a gly-cys-glu tripeptide that is present in millimolar quantities inside cells and determines the maintenance of a reducing cytosol environment^{123,124}. As part of the intracellular defence against oxidative stress, the cysteine residue of GSH is oxidized to disulfide forming oxidized-GSH (GSSG) in presence of oxidizing agents. One of the mechanisms that scavenges hydrogen peroxide inside cells involves the enzyme glutathione

peroxidase¹²⁵ that catalyze the reaction: $2\text{GSH} + \text{H}_2\text{O}_2 \rightarrow \text{GSSG} + 2\text{H}_2\text{O}$. GSSG can be converted back to glutathione by the enzyme glutathione reductase that employs a mole of NADPH per mole of GSH produced. In addition, given the high affinity of thiol groups for Cu(I) and considering the high GSH concentration into the cytosol, GSH has also the role of an intracellular copper chaperon.

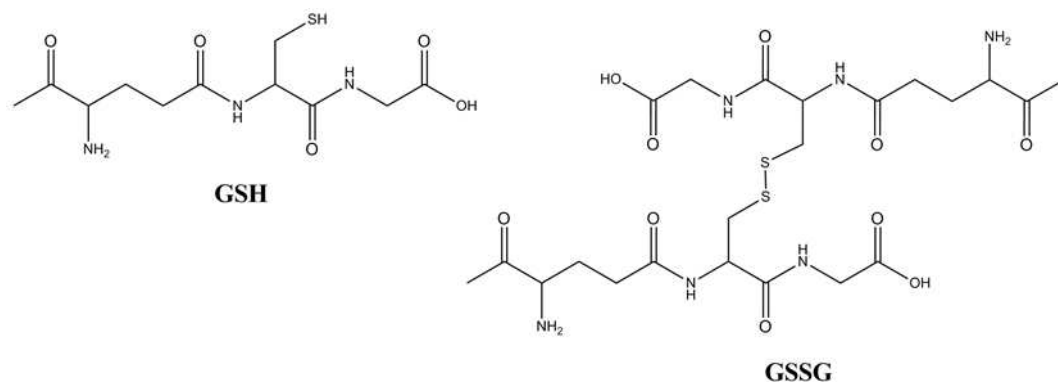


Figure 84. Glutathione (GSH) and oxidized glutathione (GSSG)

An interesting Cu(II) complex reported to be cytotoxic by formation of reactive oxygen species is 1,10-phenanthroline¹²⁶ (Figure 85). It is supposed to act as an intercalating agent that brings the redox active metal close to the DNA, producing toxic species *in situ*¹²⁷. In support of this mechanism is the fact that chelating agents that can remove copper from the ligand and other divalent metals that can compete with copper to bind 1,10-phenanthroline significantly decrease the toxicity of the complex.

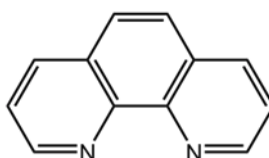


Figure 85. Schematic structure of 1,10-phenanthroline.

The second strategy is based on the sequestration of the essential element from cancer cells using chelating ligands with high affinity for copper. The main target is the decrease of the blood vessels formation which then lowers the rate of tumor growth. Chelating agents used for treatment of Wilson's disease such as D-penicillamine (**a**) or tetrathiomolybdate (**b**), TM, have been successfully used as anticancer agents¹²⁷. In addition, the synthesis of essential copper proteins and their mechanism of action are also affected by sequestering agents. The tetrathiomolybdate based ligand ATN-224 (**c**) has proven to act as a SOD1 inhibitor in multiple myeloma cell line MM1S, causing the accumulation of H₂O₂ with correlated increase of oxidative stress¹²⁸ and eventually cellular death.

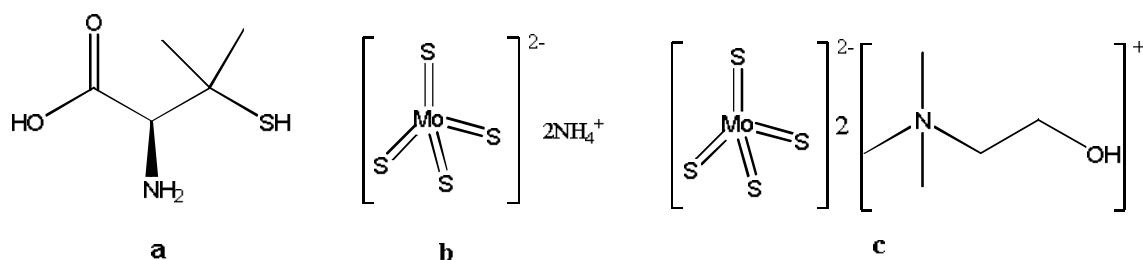


Figure 86. Schematic structures of D-penicillamine, TM and ATN-224.

The last strategy has recently provided a great number of potential antitumor agents, that act as inhibitors of the chymotrypsin-like activity of 20S proteasome. The proteasome is a multicatalytic protease responsible of the degradation of damaged or misfolded proteins. These proteins are first tagged by ubiquitine, which serves as a marker for defective proteins, and are then dismantled in (at least) three ways: with cleavage after basic residues ("trypsin-like" mechanism), with cleavage after acidic residues ("caspase-like") or with cleavage after hydrophobic residues ("chymotrypsin-like"). The activity of proteasome is implicated in normal cellular processes and its inhibition has proven to be able to induce death by apoptosis in tumoral cells, but not in normal cells, which are less sensitive to apoptosis-inducing stimuli^{21,22}. A few ligands that have been found to inhibit proteasome leading to apoptosis when complexed with copper are **d**²³ (2,4-diiodo-6-((pyridine-2-ylmethylamino)methyl)-phenol), **e**²⁴ (quinoline-2-thiosemicarbazone) and **f**²⁵ (neocuproine = 2,9-dimethyl-

1,10-phenanthroline). It was also investigated how the oxidation number of copper affects proteasome inhibition; it appears that, even though both Cu(I) and Cu(II) are active, Cu(I) is more efficient in inhibiting the protein. Moreover, Cu(I) complex of **f** is more cytotoxic because of higher concentrations of ROS formed; the toxicity caused by H₂O₂ is reduced using radical scavengers, which do not seem though to lower proteasome inhibition activity and the successive cell death.

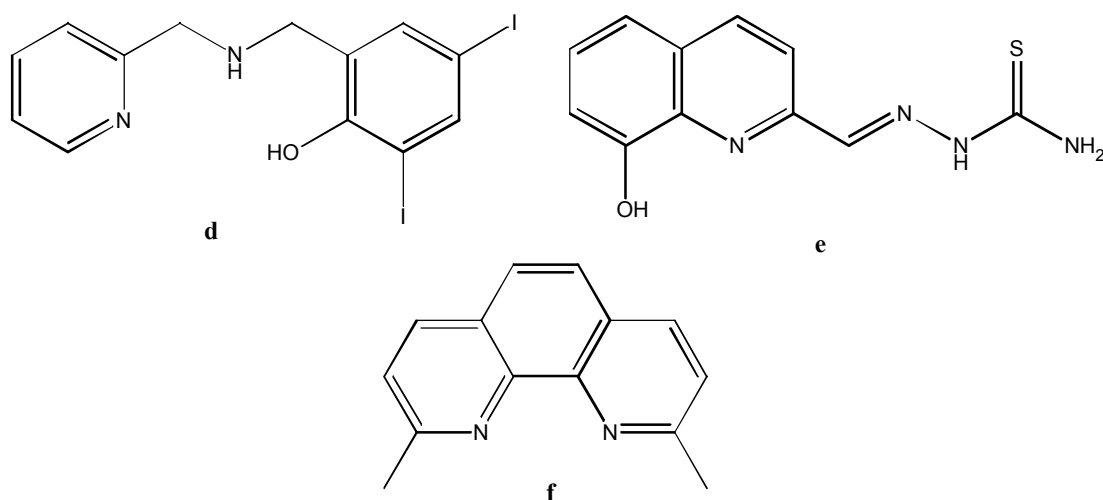
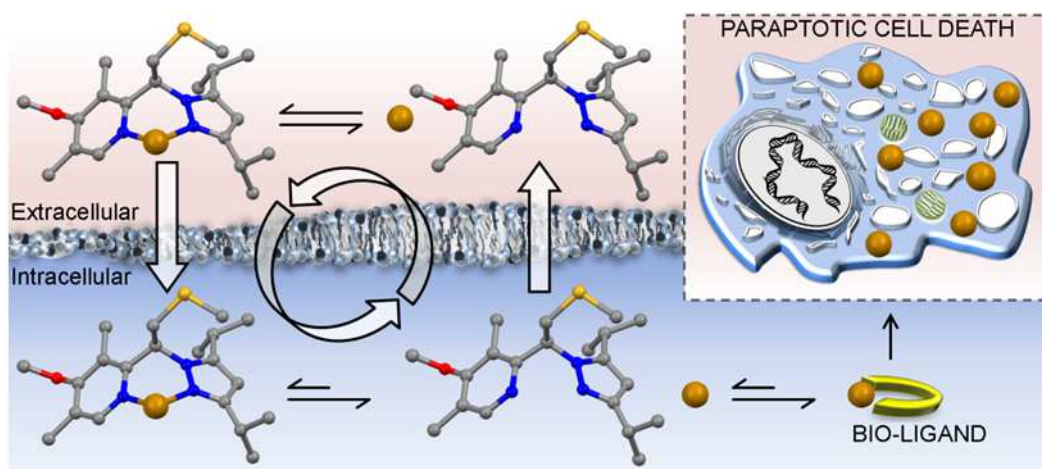


Figure 87. Previously reported ligands whose Cu(II) complexes can inhibit proteasome.

Another important aspect that deserves particular attention concerning Cu complexes is their stability, that it roughly related to the strength of the Cu-L association¹²⁹. In fact, coordination competitors such as aminoacids and proteins (albumin and transcuprein), largely present in the extracellular environment, can dislocate the ligand in complexes that are characterized by small stability. In this case the effect of a given CuL complex may be associated to an increase of the extracellular copper concentration bound to biomolecules, instead of deriving from the CuL entity. On the other hand, a complex characterized by a high stability will difficultly release copper in biological fluids (intra- and extra-cellular) and its activity will be ascribed to the chemical properties of the complex.

CHAPTER 8

Copper complexes with N_2 and N_2S donor ligands: from caspase inhibition to paraptotic cell death in human cancer cells



In this chapter we present a structure-activity relationship study¹³⁰ of new classes of pyrazole-pyridine copper complexes that establishes a clear correlation between the ability to promote copper accumulation and cytotoxicity. Intracellular metal accumulation is maximized when ligand lipophilicity allows the complex to rapidly cross the membrane. Copper and ligand follow different uptake kinetics and reach different intracellular equilibrium concentrations. These results support a model in which the ligand acts as an ionophore for the metal ion, cycling between intra- and extracellular compartments as dissociated or complexed entities. When treating cancer cells with structurally unrelated disulfiram and pyrazole-pyridine copper complexes, as well as with inorganic copper, the same morphological and molecular changes were reproduced, indicating that copper overload is responsible for the cytotoxic effects. Copper-based treatments drive sensitive cancer cells toward paraptotic cell death, a process hallmarked by endoplasmic reticulum stress and massive vacuolization in the absence of apoptotic features.

8.1 Introduction

Metal complexes have been investigated in recent decades as potential anticancer compounds, largely due to the success of cisplatin. This compound, one of the most widely employed chemotherapeutic agents, has had a major impact on the treatment of several tumor types, especially for testicular and ovarian cancers.¹³¹ The efforts of synthetic chemistry to provide novel anticancer agents have focused on low-toxicity platinum-based and non-platinum-based drugs with alternative mechanisms of action. Regarding the latter, ruthenium,¹³² gold,¹³³ and titanium have been investigated as candidates for the production of anticancer compounds. In all of these cases, ligands that are able to modulate metal ion reactivity and toxicity may contribute to a successful outcome. Copper is a fundamental component of metalloproteins because it exerts both catalytic and structural functions, and its distribution is strictly regulated at the levels of the cell, organ and body.^{134–136} In particular, copper is crucial to the angiogenic process that sustains tumor and metastasis development, and its sequestration underlies an anticancer strategy aimed at preventing establishment of the tumor blood supply.¹³⁷ Alternatively, copper complexes have shown anticancer activity, whereby the organic component (the ligand) is responsible for directing the metal to different molecular targets.¹³⁸

Although the majority of anticancer compounds trigger apoptosis, other types of programmed cell death (PCD) occur in response to common treatment regimens.^{139,140} Among the various types of PCD, paraptosis, characterized by the occurrence of large cytoplasmic vacuoles derived from the endoplasmic reticulum (ER),¹⁴¹ was observed in cancer cells treated with different copper complexes.^{142,143} To understand the structural basis of these effects, we prepared and screened a series of pyrazole-pyridine and bis-pyrazole copper complexes for cytotoxicity. The effects of the most active compound were compared with those of inorganic copper and disulfiram, a copper-interacting drug with promising anticancer properties.¹⁴⁴ The results showed that *a*) the copper complexes induce paraptosis as a function of their ability to cause intracellular copper accumulation, *b*) the metal itself is sufficient to produce paraptotic features in cancer cells (provided that high doses are used).

8.2. Experimental

8.2.1. Synthesis of ligands (L36-L55) and copper complexes (36-55).

General Procedures. All reagents and solvents were commercially available, except for 3,5-dimethylpyrazole, 3,5-diisopropylpyrazole, 3,5-ditertbutylpyrazole, 2-(phenylthio)benzaldehyde¹⁴⁵, 2-(phenylthio)acetaldehyde¹⁴⁶, bis(pyrazolyl)ketone, bis(3,5-dimethylpyrazolyl)ketone, bis(3,5-diisopropylpyrazolyl)ketone⁴⁴⁻⁴⁶, which were prepared as reported elsewhere. The synthesis of the ligands **L36** **L41**, **L45**^{147,148}, **L46**, and **L47**¹⁴⁹ was performed as previously reported. The synthesis of **L50-L54** are reported in chapter 2, 3 and 4 respectively. Tetrahydrofuran (THF) were distilled over Na/benzophenone. The syntheses of the **L36-L55** ligands were performed in inert gas (N₂) using Schlenk techniques. ¹H and ¹³C NMR spectra were recorded on a Bruker Avance 300 spectrometer using standard Bruker pulse sequences. Chemical shifts are reported in parts per million (ppm) referenced to residual solvent protons. Infrared spectra were recorded from 4000 to 700 cm⁻¹ on a Perkin-Elmer FTIR Nexus spectrometer equipped with a Smart Orbit HATR accessory (diamond crystal). Elemental analyses (C, H, and N) were performed with a Carlo Erba EA 1108 automated analyzer.

*Synthesis of 2-[(3,5-dimethyl-1H-pyrazol-1-yl)methyl]-4-methoxy-3,5-dimethylpyridine (**L37**).* 2-Chloromethyl-4-methoxy-3,5-dimethylpyridine hydrochloride (9.20 g, 41.42 mmol) and 3,5-dimethylpyrazole (3.98 g, 41.42 mmol) were mixed in toluene (100 ml). After adding NaOH (40% in water, 40 ml) and 30 drops of *n*-tetrabutylammonium hydroxide (40% in water) the mixture was refluxed 4 h with stirring. The organic phase was separated from the aqueous one, washed with water (20 ml), dried with anhydrous Na₂SO₄ and filtered. The solvent was removed under vacuum and a white powder was collected (yield 9.90 g, 85%). IR (cm⁻¹) : 2999w, 2954w, 2918w, 2225w br, 2048w br, 2031w br, 1590w, 1551m, 1473m, 1395m, 1382m, 1345m, 1318w, 1290m, 1264m, 1238m, 1216m, 1186w, 1129w, 1066s, 1027m, 993s, 904m, 867w, 820m, 771s, 722m, 663w, 637w, 623w, 580w, 516w, 502w, 467w. ¹H NMR (300 MHz, CDCl₃): δ, 2.19 (s, 3H, CH₃), 2.21 (s, 3H, CH₃), 2.23 (s, 3H, CH₃), 2.24 (s, 3H, CH₃), 3.75 (s, 3H, OCH₃), 5.32 (s, 2H, CH₂), 5.81 (s, 1H, CH Pz), 8.18 (s, 1H, CH Py). *Anal.* Calc. for C₁₄H₁₉N₃O (245.32): C, 68.54; H, 7.81; N, 17.13. Found: C, 68.31; H, 7.76; N, 16.99%.

Synthesis of 2-[(3,5-Diisopropyl-1H-pyrazol-1-yl)methyl]-4-methoxy-3,5-dimethylpyridine (L38). 2-Chloromethyl-4-methoxy-3,5-dimethylpyridine hydrochloride (5.83 g, 26.27 mmol) and 3,5-diisopropylpyrazole (4.00 g, 26.27 mmol) were mixed in toluene (100 ml). The procedure is analogous to that reported for **L37**, giving a yellow oil (yield 7.11 g, 89%). IR (cm⁻¹): 2960m, 2869m, 2158w br, 1588m, 1566m, 1542m, 1470m, 1381m, 1369m, 1362m, 1347m, 1290m, 1255m, 1223m, 1179m, 1093s, 1031m, 1000s, 978m, 911w, 867w, 808w, 784s, 720w, 683w, 646w, 618w, 561w, 522w, 450w. ¹H NMR (300 MHz, CDCl₃): δ, 1.10 (d, 6H, CH₃ i-Pr), 1.27 (d, 6H, CH₃ i-Pr), 2.22 (s, 3H, CH₃ Py), 2.28 (s, 3H, CH₃ Py), 2.93 (m, 2H, CH i-Pr), 3.69 (s, 3H, OCH₃), 5.38 (s, 2H, CH₂), 5.85 (s, 1H, CH Pz), 8.15 (s, 1H, CH Py). *Anal.* Calc. for C₁₈H₂₇N₃O (301.43): C, 71.72; H, 9.03; N, 14.94. Found: C, 71.55; H, 8.89; N, 14.67%.

Synthesis of 2-[(3,5-Di-tert-butyl-1H-pyrazol-1-yl)methyl]-4-methoxy-3,5-dimethylpyridine (L39). 2-Chloromethyl-4-methoxy-3,5-dimethylpyridine hydrochloride (2.51 g, 11.30 mmol) and 3,5-ditertbutylpyrazole (2.04 g, 11.32 mmol) were mixed in toluene (50 ml). The procedure is analogous to that reported for **L37**, but the crude product was purified by silica column chromatography (hexane/ethyl acetate 80:20, r.f. 0.25; yield 2.29 g, 62%). IR (cm⁻¹): 2964m, 2898m, 2865m, 1567m, 1539m, 1457m, 1391m, 1249m, 1227m, 1180s, 1008s, 957m, 909w, 789s, 717m. ¹H NMR (300 MHz, CDCl₃): δ, 1.23 (s, 9H, CH₃ t-Bu), 1.31 (s, 9H, CH₃ t-Bu), 2.09 (s, 3H, CH₃ Py), 2.25 (s, 3H, CH₃ Py), 3.75 (s, 3H, OCH₃), 5.53 (s, 2H, CH₂), 5.90 (s, 1H, CH Pz), 8.18 (s, 1H, CH Py). *Anal.* Calc. for C₂₀H₃₁N₃O (329.48): C, 72.90; H, 9.48; N, 12.75. Found: C, 72.86; H, 9.25; N, 12.35%.

Synthesis of 2-[(3,5-Diphenyl-1H-pyrazol-1-yl)methyl]-4-methoxy-3,5-dimethylpyridine (L40). 2-Chloromethyl-4-methoxy-3,5-dimethylpyridine hydrochloride (3.60 g, 16.21 mmol) and 3,5-diphenylpyrazole (3.57 g, 16.20 mmol) were mixed in toluene (50 ml). The procedure is analogous to that reported for **L37**, and a white powder was obtained (yield 2.70 g, 42%). IR (cm⁻¹): 3043w, 2956w, 2162w br, 2052w br, 1892w br, 1605w, 1567w, 1546w, 1486m, 1476m, 1463w, 1440m, 1395m, 1369w, 1349w, 1290m, 1261m, 1237m, 1218w, 1193w, 1147w, 1090m, 1028w, 1000m, 957m, 919w, 907w, 863w, 823w, 792w, 776m, 766m, 749m, 694s, 670m, 647w, 578m, 547m, 529w, 517w, 502w, 471w, 432w. ¹H NMR (300 MHz, CDCl₃): δ, 2.14 (s, 3H, CH₃ Py), 2.17 (s, 3H, CH₃ Py), 3.76 (s, 3H, OCH₃), 5.45 (s, 2H, CH₂), 6.65 (s, 1H, CH Pz), 7.16-7.83(m, 10H, CH Ph), 8.17 (s, 1H, CH Py). *Anal.* Calc. for C₂₄H₂₃N₃O (369.46): C, 78.02; H, 6.27; N, 11.37. Found: C, 77.97; H, 6.05; N, 11.21%.

Synthesis of 4-methoxy-3,5-dimethyl-2-[2-(methylthio)-1-(1H-pyrazol-1-yl)ethyl]pyridine (L42). A solution of 2-(pyrazolylmethyl)-4-methoxy-3,5-dimethylpyridine (0.97 g, 4.46 mmol) in THF (50 ml) was cooled to -78 °C, and then n-BuLi (3.2 ml, 1.6 M in hexane, 5.12 mmol) was slowly added. After stirring the red solution at -78 °C for 45 min, chloromethyl methyl sulfide (0.44 ml, d = 1.17 g/ml, 5.33 mmol) was added. The solution was allowed to warm to room temperature and stirred overnight. The clear yellow solution was then dried under vacuum and the residual solid was treated with diethyl ether/water (40 ml/15 ml). The organic phase was separated and washed with brine and dried with anhydrous Na₂SO₄. The solvent was removed under vacuum, giving a yellow oil that was purified by silica column chromatography (hexane:ethyl acetate 70:30; r.f. 0.2), affording a colourless oil (yield 0.54 g, 30%) IR (cm⁻¹): 2917w, 1992w br, 1566m, 1509w, 1472m, 1393m, 1290m, 1261m, 1224m, 1082m, 1026m, 999m, 961m, 917w, 880w, 849w, 822w, 748s, 655w, 621m, 597w, 532w, 439w, 412w. ¹H NMR (300 MHz, CDCl₃): δ, 2.06 (s, 3H, CH₃), 2.31 (s, 3H, CH₃), 2.37 (s, 3H, SCH₃), 3.46 (dd, J₁ = 6.9 Hz, J₂ = 6.9 Hz, 1H, CH₂), 3.54 (dd, J₁ = 7.8 Hz, J₂ = 5.6 Hz, 1H, CH₂), 3.70 (s, 3H, OCH₃), 5.85 (t, J = 7.5 Hz, 1H, CH_{central}), 6.20 (t, J = 2.1 Hz, 1H, CH Pz), 7.46 (d, J = 1.5 Hz, 1H, CH Pz), 7.51 (d, J = 2.1 Hz, 1H, CH Pz), 8.27 (s, 1H, CH Py). *Anal.* Calc. for C₁₄H₁₉N₃SO (277.39): C, 60.62; H, 6.90; N, 15.15. Found: C, 60.56; H, 6.79; N, 15.01%.

Synthesis of 2-[1-(3,5-dimethyl-1H-pyrazol-1-yl)-2-(methylthio)ethyl]-4-methoxy-(3,5-dimethyl)pyridine (L43). The same procedure used to prepare **L42** was applied by using 2-(3,5-dimethylpyrazolylmethyl)-4-methoxy-3,5-dimethylpyridine (2.79 g, 9.89 mmol), n-BuLi (7.30 ml, 1.6 M in hexane, 11.68 mmol) and chloromethyl methyl sulfide (0.96 ml, d = 1.17 g/ml, 11.63 mmol). After purification by silica column chromatography (hexane: ethyl acetate 50:50, r.f. 0.48) a colourless oil was obtained (yield 1.41 g, 41%) . IR (cm⁻¹): 2922m, 2287w, 2198w, 2185w, 2161w, 2138w, 2051w, 1980w, 1861w, 1587m, 1565m, 1548m, 1478m, 1457m, 1422m, 1394m, 1372m, 1331m, 1303m, 1267m, 1254m, 1241m, 1205m, 1147w, 1110w, 1087m, 1038m, 1018m, 995s, 934m, 899m, 885m, 821s, 785s, 751m, 713w, 698m, 666w, 643w, 613m, 601m, 592m, 540m, 512m, 502m, 424m. ¹H NMR (300 MHz, CDCl₃): δ, 2.13 (s, 3H, CH₃), 2.15 (s, 3H, CH₃), 2.20 (s, 6H, 2CH₃), 2.28 (s, 3H, SCH₃), 3.45 (dd, J₁ = 7.5 Hz, J₂ = 6.6 Hz, 1H, CH₂), 3.65 (dd, J₁ = 7.5 Hz, J₂ = 6.6 Hz, 1H, CH₂), 3.76 (s, 3H, OCH₃), 5.72 (t, 1H, CH_{central}), 5.78 (s, 1H, CH Pz), 8.33 (s, 1H, CH Py). *Anal.* Calc. for C₁₆H₂₃N₃SO (305.44): C, 62.92; H, 5.24; N, 13.75. Found: C, 62.76; H, 5.08; N, 13.36%.

Synthesis of 2-[1-(3,5-diisopropyl-1H-pyrazol-1-yl)-2-(methylthio)ethyl]-4-methoxy-(3,5-dimethyl)pyridine (L44). The same procedure used to prepare **L42** was applied by

using 2-(3,5-diisopropylpyrazolylmethyl)-4-methoxy-3,5-dimethylpyridine (8.40 g, 27.87 mmol), n-BuLi (20 ml, 1.6 M in hexane, 32.00 mmol) and chloromethyl methyl sulfide (2.8 ml, d = 1.17 g/ml, 33.92 mmol). After purification by silica column chromatography (hexane: ethyl acetate 50:50) a yellow oil was obtained (yield 5.55 g, 55%). IR (cm^{-1}): 2961m, 2925m, 2867m, 2166w, 2050w, 2036w, 1983w, 1585m, 1563m, 1542m, 1470m, 1393m, 1380m, 1361m, 1289m, 1262m, 1244m, 1177m, 1078m, 1025m, 997s, 908m, 880m, 822m, 786m, 759m, 720m, 625m, 598m, 549m, 501m, 431m. ^1H NMR (300 MHz, CDCl_3): δ , 0.88 (d, J = 6.75 Hz, 3H, CH_3 i-Pr), 1.09 (d, J = 6.75 Hz, 3H, CH_3 i-Pr), 1.20 (dd, J_1 = 2.5 Hz, J_2 = 4.3 Hz, 6H, CH_3 i-Pr), 1.99 (s, 3H, CH_3 Py), 2.07 (s, 3H, CH_3 Py), 2.24 (s, 3H, SCH_3), 2.95 (m, J = 4.9 Hz, 2H, CH i-Pr), 3.35 (dd, J_1 = 7.08 Hz, J_2 = 6.5 Hz, 1H, CH_2), 3.66 (m, 1H, CH_2 overlapped by OCH_3), 3.67 (s, 3H, OCH_3), 5.72 (t, J = 7.26 Hz, 1H, $\text{CH}_{\text{central}}$), 5.83 (s, 1H, CH Pz), 8.27 (s, 1H, CH Py). *Anal.* Calc. for $\text{C}_{20}\text{H}_{31}\text{N}_3\text{SO}$ (361.54): C, 66.44; H, 8.64; N, 11.62. Found: C, 66.13; H, 8.49; N, 11.36%.

Synthesis of bis(3,5-diisopropyl-1H-pyrazol-1-yl)methane (L48). A mixture of 3,5-diisopropylpyrazole (0.51 g, 3.35 mmol), NBu_4HSO_4 (0.05 g, 0.13 mmol), NaOH (50% in water, 4 ml) and dichloromethane (10 ml) was refluxed overnight. The organic phase was separated from the aqueous one, which was washed with diethyl ether (20 ml). The organic phases were mixed together, dried with anhydrous Na_2SO_4 and filtered. The solvent was removed under vacuum and a yellow oil was obtained (yield 0.39 g, 37%). IR (cm^{-1}): 3227m, 2964m, 2931m, 2871w, 2158w, 1561m, 1457m, 1419w, 1380m, 1353m, 1315w, 1260m, 1221m, 1156m, 1139m, 1035w, 1008m, 947m, 882w, 849m, 800s, 772m, 728m, 668m, 624m, 591w, 531w, 456m. ^1H NMR (300 MHz, CDCl_3): δ , 1.12 (d, J = 6.9 Hz, 12 H, CH_3 i-Pr), 1.20 (d, J = 6.9 Hz, 12 H, CH_3 i-Pr), 2.91 (m, J = 6.9 Hz, 2H, CH i-Pr), 3.42 (m, J = 6.9 Hz, 2H, CH i-Pr), 5.86 (s, 2H, CH Pz), 6.26 (s, 2H, CH_2). *Anal.* Calc. for $\text{C}_{19}\text{H}_{32}\text{N}_4$ (316.48): C, 72.11; H, 10.19; N, 17.70. Found: C, 72.03; H, 10.07; N, 17.38%.

Synthesis of bis(3,5-di-tert-butyl-1H-pyrazol-1-yl)methane (L49) The same procedure used to prepare **L48** was applied by using 3,5-ditertbutylpyrazole (2.00 g, 11.11 mmol), NBu_4HSO_4 (0.18 g, 0.50 mmol), NaOH (50% in water, 4 ml) and dichloromethane (20 ml). A colourless oil was obtained (yield 2.38 g, 58%). IR (cm^{-1}): 2962m, 2924m, 2866m, 2051w, 1997w, 1542m, 1461m, 1397w, 1361w, 1371s, 1257m, 1228s, 1205m, 1134w, 1085w, 1067w, 1022w, 999m, 967m, 930w, 842w, 800s, 773m, 727m, 686m, 624w, 611w, 551w, 501w, 450w. ^1H NMR (300 MHz, CDCl_3): δ , 1.21 (s, 18 H, CH_3 t-Bu), 1.25 (s, 18 H, CH_3 t-Bu), 5.91 (s, 2H, CH_2), 6.52 (s, 2H, CH

Pz). *Anal.* Calc. for $C_{23}H_{40}N_4$ (372.59): C, 74.14; H, 10.82; N, 15.04. Found: C, 73.99; H, 10.67; N, 14.88%.

Synthesis of 1,1'-(2-(phenylthio)ethane-1,1-diyl)bis(3,5-diisopropyl-1H-pyrazole)(L55). A mixture of bis(3,5-diisopropylpyrazolyl)ketone (0.77 g, 2.34 mmol), 2-(phenylthio)acetaldehyde (0.36 g, 2.34 mmol) and $CoCl_2 \cdot 6H_2O$ (5 mg) was heated at 80°C for an hour with stirring. The mixture was then cooled at room temperature and stirred overnight. Dichloromethane (30 ml) was added and the mixture was stirred for 30 minutes. The organic phase was washed with water (50 ml) and brine (20 ml), dried with anhydrous Na_2SO_4 and filtered. The solution was concentrated under vacuum and a yellow powder was precipitated with hexane, which was filtered and vacuum dried. The solvent was removed under vacuum and the crude was purified by silica column chromatography (hexane: ethyl acetate 95:5, r.f. 0.22) and a dark green oil was obtained (yield 0.30 g, 29%). IR (cm^{-1}): 2972m, 2932m, 2868w, 1665w, 1546m, 1473m, 1459w, 1331w, 1315m, 1260w, 1178w, 1064m, 1016m, 931w, 808s, 750m, 701m, 652w, 557w. 1H NMR (300 MHz, $CDCl_3$): δ , 0.86 (d, J = 6.9 Hz, 12 H, CH_3 i-Pr), 1.26 (d, 12 H, CH_3 i-Pr), 2.91 (m, J = 6.9 Hz, CH i-Pr), 3.21 (m, 2H, CH i-Pr), 4.09 (d, J = 7.2 Hz, 2H, CH_2) 5.84 (s, 2H, CH Pz), 6.59 (t, J = 7.2 Hz, 1H, $CH_{central}$), 7.16-7.24 (m, 3H, CH Ph), 7.36 (d, 2H, CH Ph). *Anal.* Calc. for $C_{26}H_{38}N_4S$ (438.67): C, 71.19; H, 8.73; N, 12.77. Found: C, 70.99; H, 8.66; N, 12.39%.

Synthesis of $[CuCl_2(L36)]_2$ (36). A pale green solution of $CuCl_2 \cdot 2H_2O$ (139 mg, 0.82 mmol) in 3 ml of methanol was added to a colourless solution of **L36** (206 mg, 0.82 mmol) in 3 ml of methanol. A green precipitate immediately formed, which was filtered, washed with methanol and vacuum dried (yield 140 mg, 44%). IR (cm^{-1}): 3139w, 3128w, 3095w, 3024w, 2964w, 2962w, 1600w, 1572m, 1517w, 1470m, 1428m, 1402s, 1277m, 1257s, 1161w, 1087s, 1072s, 993s, 881w, 757s, 646w, 606w. *Anal.* Calc. for $C_{12}H_{15}N_3OCuCl_2$ (335.72): C, 42.93; H, 4.50; N, 12.52. Found: C, 42.46; H, 4.28; N, 12.48%.

Synthesis of $[CuCl_2(L37)]_2$ (37). A pale green solution of $CuCl_2 \cdot 2H_2O$ (123 mg, 0.70 mmol) in 3 ml of methanol was added to a colourless solution of **L37** (204 mg, 0.71 mmol) in 3 ml of methanol yielding a dark green solution. The solvent was then concentrated under vacuum and a bright green solid was precipitated after addition of diethyl ether. The precipitate was filtered and vacuum dried (yield 125 mg, 42%). IR (cm^{-1}): 3123w, 3083w, 3016w, 2919w br, 2219w br, 2010w br, 1593m, 1574m, 1554m, 1470m, 1437m, 1419m, 1397m, 1351m, 1291m, 1258s, 1207w, 1161w, 1135w, 1091m, 1058m, 1033m, 999m, 939w, 880m, 835m, 815m, 789m, 767m,

717m, 645m, 569m, 530w, 476w. *Anal.* Calc. for $C_{28}H_{38}Cl_4Cu_2N_6O_2$ (759.54): C, 44.28; H, 5.04; N, 11.06. Found: C, 44.06; H, 4.88; N, 10.97%.

Synthesis of $[CuCl_2(L38)]_2$ (38). A pale green solution of $CuCl_2 \cdot 2H_2O$ (115 mg, 0.67 mmol) in 3 ml of methanol was added to a colourless solution of **L38** (200 mg, 0.66 mmol) in 3 ml of methanol yielding a dark green solution. The solvent was then concentrated under vacuum and a green solid was precipitated after addition of diethyl ether. The solid was filtered and vacuum dried (yield 192 mg, 66%). IR (cm^{-1}): 3424m, 2964m, 2931w, 2860w, 1600w, 1545w, 1474m, 1435w, 1369w, 1282s, 1260s, 1079s, 1030s, 980s, 876w, 810m, 778m, 728w. . *Anal.* Calc. for $C_{38}H_{58}Cl_8Cu_2N_6O_2$ (1041.62): C, 42.82; H, 5.61; N, 8.06. Found: C, 42.68; H, 5.58; N, 7.89%.

Synthesis of $[CuCl_2(L39)]$ (39). A pale green solution of $CuCl_2 \cdot 2H_2O$ (84 mg, 0.49 mmol) in 3 ml of methanol was added to a colourless solution of **L39** (161 mg, 0.49 mmol) in 3 ml of methanol. A green precipitate immediately formed which was filtered, washed with methanol and vacuum dried (yield 148 mg, 52%). IR (cm^{-1}): 2966m, 2172w br, 2036w br, 1589m, 1536m, 1464m, 1428m, 1395m, 1371m, 1290m, 1258s, 1227m, 1134w, 1081s, 1030m, 986m, 975m, 929w, 883w, 810m, 802m, 771m, 727w, 697w, 618w, 520w, 460w. . *Anal.* Calc. for $C_{40}H_{62}Cl_4Cu_2N_6O_2$ (927.86): C, 51.78; H, 6.74; N, 9.06. Found: C, 51.57; H, 6.39; N, 9.01%.

Synthesis of $[CuCl_2(L40)]$ (40). A pale green solution of $CuCl_2 \cdot 2H_2O$ (73 mg, 0.43 mmol) in 3 ml of methanol was added to a colourless solution of **L40** (170 mg, 0.43 mmol) in 3 ml of methanol giving a dark green solution. The solvent was then concentrated under vacuum and a green solid was precipitated after addition of hexane. The solid was filtered and vacuum dried (yield 70 mg, 31%). IR (cm^{-1}): 3735w br, 2969w, 1735m, 1596m, 1576m, 1553m, 1463m, 1397m, 1378m, 1259m, 1217m, 1156m, 1085m, 1031m, 1014m, 981m, 920m, 879m, 825m, 758m, 697m, 583m, 566m, 526m, 430m, 419m. . *Anal.* Calc. for $C_{24}H_{23}Cl_2CuN_3O$ (503.91): C, 57.20; H, 4.60; N, 12.61. Found: C, 57.01; H, 4.28; N, 12.30%.

Synthesis of $[CuCl_2(L41)]$ (41). A pale green solution of $CuCl_2 \cdot 2H_2O$ (50 mg, 0.29 mmol) in 3 ml of methanol was added to a yellow solution of **L41** (92 mg, 0.27 mmol) in 3 ml of methanol yielding a dark brown solution. The solvent was then concentrated under vacuum and a green solid precipitated. The precipitate was filtered, washed with methanol and vacuum dried (yield 76 mg, 60%). IR (cm^{-1}): 3074w, 3008w, 2918w, 2167w br, 2020w br, 1598w, 1501w, 1478w, 1433m, 1359m, 1320w, 1294w, 1263m, 1228m, 1092m, 1070m, 975m, 956w, 904w, 887w, 791m, 765s, 690w, 573w. *Anal.*

Calc. for $C_{19}H_{21}Cl_2CuN_3OS$ (473.91): C, 48.15; H, 4.46; N, 8.87. Found: C, 48.03; H, 4.22; N, 8.55%.

Synthesis of $[CuCl_2(L42)]_2$ (42). A pale green solution of $CuCl_2 \cdot 2H_2O$ (125 mg, 0.73 mmol) in 5 ml of methanol was added to a colourless solution of **L42** (202 mg, 0.73 mmol) in 5 ml of methanol yielding a green precipitate, which was filtered, washed with methanol and vacuum dried (240 mg, 80%). IR (cm^{-1}): 3100m, 2901w, 2361w, 2341w, 1595w, 1569w, 1507w, 1477m, 1426m, 1409m, 1376m, 1333w, 1298m, 1267m, 1203m, 1164m, 1082m, 1070s, 1038m, 1018m, 995s, 920m, 903m, 883m, 829m, 774s, 755m, 729m, 709m, 681w, 658w, 614m, 532m, 470m. *Anal.* Calc. for $C_{28}H_{38}Cl_4Cu_2N_6O_2S$ (791.61): C, 42.48; H, 4.84; N, 10.62. Found: C, 42.25; H, 4.69; N, 10.35%.

Synthesis of $[CuCl_2(L43)]_2$ (43). A pale green solution of $CuCl_2 \cdot 2H_2O$ (80 g, 0.47 mmol) in 5 ml of methanol was added to a colourless solution of **L43** (160 mg, 0.47 mmol) in 5 ml of methanol yielding a green solution. The solvent was then concentrated under vacuum and a green solid was precipitated after addition of diethyl ether, which was filtered and vacuum dried (yield 130 mg, 58%). IR (cm^{-1}): 2922m, 2185w, 2161w, 2051w, 1980w, 1587m, 1565m, 1548m, 1478m, 1457m, 1422m, 1394m, 1372m, 1331m, 1303m, 1267m, 1084m, 1058m, 1032m, 1015m, 996s, 834m, 814m, 796m, 752m, 530m. *Anal.* Calc. for $C_{33}H_{50}Cl_4Cu_2N_6O_3S_2$ (911.82): C, 43.47; H, 5.53; N, 9.21. Found: C, 43.28; H, 5.36; N, 9.10%.

Synthesis of $[CuCl_2(L44)]_2$ (44). A pale green solution of $CuCl_2 \cdot 2H_2O$ (137 mg, 0.80 mmol) in 5 ml of methanol was added to a yellow solution of **L44** (292 mg, 0.81mmol) in 5 ml of methanol yielding a bright green solution. A green solid precipitated after 10 min, which was filtered, washed with methanol and vacuum dried (200 mg, 50%). IR (cm^{-1}): 2967m, 2927m, 2868m, 2324w, 2168w, 2051w, 1981w, 1592m, 1546m, 1473m, 1443m, 1409m, 1379m, 1367m, 1358m, 1344m, 1332m, 1304m, 1260s, 1182m, 1081m, 1058m, 1039m, 101m, 995s, 928m, 911m, 892m, 834m, 806m, 789m, 760m, 723m, 699w, 663w, 607m, 563w, 536m, 438w. *Anal.* Calc. for $C_{40}H_{62}Cl_4Cu_2N_6O_2S_2$ (991.99): C, 48.43; H, 6.30; N, 8.47. Found: C, 48.22; H, 6.16; N, 8.38%.

Synthesis of $[CuCl_2(L45)]$ (45). A pale green solution of $CuCl_2 \cdot 2H_2O$ (91 mg, 0.53 mmol) in 3 ml of methanol was added to a colourless solution of **L45** (201 mg, 0.50 mmol) in 3 ml of methanol yielding a dark green solution. The solvent was then concentrated under vacuum and a green solid precipitated. The solid was filtered, washed with

methanol and vacuum dried (208 mg, 78%). IR (cm^{-1}): 3083w, 2997w, 2924w, 2026w br, 1596w, 1573w, 1499w, 1474m, 1431m, 1366w, 1352m, 1299w, 1265m, 1234m, 1220m, 1134w, 1116w, 1084m, 1016m, 986m, 952m, 909w, 971w, 828m, 801w, 786w, 774s, 758m, 745m, 730w, 689w, 664w, 648w, 621w, 463m, 432m. *Anal.* Calc. for $\text{C}_{21}\text{H}_{25}\text{Cl}_2\text{CuN}_3\text{OS}_2$ (534.02): C, 47.23; H, 4.71; N, 7.87. Found: C, 47.14; H, 4.56; N, 7.51%.

Synthesis of $[\text{Cu}(\text{L46})_2][\text{CuCl}_4]$ (46). A pale green solution of $\text{CuCl}_2 \cdot 2\text{H}_2\text{O}$ (187 mg, 1.1 mmol) in 5 ml of methanol was added to a colourless solution of **L46** (163 mg, 1.1 mmol) in 5 ml of methanol yielding a green precipitate, which was filtered, washed with methanol and vacuum dried (160 mg, 51%). IR (cm^{-1}): 3350m, 3145w, 3106w, 2997w, 2953w, 2860w, 2158w, 1638w, 1463w, 1403m, 1279m, 1205w, 1059m, 989m, 785m, 761s, 729m, 644m, 499m. *Anal.* Calc. for $\text{C}_{14}\text{H}_{16}\text{Cl}_4\text{Cu}_2\text{N}_8$ (565.23): C, 29.75; H, 2.85; N, 19.82. Found: C, 29.38; H, 2.72; N, 19.44%.

Synthesis of $[\text{CuCl}_2(\text{L47})]$ (47). A pale green solution of $\text{CuCl}_2 \cdot 2\text{H}_2\text{O}$ (137 mg, 0.80 mmol) in 5 ml of methanol was added to a colourless solution of **L47** (163 g, 0.80 mmol) in 5 ml of methanol yielding a green precipitate, which was filtered, washed with methanol and vacuum dried (203 mg, 75%). IR (cm^{-1}): 3473w br, 3145w, 3123w, 2960w, 2860w, 2043w, 1556m, 1464m, 1418m, 1384m, 1276s, 1150w, 1041m, 1004w, 830m, 704w, 678m, 660w, 626w, 597w, 491w, 474w, 420w. *Anal.* Calc. for $\text{C}_{22}\text{H}_{38}\text{Cl}_2\text{CuN}_8\text{O}_3$ (597.04): C, 44.26; H, 4.41; N, 18.77. Found: C, 44.03; H, 4.28; N, 18.56%.

Synthesis of $[\text{CuCl}_2(\text{L48})]$ (48). A pale green solution of $\text{CuCl}_2 \cdot 2\text{H}_2\text{O}$ (172 mg, 1.00 mmol) in 5 ml of methanol was added to a colourless solution of **L48** (316 mg, 1.00 mmol) in 5 ml of methanol yielding a green solution. The solvent was then concentrated under vacuum and a green solid was precipitated after addition of diethyl ether, which was filtered and vacuum dried (300 mg, 67%). IR (cm^{-1}): 3134w, 1964m, 2931m, 2871w, 2361w, 1550m, 1460m, 1430m, 1380m, 1336w, 1309w, 1276s, 1216w, 1183m, 1161w, 1112w, 1068m, 1019m, 980m, 926w, 876w, 816m, 717m, 646m, 542m. *Anal.* Calc. for $\text{C}_{19}\text{H}_{32}\text{Cl}_2\text{CuN}_4$ (450.93): C, 50.61; H, 7.15; N, 12.42. Found: C, 50.44; H, 7.03; N, 12.11%.

Synthesis of $[\text{CuCl}_2(\text{L49})]$ (49). A pale green solution of $\text{CuCl}_2 \cdot 2\text{H}_2\text{O}$ (75 mg, 0.44 mmol) in 5 ml of methanol was added to a brown solution of **L49** (163 mg, 0.44 mmol) in 5 ml of toluene yielding a dark yellow precipitate, which was filtered, washed with toluene and vacuum dried (189 mg, 84%). IR (cm^{-1}): 3444w br, 3127w, 2962w, 2362w,

2163w, 2051w, 1982w, 1617w, 1557m, 1463m, 1438m, 1486m, 1366m, 1281s, 1276s, 1161w, 1041m, 1006w, 830m, 704w, 679m, 660w, 626w, 473m. *Anal.* Calc. for $C_{23}H_{40}Cl_2CuN_4$ (507.04): C, 54.48; H, 7.95; N, 11.05. Found: C, 54.37; H, 7.21; N, 7.08%.

Synthesis of $[CuCl_2(L50)]_2$ (50). A pale green solution of $CuCl_2 \cdot 2H_2O$ (86 mg, 0.50 mmol) in 5 ml of methanol was added to a colourless solution of **L50** (162 mg, 0.49 mmol) in 5 ml of methanol yielding a green precipitate, which was filtered, washed with methanol and vacuum dried (130 mg, 57%). IR (cm^{-1}): 3128w, 3106w, 3057w, 1511w, 1468m, 1456m, 1443m, 1421m, 1409s, 1290m, 1256m, 1210w, 1134w, 1062s, 992w, 915w, 849w, 830w, 781s, 744s, 716s, 693s, 621s, 597m, 531m. *Anal.* Calc. for $C_{38}H_{32}Cl_4Cu_2N_8S_2$ (933.74): C, 48.87; H, 3.45; N, 12.00. Found: C, 48.62; H, 3.16; N, 11.85%.

Synthesis of $[Cu_2Cl_3(L51)_2]Cl$ (51). A pale green solution of $CuCl_2 \cdot 2H_2O$ (64 mg, 0.37 mmol) in 5 ml of methanol was added to a colourless solution of **L51** (145 mg, 0.37 mmol) in 5 ml of methanol yielding a green solution. The solvent was then concentrated under vacuum and a green solid was precipitated after addition of hexane, which was filtered and vacuum dried (100 mg, 51%). IR (cm^{-1}): 3254w, 3134w, 3052w, 2986w, 2920w, 1682w, 1560m, 1462m, 1457m, 1438m, 1415m, 1402m, 1377m, 1312m, 1255m, 1039m, 1024m, 793m, 739s, 690s, 616m, 531w, 421w. *Anal.* Calc. for $C_{46}H_{50.50}Cl_4Cu_2N_8O_{1.25}S_2$ (1068.48): C, 51.71; H, 4.76; N, 10.49. Found: C, 51.36; H, 4.55; N, 10.37%.

Synthesis of $[CuCl_2(L52)]$ (52). A pale green solution of $CuCl_2 \cdot 2H_2O$ (65 mg, 0.38 mmol) in 5 ml of methanol was added to a colourless solution of **L52** (190 mg, 0.38 mmol) in 5 ml of methanol yielding a green precipitate, which was filtered, washed with methanol and vacuum dried (160 mg, 66%). IR (cm^{-1}): 3050w, 2968m, 2929w, 2868 w, 1961w, 1735w, 1579w, 1547m, 1467m, 1437m, 1401w, 1381m, 1361m, 1344w, 1319m, 1305m, 1291m, 1275m, 1246m, 1225m, 1185m, 1111w, 1079m, 1057m, 1020m, 966w, 929w, 911w, 895w, 881w, 854m, 824m, 807m, 800m, 757m, 737s, 727m, 716m, 701m, 689m, 670m, 625m, 547w, 487w, 468w, 454w. *Anal.* Calc. for $C_{31}H_{46}Cl_2CuN_4S$ (641.24): C, 58.06; H, 7.23; N, 8.74. Found: C, 57.96; H, 7.11; N, 8.58%.

Synthesis of $[CuCl_2(L53)]$ (53). A pale green solution of $CuCl_2 \cdot 2H_2O$ (66 mg, 0.39 mmol) in 5 ml of methanol was added to a colourless solution of **L53** (105 mg, 0.39 mmol) in 5 ml of methanol yielding a green precipitate, which was filtered, washed with methanol and vacuum dried (114 mg, 72%). IR (cm^{-1}): 3120w, 2969w, 1512w, 1406m, 1285m, 1662m, 987w, 901w, 750s, 734s, 101w, 689m, 611s, 476w. *Anal.* Calc. for

C₁₄H₁₄Cl₂CuN₄S (404.80): C, 41.54; H, 3.49; N, 13.84. Found: C, 41.38; H, 3.37; N, 13.71%.

Synthesis of [CuCl₂(L54)] (54). A pale green solution of CuCl₂·2H₂O (32 mg, 0.19 mmol) in 5 ml of methanol was added to a colourless solution of **L54** (62 mg, 0.19 mmol) in 5 ml of methanol yielding a green precipitate, which was filtered, washed with methanol and vacuum dried (48 mg, 55%). IR (cm⁻¹): 2997w, 2980w, 2936w, 1558m, 1462m, 1441w, 1419w, 1383m, 1319w, 1267w, 1232w, 1064m, 922m, 865w, 797w, 748s, 705m, 690m, 487w. *Anal.* Calc. for C₁₈H₂₂Cl₂CuN₄S (460.91): C, 46.90; H, 4.81; N, 12.15. Found: C, 46.72; H, 4.66; N, 12.03%.

Synthesis of [CuCl₂(L55)] (55). A pale green solution of CuCl₂·2H₂O (90 mg, 0.53 mmol) in 5 ml of methanol was added to a solution of **L55** (237 mg, 0.53 mmol) in 5 ml of methanol yielding a yellow precipitate, which was filtered, washed with methanol and vacuum dried (230 mg, 74%). IR (cm⁻¹): 3676w, 3481w br, 2972m, 2932m, 2868m, 1616w, 1546m, 1473m, 1459m, 1439m, 1396m, 1383m, 1364m, 1315m, 1292m, 1278m, 1263m, 1223m, 1184m, 1092w, 1064m, 1016m, 928m, 912w, 882w, 839m, 808s, 773m, 750m, 743m, 695m, 660m, 557m, 512w, 487m, 432w. *Anal.* Calc. for C₂₆H₃₈Cl₂CuN₄S (573.12): C, 54.48; H, 6.68; N, 9.77. Found: C, 54.36; H, 6.41; N, 9.63%.

8.2.2. Stability constants determination

The thermodynamic stability of Cu(II) complexes with the **L38**, **L44**, **L45**, **L51**, and **L54** ligands was studied in a methanol:water 90:10 (v/v) mixture (*T* = 25 °C) by spectrophotometric titrations in the visible range (400 – 900 nm). Cu(II) stock solutions (*C*_{Cu} = ca. 0.0105 M) were prepared by weight from CuCl₂·2H₂O. Their titre was determined by complexometric titrations with standard EDTA²⁻ solutions using fast sulphon black F as indicator. Ligand stock solutions (0.02 M) were prepared by weight and used within two days. Attempts to use Hepes buffered ligands solutions (pH 7.4) resulted in the precipitation of copper(II) hydroxide during the titrations.

All Cu(II)/ligand systems were studied by spectrophotometric titrations by collecting visible spectra of batch samples containing a fixed metal ion concentration with increasing concentrations of ligand up to 1/2.6 (Cu(II)/ligand) ratio. The spectra were collected using a Perkin Elmer Lambda 25 spectrophotometer equipped with a Peltier device, using matched quartz cells of 1 cm path length. Visible spectrophotometric data were treated by means of the SPECFIT32^{150,151} and Hyperquad 2006¹⁵² programs,

which allowed determination of both the complexation $\log \beta$ values and the molar absorbances of the absorbing species.

8.2.3. Single Crystal X-ray Structures

Single crystal data were collected with a Bruker Smart 1000 and on a Bruker Smart APEXII area detector diffractometers (Mo $K\alpha$; $\lambda = 0.71073 \text{ \AA}$). Cell parameters were refined from the observed setting angles and detector positions of selected strong reflections. Intensities were integrated from several series of exposure frames that covered the sphere of reciprocal space⁴⁸. A multiscan absorption correction was applied to the data using the program SADABS. The structures were solved by direct methods SIR97¹⁰⁴ and SIR2004⁴⁹ and refined with full-matrix least-squares (SHELXL-97)⁵⁰, using the Wingx software package⁵¹. Graphical material was prepared with Mercury 2.0⁵² programs. Crystallographic data are reported in Appendix ix-xii.

8.2.4. Cell lines and culture

HT1080 and SW872 cell lines derived from human fibrosarcoma and liposarcoma, respectively, were obtained from the Istituto Zooprofilattico Sperimentale (Brescia, Italy); HeLa cell line, derived from a human cervix carcinoma, was obtained from ATCC. Human foreskin fibroblasts (HF) were obtained as previously described¹⁵³. Cells were all grown in Dulbecco's modified Eagle's medium (DMEM 4.5g/L glucose) supplemented with 10% fetal bovine serum (FBS), 4 mM glutamine, 100 U/mL penicillin, and 100 $\mu\text{g/mL}$ streptomycin. Cells were cultured at 37 °C in an atmosphere of 5% CO_2 in air, pH 7.4.

8.2.5. Cell viability assay

Cells were seeded in a complete growth medium in 96-well plates (Costar Corning, NY), at a density of $7.5 \cdot 10^3$ cells/well, 24 h before treatment. Compounds to be tested were freshly dissolved 15mM in DMSO (final DMSO concentration $\leq 0.2\%$). The growth medium was then substituted with fresh complete medium containing the compound at the selected concentration and cells incubated for 48 hours. Cell viability was tested replacing the culture medium with a solution of resazurin and reading fluorescence at 572 nm with a fluorimeter (Wallac 1420 Victor2 Multilabel Counter, Perkin Elmer). Viability and Cytotoxicity were expressed as % value calculated from the equations: $\text{Viability} = [(V_t - B)/(V_u - B)] \cdot 100$ and $\text{Cytotoxicity} = (100 - \text{Viability})$, where

V_t and V_u are the fluorescence values obtained in treated and untreated cells, respectively, and B is the background value. Dose response curves were fitted with non linear regression and IC_{50} values were calculated with GraphPad Prism 5.0™.

8.3. Results and Discussion

8.3.1 Synthesis

Ligands **L36-L41** were prepared by reacting the electrophilic chloroethyl-dimethylpyridine and pyrazole, in biphasic solvent (toluene/water) *via* phase transfer catalysis (*n*-Bu₄NOH).¹⁴⁸ The preparation of **L42-L45** ligands is performed by treating the pyrazole-pyridine parent compounds with *n*-BuLi and an electrophile bearing a thioether function (ClCH₂SCH₃).¹⁴⁷

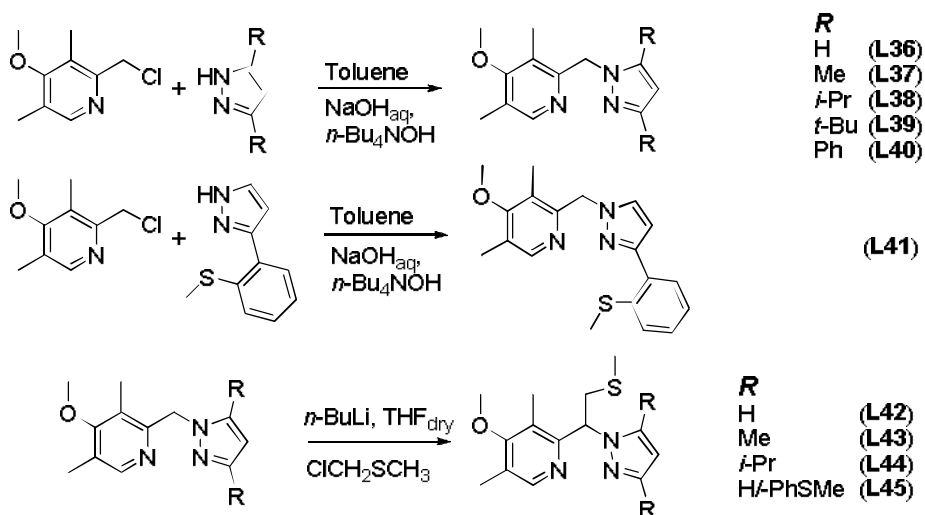


Figure 88. Synthesis of pyrazole-pyridine ligands **L36-L45**

The bis-pyrazole ligands **L46-L49** were prepared by refluxing deprotonated pyrazoles in dichloromethane, whereas ligands **L50-L55** were prepared by treating bis(pyrazolyl)ketones with aldehydes bearing the desired sulfur donor groups that were to be attached to the bispyrazole scaffold.^{103,109}

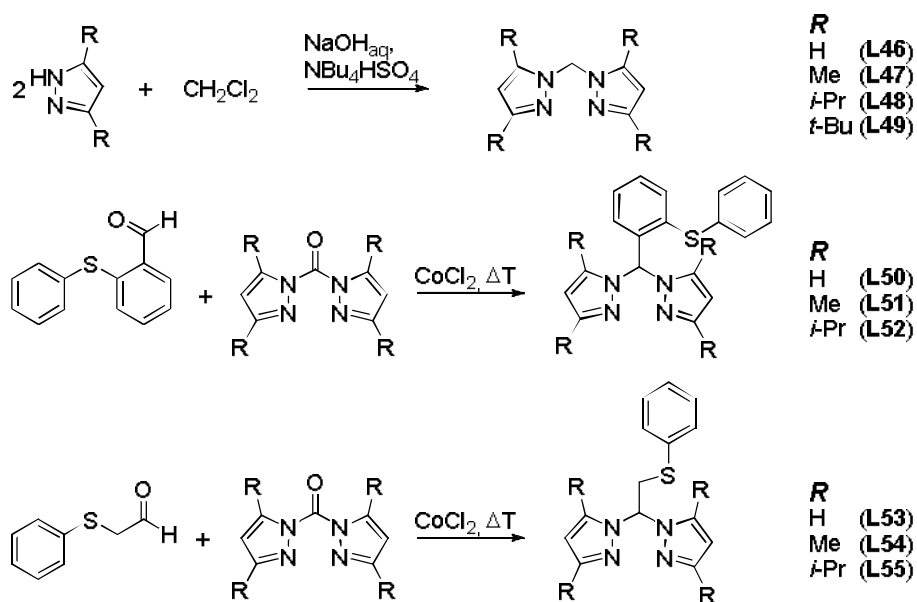


Figure 89. Synthesis of bispyrazole ligands **L46-L55**.

8.3.2. Solid state structures

According to the molecular backbone and the nature of a thioether third arm on the carbon center linking the two rings, the ligands could be divided into five classes (**a-e**, Figure 97). Within each class, peripheral residues on the pyrazole ring were modified to vary the hydrophobicities or coordinative abilities of ligands. Specifically, hydrophobicity was modulated by substituting the H-atom of the parent compound with Me and *i*-Pr as well as *t*-Bu and Ph when synthetically feasible. To influence coordinative ability, a thioether group was introduced on the pyrazole ring of compounds **41** and **45**. According to the X-ray structures reported in Figures 90-94, the invariant feature of the Cu(II) complexes is an N,N-chelation motif, whereas sulfur binding strongly depends on the types of thioether fragments introduced. In fact, the sulfur atom participates in metal coordination only when it is introduced in a favorable steric position (compounds **41** and **45**, Figures 90 and 91). When the thioether was attached as a flexible (compounds **42-44** and **53-55**) or rigid (**50-52**) central arm, it influenced the hydrophobicity of the ligand, but not its coordinative properties. The molecular structures can be grouped in two categories: mononuclear and dinuclear. In the first case, the metal geometry is flattened tetrahedral (compounds **39**, **40**, **48**, **52**, **54**, and **55**), whereas for the dinuclear case, the metal geometry is square pyramidal, with the apex of the pyramid occupied by a bridging chloride anion (compounds **37**, **38**, **42**, **43**, **44**, **50**, and **51**). Exception are represented by compounds **41** and **45** that exhibit a trigonal bipyramidal geometry by virtue of the presence of the N,N,S ligand donor set, and by compound **46** that forms chains constituted by the tetrahedral $[\text{CuCl}_4]^{2-}$ anion and the octahedral $[\text{Cu}(\text{L46})_2]^{2+}$ cation.

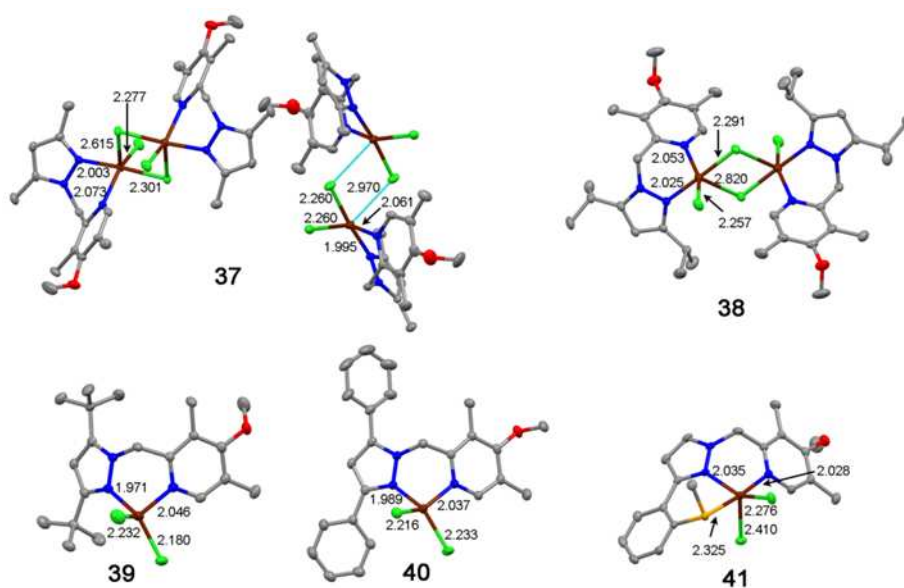


Figure 90. Molecular structures of **37-41** copper complexes. Hydrogen atoms were omitted for clarity. Selected bond distances are reported in Å. C (grey), N (blue), Cl (green), O (red), S (yellow), Cu (brown).

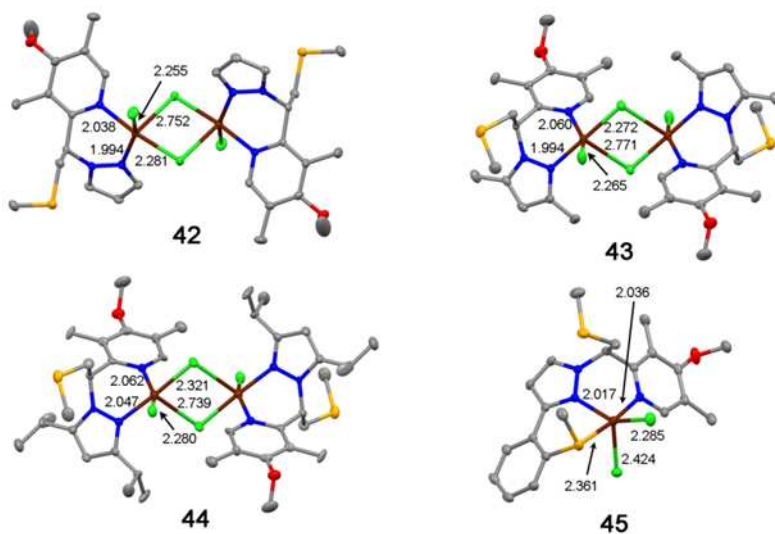


Figure 91. Molecular structures of **42-45** copper complexes. Hydrogen atoms were omitted for clarity. Selected bond distances are reported in Å. C (grey), N (blue), Cl (green), O (red), S (yellow), Cu (brown).

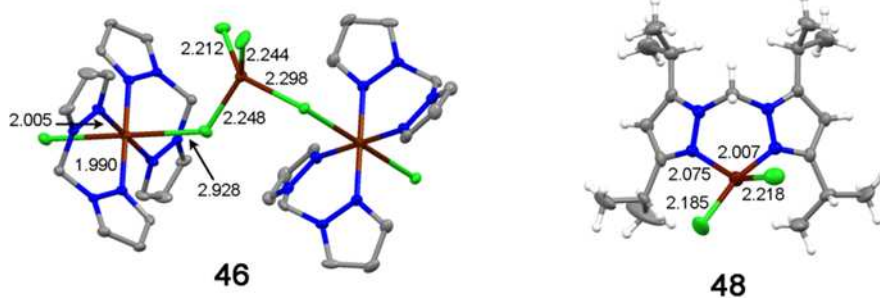


Figure 92. Molecular structures of **46** and **48** copper complexes. Hydrogen atoms are removed for clarity in **11**. Selected bond distances are reported in Å. C (grey), N (blue), Cl (green), Cu (brown).

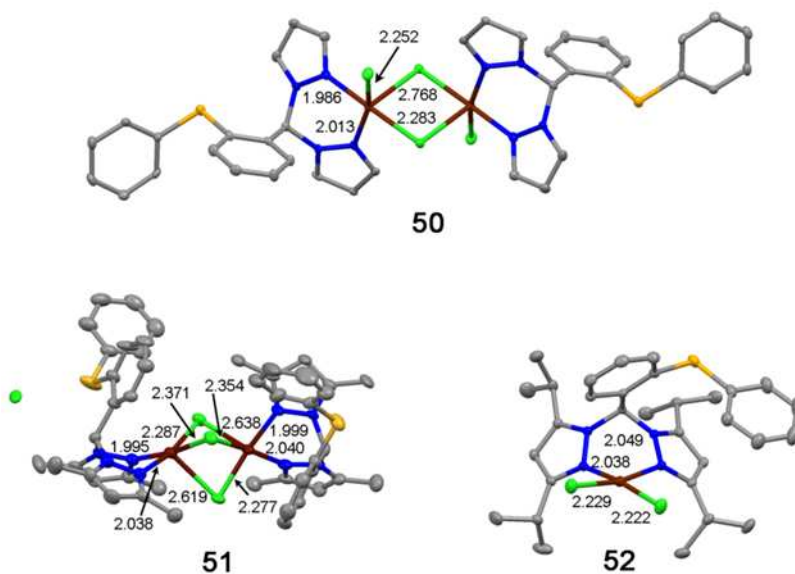


Figure 93. Molecular structures of **50-52** copper complexes. Hydrogen atoms were omitted for clarity. Selected bond distances are reported in Å. C (grey), N (blue), Cl (green), S (yellow), Cu (brown).

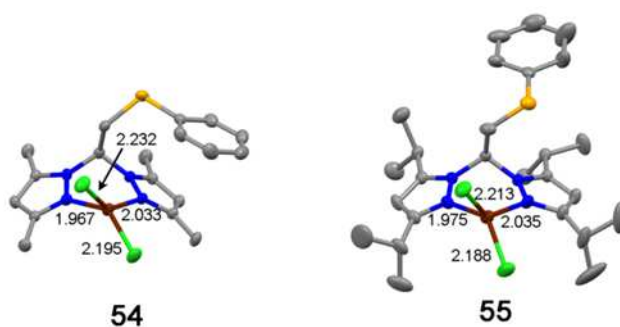


Figure 94. Molecular structures of **54** and **55** copper complexes. Hydrogen atoms were omitted for clarity. Selected bond distances are reported in Å. C (grey), N (blue), Cl (green), S (yellow), Cu (brown).

8.3.3. Stability Constants

The stability of the Cu(II)-ligand complexes was assessed by evaluating the equilibrium formation constant β as derived from the following equation: $\text{Cu(II)} + \text{L} \rightleftharpoons \text{Cu(II)L}$ ($\beta = [\text{Cu(II)L}]/([\text{Cu(II)}]\cdot[\text{L}])$). The log β value was determined for five complexes; it varied between 3.34 ± 0.15 and 4.69 ± 0.08 (Figure 95A). As expected, the highest stability was found for compound **45**, which employs three donor atoms (N,N,S) for copper binding instead of the bidentate N,N coordination seen in all of the other complexes. Higher stability was not associated with increased cytotoxicity. Speciation calculations (Figure 95B) showed that when the ligand of compound **44** and copper were present at 5 μM each, the expected concentration of the complex was less than 50 nM, a value that would decrease further if copper-binding competitors were taken into account.

Cell copper content was determined for the eleven active complexes ($\text{IC}_{50} < 30 \mu\text{M}$) by means of ICP-AES. When cells were incubated with the complexes at constant concentrations corresponding to the mean IC_{50} (13.2 μM), a strong correlation emerged between cytotoxic activity and cell copper content (non-parametric Spearman $r=1$). Figure 96 describes the relationship between these two parameters and indicates that the ability of a complex to promote copper accumulation in the cell depends on the ligand structure and is predictive of its cytotoxic activity.

A

Complex	$\log \beta_1$	$\log \beta_2$
38	3.93 ± 0.03	5.71 ± 0.05
44	3.34 ± 0.15	6.73 ± 0.22
45	4.69 ± 0.08	-
51	3.46 ± 0.04	4.89 ± 0.23
54	3.55 ± 0.10	7.56 ± 0.10

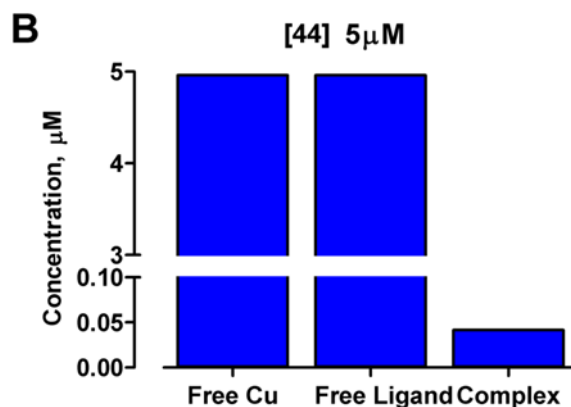


Figure 95. Stability of selected Cu(II) complexes. (A) The Log β_1 and Log β_2 values are presented. (B) Expected concentrations of the indicated species, calculated in accordance with the reported Log β for **44**, at the concentration of 5 μ M in the absence of other competitors for copper binding.

8.3.4. Cytotoxicity

The anticancer activities of the complexes were evaluated in human fibrosarcoma HT1080 cells by means of a resazurin-based viability assay. The IC_{50} values, extrapolated from the dose response curves reported in Figure 102, allowed us to identify the following structure-activity relationships: i) substitution of the H-atom on the pyrazole ring is essential to the activity of the complex, ii) the presence of the pyridine in place of pyrazole (compare classes **a** with **c**) and the presence of the central thioether arm (compare classes **a** with **b** and **c** with **d** and **e**) both enhance activity. The highest activity was observed for classes with flexible thioether groups (compare classes **b** with **d** and **e**). Among the twenty compounds, **44** was the most active ($IC_{50} = 3.3 \mu M$). The rank of the IC_{50} values within each class points to the fundamental role of ligand hydrophobicity in the biological response of the corresponding Cu(II) complex. The relationship between the calculated logP value¹⁵⁴ of the ligand and the cytotoxic activity of the respective complex suggests that, for each class of compounds, there is an optimal logP value (between 4 and 6) at which activity is maximal (Figure 96).

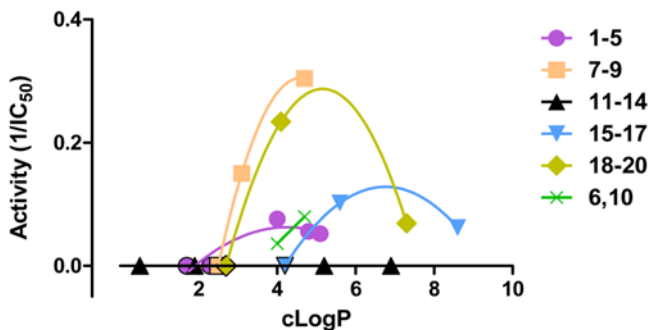


Figure 96. Relationship between hydrophobicity and cytotoxic activity of copper complexes. Copper complexes **1-20** are clustered in 6 groups according to their similarity. For each group a nonlinear regression curve (second order polynomial curve) is presented with the exception of the group of inactive complexes (**11-14**). The R^2 for the goodness of fit was > 0.85 for the presented curves. S.D are not presented for simplicity. Data were analyzed with GraphPad Prism 5.0.

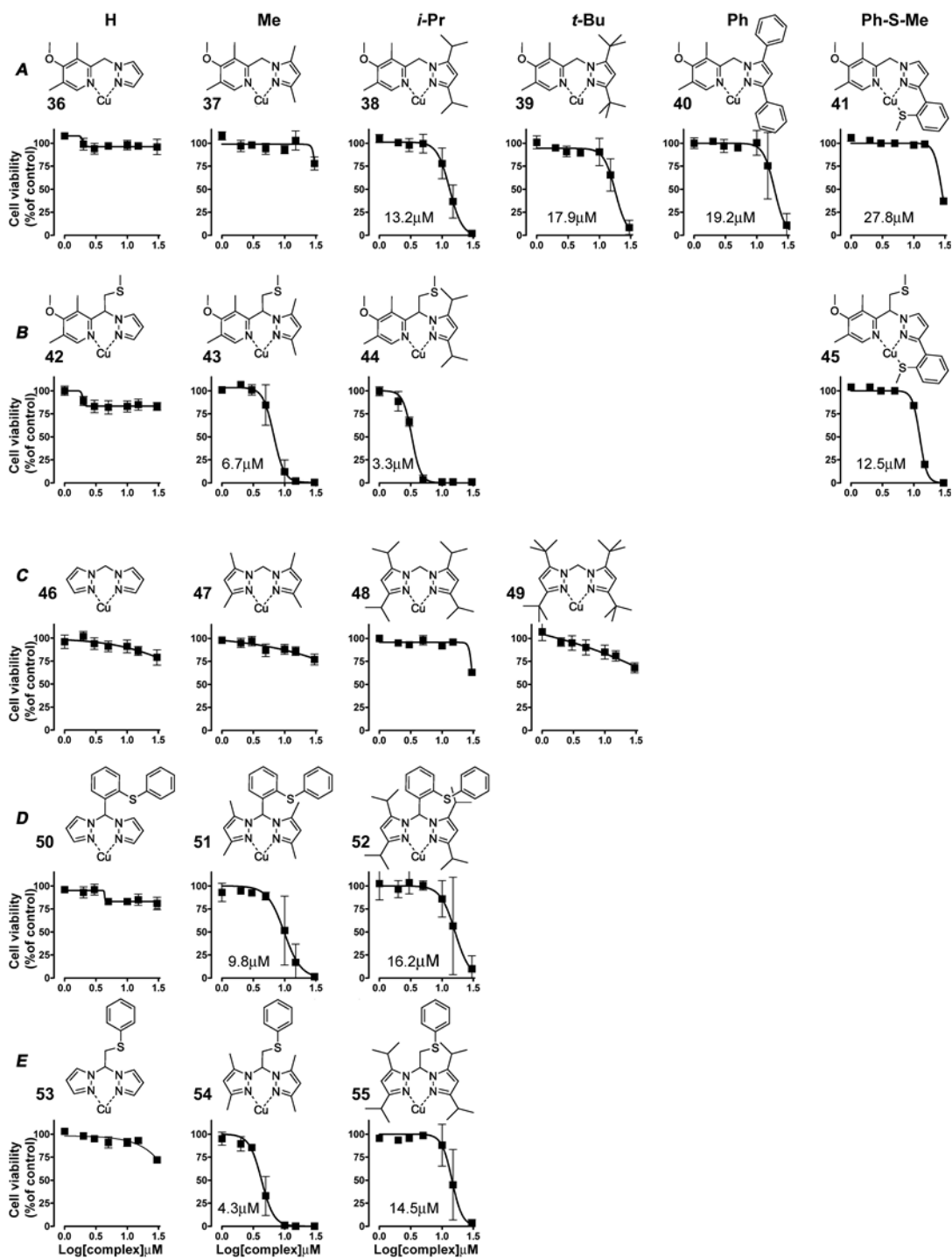


Figure 97. Structure and cytotoxic activity of novel copper complexes. Pyrazole-pyridine based (rows **a**, **b**) and bis-pyrazole based (rows **c**, **d**, **e**) copper(II) complexes together with the relative dose response curve in HT1080 cells. The chlorine atoms were removed for clarity. The different functional groups are indicated at

To correlate cytotoxic activity and complex bioavailability, we assessed ligand uptake of the most active compound **44**, and of an inactive compound, **42**. The cell extracts were analyzed by means of Reversed-Phase Liquid Chromatography (RPLC) combined with an electrospray ionization linear ion trap (ESI-LIT) mass spectrometry. As shown in Figure 98A, the accumulation of **44**-ligand was 30-fold higher than that observed for the ligand of the inactive (and less lipophilic) compound **42**. This evidence strongly suggests that passive diffusion accounts for membrane crossing for this class of complexes. To verify this hypothesis, a dose-dependent uptake experiment was performed in live cells. Figure 98B shows the linear relationship between the intracellular concentration of **44**-ligand and the extracellular concentration of **44**. These results indicate that, in the range of concentrations tested, ligand transport is not saturated and follows the Fick law for passive diffusion. The accumulation of **44**-ligand reached a plateau by approximately 30 minutes (Figure 98C). On the contrary, under the same experimental conditions, copper uptake showed much slower kinetics, approaching a steady state at 360 minutes. However, at this time, the copper concentration was approximately four-fold higher than the ligand concentration. These results suggest that the ligand carries copper across the membrane bilayer by virtue of its lipophilicity and favors its accumulation in the intracellular compartment, acting as an ionophore for the metal.

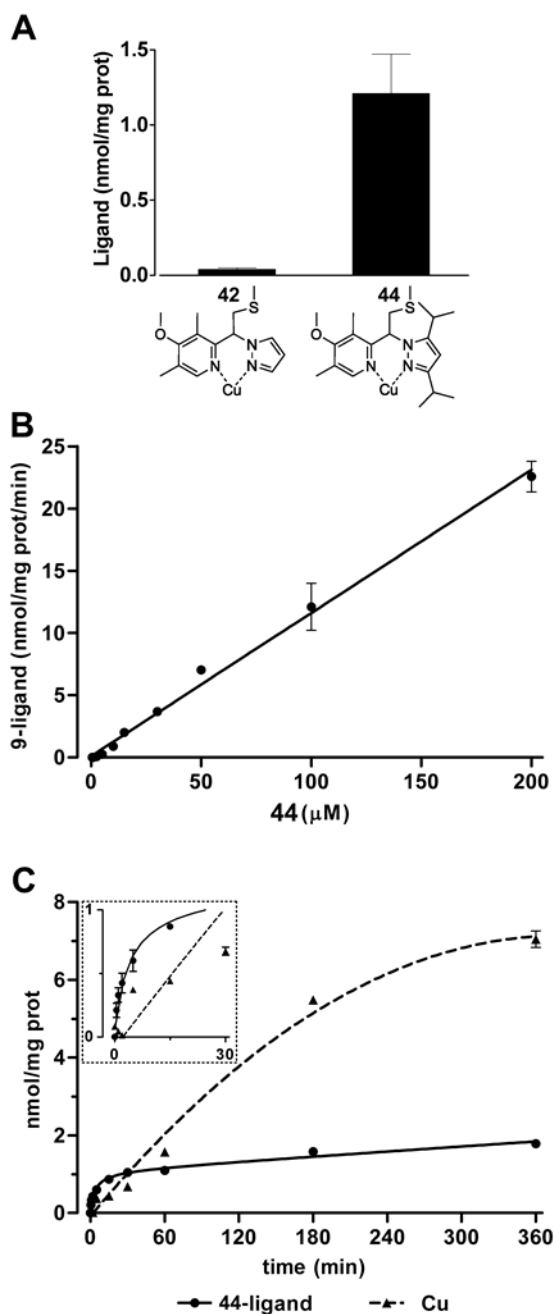


Figure 98. (A) Cellular concentrations of **42**- and **44**-ligands were determined by RPLC ESI-MS. HT1080 cells were incubated for 6 hours with 5 μM of the indicated complexes. (B) Uptake of **44**-ligand in HT1080 cells incubated for 2 min with the

indicated concentrations of compound **44** (5-200 μ M). (C) Uptake kinetics of **44**-ligand (solid line) and copper (dotted line). HT1080 cells were incubated with compound **44** (5 μ M) for the indicated time periods (0.5-360 min). The inset is an enlargement of the first 30 min of uptake. All data are means \pm SEM of two independent experiments with three replicates each.

Given the positive correlation between cell copper content and cytotoxic activity of **36-55** (see Figure 99A and B), we investigated whether inorganic copper (CuCl_2) was sufficient to produce similar effects. The cytotoxic response to CuCl_2 was assessed in three human tumor cell lines (HT1080, HeLa, and SW872) and normal fibroblasts (HF) and compared to the effects of the most active compound **44**. The dose response curve showed that CuCl_2 was toxic above 200 μ M, while compound **44** was active at concentrations less than 10 μ M. When CuCl_2 was used at a toxic concentration, the morphological changes induced were identical to those caused by compound **44**. These alterations were similar to those described for a thioxotriazole copper(II) complex that induces paraptosis, a non-apoptotic cell death process.^{142,155}

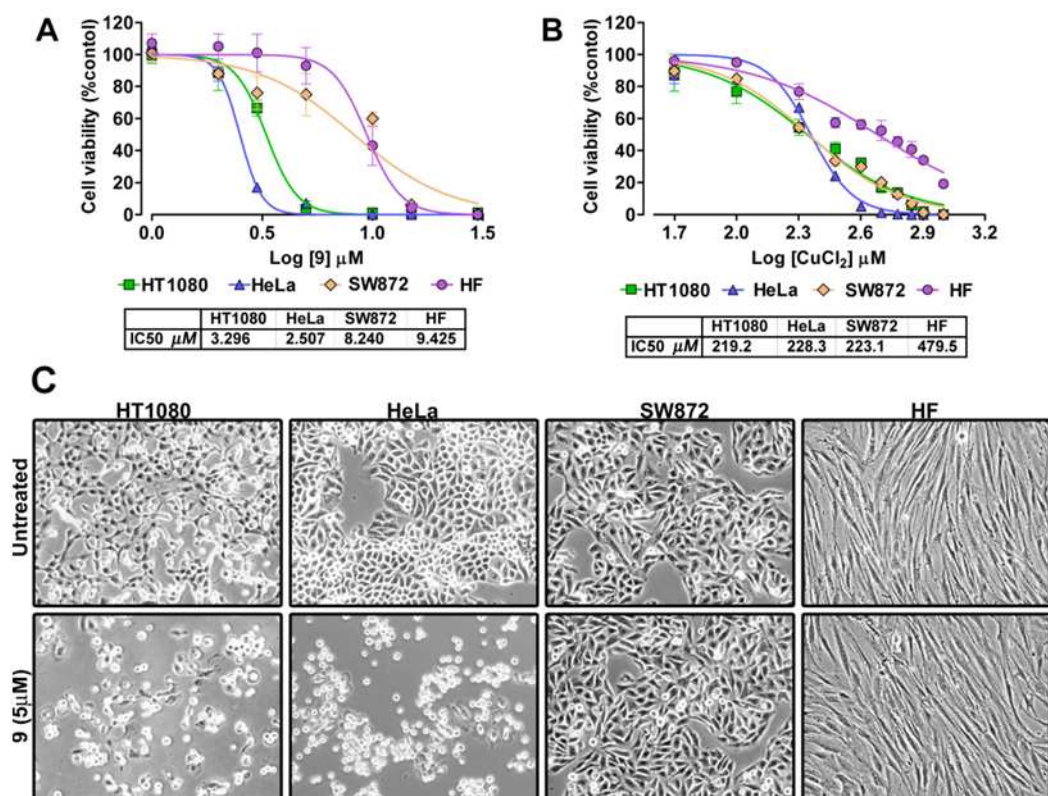


Figure 99. Effects of treatment with **44** and CuCl_2 in normal fibroblasts (HF) and tumor cell lines (HT1080, HeLa, SW872). (A) Cells were incubated with rising concentrations of the complex **44** (1-30 μM) or (B) with increasing concentrations of CuCl_2 (50-1000 μM) for 48h and viability assessed with the resazurin method. The IC₅₀s obtained from the curves are reported. Data are means \pm SEM of three independent experiments with 6 replicates each. (C) Phase contrast images representative of untreated cells or cells incubated for 24 hours with 5 μM **44**. Cytotoxicity is evident in HT1080 and HeLa cells while SW872 and HF cultures are spared (original magnification 100x).

Therefore, copper itself appears to be responsible for the biological alterations induced in tumor cell lines, as this correlation is independent of cancer cell type and the presence or structure of the ligand. An exception was represented by normal human fibroblasts (HF), where high intracellular copper concentration did not translate into cytotoxicity, as expected from the curve in Figure 104A. This result suggests that HF cells are able to withstand supraphysiological copper concentrations

better than cancer cells. Notably, the different sensitivities of the four cell lines to compound **44** (HeLa \approx HT1080 \gg SW872 \approx HF, Figure 99A) and cellular copper concentrations (Hela \approx HT1080 \approx HF $>$ SW872) were not related to the cellular concentration of **44**-ligand. In fact, when the four cell types were treated for 6 hours with 5 μ M compound **44**, copper always reached significantly higher cell levels than the ligand, with a copper/ligand ratio that varied from 1.6 to 3.7 (Figure 99B). These results confirm that ligand and copper establish different transmembrane gradients.

When equimolar amounts of CuCl_2 and DSF were administered to HT1080 and HeLa cells (Figure 100A), massive cytoplasmic vacuolization in the absence of apoptotic features was observed. These morphological changes coincided with the paraptotic morphology^{141,142} caused by complex **44** or CuCl_2 and previously observed with $[\text{Cu}(8\text{-hydroxyquinoline})_2]$ and $[\text{Cu}(\text{clioquinole})_2]$, which promote copper transport into the cell (Figure 100). Our findings point to a mechanism of action for copper binding agents that can also apply to disulfiram (DSF), a copper-interacting drug described extensively as an apoptotic inducer in several *in vitro* and *in vivo* cancer models.^{156,157} In our models, DSF concentrates copper in the cell (Figure 100B), reproducing the morphological and molecular changes observed with other copper complexes, indicative of paraptotic cell death (Figure 100).

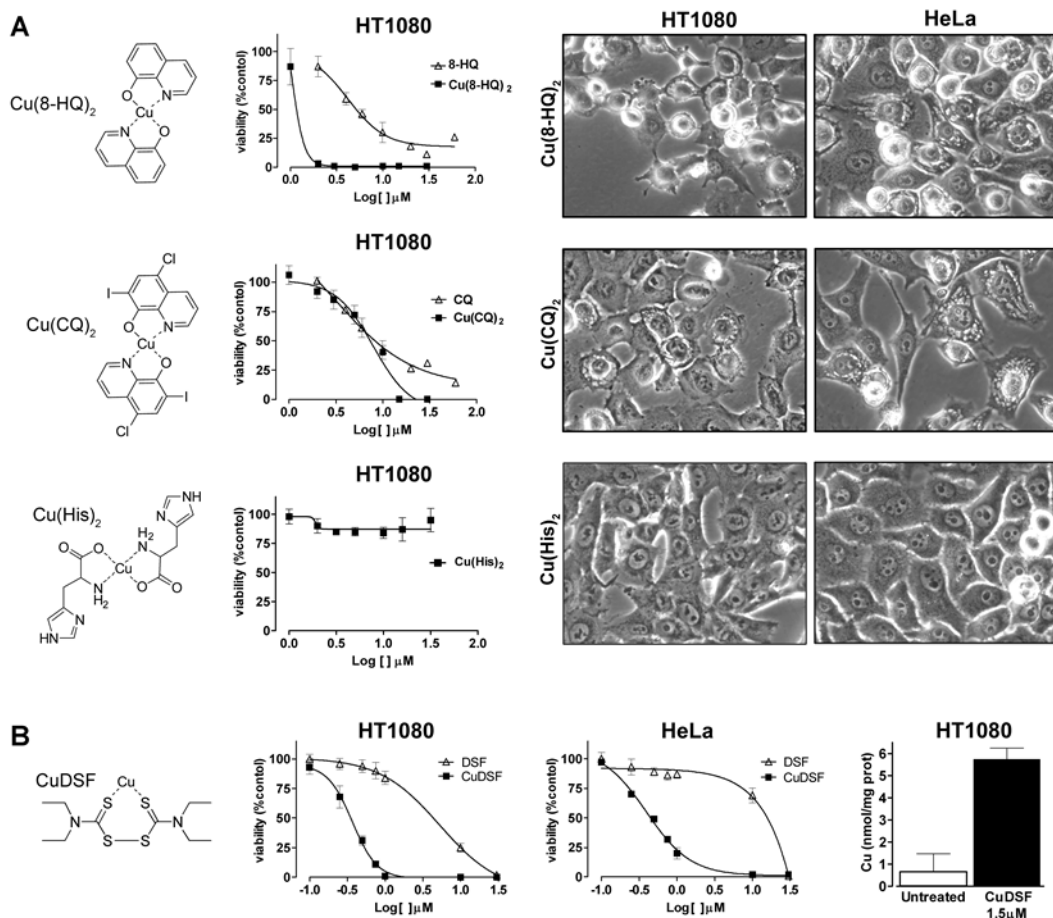


Figure 100. Cytotoxicity of 8-hydroxyquinoline (8-HQ), clioquinol (CQ), histidine (His), and disulfiram (DSF) copper complexes. The copper complexes of the indicated compounds were obtained as described in the Supplementary Material and Methods section. (A and B) Dose responses: HT1080 or HeLa cells were incubated for 48h with the indicated concentration of the ligands alone or complexed with copper. Data \pm SEM are means of two independent experiments with six determination each. The morphology of HT1080 and HeLa cells treated for 15 hours with 1.5 μ M Cu(8-HQ)₂, 12.5 μ M Cu(CQ)₂, or with 30 μ M Cu(His)₂ is presented. Cytoplasmic vacuolization is evident in both HT1080 and HeLa cells treated with Cu(8-HQ)₂, and Cu(CQ)₂ but not with Cu(His)₂, (original magnification 100x). (B) HT1080 cells were incubated with the CuDSF complex for 6 hours or left untreated. Cellular copper content was determined

by means of ICP-AES. Data \pm SD are means of two independent experiments with three determination each.

For the copper complexes examined in this chapter, as well as for other previously described compounds,^{143,158} the biological effects that we consistently observed are the intracellular accumulation of high amounts of copper, the appearance of cytoplasmic vacuolization, and the activation of caspase-independent cell death. These observations can be reasonably explained if the ligand is considered to be a copper ionophore that exacerbates the intrinsic toxicity of the metal by increasing its intracellular concentration. If a ligand has autonomous biological activities, as in the case of DSF, the two effects might be synergistic, leading to potent cytotoxic behavior. While the selectivity of copper complexes to induce cell death in specific cancer cells remains to be explained, an understanding of the mechanisms underlying the toxicity of copper complexes may lead to more effective anticancer drugs. Because DSF associated with copper is currently under clinical investigation as an anticancer agent, these findings may be useful for designing an effective therapeutic combination with pro-apoptotic drugs.

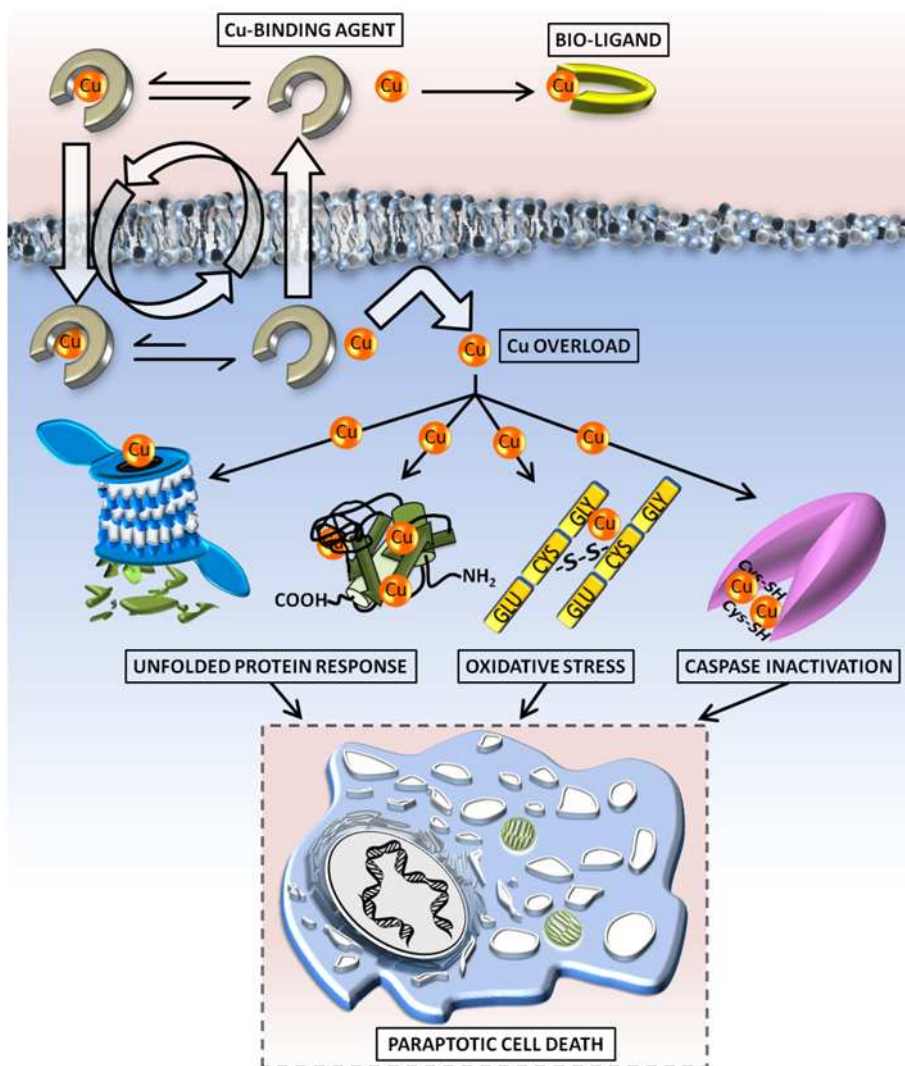
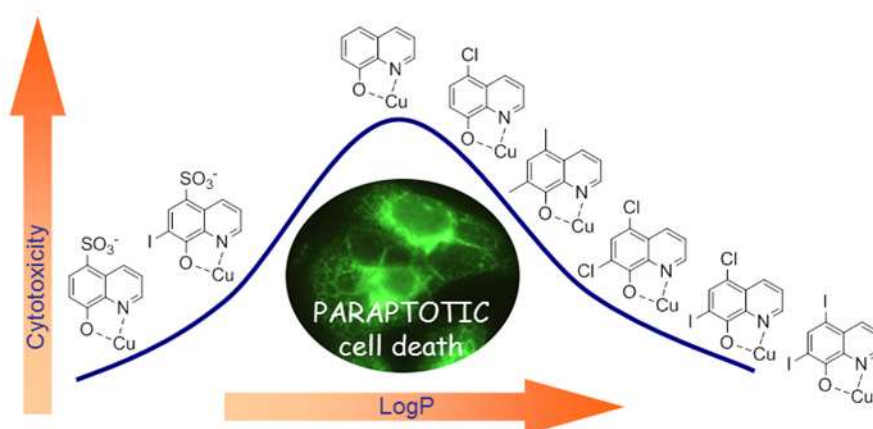


Figure 101. A proposed model for a copper-binding agent mechanism of action. A copper complex dissolved in the extracellular environment partially dissociates as a consequence of its stability and concentration of other bio-ligands (amino acids and serum proteins). According to the diffusion laws, the fraction of undissociated complex pass through the plasma membrane, reaching the intracellular space. Here the complex completely dissociate because of very high concentration of endogenous high affinity copper ligands. The ligand can freely cross back the membrane to start another shuttling cycle. The intracellular concentration of copper progressively increases and saturates the copper handling ability of the cell until metal overload

translates into proteasome inhibition, impairment of correct protein folding, consumption of reduced glutathione, and caspase inactivation. The cell is forced to an unsolvable oxidative- as well as ER-stress. The apoptotic response is prevented because of copper dependent caspase inhibition, while the paraptotic cell death, with the typical vacuolization, is triggered as a backup suicide program.

Copper-dependent cytotoxicity of 8-Hydroxyquinoline derivatives.



In this chapter we present a study that assesses the structure-activity relationship¹³⁰ of a series of 8-HQ derivatives and focuses on the copper-dependent activity of 5-Cl-7-I-8-HQ (clioquinol, CQ) copper complex (Cu(CQ)). 8-HQs alone caused a dose-dependent loss of viability of the human tumor HeLa and PC3 cells. The combination of 8-HQs with copper increased the ligands effects, with extensive cell death occurring in both cell lines. In particular cytotoxic doses of Cu(CQ) promotes intracellular copper accumulation and extensive endoplasmic reticulum vacuolization that precede a non-apoptotic (paraptotic) cell death. The cytotoxic effect of Cu(CQ) was reproduced in normal human endothelial cells (HUVEC) only at concentrations double than those effective in tumor cells, pointing to a potential therapeutic window for this complex. Finally, the results showed that the paraptotic cell death induced by Cu(CQ) while depending on copper accumulation does not require nor involve caspases, giving an indication for the current clinical assessment of clioquinol as an antineoplastic agent.

9.1 Introduction

Several types of programmed cell death (PCD) have been reported in the literature.¹⁵⁹ Caspase-dependent apoptosis is the most common type of PCD through which normal and tumor cells die in an organized manner, both during tissue development or under conditions of stress, such as chemotherapeutic treatment.¹⁶⁰ From a morphological point of view, apoptosis manifests with cell shrinkage, chromatin condensation, and the appearance of apoptotic bodies containing nuclear fragments. The apoptotic process can be activated either by extracellular ligands through transmembrane death receptors (extrinsic pathway) or as a consequence of cellular injury that ultimately leads to mitochondrial membrane permeabilization and release of cytochrome C (intrinsic pathway). The complex biochemical machinery activated during the cell death process usually promotes the activation of caspase-3, which dismantles cellular architecture and leads to cell death.^{161,162} However, caspase-independent apoptosis has also been documented.¹ Caspase-independent apoptotic cell death usually comprises the translocation of endonucleases (ENDOG) and/or apoptosis-inducing factor (AIF) from the mitochondria to the nucleus.^{163,164} The extensive stress on the endoplasmic reticulum (ER) caused by the accumulation of unfolded proteins in its lumen can trigger the apoptotic pathway. In the presence of this stress, cells activate the unfolded protein response (UPR) and inhibit protein synthesis in an effort to relieve the ER from excessive protein overload. If the stress persists, the expression of the transcription factor CHOP (CCAAT-enhancer-binding protein homologous protein) increases, initiating the apoptotic cascade.^{165,166}

Copper is an essential metal ion involved in several highly conserved biochemical processes. Its oxidation state shifts from +2 to +1 upon internalization due to the reducing intracellular environment. A mild intracellular excess of copper can normally be balanced by the cells through an increased expression of metallothioneins or through the activation of specific pumps, such as ATP7A and ATP7B,^{167,168} whereas high copper concentrations cause the activation of the UPR, as described above. For this reason, despite its essential role in living cells, copper has been frequently employed in the preparation of cytotoxic complexes. In many instances, the choice of Cu(II)-based compounds as cytotoxic agents originates from the overproduction of reactive oxygen species (ROS) driven by the metal. Alternatively, copper-binding agents have been employed for their ability to direct the toxicity of the metal towards specific intracellular targets.¹³⁸

In cultured cells, the internalization of copper complexes does not usually involve the hCTR1 copper-specific transporter but rather occurs primarily via passive

diffusion.^{130,169} For this reason, the chemical features of the ligand appear to be the main determinants of the activity of the complex because it may i) modulate its permeability through the cell membranes by virtue of its lipophilic character, ii) stabilize a specific redox state of the metal, iii) drive the complex to specific cellular targets, and iv) exhibit an intrinsic cytotoxic activity when dissociated from the metal. 8-Hydroxyquinoline (8-HQ) derivatives are planar, N,O-donating ligands that have a high affinity for Cu(II). Particular interest has been recently dedicated to 5-Cl-7-I-8-HQ (clioquinol, CQ) because CQ was already recognized as an anti-parasitic drug, even though its use was discontinued in some countries due to the occurrence of subacute myelo-optic neuropathy. In mice, CQ proved to be able to inhibit the accumulation of β amyloid (A β) in the brain and to mobilize the A β from existing deposits,¹²⁵ which are of great relevance for treatments of Alzheimer disease.^{170,171} The CQ-related compound PBT2¹⁷² has recently underwent phase II clinical trials as an anti-Alzheimer compound.¹⁷³ Moreover, CQ has entered Phase I clinical trials for the treatment of relapsed or refractory hematological malignancy (NCT00963495).

In previous chapter (chapter 8), we have shown that nitrogen donor ligands behave as copper ionophores in cancer cells, thus leading to a toxic accumulation of the metal, which eventually triggers paraptotic cell death.^{130,144} The goal of this project is to investigate whether non-apoptotic programmed cell death is activated in tumor cell lines by the combined treatment of copper and 8-HQ analogs, with a particular focus on the copper ionophore CQ.¹⁷⁴

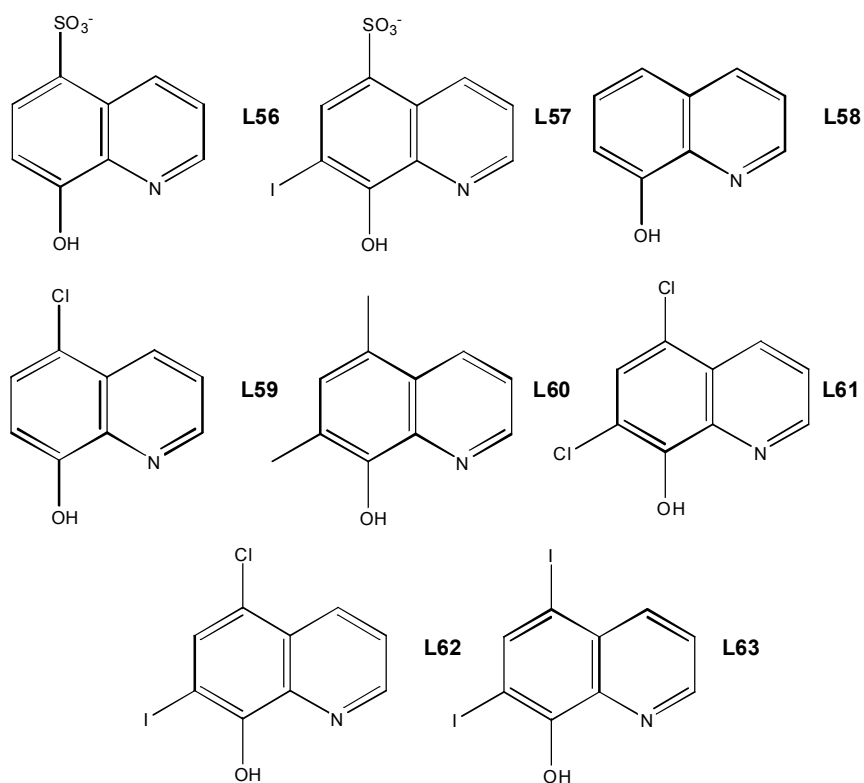


Figure 102. Ligands used in the study presented in this chapter.

9.2 Experimental

9.2.1. Synthesis

All reagents and solvents were commercially available. Infrared spectra were recorded from 4000 to 700 cm^{-1} on a Perkin-Elmer FT-IR Nexus spectrometer equipped with a Thermo-Nicolet microscope. Elemental analyses (C, H, and N) were performed with a Carlo Erba EA 1108 automated analyzer.

Synthesis of $[\text{Cu}(\text{L56})_2](\mathbf{56})$. A pale green solution of $\text{CuCl}_2 \cdot 2\text{H}_2\text{O}$ (94 mg, 0.55mmol) dissolved in Methanol(5 ml) has been added to a solution of 8-Hydroxyquinoline-5-sulfonic acid (L56) (250mg, 1.11mmol) in 10 ml of Methanol/Water (1:1) and then the mixture was stirred for 30 min. The solvent was removed under vacuum and a green solid precipitated. The solid was filtered and vacuum dried (172 mg, yield 61%). IR (cm^{-1}): 454s, 547m, 624m, 706m, 778w, 1024m, 1139s, 1320w, 1369w, 1490m, 1572w, 3095w. *Anal.* Calc. for $\text{C}_{18}\text{H}_{14}\text{CuN}_2\text{O}_8\text{S}_2$ (513.99): C, 42.06; H, 2.75; N, 5.45. Found: C, 43.96; H, 3.42; N, 11.40%.

Synthesis of $[\text{Cu}(\text{L57})_2](\mathbf{57})$. A pale green solution of $\text{CuCl}_2 \cdot 2\text{H}_2\text{O}$ (61 mg, 0.35mmol) dissolved in Methanol(5 ml) has been added to a pale yellow solution of 8-Hydroxy-7-iodo-5-quinoline sulfonic acid (L57) (250mg, 0.71mmol) in 30 ml of Methanol/Water (8:2) and the mixture was stirred for 30 min. The solvent was then removed under vacuum and a green solid precipitated. The solid was filtered and vacuum dried (193 mg, yield 72%). IR (cm^{-1}): 591s, 728m, 816m, 1035s, 1167s, 1380m, 1484m, 1556w, 1616w, 3079w, 3523w. *Anal.* Calc. for $\text{C}_{18}\text{H}_{12}\text{CuI}_2\text{N}_2\text{O}_8\text{S}_2$ (765.78): C, 28.23; H, 1.58; N, 3.66. Found: C, 43.96; H, 3.42; N, 11.40%.

Synthesis of $[\text{Cu}(\text{L58})_2](\mathbf{58})$. A pale green solution of $\text{CuCl}_2 \cdot 2\text{H}_2\text{O}$ (147 mg, 0.86mmol) dissolved in Methanol(5 ml) has been added to a yellow solution of 8-Hydroxyquinoline (L58) (250mg, 1.72mmol) in 20 ml of Methanol and suddenly a brown solid precipitated. After 30 min of stirring the solid was filtered and vacuum dried (233 mg, yield 77%). IR (cm^{-1}): 504m, 635w, 739s, 821s, 1106s, 1265m, 1315s, 1375s, 1495s, 1578m, 3057w. *Anal.* Calc. for $\text{C}_{18}\text{H}_{14}\text{CuN}_2\text{O}_2$ (353.86): C, 61.10; H, 3.99; N, 7.92. Found: C, 43.96; H, 3.42; N, 11.40%.

Synthesis of $[\text{Cu}(\text{L59})_2](\mathbf{59})$. A pale green solution of $\text{CuCl}_2 \cdot 2\text{H}_2\text{O}$ (119 mg, 0.69mmol) dissolved in Methanol(5 ml) has been added to a yellow solution of 5-Chloro-8-quinolinol (L59) (250mg, 1.39mmol) in 20 ml of Methanol and suddenly a brown solid precipitated. After 30 min of stirring the solid was filtered and vacuum dried (196 mg,

yield 66%). The compound was recrystallized by stratifying diethyl ether over an acetone solution of the complex, yielding colorless crystals.. IR (cm^{-1}): 504m, 635w, 739s, 821s, 1106s, 1265m, 1315s, 1375s, 1495s, 1578m, 3057w. *Anal.* Calc. for $\text{C}_{18}\text{H}_{12}\text{CuCl}_2\text{N}_2\text{O}_2$ (422.75): C, 51.14; H, 2.86; N, 6.63. Found: C, 43.96; H, 3.42; N, 11.40%.

Synthesis of $[\text{Cu}(\text{L60})_2]$ (60). A pale green solution of $\text{CuCl}_2 \cdot 2\text{H}_2\text{O}$ (123 mg, 0.72mmol) dissolved in Methanol(5 ml) has been added to a pale pink solution of 5,7-Dimethyl-8-quiloninol (L60) (250mg, 1.44mmol) in 20 ml of Methanol and suddenly a green solid precipitated. After 30 min of stirring the solid was filtered and vacuum dried (221 mg, yield 75%). The compound was recrystallized by stratifying diethyl ether over an acetone solution of the complex, yielding colorless crystals.. IR (cm^{-1}): 443m, 663s, 745m, 789s, 997w, 1134m, 1167m, 1353s, 1435m, 1506m, 1572w, 2915w.. *Anal.* Calc. for $\text{C}_{22}\text{H}_{22}\text{CuN}_2\text{O}_2$ (409.97): C, 64.45; H, 5.41; N, 6.83. Found: C, 43.96; H, 3.42; N, 11.40%.

Synthesis of $[\text{Cu}(\text{L61})_2]$ (61). A pale green solution of $\text{CuCl}_2 \cdot 2\text{H}_2\text{O}$ (100 mg, 0.58mmol) dissolved in Methanol(5 ml) has been added to a solution of 5,7-Dichlor-8-quiloninol (L61) (250mg, 1.16mmol) in 10 ml of Acetone and suddenly a dark green solid precipitated. After 30 min of stirring the solid was filtered and vacuum dried (132 mg, yield 46%). The compound was recrystallized by stratifying diethyl ether over an acetone solution of the complex, yielding colorless crystals.. IR (cm^{-1}): 482m, 657m, 750s, 980m, 1112m, 1254w, 1369s, 1435s, 1479m, 1539m, 1764w, 3736w. *Anal.* Calc. for $\text{C}_{18}\text{H}_{10}\text{CuCl}_4\text{N}_2\text{O}_2$ (491.64): C, 43.97; H, 2.05; N, 5.70. Found: C, 43.96; H, 3.42; N, 11.40%.

Synthesis of $[\text{Cu}(\text{L62})_2]$ (62). A pale green solution of $\text{CuCl}_2 \cdot 2\text{H}_2\text{O}$ (70 mg, 0.41mmol) dissolved in Methanol(5 ml) has been added to a solution of Clloquinol (L62)(250mg, 1.16mmol) in 10 ml of Acetone and suddenly a dark green solid precipitated. After 30 min of stirring the solid was filtered and vacuum dried (207 mg, yield 75%). IR (cm^{-1}): 487m, 586m, 657s, 750s, 975m, 1112m, 1375s, 1435s, 1539m, 1753w. *Anal.* Calc. for $\text{C}_{18}\text{H}_{10}\text{CuCl}_2\text{I}_2\text{N}_2\text{O}_2$ (674.55): C, 32.05; H, 1.49; N, 4.15. Found: C, 43.96; H, 3.42; N, 11.40%.

Synthesis of $[\text{Cu}(\text{L63})_2]$ (63). A pale green solution of $\text{CuCl}_2 \cdot 2\text{H}_2\text{O}$ (53 mg, 0.31mmol) dissolved in Methanol(5 ml) has been added to a solution of 5,7-Diiodo-8-hydroxyquinoline (L63) (250mg, 0.62mmol) in 20 ml of Acetone/Chloroform (1:1) and

suddenly a green solid precipitated. After 30 min of stirring the solid was filtered and vacuum dried (238 mg, yield 90%). The compound was recrystallized by stratifying diethyl ether over an acetone solution of the complex, yielding colorless crystals.. IR (cm^{-1}): 482w, 657m, 750s, 980m, 1112m, 1249w, 1364s, 1435s, 1545s, 1753w. *Anal.* Calc. for $\text{C}_{18}\text{H}_{10}\text{CuI}_4\text{N}_2\text{O}_2$ (857.45): C, 25.21; H, 1.18; N, 3.27. Found: C, 43.96; H, 3.42; N, 11.40%.

9.2.2. X-ray crystallography

Single crystal data were collected with a Bruker Smart APEXII area detector diffractometers (Mo $\text{K}\alpha$; $\lambda = 0.71073 \text{ \AA}$). Cell parameters were refined from the observed setting angles and detector positions of selected strong reflections. Intensities were integrated from several series of exposure frames that covered the sphere of reciprocal space.⁴⁸ A multiscan absorption correction was applied to the data using the program SADABS.¹⁰⁴ The structures were solved by direct methods (SIR2004) and refined with full-matrix least-squares (SHELXL-97),⁵⁰ using the Wingx⁵¹ software package. Graphical material was prepared with the Mercury 3.0⁵² programs. Crystallographic data are reported in Appendix xii.

9.2.3. Stability constants determination

The thermodynamic stability of Cu(II) complexes with the **L58** and **L56** ligands was studied in DMSO:water 1:1 (w/w) ($T = 25 \text{ }^\circ\text{C}$, $I = 0.1 \text{ M}$ (KCl)) by potentiometric titrations, using an apparatus already described in the literature¹⁷⁵. Freshly boiled, N_2 -saturated doubly distilled water and N_2 -fluxed DMSO (heated at $180 \text{ }^\circ\text{C}$) were used for the preparation of the DMSO:water mixtures. The Cu(II) stock solution ($C_{\text{Cu}} = \text{ca. } 0.016 \text{ M}$) was prepared by weight from $\text{CuCl}_2 \cdot 2\text{H}_2\text{O}$, and its titre was determined by complexometric titrations with standard EDTA solutions using pyrocatechol violet as the indicator. HCl aqueous solutions ($\text{ca. } 0.2 \text{ M}$) and KOH solutions ($\text{ca. } 0.2 \text{ M}$ in DMSO:water 1:1 (w/w)) were prepared by diluting concentrated Merck Titrisol ampoules with the proper amounts of CO_2 -free water and DMSO, and standardized with the usual procedure of this laboratory.¹⁷⁵ Solutions of the ligands **L58** and **L56** ($\text{ca. } 0.1 \text{ M}$) were prepared by weight in DMSO:water 1:1 (w/w) using the pure ligands and adding a stoichiometric amount of HCl (aqueous 10 N solution). The suspensions were stirred overnight to attain complete ligand dissolution, and the solutions filtered through a $0.45 \text{ }\mu\text{m}$ nylon filter. Their titre (ligand content and excess of acid) was checked by potentiometric titration with standard KOH solutions. These solutions

were used within 4-5 days. The titrations were carried out at $T = 25.0 \pm 0.1$ °C and $I = 0.1$ M (KCl) under a stream of N_2 , using 50 ml samples. Prior to its use, the reference compartment of the Hamilton combined glass electrode (P/N 238000) was filled with a 0.1 M KCl solution in DMSO:water 1:1 (w/w), and left to equilibrate overnight. The electrode was calibrated in terms of $[H^+]$ by titrating HCl solutions with standard KOH solutions and the calculated pK_w value resulted to be 15.25(5).

The protonation constants of the ligands were determined by alkalimetric titration of three samples ($6.1\text{-}9.1 \times 10^{-3}$ M for L58, $3.3\text{-}3.8 \times 10^{-3}$ M for **L56**) in the pH range 2-11. The complex formation constants of the Cu^{2+} /**L58** or **L56** systems were determined by alkalimetric titrations of three samples (Cu^{2+} /L58 = 1 : 1.0-1.2, $C_{Cu} = 7.0\text{-}7.9 \times 10^{-4}$ M; Cu^{2+} /L56 = 1 : 2.0-2.2, $C_{Cu} = 1.5\text{-}1.6 \times 10^{-3}$ M) in the pH range 2-9. The **L58**/ Cu^{2+} has been limited to *ca.* 1.2 and pH 4.5 because of the poor solubility of the **58** complexes in the solvent mixture.

9.3. Results and Discussion

9.3.1. Solid state structures

The Cu(II) complexes can be prepared by mixing $\text{CuCl}_2 \cdot 2\text{H}_2\text{O}$ and the corresponding ligands in the 1:1 or 1:2 molar ratio. Complexes of formula $[\text{Cu}(\text{L})(\text{H}_2\text{O})_2]$ are obtained with the **L56** and **L57** ligands, whereas the remaining ligands give rise to complexes of $[\text{Cu}(\text{L})_2]$ general formula (Figure 103). Given the different lipophilic properties of the ligands, different solvents were employed to prepare solutions of the ligands, whereas $\text{CuCl}_2 \cdot 2\text{H}_2\text{O}$ was dissolved in methanol. The $[\text{Cu}(\text{L})(\text{H}_2\text{O})_2]$ or $[\text{Cu}(\text{L})_2]$ complexes readily precipitated from the reaction mixtures as brown or green powders. These compounds are usually insoluble in aqueous media, in common organic solvents and are poorly soluble in DMSO. For this reason, the biological tests were performed by mixing $\text{CuCl}_2 \cdot 2\text{H}_2\text{O}$ and the corresponding ligands directly into the cell culture media at a 1:1 molar ratio. The final concentration of the complex for the biological tests was in the 1-30 μM range such that it did not precipitate in the medium. On the basis of our determined stability constants for **L58** and **L56** (see below) in this range of concentrations, we expect that 40-50 % of the total Cu(II) forms $[\text{Cu}(\text{L})]$, while the remaining 50 %-60 % are present as $[\text{Cu}(\text{L})_2]$ and “free” Cu^{2+} ions (25-30 % each).

L58 and its derivatives are characterized by the presence of a N,O-binding system that is suitable to interact strongly with Cu(II) ions. The presence of the $-\text{SO}_3^-$ group leads to the formation of complexes in which the metal:ligand ratio is 1:1 due to the involvement of the sulfonate moiety in metal coordination. When R and R' are halogen or alkyl substituents, the metal:ligand ratio becomes 1:2, and the ligands are arranged in a *trans* geometry, with the nitrogen and oxygen atoms on the opposite side with respect to the metal center. The molecular structures of **58** and **62**¹⁷⁶ were previously reported, whereas the **60** is reported in Figure 103B.

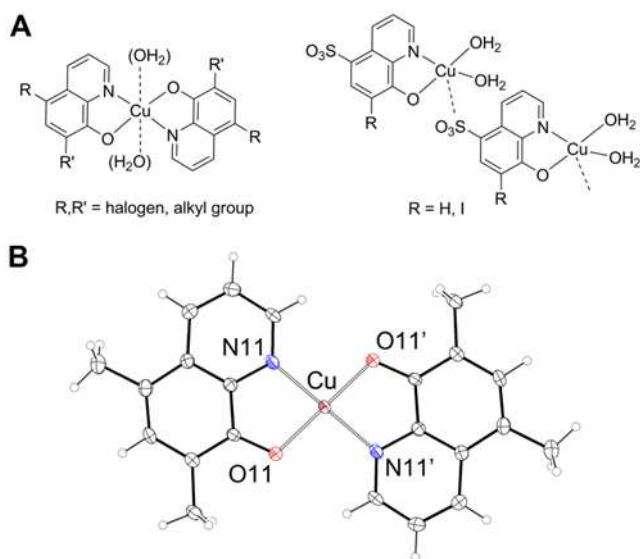


Figure 103. A. The molecular structures of Cu(II) complexes with **L58** derivatives. B. ORTEP diagram of the X-ray molecular structure of **60**, symmetry code ' = -x; 1-y, -z.

The complex crystallizes in the P-1 space group. The unit cell contains three complex molecules, and the Cu(1) atom lies on an inversion center. The metal coordination is square planar with the Cu-N bond distances that are significantly longer than the Cu-O ones. The arrangement of the two **L60** surrounding each metal gives rise to a *trans* geometry. The three molecular entities comprising the unit cell may be described as a trimer according to the presence of very weak interactions between the metal and the oxygen atoms of superimposed molecules.

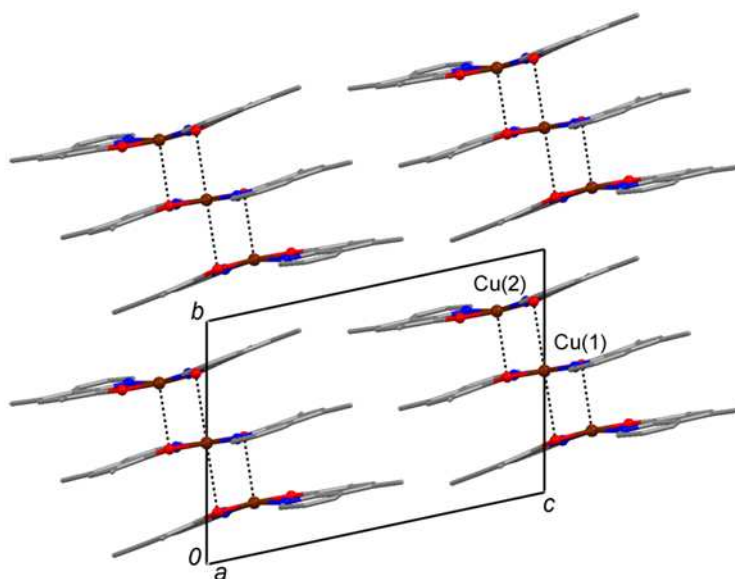


Figure 104. Above, molecular structures of **60**. The Cu(1) atom lies on an inversion center, symmetry code $' = -x; 1-y; -z$. Selected bond distances are reported in Å. C (grey), H (white), N (blue), O (red), Cu (brown). Below, crystal packing of **60** projected along the *a* crystallographic axis.

9.3.2. Stability constants determination.

The stability constants of **56** and **58** were determined by potentiometry in a 1:1 DMSO:water (w/w) solution. The Cu(II) complexes with these ligands were remarkably stable, with $\text{Log } \beta_1$ and $\text{Log } \beta_2$ values on the order of 11.5 and 22.5 for both **58** and **56** (Table 10). Previous studies reported the stability of these ligands in water, although most studies were performed in water/organic mixtures such as alcohol¹⁷⁷ or water/dioxane mixtures¹⁷⁸ to address solubility problems. These studies reported formation constants that fall in the range $\text{Log } \beta_1$ 11-14 and $\text{Log } \beta_2$ 22-25. In this study, we used a DMSO:water mixture as an attempt to increase the solubility of the various species in order to determine the stability constants in homogeneous conditions. Unfortunately, the poor solubility of the remaining ligands (or their complexes) in this mixture made it difficult to measure the stability constants for the other complexes. Our values fall within the range determined in different solvents, showing that the presence of DMSO does not significantly affect the stability of the complexes. Moreover, the similarity of the values of $\text{Log } \beta$ for **56** and **58** suggests that any interaction between the $[\text{Cu}(\text{L})]$ species and a ligand molecule via the sulfonate group (as found in the solid state) is negligible in solution. The influence exerted by the substituents in the 5 and 7 positions on the hydroxyquinoline moiety is also expected to have minimal steric influence on the geometry of the Cu(II) complexes and therefore on their stability due to the positioning of these groups at the exterior of the coordination site.

Interestingly, the $[\text{Cu}(\text{L})_2]$ compounds can precipitate out as solids when using the 1:1 molar ratio (except those with the **L56** and **L57** ligands that form complexes with Cu:L 1:1 stoichiometry). This behavior can be accounted for by their $\text{Log } \beta$ values: in fact, the stability constants of the coordination of Cu(II) with the first ligand (giving $[\text{Cu}(\text{L})]$, $\text{Log } \beta_1$) and the second ligand ($[\text{Cu}(\text{L})_2]$, $\text{Log } K_2 = \text{Log } \beta_2 - \text{Log } \beta_1$) are approximately the same. As a result, the amount of $[\text{Cu}(\text{L})_2]$ in solution for a HL:Cu(II) ratio of 1 is quite high (ca. 20 % total copper for both ligands), likely leading to the precipitation of this neutral complex from the solution. This finding is in agreement with the poor solubility of the $[\text{Cu}(\text{L})_2]$ complex with **L58** (ca. 10^{-6} M), which precipitates out of solution at a HL:Cu(II) ratio greater than 1.2, even at pH ca. 4.5 and C_{Cu} ca. 10^{-4} M.

Table 10. Logarithms of proton dissociation and of complex formation constants of the [Cu(L)] and [Cu(L)₂] complexes for the ligands **L58** and **L56** in DMSO:water 1:1 (w/w) (*T* = 25.0 ± 0.1 °C and *I* = 0.1 M (KCl). The p*K*_a values refer to the ligands in the H₂L form. Charges are omitted for simplicity.

Ligand	p <i>K</i> _{a1} , p <i>K</i> _{a2}	Log β ₁ , Log β ₂
L58	3.99(1), 10.53(1)	11.26(4), 22.31(3)
L56	3.14(4), 9.26(2)	11.72(9), 22.76(7)

For both ligands, the first proton dissociation occurs with a p*K*_a of 3.1-4 and is associated to the release of the proton from the protonated quinolinic nitrogen atom. The second dissociation, occurring with p*K*_a values of 9.2-10.5, is associated to the release of protons from the hydroxyl group. Due to its low basicity, the sulfonate group results always deprotonated in the pH ranges where the measurements have been performed (2-11). On the basis of these protonation constants, it results that the predominant forms of the ligands at pH 7.4 are the neutral form HL for **L58** and the negative charged HL⁻ for **L56**. These protonation constants are quite similar to those reported for alcoholic solutions of the two ligands, at a 0.1 M ionic strength and *T* = 25 °C (**L58**: 4.97, 9.65; **L56**: 3.90, 8.37)¹⁷⁹. Both for our experimental values and for the literature ones, the presence of sulfonate group in position 5 produces a decrease in the p*K*_{a2} value.

Since the stability constant values are the same for **58** as well as for the sulfonate-containing **56**, it can be expected that the interaction between the sulfonate group and Cu(II) of a [CuL] unit present in the solid state is actually absent in solution. Furthermore these similar values suggest that the formation constants for the ligands in the series we are presenting in this work might fall in the same order of magnitude, being the donor atoms set the same, with similar molecular geometries. As a result, these values show that the stability of these hydroxoquinolinic ligands is remarkably high (Log β₁ *ca.* 22) even in the presence of a large excess of a competing, soft monodentate ligand such as DMSO, and that the values determined in this medium (DMSO:water 1:1 (w/w)) compare very well with those reported for the same systems in both aqueous and water/organic solvent mixtures.^{180,181}

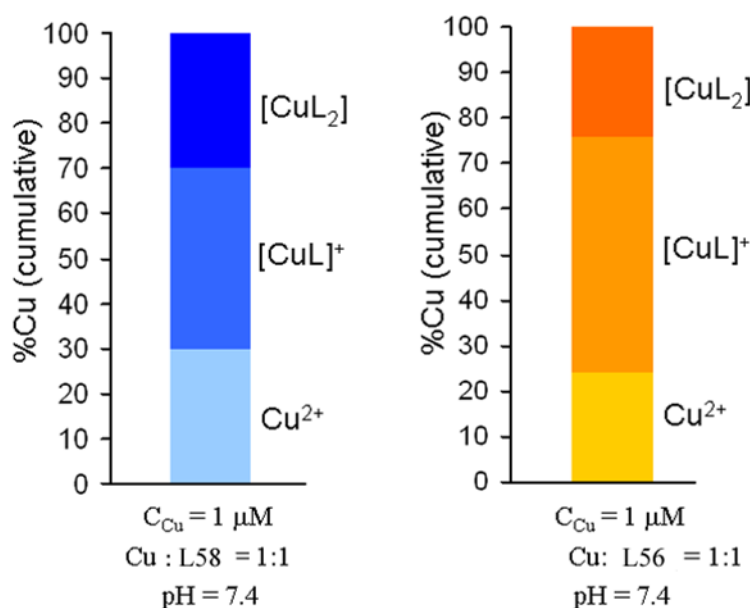
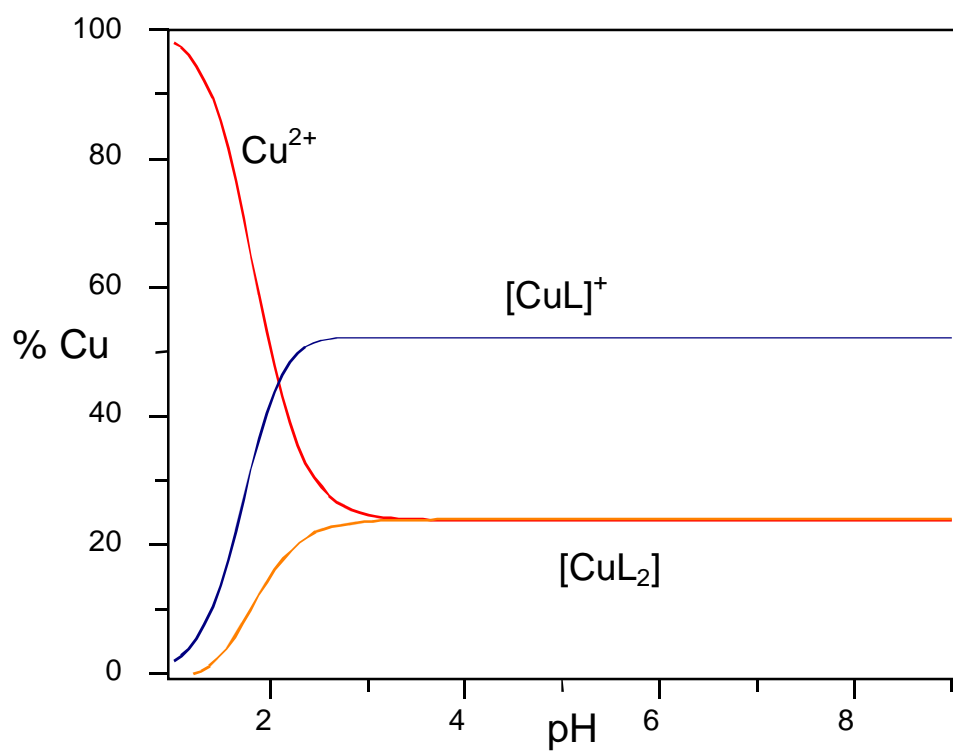


Figure 105. Expected concentrations of the indicated species, calculated in accordance with the reported Log β₁ and Log β₂, at the concentration of 1 μM in the absence of other competitors for copper binding



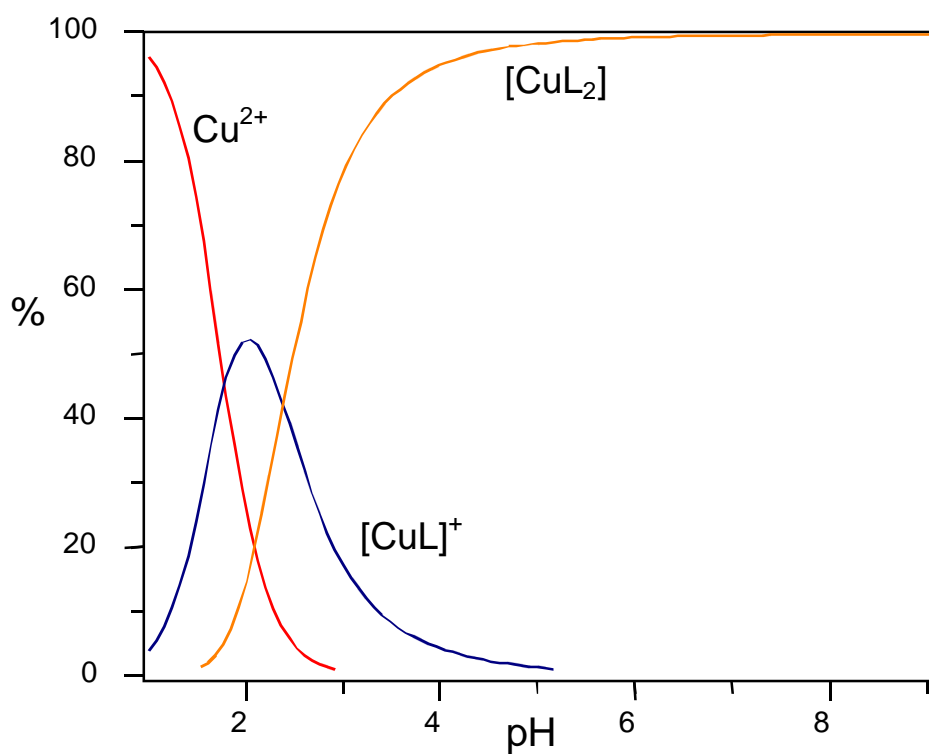
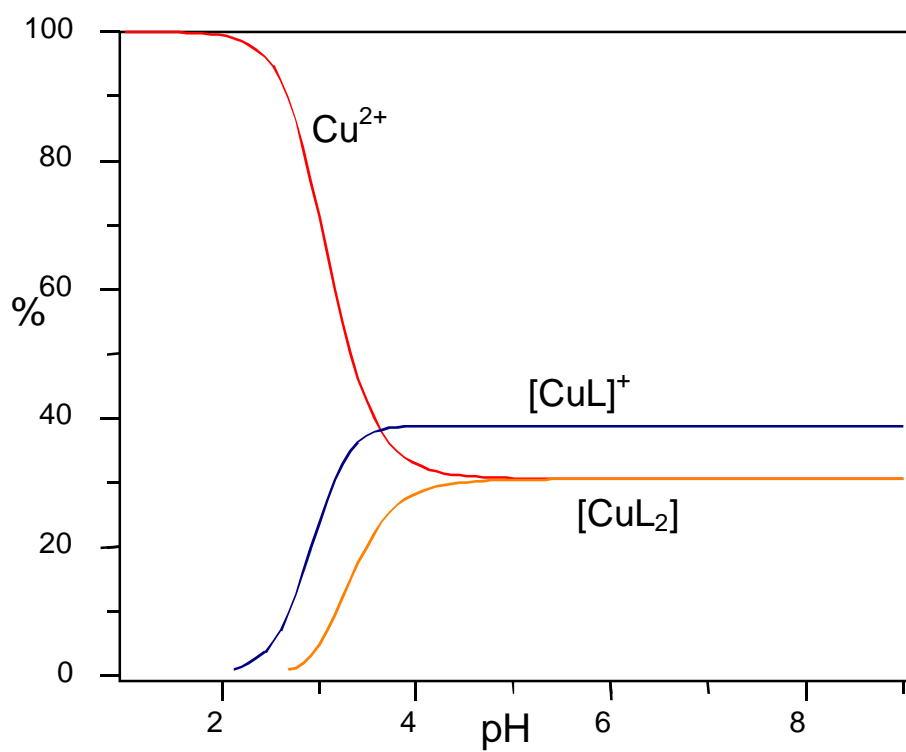


Figure 106. Distribution diagrams of the system $\text{Cu}^{2+}/\text{L56}$. Above, $\text{Cu}^{2+}/\text{L56} = 1/1$, $C_{\text{Cu}} = 1 \times 10^{-3}$ M. Below, $\text{Cu}^{2+}/\text{L56} = 1/2$, $C_{\text{Cu}} = 1 \times 10^{-3}$ M.



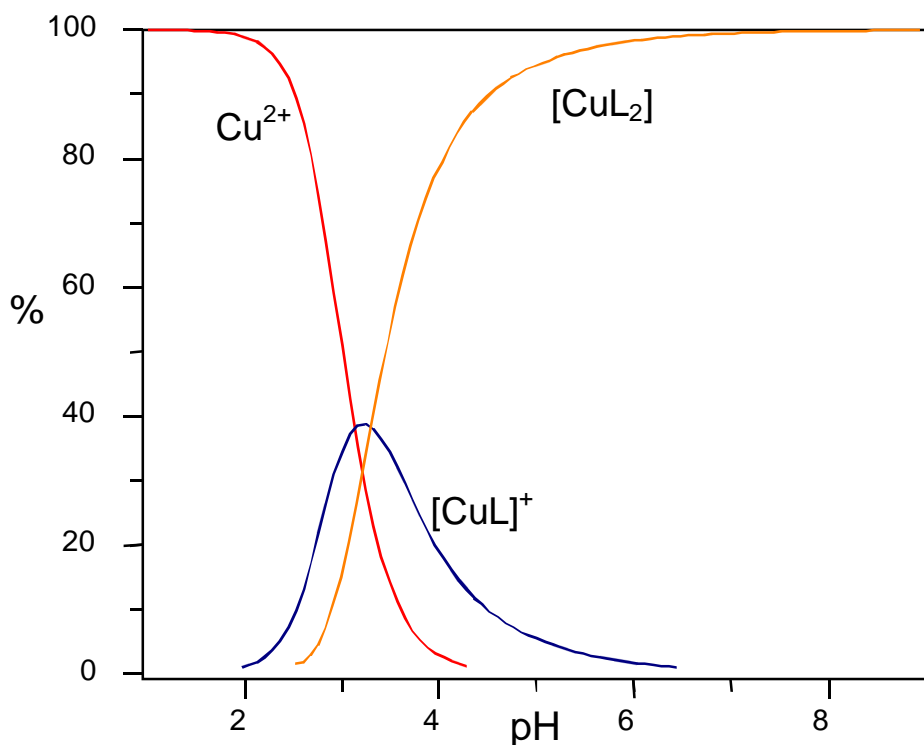


Figure 107. Distribution diagrams of the system $\text{Cu}^{2+}/\text{L58}$. Above, $\text{Cu}^{2+}/\text{L58} = 1/1$, $C_{\text{Cu}} = 1 \times 10^{-3}$ M. Below, $\text{Cu}^{2+}/\text{L58} = 1/2$, $C_{\text{Cu}} = 1 \times 10^{-3}$ M.

9.3.3 Citotoxicity

The cytotoxic potential of the ligands has been evaluated in two human tumor cell lines derived from cervical carcinoma, HeLa, and prostatic adenocarcinoma, PC3. As shown in Figure 108, all ligands present cytotoxic activity except for **L56** and **L57**, which are almost ineffective on both cell lines up to the maximal concentration employed ($30 \mu\text{M}$). For six out of the eight **L58** derivatives, adding an equimolar amount of CuCl_2 dramatically increases the effect of the ligands in both HeLa and PC3 cells, decreasing the IC_{50} values of the active ligands in both cell models. The addition of copper shifts the range of ligands IC_{50} from $13.5\text{--}25.2 \mu\text{M}$ to $1.9\text{--}12.8 \mu\text{M}$ and from $8.6\text{--}25.7 \mu\text{M}$ to $1.3\text{--}16.2 \mu\text{M}$, in HeLa and PC3, respectively (Figure 108).

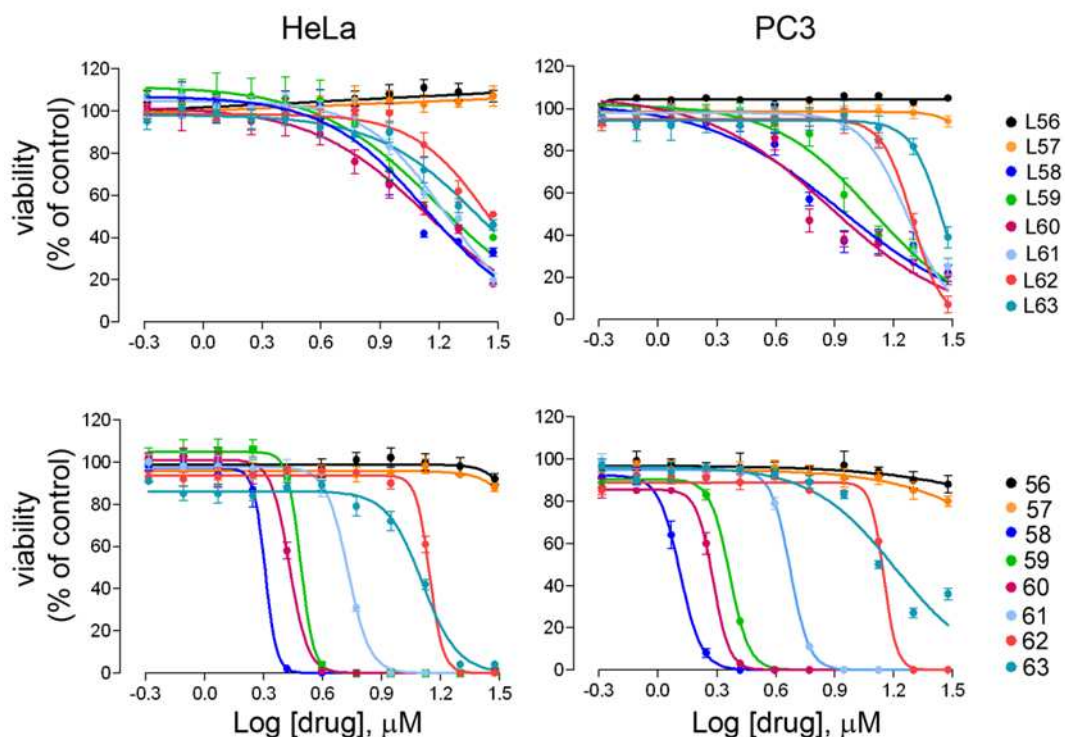
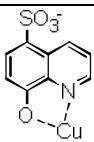
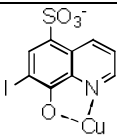
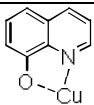
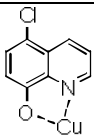
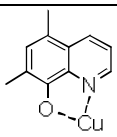
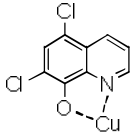
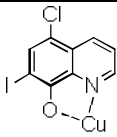


Figure 108. Dose-response curves for ligands and copper complexes in HeLa and PC3 cells. HeLa and PC3 cells were incubated for 48 h with different concentrations of ligands (upper panels) or copper complexes (lower panels). Cell viability after treatment was assessed using the resazurin method. The data presented are the means \pm SEM of three independent experiments, each performed in triplicate. Error bars are visible when larger than the symbols.

Figure 109. Schematic depiction of the molecular structures of the copper complexes^a together with the IC₅₀ (μM) values^b in HeLa and PC3 human tumor cell lines.

Complex	Structure	Ligand	IC ₅₀	IC ₅₀
		LogP	(HeLa)	(PC3)
56		-0.21	n.d.	n.d.
57		0.70	n.d.	n.d.
58		1.84	1.9	1.3
59		2.58	3.1	2.3
60		2.66	2.7	1.9
61		3.22	5.3	4.7
62		3.50	8.9	9.0

^a Only the CuL fragment is depicted. ^b The cytotoxic activity is measured for mixtures composed of CuCl₂ and hydroxyquinoline derivatives in a 1:1 molar ratio.

Interestingly, a non-linear correlation between the lipophilic character of the ligand, which is modulated by the peripheral functional groups, and the cytotoxic activity of the corresponding copper complex was found. When the ligands are ranked by increasing lipophilic character, i.e., with increasing LogP values, the activities of the corresponding complexes describe a bell-shaped curve (Figure 110). According to this relationship, the highest cytotoxic activity is expected to be exhibited by ligands with intermediate LogP values, namely between 1.5 and 3.

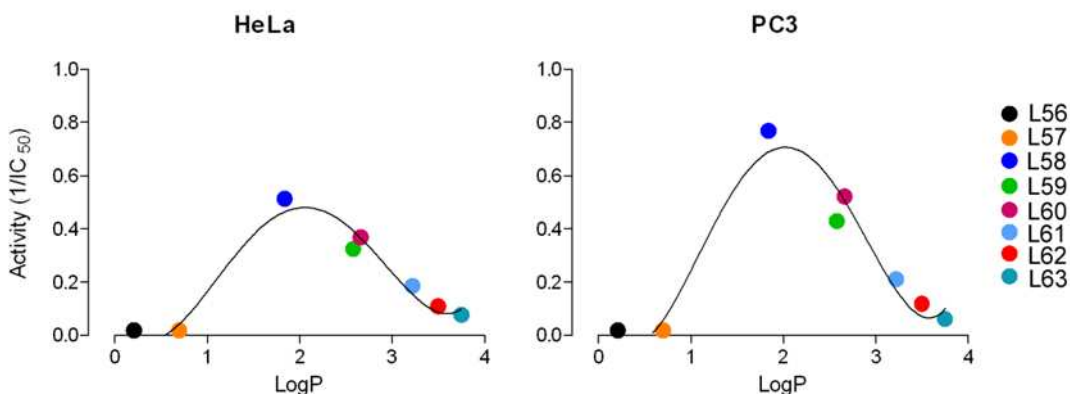


Figure 110. Correlation between cytotoxic activity of copper complexes and ligand LogP. The activities of the copper complexes, calculated as the inverse of IC₅₀ in HeLa and PC3 cells, were matched with corresponding ligand LogP values. The curves were extrapolated with the GraphPad Prism software.

Although the complex **62** is significantly less active than **58** in both cell lines, we decided to further investigate its biological behavior, given the known and documented use of clioquinol as a drug¹⁸² and the recent attention paid to its anticancer potential *in vitro* and *in vivo*.^{174,183} It has been reported that the cytotoxicity induced by clioquinol is maximally increased by the presence of copper and is associated with caspase activation. To assess whether the metal and/or caspases are

required for the Cu(CQ) cytotoxic effect, HeLa and PC3 cells were incubated with increasing doses of Cu(CQ) in the presence of a high affine extracellular copper chelator, ammonium tetrathiomolybdate (TM). The addition of TM dramatically reduces the cytotoxic effect of the complex: the IC_{50} of **62** moves from 9 μ M and 8.9 μ M to 24.5 μ M and 21.5 μ M in HeLa and PC3, respectively, and the dose-response profile of the complex in the presence of TM becomes similar to that of the **L62** ligand alone. Interestingly, higher doses of TM have a moderately toxic effect on HeLa cells, as shown by the dose-response curve of **62** in the presence of 40 μ M TM. To directly assess the effect of **62** on cellular copper homeostasis, the intracellular content of the metal has been measured by means of ICP-AES in cells treated for different times with 14 μ M **62**. A marked time-dependent accumulation of copper can be observed in both cell models (Figure 111B), with the maximal effect being evident after 6 h, when copper content is 70- and 50-fold increased in HeLa and PC3 cells, respectively, with respect to control (untreated cells). As expected, the simultaneous incubation of the cells with **62** and 20 μ M TM lowers the intracellular copper content to values comparable to those of untreated cells (Figure 111), thus confirming the ionophoric properties of clioquinol.

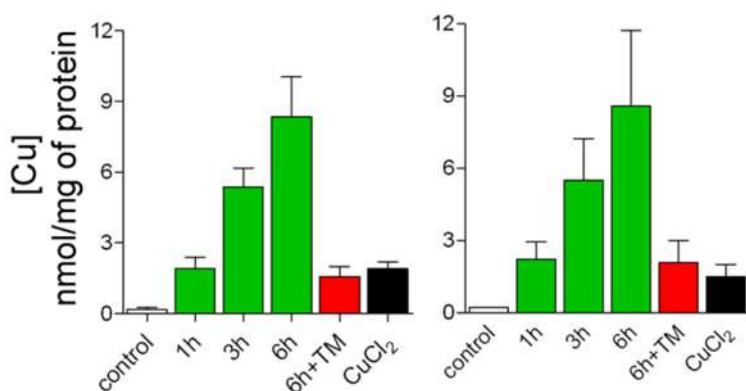
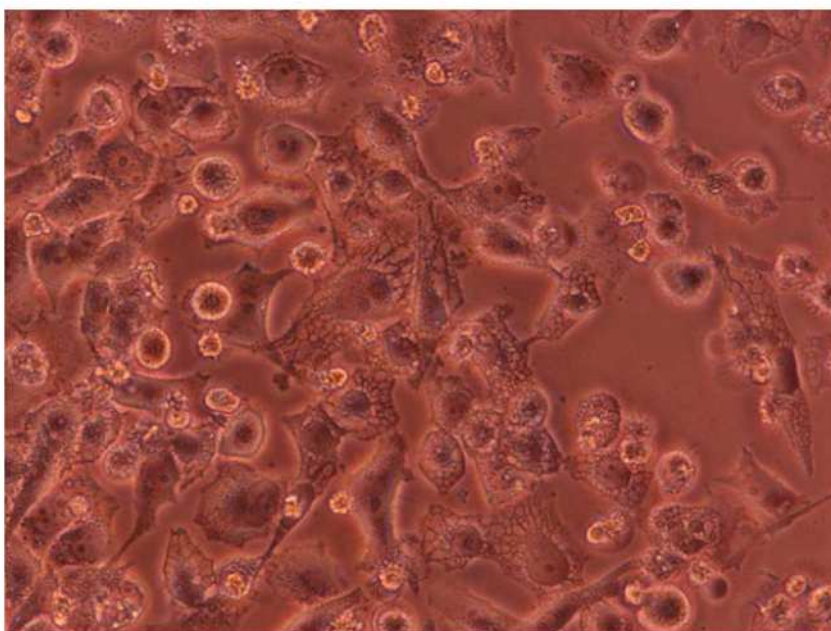


Figure 111. Characterization of **62**-dependent cytotoxicity. HeLa and PC3 cells were treated for 48 h with different concentrations of **L62** or **62**, either in the absence or presence of 20 μ M TM or 50 μ M z-VAD. Cell viability was assayed using the resazurin method. The data presented are the means \pm SEM of three independent experiments, each performed in quadruplicate. Error bars are visible when larger than the symbols.

These results confirm the ionophoric nature of **L58** derivatives for copper, and highlights the ligand hydrophobicity as a determinant of the activity of the complex.

CHAPTER 10

Synthesis of Copper(II) complexes with functionalized quinoline derivatives. Study of the citotoxic activity on cancer human cells.



In this chapter we report a series of ligand that derives by the 8-HQ described in the previous chapter.. Sixteen ligands were synthesized by addition of a substituted aromatic side arm with potential coordinating ability to 8-hydroxyquinoline and 5,7-dichloro-8-hydroxyquinoline, to investigate how different chelating abilities could affect cytotoxic activity. The ligands were tested on the human tumor cell line HeLa (cervical carcinoma), alone and in presence of equimolar quantities of CuCl_2 . The molecular structures of some Cu(II) complexes were ascertained by means of single crystal X-ray diffraction.

Acoording to biological tests, some of the ligands have showed considerable cytotoxic activity. In agreement with previous studies (Chapter 8 and 9), a different behavior between ligands and Cu(II) complexes emerged. In fact, cuprocomplexes exhibited always significantly higher activities with respect to the ligands. Some ligands are fairly cytotoxic, but the simultaneous administration of CuCl_2 always increases their antitumor efficacy.

10.1 Introduction

The biological properties of 8-hydroxyquinoline (8-HQ), **L58**, and of its derivatives was studied and a great amount of data can be found in literature. 8-HQ and its alogenated derivatives have long been known for their antimicrobial and fungicide action; nowadays they are commonly used as constituents of antiseptics, antimicrobials and fungicides¹⁸⁴. In particular oxine-copper $\text{Cu}(\text{8-HQ})_2$ (**58**) complex is extensively used as fungicide thanks to its low toxicity (4700 mg/kg for rats and 9000 mg/kg for mice and a reference suggested dose of 0.05 mg/kg per day)¹²⁴.

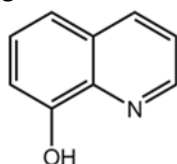


Figure 112. Schematic structure of 8-hydroxyquinoline **L58**.

The most known and discussed alogenated derivative of 8-hydroxyquinoline is clioquinol (5-chloro-7-iodo-8-hydroxyquinoline, abbreviated (CQ, **L62**), which has been used since the first half of the twentieth century as an antibiotic for the treatment of diarrhea and skin infections. In the 1970's it was claimed to be the cause of an epidemic spread of subacute myelo-optic neuropathy (SMON) in Japan and therefore banned in many countries. The link between CQ and SMON was never confirmed, and the pathology was linked to a deficiency in vitamin B12¹⁷⁴. Lately **L62** has drawn attention for its anti-Alzheimer ability and as a potential antitumoral agent¹⁸⁵.

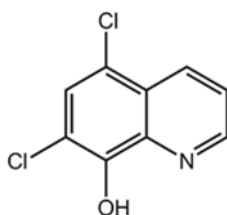


Figure 113. Schematic structure of clioquinol.

8HQs are excellent metal chelators; for instance $\log\beta_1$ and $\log\beta_2$ for the complex **58** are respectively 12.0 and 22.9¹⁸⁴ and the pKa for the deprotonation of the phenolic group is 9.54 for **L58** and 8.07 for **L62**, low enough to allow deprotonation by coordination^{184,185}. Thus, these compounds can exhibit a wide range of biological functions related to metal transportation. It has been shown that **L58** and **L62** act as

Zn(II) and Cu(II) ionophore, increasing the uptake of the metals into the cytosol; they can raise the concentration of Cu inside the cell of 135% for **L58** and of 55% for **L62**¹⁸⁶. This property has been shown in literature to make quinoline derivatives suitable for anti-Alzheimer drugs^{187,188}, HIV-Integrase inhibition¹⁸⁹, anticancer therapy¹⁹⁰, metal intoxication therapy^{191,192}.

Cytotoxic activity of 8-HQ derivatives has been studied extensively, either alone or complexed with copper and zinc. The majority of the studies on 8-HQ and its alogenated derivatives are related to their copper complexes on the other hand, for more diversely substituted quinolines, fewer studies take into account the role of copper. The most studied complexes are those of **58** and **62**. The copper complexes transfer through the cellular membrane can occur in two ways: by active transport, which involves the pump hCtr1, or by passive transport. For an efficient passive crossing, the characteristics of the molecule are of primary importance; the small dimensions and no net charge are favorable, but above all a suitable lipophilicity is required. As a matter a fact, a too hydrophilic compounds would not be able to cross the membrane, whilst too lipophilic molecules would get stuck inside the membrane. Thus, lipophilicity can sometimes clearly correlate to cytotoxic activity.

Once inside the cytosol, it is likely that the Cu(II) complex is reduced to Cu(I), due to the intra-cellular reducing environment, rich in thiols, leading to a loss of affinity for the ligands and possible substitution³⁹. Cu(I) complex becomes less stabile with hard donors like nitrogen and oxygen, while more stable with soft donors like competing cystein thiols.

The mechanism of action of copper complexes 8-HQ derivatives has been widely discussed, and it appears to be strongly dependent on proteasome inhibition (in cooperation to some extent with oxidative stress caused by formation of ROS) that would successively trigger a programmed cell death (PCD) pathway. While much debate still remains on the type of PCD occurring, it seems that, once the complex is inside the cytosol, proteasome could be its main target.

It has been shown that whilst treatment with **L58** alone on Jurkat cells (T cell leukemia) would result in no proteasome inhibition, treatment with CuCl₂ alone at the same concentration brought to 30% of inhibition of proteasome. Administering the complex **58** gives instead full inhibition of proteasome already at 10 μM. The presence of the copper atom is necessary for activity, but this one is tremendously increased by adding the right ligand. Moreover, treatment with **L58** alone proved to be successful in case of pre-administration of CuCl₂ to the cells. This means that in presence of copper, the ligand could form *in situ* the antiproliferative complex. Finding a ligand with sufficient activity could bring to a double action: sequestration

of copper atoms fundamental for angiogenesis processes and, at the meantime, forming a proteasome inhibiting species. Another hint of the importance of copper chelation over cytotoxicity is the large increase in activity between a clioquinole and their respective Zn(II) and Cu(II) complexes¹⁹³, shown in Table 11.

Table 11. IC₅₀ (μM) for tested compounds and relative Cu(II) complexes on different cell lines.

Compound	Panc-1	HL60	DHL-4
L58	5.89	12.90	2.71
L58+ Cu	2.07	8.60	2.27
L58+ Zn	0.76	7.51	0.69

Figure 114 shows a schematic representation of the hypothesized mechanism of action for quinolinic ionophores such as clioquinol.

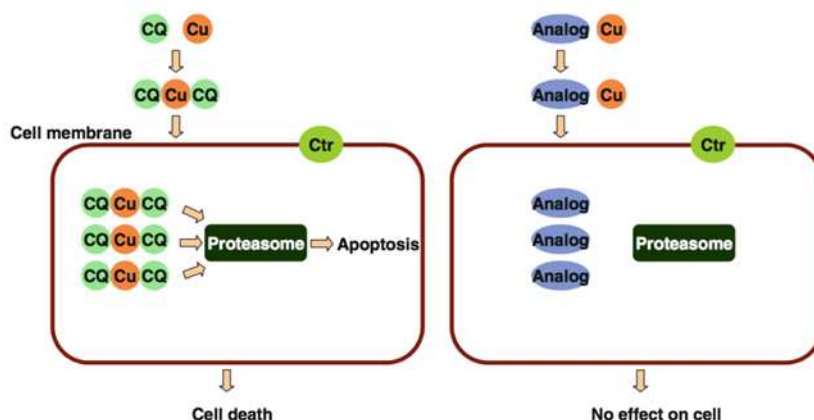


Figure 114. Schematic representation of the mechanism of action of copper ionophores compared to non chelating ligands¹⁸⁶.

In addition, **58** complex was shown to induce DNA damages through formation of ROS in leukemic cell line HL60¹²⁴. This hypothesis was supported by measuring the

intracellular ROS level and by observing that antioxidants like vitamin C and E significantly decrease both ROS generation and DNA damage.

As a continuation of the study presented in chapter 9, we decided to investigate, through a structure/activity relationship study, how the addition of an aromatic side arm with potential coordinating ability to 8-hydroxyquinoline moieties could affect anticancer activity. Moreover, we attempted to determine the effects on cytotoxicity brought by a different mobility of the peripheral arm and by changes in ligand lipophilicity.

Mobility was modulated by introducing between the two aromatic residues a vinylic or an ethylenic linker, while lipophilicity was varied using two quinolinic precursors with different lipophilicity, namely 8-hydroxyquinoline and 5,7-dichloro-8-hydroxyquinoline. A series of 16 diversely substituted ligands was therefore obtained (shown below in Figure 115); the 16 ligands can be divided in two series of eight ligands each, that differ for the type of linker used. Of the eight ligands in each class, six are derivatives of 8-hydroxyquinoline and two are derivatives of 5,7-dichloro-8-hydroxyquinoline.

The ligands were biologically tested for antitumoral activity in different concentrations in presence of equimolar quantities of CuCl_2 on the human tumor cell line HeLa (cervical carcinoma). A correlation was searched for between the exhibited cytotoxicities and structural features, in order to determine common traits leading to better antitumor activities.

Finally, the molecular structures given by a few ligands in presence of CuCl_2 were analyzed by means of X-ray crystallography.

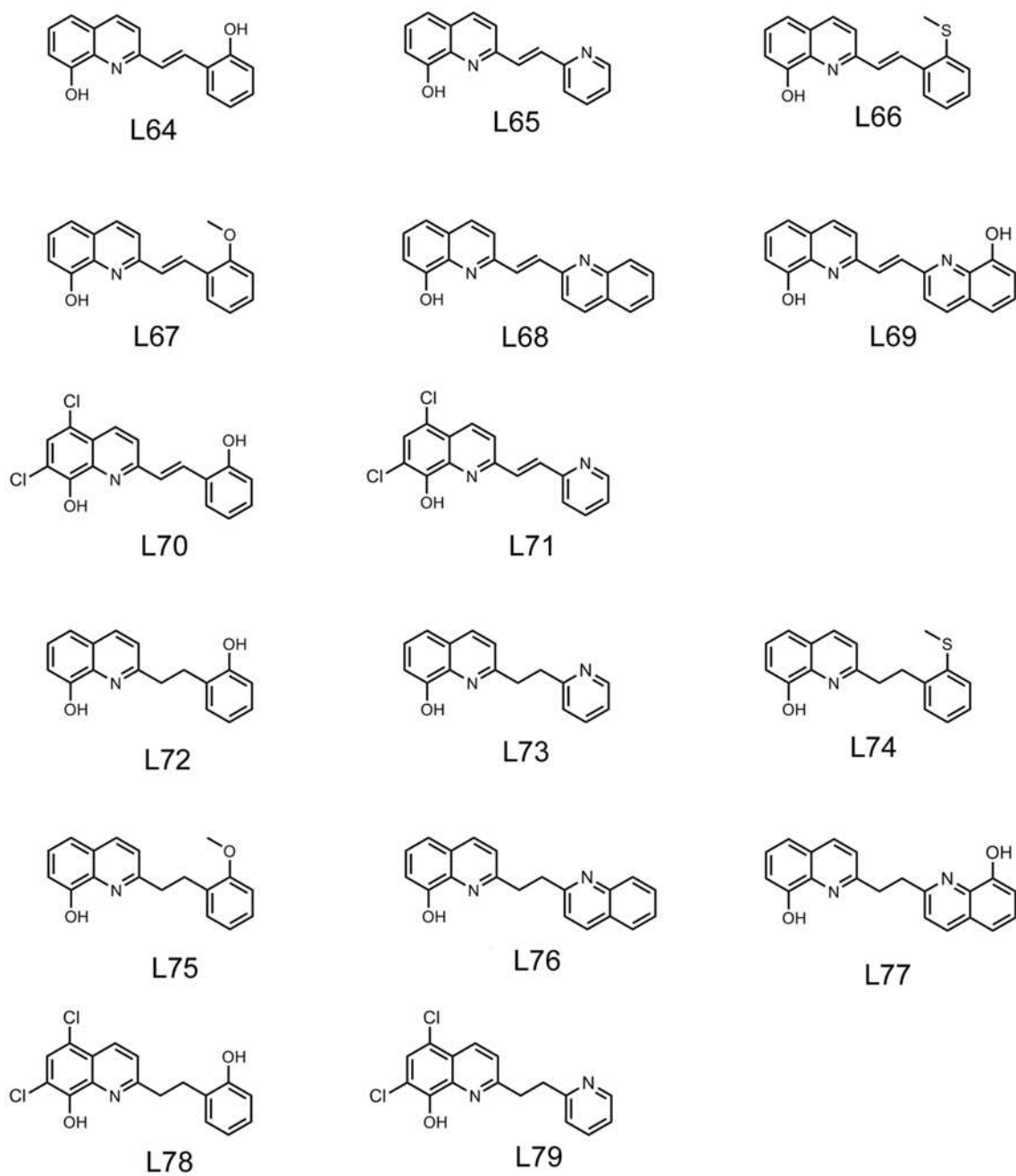


Figure 115. Synthesized ligands.

10.2 Experimental

10.2.1. Synthesis

All reagents were commercially available, except for 2-methoxyaldehyde, which was prepared as reported elsewhere¹⁹⁴. The ligand synthesis were slightly modified from procedures reported in literature^{195,196}. The ¹H-NMR spectra were registered on 300 and 400 MHz Bruker Avance spectrometers using standard pulse sequences. Chemical shifts were reported in parts per million (ppm) and referred to residual solvent protons. Infrared spectra were registered between 4000 and 400 cm⁻¹ on a Perkin-Elmer Nexus FTIR with KBr windows. Elemental analysis (C, H and N) were performed on a Carlo Erba EA 1108 automated analyzer.

Synthesis of 2-(2-hydroxystyryl)quinolin-8-ol (L64). Under nitrogen, 2-methylquinolin-8-ol (1.70 g, 10.70 mmol) and 2-hydroxybenzaldehyde (1.30 ml, 12.42 mmol) were mixed in acetic anhydride (15 ml), and the mixture was heated at 95°C for 72 hours with stirring. After cooling, water (50 ml) was added and stirred for two hours; the mixture was then neutralized using NaOH (10% in water). The product was extracted with dichloromethane (50 ml) and the organic phase was separated from the aqueous one, washed with water (3x30 ml) and Brine (2x30 ml), dried with anhydrous Na₂SO₄ and filtered. The solvent was removed under vacuum and a red powder (1.23 g, 33%) was precipitated with hexane, filtered and vacuum dried. For the deacetylation, the red powder (1.00 g, 3.00 mmol) was added to a solution of sodium methoxide (0.49 g, 9.00 mmol) in methanol (70 ml) and the mixture was stirred for two hours. The mixture was neutralized with HCl (35% in water), the solvent was removed under vacuum and then dichloromethane was added (20 ml). The organic phase was then washed with water (3x30 ml), dried with anhydrous Na₂SO₄, filtered and vacuum dried. The product was recrystallized by dichloromethane/hexane, yielding a pale yellow solid (0.71 g, 90%). Total yield = 30%. IR (cm⁻¹): 3436m, 3386m, 1634m, 1588m, 1555s, 1509s, 1451s, 1392w, 1326m, 1313s, 1255s, 1238s, 1196s, 1155s, 1092s, 971m, 871m, 833s, 754s, 629m, 562m, 495w, 450w. ¹H NMR (300 MHz, Acetone) δ 8.89 (bs, 2H, (2OH)), 8.32 (d, J = 8.6 Hz, 1H), 8.26 (d, J = 16.4 Hz, 1H, (CH=)), 7.85 (d, J = 8.6 Hz, 1H), 7.74 (dd, J₁ = 7.7 Hz, J₂ = 1.5 Hz, 1H), 7.59 (d, J = 16.4 Hz, 1H, (CH=)), 7.43 (m, 2H), 7.24 (td, J₁ = 7.0 Hz, J₂ = 1.0 Hz, 1H), 7.15 (dd, J₁ = 6.9 Hz, J₂ = 1.9 Hz, 1H), 7.04 – 6.91 (m, 2H)

Synthesis of 2-(2-(pyridin-2-yl)vinyl)quinolin-8-ol (L65). The procedure is analogous to that reported for L64. Under nitrogen, 2-methylquinolin-8-ol (1.59 g, 10.00 mmol) and

picolinaldehyde (0.95 ml, 10.00 mmol) were mixed in acetic anhydride (15 ml), and the mixture was heated at 90°C for 72 hours with stirring, yielding, in the first step, a dark glue (0.61 g, 2.22 mmol, 21%) and this crude was added, in the second step, to a solution of sodium methoxide (0.36 g, 6.66 mmol) in methanol (40 ml). The product was a dark oil (0.43 g, 79%) obtained pure without recrystallization. Total yield = 17%. IR (cm⁻¹): 3303w, 3065w, 3040w, 2990w, 1580s, 1555s, 1501s, 1451s, 1426s, 1380m, 1309m, 1280m, 1234s, 1184s, 1138s, 1084w, 967m, 829m, 762m, 733s, 612w, 441m. ¹H NMR (300 MHz, CDCl₃) δ 8.67 (d, J = 3.7 Hz, 1H), 8.09 (d, J = 8.5 Hz, 1H), 7.80 (d, 5.3 Hz, 2H, CH(Ph)), 7.70 (td, J₁ = 13.0 Hz, J₂ = 5.4 Hz, 1H), 7.62 (d, J = 8.5 Hz, 1H), 7.49 (d, J = 7.6 Hz, 1H, CH(Ph)), 7.41 (t, J = 7.9 Hz, 1H, CH(Ph)), 7.33 – 7.25 (m, 1H, CH(Ph)), 7.20 (dd, J₁ = 14.1 Hz, J₂ = 5.0 Hz, 2H, CH(Ph)).

Synthesis of 2-(2-(methylthio)styryl)quinolin-8-ol (L66). The procedure is analogous to that reported for **L64**. Under nitrogen, 2-methylquinolin-8-ol (0.52 g, 3.28 mmol) and 2-(methylthio)benzaldehyde (0.42 ml, 3.28 mmol) were mixed in acetic anhydride (15 ml), and the mixture was heated at 130°C for 72 hours with stirring, yielding, in the first step, a brown oil that was further purified through silica column chromatography (hexane/ethyl acetate 7/3) (0.25 g, 0.76 mmol, 23%) and this crude was added, in the second step, to a solution of sodium methoxide (0.12 g, 2.27 mmol) in methanol (40 ml). The product was a grey powder (0.20 g, 88%) obtained pure without recrystallization. Total yield = 20%. IR (cm⁻¹): 3432m, 3053w, 1626s, 1593s, 1555m, 1501m, 1438s, 1380s, 1326s, 1271m, 1238m, 1159m, 1100s, 954m, 833m, 746s, 616w, 462w. ¹H NMR (400 MHz, CDCl₃) δ 8.19 (d, J = 16.1 Hz, 1H, (CH=)), 8.14 (d, J = 8.6 Hz, 1H), 7.77 – 7.69 (m, 2H, CH(Ph)), 7.43 (t, J = 7.9 Hz, 1H, CH(Ph)), 7.40 – 7.23 (m, 5H, CH(Ph)), 7.20 (d, J = 7.5 Hz, 1H, CH(Ph)), 2.54 (s, J = 8.8 Hz, 3H, (SCH₃)).

Synthesis of 2-(2-methoxystyryl)quinolin-8-ol (L67). The procedure is analogous to that reported for **L64**. Under nitrogen, 2-methylquinolin-8-ol (1.17 g, 7.34 mmol) and 2-methoxybenzaldehyde (1.00 g, 7.34 mmol) were mixed in acetic anhydride (15 ml), and the mixture was heated at 130°C for 72 hours with stirring, yielding a red glue that was recrystallized in dichloromethane/hexane and left in the freezer for 12 hours. A light brown precipitate is obtained (0.87 g, 2.75 mmol, 37%) and this crude was added, in the second step, to a solution of sodium methoxide (0.45 g, 8.50 mmol) in methanol (40 ml). The product was recrystallized in dichloromethane/hexane yielding a yellow powder (0.70 g, 93%). Total yield = 34%. IR (cm⁻¹): 3357w, 3044w, 3003w, 2944w, 2827w, 1622w, 1597s, 1563s, 1513s, 1463s, 1434s, 1392m, 1371m, 1317s, 1238s, 1192s, 1109s, 1079s, 1021s, 954s, 867w, 829s, 787m, 742s, 712s, 612s, 446s. ¹H NMR (400 MHz, CDCl₃) δ 8.11 (s, 1H) 8.08 (d, J=10.2 Hz, 1H, (CH=)), 7.71 (t, J = 8.6

Hz, 2H), 7.46 – 7.38 (m, 2H, CH(Ph)), 7.38 – 7.27 (m, 2H, CH(Ph)), 7.20 (t, $J = 7.5$ Hz, 1H), 7.05 (t, $J = 7.5$ Hz, 1H), 6.97 (d, $J = 8.2$ Hz, 1H), 3.96 (s, 3H, (OCH₃)).

Synthesis of 2-(2-(quinolin-2-yl)vinyl)quinolin-8-ol (L68). The procedure is analogous to that reported for **L64**. Under nitrogen, 2-methylquinolin-8-ol (0.50 g, 3.14 mmol) and 2-quinolincarboxaldehyde (0.50 g, 3.14 mmol) were mixed in acetic anhydride (15 ml), and the mixture was heated at 90°C for 72 hours with stirring, yielding a brown solid that was recrystallized in dichloromethane/hexane to obtain a yellow glue (0.45 g, 1.51 mmol, 48%) and this crude was added, in the second step, to a solution of sodium methoxide (0.21 g, 3.93 mmol) in methanol (40 ml). The product was recrystallized in dichloromethane/hexane. The yellow solution obtained was dried under vacuum yielding a yellow solid (0.28 g, 70%). Total yield = 34%. IR (cm⁻¹): 3349w, 3048w, 1705w, 1593s, 1555m, 1505s, 1463s, 1422s, 1388w, 1346m, 1317m, 1221m, 1184m, 1142m, 996m, 913w, 879w, 833s, 754m, 621w, 546w, 450m. ¹H NMR (400 MHz, CDCl₃) δ 8.18 (d, $J = 8.6$ Hz, 1H, CH(Ph)), 8.15 (d, $J = 8.5$ Hz, 2H, CH(Ph)) 7.99 (d, $J = 16.3$ Hz, 1H, (CH=)), 7.87 (d, $J = 16.3$ Hz, 1H, (CH=)), 7.84 - 7.78 (m, 2H, CH(Ph)), 7.75 (t, $J = 8.5$ Hz, 2H, CH(Ph)), 7.54 (t, $J = 7.4$ Hz, 1H, CH(Ph)), 7.44 (t, $J = 7.9$ Hz, 1H, CH(Ph)), 7.32 (d, $J = 8.1$ Hz, 1H, CH(Ph)), 7.21 (d, $J = 7.5$ Hz, 1H).

Synthesis of 1,2-bis(2-quinolinyl-8-ol)ethene (L69). The procedure is analogous to that reported for **L64**. Under nitrogen, 2-methylquinolin-8-ol (0.55 g, 3.46 mmol) and 8-hydroxy-2-quinolincarboxaldehyde (0.60 g, 3.46 mmol) were mixed in acetic anhydride (15 ml), and the mixture was heated at 90°C for 72 hours with stirring, yielding a light brown glue recrystallized in hot methanol to obtain a yellow powder (0.82 g, 2.12 mmol, 61%) and this crude was added, in the second step, to a solution of sodium methoxide (0.33 g, 6.18 mmol) in methanol (40 ml). The product was a pale yellow powder (0.51 g, 79%) obtained pure without recrystallization. Total yield = 48%. IR (cm⁻¹): 3340m, 3036w, 2919w, 2852w, 1588m, 1559m, 1505s, 1463s, 1434m, 1352 s, 1313s, 1230m, 1180m, 1150m, 1088 m, 979m, 883w, 833s, 746s, 704w, 579w, 546w, 437m. ¹H NMR (300 MHz, CDCl₃) δ 8.19 (d, $J = 8.6$ Hz, 2H), 7.93 (s, 2H, (CH=)), 7.77 (d, $J = 8.6$ Hz, 2H), 7.45 (t, $J = 8.0$ Hz, 2H), 7.34 (dd, $J_1 = 8.2$ Hz, $J_2 = 1.1$ Hz, 2H), 7.21 (dd, $J_1 = 7.5$ Hz, $J_2 = 1.2$ Hz, 2H).

Synthesis of 5,7-dichloro-2-(2-hydroxystyryl)quinolin-8-ol (L70). The procedure is analogous to that reported for **L64**. Under nitrogen, 5,7-dichloro-2-methylquinolin-8-ol (1.01 g, 4.43 mmol) and 2-hydroxybenzaldehyde (0.92 ml, 4.43 mmol) were mixed in acetic anhydride (15 ml), and the mixture was heated at 90°C for 72 hours with stirring, yielding a dark glue recrystallized in dichloromethane/hexane obtaining a

light brown powder (0.61 g, 1.50 mmol, 34%) and this crude was added, in the second step, to a solution of sodium methoxide (0.24 g, 4.49 mmol) in methanol (40 ml). The product was a red powder (0.50 g, 98%) obtained pure without recrystallization. Total yield = 33%. IR (cm^{-1}): 3441m, 3345m, 3065w, 1580s, 1551s, 1492s, 1438s, 1384s, 1338m, 1305s, 1213s, 1184s, 1138s, 1088m, 1004m, 963s, 938m, 850m, 817m, 737s, 721s, 596w, 571w. ^1H NMR (300 MHz, MeOD) δ 8.38 (d, J = 8.9 Hz, 1H, (B)), 8.15 (d, J = 16.5 Hz, 1H, (CH=)), 7.82 (d, J = 8.9 Hz, 1H), 7.63 (d, J = 7.0 Hz, 1H), 7.47 (d + s, J = 8.2 Hz, 2H, (CH= + H)), 7.15 (t, J = 7.7 Hz, 1H), 6.86 (t + d, J = 7.3 Hz, 2H).

Synthesis of 5,7-dichloro-2-(2-(pyridin-2-yl)vinyl)quinolin-8-ol (L71). The procedure is analogous to that reported for **L64**. Under nitrogen, 5,7-dichloro-2-methylquinolin-8-ol (1.50 g, 6.57 mmol) and picolinaldehyde (0.60 ml, 6.57 mmol) were mixed in acetic anhydride (15 ml), and the mixture was heated at 90°C for 72 hours with stirring, yielding a dark red glue that was recrystallized in dichloromethane/hexane to obtain a black powder (1.07 g, 2.97 mmol, 45%) and this crude was added, in the second step, to a solution of sodium methoxide (0.41 g, 8.91 mmol) in methanol (40 ml). The product was recrystallized in dichloromethane/hexane yielding a brown powder (0.79 g, 84%). Total yield = 38%. IR (cm^{-1}): 3382m, 1626w, 1584m, 1555m, 1522m, 1430s, 1346s, 1146s, 1113s, 988w, 954m, 871w, 812m, 767m, 737m, 637m, 608m, 550w, 508w. ^1H NMR (300 MHz, MeOD) δ 8.55 (d, J = 4.8 Hz, 1H), 8.38 (d, J = 8.8 Hz, 1H), 7.90 – 7.79 (m, 4H, CH(Ph)), 7.75 (d, J = 7.9 Hz, 1H, CH(Ph)), 7.48 (s, 1H), 7.35 – 7.27 (m, 1H).

Synthesis of 2-(2-hydroxyphenylethyl)quinolin-8-ol (L72). After two H_2 cycles to rinse the Parr vessel with hydrogen, the mixture of **L64** (0.50 g, 1.90 mmol) and 10% Pd/C (5% in weight of the substrate) in EtOH (50 ml) was vigorously stirred at room temperature under 2 atm of hydrogen for 12 hours. The reaction mixture was filtered and the filtrate was concentrated to provide a white precipitate, which was filtered and washed with hexane. A white powder was obtained (0.250 g, 51%). Final yield = 15%. IR (cm^{-1}): 3203s, 2936w, 2911w, 2886w, 1605m, 1563s, 1484s, 1426s, 1363m, 1271s, 1242s, 1205m, 1079m, 1059m, 933w, 838m, 800m, 762s, 725w, 554w, 483w. ^1H NMR (400 MHz, Acetone) δ 8.71 (bs, 1H, (OH)), 8.40 (bs, 1H, (OH)), 8.21 (d, J = 8.5 Hz, 1H), 7.45 (d, J = 8.5 Hz, 1H), 7.34 (m, 2H), 7.16 (dd, J_1 = 7.4 Hz, J_2 = 1.3 Hz, 1H), 7.11 (dd, J_1 = 7.3 Hz, J_2 = 1.3 Hz, 1H), 7.03 (td, J_1 = 7.8 Hz, J_2 = 1.6 Hz, 1H), 6.87 (d, J = 7.9 Hz, 1H), 6.75 (t, J = 7.4 Hz, 1H), 3.33 (m, 2H, (CH_2)), 3.22 (m, 2H, (CH_2)).

Synthesis of 2-(2-(pyridin-2-yl)ethyl)quinolin-8-ol (L73). After two H_2 cycles to rinse the Parr vessel with hydrogen, the mixture of **L65** (0.72 g, 2.89 mmol) and 10% Pd/C (5%

in weight of the substrate) in EtOH (50 ml) was vigorously stirred at room temperature under 2 atm of hydrogen for 72 hours. The reaction mixture was filtered and the filtrate was concentrated to provide a brown oil (0.64 g, 88%). Final yield = 15%. IR (cm⁻¹): 3375m 3044w 2925w 1592s 1571s 1503s 1474s 1427s 1325 m 1244m 1202w 1155w 1083w 994w 828 m 748m 599w. ¹H NMR (300 MHz, CDCl₃) δ 8.68 (d, J = 4.8 Hz, 1H), 8.09 (d, J = 8.4 Hz, 1H), 7.75 (td, J₁ = 7.6 Hz, J₂ = 6.3 Hz, 1H), 7.45 – 7.21 (m, 6H, CH(Ph)), 3.60 – 3.43 (m, 4H, (2CH₂)).

Synthesis of 2-(2-(methylthio)phenylethyl)quinolin-8-ol (L74). After two H₂ cycles to rinse the Parr vessel with hydrogen, the mixture of **L66** (0.20 g, 0.67 mmol) and 10% Pd/C (5% in weight of the substrate) in EtOH (50 ml) was vigorously stirred at room temperature under 2.5 atm of hydrogen for 72 hours. The reaction mixture was filtered, the filtrate was concentrated and recrystallized in warm diethyl ether using an ultrasound emitter, to provide a yellow solution, which was evaporated, obtaining a yellow oil (0.15 g, 77%). Final yield = 16%. IR (cm⁻¹): 3378w, 3053w, 2915w, 2848w, 1597m, 1576m, 1505s, 1467s, 1434m, 1371m, 1326w, 1234s, 1205m, 1088m, 1042w, 967w, 833m, 746s, 600w, 466w. ¹H NMR (400 MHz, CDCl₃) δ 8.08 (d, J = 8.4 Hz, 1H), 7.42 (t, J = 7.9 Hz, 1H, CH(Ph)), 7.33 (t, J = 8.9 Hz, 2H, CH(Ph)), 7.25 (m, 2H, CH(Ph)), 7.19 (d, J = 7.5 Hz, 2H, CH(Ph)), 7.13 – 7.07 (m, 1H, CH(Ph)), 3.39 – 3.32 (m, 2H, (CH₂)), 3.32 – 3.26 (m, 2H, (CH₂)), 2.53 (s, 3H, (SCH₃)).

Synthesis of 2-(2-methoxyphenylethyl)quinolin-8-ol (L75). After two H₂ cycles to rinse the Parr vessel with hydrogen, the mixture of **L67** (0.20 g, 0.72 mmol) and 10% Pd/C (5% in weight of the substrate) in EtOH (50 ml) was vigorously stirred at room temperature under 0.8 atm of hydrogen for one hour. The reaction mixture was filtered and the filtrate was concentrated to provide a brown powder (0.14 g, 70%). Final yield = 24%. IR (cm⁻¹): 3353m, 3011w, 2948w, 2932w, 2831w, 1605m, 1572m, 1513s, 1497s, 1484s, 1371m, 1317m, 1238s, 1155m, 1104s, 1025s, 967w, 829s, 750s, 725m, 621m, 466w. ¹H NMR (400 MHz, CDCl₃) δ 8.07 (d, J = 8.4 Hz, 1H), 7.46 – 7.38 (m, 1H, CH(Ph)), 7.33 – 7.29 (m, 2H, CH(Ph)), 7.23 (td, J₁ = 7.5 Hz, J₂ = 1.4 Hz, 1H, CH(Ph)), 7.18 (td, J₁ = 7.5 Hz, J₂ = 1.4 Hz, 2H, CH(Ph)), 6.92 – 6.85 (m, 2H, CH(Ph)), 3.85 (s, 3H, (OCH₃)), 3.32 (m, 2H, (CH₂)), 3.20 (m, 2H, (CH₂)).

Synthesis of 2-(2-(quinolin-2-yl)ethyl)quinolin-8-ol (L76). After two H₂ cycles to rinse the Parr vessel with hydrogen, the mixture of **L68** (0.26 g, 0.86 mmol) and 10% Pd/C (5% in weight of the substrate) in EtOH (50 ml) was vigorously stirred at room temperature under 0.8 atm of hydrogen for one hour. The reaction mixture was filtered and the filtrate was concentrated to provide a brown powder (0.15 g, 56%).

Final yield = 19%. IR (cm⁻¹): 3384w, 3049w, 2921w, 1597m, 1563m, 1508s, 1469m, 1427m, 1376m, 1325m, 1240m, 1193w, 1134w, 1083w, 833m, 743m, 667w, 612w, 472w. ¹H NMR (400 MHz, MeOD) δ 8.25 (d, J = 8.5 Hz, 1H, CH(Ph)), 8.13 (d, J = 8.4 Hz, 1H, CH(Ph)), 8.02 (d, J = 8.5 Hz, 1H, CH(Ph)), 7.89 (d, J = 8.1 Hz, 1H, CH(Ph)), 7.75 (ddd, J₁ = 8.4 Hz, J₂ = 7.0 Hz, J₃ = 1.4 Hz, 1H, CH(Ph)), 7.56 (t, J = 7.5 Hz, 1H, CH(Ph)), 7.50 (d, J = 8.5 Hz, 1H, CH(Ph)), 7.43 – 7.29 (m, 3H, CH(Ph)), 7.09 (dd, J₁ = 7.4 Hz, J₂ = 1.3 Hz, 1H, (A)), 3.56 (m, 2H, (CH₂)), 3.51 (m, 2H, (CH₂)).

Synthesis of 1,2-bis(2-quinolinyl-8-ol)ethane (L77). After two H₂ cycles to rinse the Parr vessel with hydrogen, the mixture of **L69** (0.38 g, 1.20 mmol) and 10% Pd/C (5% in weight of the substrate) in EtOH (50 ml) was vigorously stirred at room temperature under 0.8 atm of hydrogen for one hour. The reaction mixture was filtered and the filtrate was concentrated to provide a light brown solid, which was recrystallized in hot chloroform/diethyl ether and left in freezer for 12 hours, yielding a dark yellow powder filtered and washed with diethyl ether (0.19 g, 49%). Final yield = 24%. IR (cm⁻¹): 3449w, 3048w, 2932w, 2865w, 1593m, 1563s, 1505s, 1451s, 1392m, 1367m, 1330s, 1271s, 1242s, 1134m, 1088s, 1054m, 829s, 754s, 725s, 541m. ¹H NMR (300 MHz, CDCl₃) δ 8.06 (d, J = 8.4 Hz, 2H), 7.44 – 7.21 (m, 6H, CH(Ph)), 7.14 (d, J = 7.4 Hz, 2H), 3.59 (s, 4H, (2CH₂)).

Synthesis of 5,7-dichloro-2-(2-hydroxyphenylethyl)quinolin-8-ol (L78). To a solution of **L70** (0.10 g, 0.30 mmol) in EtOH (8 ml) hydrate hydrazine (2 ml) was added at 70°C. The mixture was heated under reflux at 80°C for 20 hours. The solvent was then evaporated, the product was extracted with dichloromethane (40 ml) and washed with H₂O (2x20 ml), dried with anhydrous Na₂SO₄ and filtered. The solvent was evaporated under vacuum and a brown solid was obtained, which was recrystallized in dichloromethane/hexane. The brown precipitate was filtered and dried (0.03 g, 25%). Final yield = 9%. ¹H NMR (400 MHz, Acetone) δ 8.39 (d, J = 8.6 Hz, 1H), 7.60 (m, 2H), 7.13 (d, J = 7.4 Hz, 1H), 7.02 (t, J = 7.2 Hz, 1H), 6.88 (d, J = 7.9 Hz, 1H), 6.74 (t, J = 7.4 Hz, 1H), 3.37 (m, 2H, (CH₂)), 3.21 (m, 2H, (CH₂)).

Synthesis of 5,7-dichloro-2-(2-(pyridin-2-yl)ethyl)quinolin-8-ol (L79). The procedure is analogous to that reported for **L78**. The mixture of **L71** (0.65 g, 2.05 mmol) with hydrate hydrazine (13 ml) in EtOH (30 ml) was heated under reflux for 20 hours, yielding a dark yellow solid (0.42 g, 65%), obtained pure without recrystallization. Final yield = 25%. IR (cm⁻¹): 3332w, 3044w, 3011w, 2923w, 2652w, 1584s, 1563s, 1534m, 1488m, 1434s, 1392m, 1346s, 1234m, 1188, 1146w, 1100m, 1004w, 942m, 858m, 817m, 771m, 733m, 616w, 554m. ¹H NMR (300 MHz, CDCl₃) δ 8.55 (d, J = 3.7

Hz, 1H), 8.32 (d, $J = 8.6$ Hz, 1H), 7.58 (td, $J_1 = 7.7$ Hz, $J_2 = 1.6$ Hz, 1H), 7.48 (s, 1H), 7.39 (d, $J = 8.3$ Hz, 1H), 7.19 – 7.07 (m, 2H), 3.47 (m, 2H, (CH₂)), 3.35 (m, 2H, (CH₂)).

10.2.2. X-rays structural determination

A summary of data collection and structure refinement for [Cu(**L64**)]₂, [Cu(**L67**)]₂, **L72** and [Cu(**L73**)]₂ is reported in Appendix xiii. Single crystal data were collected with a Bruker Smart APEXII area detector diffractometers, Mo K α : $\lambda = 0.71073$ Å. The unit cell parameters were obtained using 60 ω -frames of 0.5° width and scanned from three different zone of reciprocal lattice. The intensity data were integrated from several series of exposures frames (0.3° width) covering the sphere of reciprocal space⁴⁸. An absorption correction was applied using the program SADABS¹⁰⁴. The structures were solved by direct methods (SIR2004) and refined on F² with full-matrix least squares (SHELXL-97⁵⁰), using the Wingx software package⁵¹. The hydrogen atoms were placed at their calculated positions, and the non-hydrogen atoms of [Cu(**L64**)]₂, [Cu(**L67**)]₂ and **L72** were refined anisotropically. Due to the poor data set of [Cu(**L75**)]₂, the atoms in this model were refined with isotropic thermal parameters. Graphical material was prepared with Mercury 3.0⁵² programs.

10.3. Results and Discussion

10.3.1. Ligand synthesis

The synthetic route (Figure 116) comprises three steps: the first two steps lead to the synthesis of the styrylquinolinic compounds **L64-L71** and the third step leads to their reduction to arylethylenquinolinic species **L72-L79**.

The first is a condensation in acetic anhydride, depicted by others as a Perkin-like condensation^{56,57}, between the nucleophilic carbanion of 2-methyl-8-hydroxyquinoline, which is stabilized by resonance, and an appropriate aldehyde. This reaction occurs together with protection of the nucleophilic hydroxyl group of 8-hydroxyquinoline by means of nucleophilic acyl substitution with acetic anhydride, which yields the acetylated intermediate and an acetate ion. Without this protection, the hydroxyl group could act as nucleophile for the aldehydic carbonyl, competing with the formation of the styrylquinoline intermediate and generating unwanted sideproducts.

The reaction mechanism has not been further investigated.

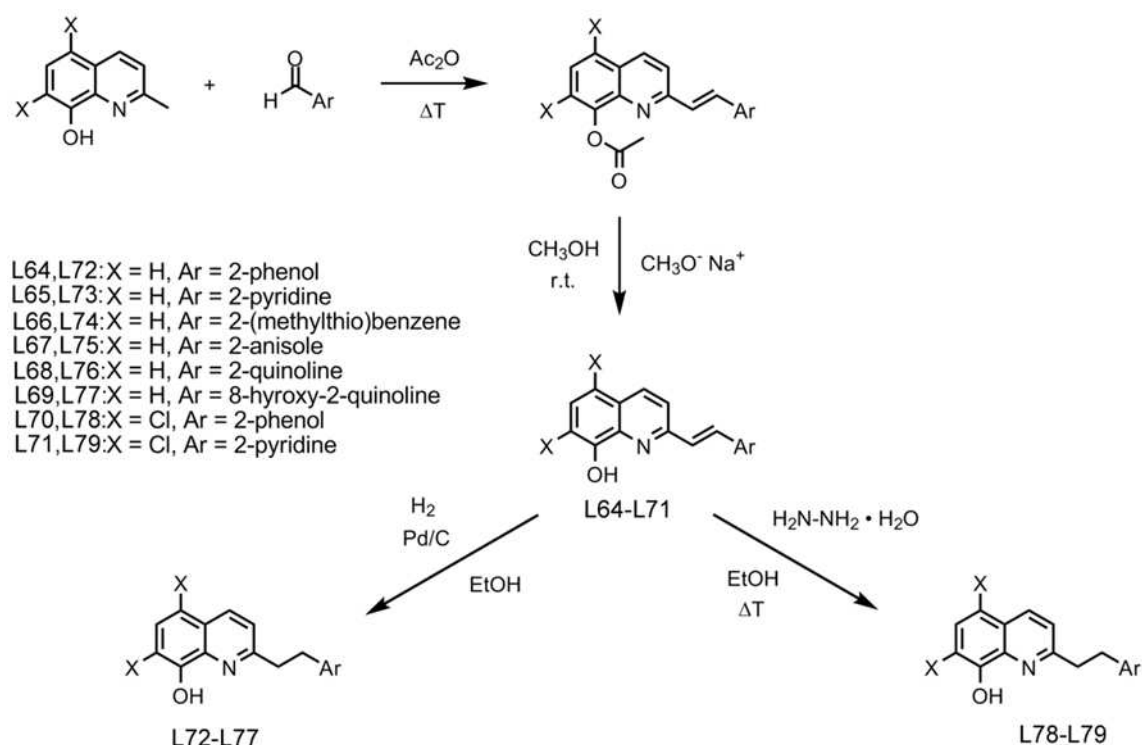


Figure 116. Synthetic scheme.

The yields of this step are modest and range from 25% for compound **L65** (Ar = pyridine, X = H) to 61% for compound **L69** (Ar = 8-HQ, X = H).

The second step is the deacetylation of the intermediate in basic environment by means of NaOCH₃ or NaOH¹⁹⁵. The highly nucleophilic methoxide anion reacts with the 8-acetylic carbonyl, providing methylacetate and the quinolin-8-olate anion, which is subsequently neutralized to obtain the styrylquinolinic product (compounds **L64-L71**). Yields of this step are high and range from 70% for product **L68** (Ar = quinoline, X = H) to 98% for product **L70** (Ar = phenol, X = H). Final yields, accounting for both steps, vary between 17% for compound **L70** (Ar = pyridine, X = H) and 48% for compound **L69** (Ar = 8-HQ, X = H).

An alternative synthetic path¹⁹⁴ could rely on a first separate protection of the 8-hydroxyl group by methylation with CH₃I, followed by deprotonation of the 2-methyl group through a non-nucleophilic base like LDA (lithium diisopropylamide), to give the quinolinic carbanion. This could successively react with the desired aldehyde affording the methylated styrylquinoline intermediate. At last, the deprotection in acid environment of the phenolic group would provide the final product.

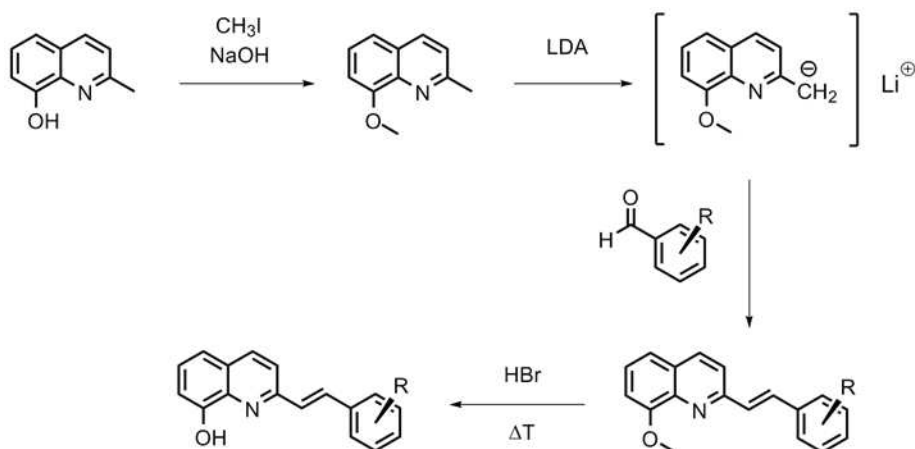


Figure 117. Alternative synthetic path.

The higher number of steps that this procedure requires and the fact that the final demethylation could result in a more complex reaction than the efficient deacetylation made us choose to follow the first, more affordable, synthetic route. Other more complex synthesis pathways have also been proposed¹⁹⁷.

The double bond hydrogenation was achieved in two different ways due to anomalous behavior of the 5,7-dichloro-8-hydroxyquinoline derivatives, which were more inert than the other ligands towards Pd-catalyzed hydrogenation. For ligands **L64** - **L69** we

proceeded through catalyzed hydrogenation with $\text{H}_2(\text{g})$ and Pd/C (10% in weight) in ethanol⁵⁹. Different H_2 pressures and times were used, because of dissimilar reactivity of the compounds, ranging from 0.8 atm/1h to 2.5 atm/72h.

Ligands **L70** and **L71** were resistant to catalytic hydrogenation and were then reduced with hydrate hydrazine, which acted both as the reductant and as the solvent¹⁹⁸.

Since the cytotoxic assays on human tumor cell lines comprise the administration of CuCl_2 and of ligands directly into the cell growth medium, the final synthesis of copper complexes was not deeply investigated. The mixing of equimolar quantities of the ligands and of CuCl_2 in methanol would result in the instantaneous formation of a dark precipitate, insoluble in any common laboratory solvent, with a wide range of polarity. Copper complexes crystals suitable for X-ray analysis were obtained only for compounds **L64**, **L67** and **L73** by *in-gel* crystallization. This method consists in the stratification of ligand MeOH solutions over agar gels of CuCl_2 .

10.3.2. Molecular Structures

Four crystal structures were obtained:

- two complexes of olefinic ligands - [Cu(**L64**)₂] and [Cu(**L67**)₂],
- one hydrogenated ligand (**L72**),
- one complex with an hydrogenated ligand - [Cu(**L73**)₂].

The complex [Cu(**L64**)₂] - (**L64** = 2-(2-hydroxystyryl)quinolin-8-ol) crystallizes in the *P2₁/c* space group (monoclinic crystal system). The asymmetric unit is a complex with stoichiometry M:L 1:2, in which a copper atom surrounded by two N,O chelate ligands. The 8-hydroxyl group is deprotonated upon metal coordination, whereas the 2-hydroxyl group of the phenolic side arm is not deprotonated and does not participate into the metal coordination; the doubly positive charge brought by the copper ion is then neutralized by the two quinolinic moieties, yielding a neutral complex. Cu(II) shows a slightly distorted square planar geometry. The ligand adopts a trans geometry with respect to the double bond system and the lateral phenolic arm cannot therefore cooperate into the metal coordination. This group takes part into an extensive hydrogen bond network. As a matter of fact, the complex exchanges two significative hydrogen bonds with the phenolic arm, one towards the phenolic side arm ($d(\text{O}-\text{O}) = 2.80 \text{ \AA}$) and one towards the quinolinic hydroxy group ($d(\text{O}-\text{O}) = 2.68 \text{ \AA}$) of two different ligand molecules.

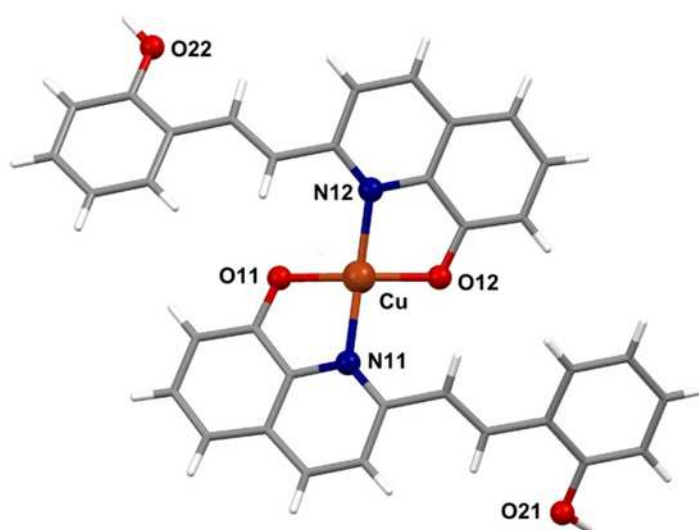


Figure 118. Crystal structure of $[\text{Cu}(\text{L64})_2]$.

Table 12. Selected bond lengths (Å) and angles (°) for $[\text{Cu}(\text{L73})_2]$, $[\text{Cu}(\text{L64})_2]$ and $[\text{Cu}(\text{L67})_2]$.

$[\text{Cu}(\text{L73})_2]$		$[\text{Cu}(\text{L67})_2]$	
Cu-O(1)	1.88(2)	Cu-O(1)	1.91(3)
Cu-N(1)	2.12(2)	Cu-N(12)	2.06(4)
O(1)-Cu-N(1')	95.2(8)	N(1)-Cu-O(1)	83.9(1)
O(1)-Cu-N(1)	84.8 (8)	O(1)-Cu-N(1')	101.2(1)
$[\text{Cu}(\text{L64})_2]$			
Cu-O(11)	1.89(1)		
Cu-N(11)	2.06(4)		
Cu-O(12)	1.91(1)		
Cu-N(12)	2.06(2)		
N(11)-Cu-O(11)	84.05(6)		
O(11)-Cu-N(12)	98.83 (6)		
N(12)-Cu-O(12)	83.69(6)		
O(12)-Cu-N(11)	99.11(7)		

The complex $[\text{Cu}(\text{L67})_2]$ - (**L67** = 2-(2-methoxystyryl)quinolin-8-ol) crystallizes in the $C2/c$ space group (monoclinic crystal system). In this structure the asymmetric unit comprises only one ligand molecule. The metal complex of stoichiometry M:L 1:2 is generated by symmetry ($C2$ rotation axes). The structure is very similar to that of complex $[\text{Cu}(\text{L64})_2]$, but the metal has more pronounced, though distorted, tetrahedral coordination geometry. The coordinating atoms are two nitrogens and two oxygen atoms of two different quinolinic moieties. The 8-hydroxyl groups are deprotonated giving rise a neutral complex. Due to the methylation of the peripheral phenolic function, this group does not exchange hydrogen bonds with surrounding molecules.

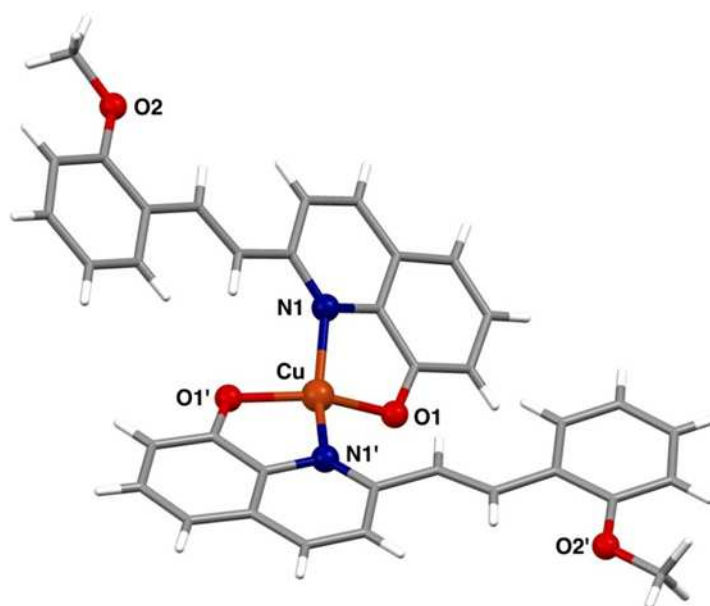


Figure 119. Crystal structure of complex $[\text{Cu}(\text{L67})_2]$; symmetry operation $' = -x, y, -z + 1/2$.

The hydrogenated ligand **L72** - (**L72** = 2-(2-hydroxyphenylethyl)quinolin-8-ol) crystallizes in the $P2_1/n$ space group (monoclinic crystal system). The asymmetric unit comprises one ligand molecule. The phenolic side arm is oriented toward the quinolinic N,O coordinating system and the second hydroxyl group is turned inwards, as would be the case in presence of a metal ion. This conformation is stabilized by the formation of two hydrogen bonds, an intramolecular one, between the phenolic arm and the pyridinic nitrogen ($d(\text{O} \cdots \text{N}) = 2.76 \text{ \AA}$) and an intermolecular one, between the quinolinic phenol and the lateral

phenolic arm ($d(\text{O}-\text{O}) = 2.72 \text{ \AA}$). The four ligand molecules in the unit cell are thus held in pair by four hydrogen bonds and are correlated by an inversion centre. This ligand conformation would be then favorable to three-term O,N,O chelation on Cu(II), possibly forming a doubly deprotonated M:L 1:1 neutral complex.

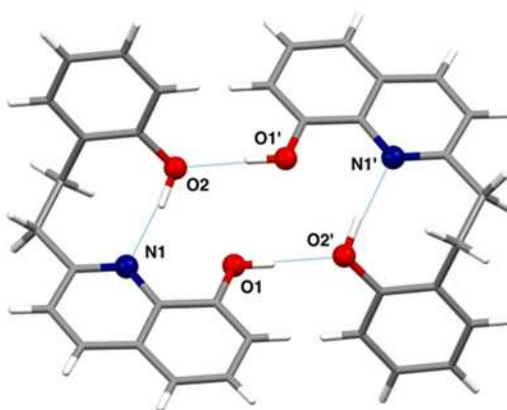


Figure 120. Crystal structure of ligand **L72** and its coupling through hydrogen bonds; symmetry operation $' = -x, -y, -z$.

The complex $[\text{Cu}(\text{L73})_2]$ - (**L 73** = 2-(2-(pyridin-2-yl)ethyl)quinolin-8-ol) crystallizes in the $P2_1/c$ space group (monoclinic crystal system). The asymmetric unit contains only one ligand molecule that forms the M:L 1:2 complex by symmetry (inversion centre coincident with the copper atom position). Copper is again coordinated by two different quinolinic N,O systems and it is a regular square planar geometry (sum of coordination angles of 360°). The complex is neutral due to the two deprotonated 8-hydroxyl groups. The pyridinic side arm is not involved into the metal coordination and is held backwards, even though it is not conformationally blocked as in the first two structures. The nitrogen atom of this pyridine residue forms a strong hydrogen bond with a solvent water molecule ($d(\text{O}-\text{N}) = 2.68 \text{ \AA}$) that sets up a 2D hydrogen bond network of water molecules forming a zig-zag strand. The flexibility of this peripheral group together with the energy gained from the hydrogen bond network might explain the exclusion of the pyridine ring from metal chelation.

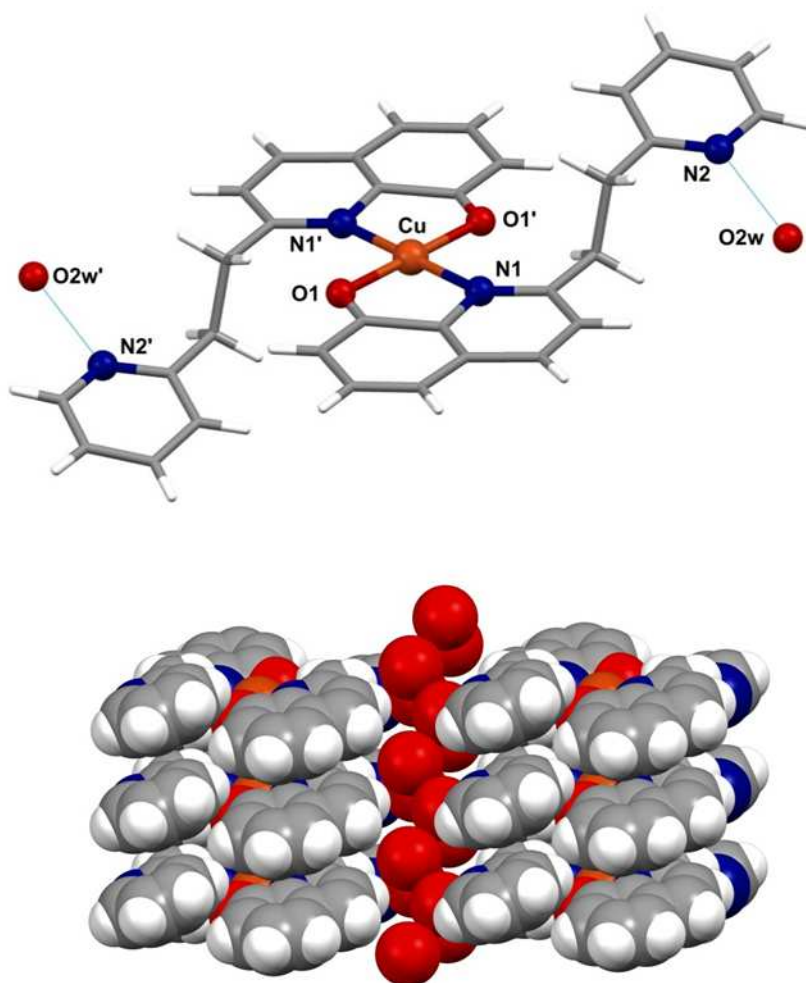


Figure 121. Above: crystal structure of complex $[\text{Cu}(\text{L73})_2]$; symmetry operation $' = -x, -y, -z+1$. Under: supramolecular packing and water strand-like channel in complex $[\text{Cu}(\text{L73})_2]$.

From the crystal structures it appears that these ligand systems tend to use only the N,O donor set, irrespective of the presence of additional donor groups. The resulting stoichiometry is therefore usually M:L 1:2 in analogy to that reported for $[\text{Cu}(\text{CQ})_2]$, Figure 122.

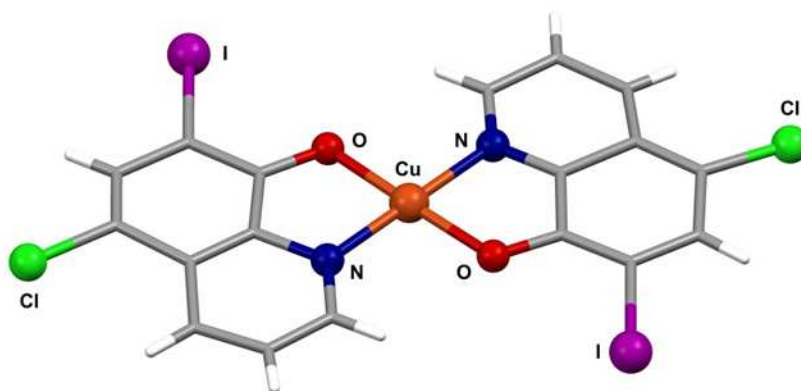


Figure 122 Crystal structure of 5-chloro-7-iodo-8-hydroxyquinoline.

The *trans* (*Z*) isomerism of the olefinic ligands **L64-L71** rules out any possible involvement of the peripheral group into the metal coordination. This is in agreement with the structures of $[\text{Cu}(\text{L64})_2]$ and $[\text{Cu}(\text{L67})_2]$. In fact a tridentate chelation would require a configuration rearrangement leading to the *cis* (*E*) isomer through rotation around a double bond, which is energetically demanding. Ligands **L64-L71** were prepared in acetic anhydride and the (*E*) isomer is preferentially formed, due to the less steric hindrance that these species suffer rather than the (*Z*) isomers. The formation of the (*E*) isomer was proved by $^1\text{H-NMR}$ coupling constants of the synthesized ligands. Figure 132 shows the aromatic signals of the $^1\text{H-NMR}$ spectra of ligand **L64**; two doublets that integrate for one proton each have a coupling constant of 16.4 Hz, a typical value for signals of vinylic protons with *trans* isomerism (*E*).

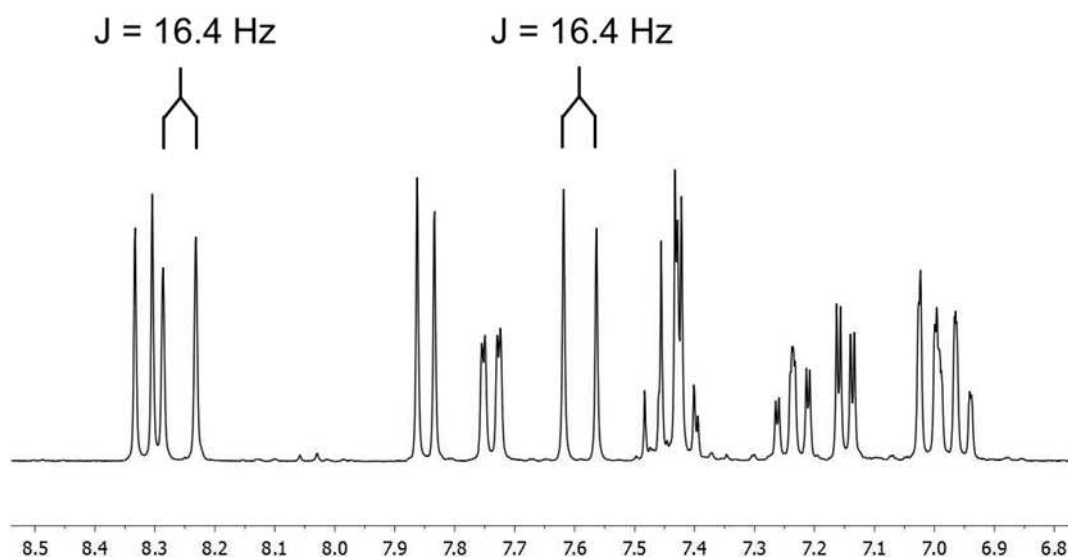


Figure 123. Expansion of the aromatic pattern for ^1H -NMR spectra of ligand **L64**. Isomer over the E one can also be appreciated by inspecting the crystal structure of the $[\text{Cu}(\text{L77})]$ shown in Figure 125.

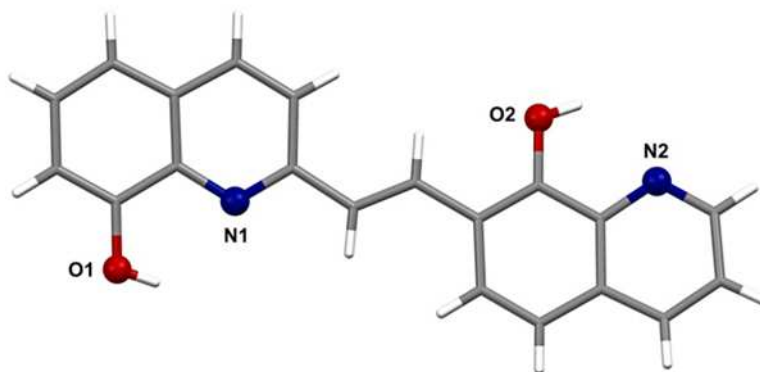


Figure 124.: Crystal structure of compound 2,7'-ethylenebis(8-hydroxyquinoline).

In order to investigate how a higher stability of the cuprocomplexes could influence cytotoxic activity, we were interested in synthesizing new ligands able to chelate copper atoms with both quinolinic N,O system and a diversely substituted side arm (compounds **L72-L79**) and to compare their cytotoxic activity with the activity of analogue ligands not able to sustain a 3/4-term chelation (compounds **L64-L71**) see Figure 118.

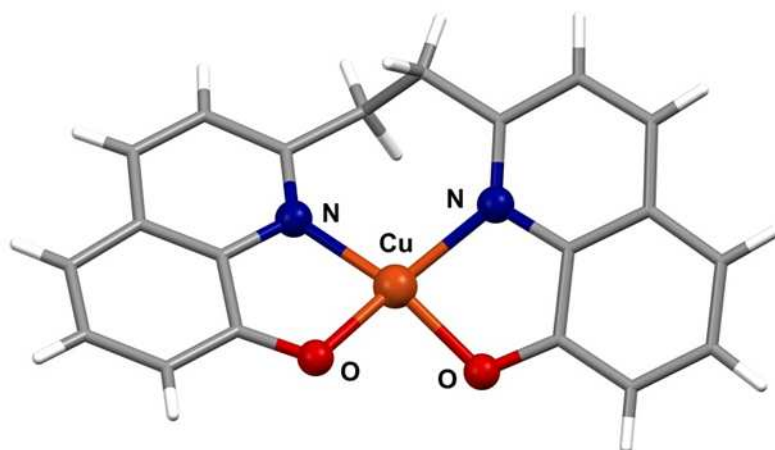


Figure 125. Crystal structure of complex [Cu(L77)] reported by others.

The only structure in which both ligand parts intervene into the metal coordination is the one with the symmetric L77 ligand, Figure 125. In this structure both systems coordinate the metal with the identical N,O chelate moiety giving rise to a neutral complex. In the other hand, less symmetric ligand such as those reported in Figure 126, may be able to coordinate on a tridentate fashion. They can in fact be deprotonated on both phenol groups and giving rise to more stable neutral complexes.

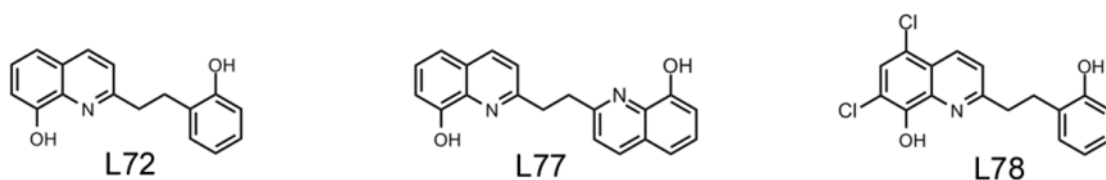


Figure 126. Ligands with two deprotonable phenolic moieties.

10.3.3. Cytotoxicity

As a continuation of the previous studies (Chapter 9) we then decided to investigate more in details how variations of coordination properties and of lipophilicity of a ligand series can affect cytotoxicity. The 8-hydroxyquinolinic moiety was then functionalized with a moderately lipophilic side arm with a potential coordinating ability. The 16 ligands previously described differ from each other for three main aspects:

- type and position of the third/fourth coordination atom,
- rigidity of the coordination structure,
- lipophilicity of the ligand.

Structural rigidity was modulated by varying the type of linker placed between the aromatic moieties, using a double bond for ligands **L64-L71** (vinylic linker) and a single bond for ligands **L72-L79** (ethylenic linker).

Variations of lipophilicity were obtained in the first place by different substitution of the aromatic ring of the side arm and, in the second place, by using two different starting quinolines, 8-hydroxyquinoline (ligands **L64-L69** and **L72-L77**) and 5,7-dichloro-8-hydroxyquinoline (ligands **L70**, **L71**, **L78** and **L79**), which is more lipophilic thanks to the two chlorine atoms. An estimation of lipophilicity was achieved by calculating the octanol/water partition coefficient ($\log P_{ow}$) through the freeware software ALOGPS 2.1 (available on <http://www.vcclab.org/lab/alogps/>). Figure 127 shows a summary of the $\log P_{ow}$ of the synthesized ligands and of the IC_{50} for their complexes.

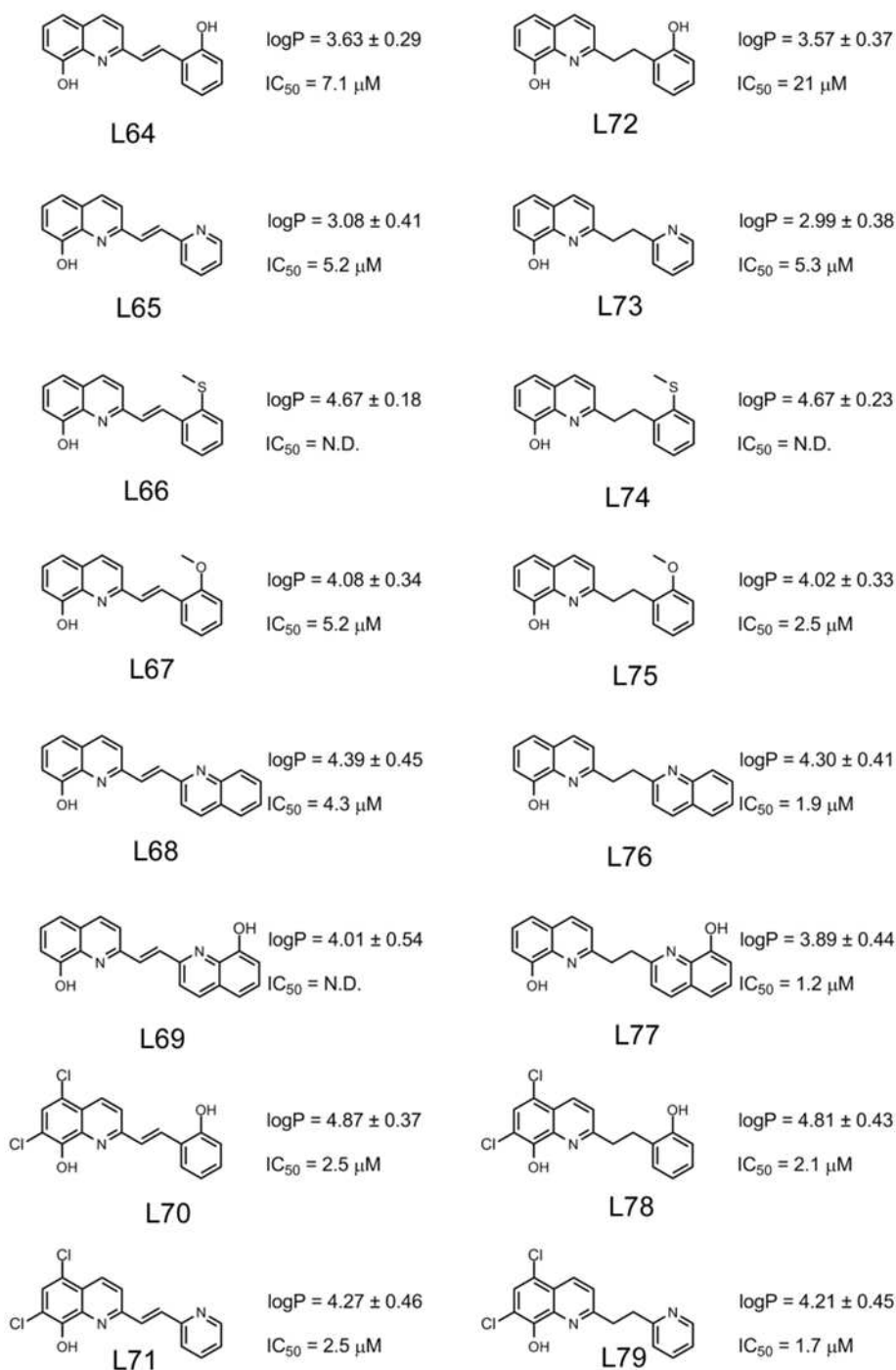


Figure 127. Calculated LogP of synthesized ligands and cytotoxicity of their corresponding Cu complexes.

Cytotoxicity of the ligands and of their copper complexes in stoichiometry 1:1 was evaluated on human tumoral cells, namely HeLa cell line (cervical carcinoma). Biological tests were performed both on the free ligand and on the metal complexes for comparison purposes and to better evaluate the role of the metal.

Dose/response diagrams for the compounds are shown in Figures 128 and 129.

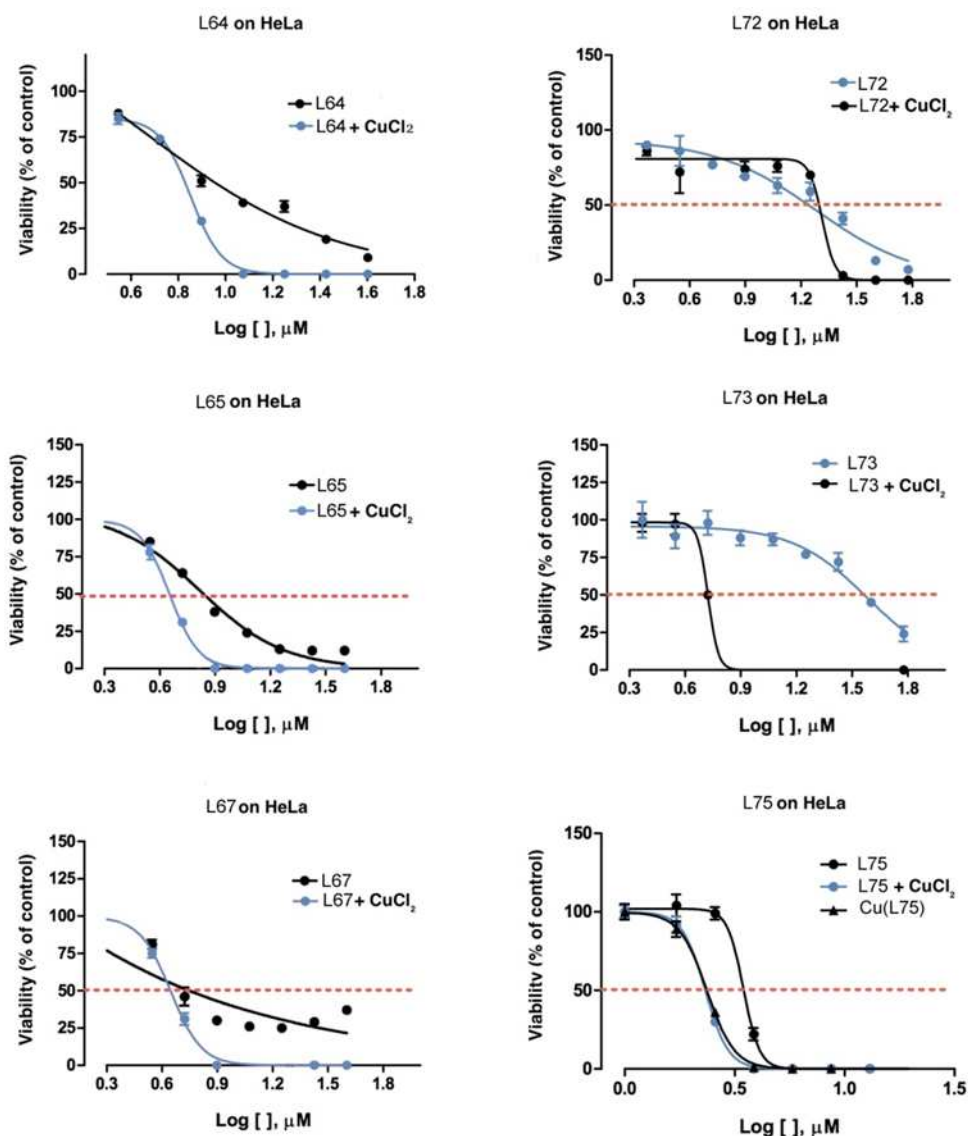


Figure 128. Dose/response diagrams for six ligands and respective Cu(II) complexes.

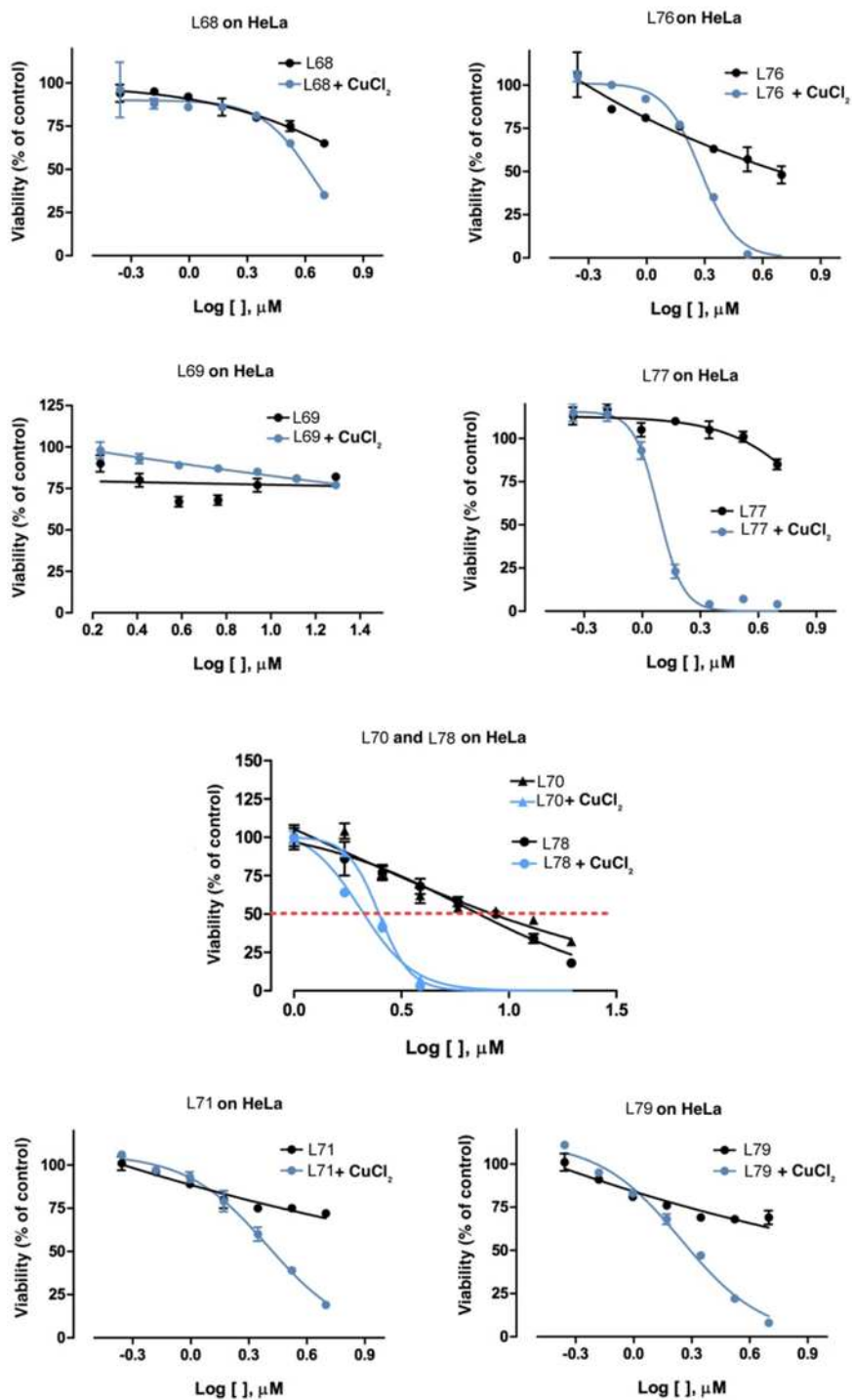


Figure 129. Dose/response diagrams for the other ligands and Cu(II) complexes.

Cells were incubated for 48 hours in presence of different concentration of the tested compounds and their viability was then measured by fluorimetry using the resazurin method. The antitumoral activity of the cuprocomplexes was evaluated by *in-situ* complexation of the 1:1 complex, from equimolar solutions of the ligands and of CuCl₂.

This was done mainly because copper complexes showed poor solubility (complete insolubility for complex of **L66** and **L74**) in DMSO and complete insolubility in water, the usual media used for biological tests.

Complexes of ligands **L66** and **L74** were not tested due to their complete insolubility in water and DMSO.

In agreement with previously reported observations, a neat increase of cytotoxicity was observed when CuCl₂ was co-administered with the ligands. IC₅₀ values for the ligands were not calculated because the model used for interpolation of experimental points of the dose/response did not fit the data well enough, as can be seen for ligand **L67**. Nevertheless it can be noted that cytotoxicity of the complexes is always greater than that of the ligands.

In agreement with results obtained for previously tested quinolines, some ligands prove fairly cytotoxic, above all ligands **L65**, **L67** and **L75**.

Almost all copper complexes show good antitumoral activities, except from complexes of ligands **L69** and **L72**; most active ones are complexes with ligands **L70**, **L71**, **L75**, **L76**, **L77**, **L78** e **L79**. Best activities was observed with complexes of **L77** (IC₅₀ = 1.2 μM) and **L79** (IC₅₀ = 1.7 μM), which are more cytotoxic than 8-hydroxyquinoline (IC₅₀ = 1.9 μM). Complex of **L76** is also very active and has an IC₅₀ = 1.9 μM, equal to that of 8-HQ. Complexes of **L70**, **L71**, **L75** and **L78** show slightly less activity, ranging from IC₅₀ = 2.1 μM to IC₅₀ = 2.5 μM.

Apart from introduction of the metal atom, also the hydrogenation of the double bond has generally led an increase of antitumoral activity. In particular, **L69** and **L77** showed the highest increase of activity after hydrogenation of the vinylic linker. Two exceptions to the higher activity brought by hydrogenation are though represented by complex pairs [Cu(**L65**)]/[Cu(**L73**)] and [Cu(**L64**)]/[Cu(**L72**)]; in the first case activity did not raise after reduction of the double bond, but kept almost unvaried; in the second case there was a drastic lowering of the activity, in fact the IC₅₀ shifted from 7.1 μM to almost 21 μM.

Even though the series of ligands derived from 5,7-dichloro-8-hydroxyquinoline (**L70**, **L71**, **L78** and **L79**) is too small to allow any significant hypothesis, complexes of ligands **L70** and **L71** are the most active of the whole vinylic series (IC₅₀ = 2.5 μM for both complexes). Their cytotoxicity slightly increases with hydrogenation of the double bond to give ligands **L78** and **L79** (IC₅₀ = 2.1 and 1.7 μM, respectively).

No neat correlation was found between activity and lipophilicity, maybe due to the narrow range of lipophilicity exhibited by the ligands and the different residual charges that complexes can present.

Even though the quinolinic moiety is invariable in the ligand structures, the presence of very different peripheral groups (pyridinic, phenolic, anisolic, quinolinic and 8-hydroxyquinolinic) may introduce several other activity modulators, apart from lipophilicity.

Ligand **L75** has lower coordinating ability than the other ligand, for its 2-methoxide substituent. Nevertheless its complex shows great cytotoxicity, comparable to that of above said complexes and even its vinylic analogue Cu(**67**) has a fair activity ($IC_{50} = 5.2 \mu M$). Apparently, coordination with a supplemental side arm can be important but is not enough to cause higher activity, and other not yet well defined factors could play important roles. A few of these could be the residual net charge and the stoichiometry of the formed complexes.

Comparing the obtained activities with those of the starting quinolines, it can be seen that, even though every complex with 8-HQ based ligand shows good activity, only complexes of **L75**, **L76** and **L77** have activities comparable with that of [Cu(8-HQ)]. A neat increase of activity was seen when comparing **L70**, **L71**, **L78** and **L79** with 5,7-dichloro-8-hydroxyquinoline, whose cuprocomplex has an IC_{50} of $5.3 \mu M$ on HeLa cells. The analogue complexes [Cu(**L70**)], [Cu(**L71**)], [Cu(**L78**)] e [Cu(**L79**)] show an activity two to three fold greater than the corresponding 5,7-dichloro-8-hydroxyquinoline.

In conclusion no neat correlation between lipophilicity and cytotoxicity has been found, perhaps because the $\log P_{ow}$ range exhibited by ligands is too narrow.

On the contrary, an evident increase in activity was found for almost all hydrogenated ligands.

It was concluded that some other not yet examined factors, like residual net charge and stoichiometry of the complexes formed in the cellular medium, might play fundamental roles in cytotoxic activity, maybe acting together in a cooperative way.

In order to design new complexes with increased anticancer action, it will be required to bring systematic structural modifications to the ligands that have been shown so far as the most actives, namely [Cu(**L76**)], [Cu(**L77**)], [Cu(**L78**)] e [Cu(**L79**)].

11. Bibliography

1. Maddox, J. Crystals from first principles. *Nature* **335**, 201–201 (1988).
2. Moulton, B. & Zaworotko, M. J. From molecules to crystal engineering: Supramolecular isomerism and polymorphism in network solids. *Chemical Reviews* **101**, 1629–1658
3. Dalgarno, S. J., Power, N. P. & Atwood, J. L. Metallo-supramolecular capsules. *Coordination Chemistry Reviews* **252**, 825–841
4. Chakrabarty, R., Mukherjee, P. S. & Stang, P. J. Supramolecular Coordination: Self-Assembly of Finite Two- and Three-Dimensional Ensembles 7. *Chemical Reviews* **111**, 6810–6918 (2011).
5. Janiak, C. Engineering coordination polymers towards applications. *Dalton Transactions* 2781 (2003).doi:10.1039/b305705b
6. Leong, W. L. & Vittal, J. J. One-dimensional coordination polymers: complexity and diversity in structures, properties, and applications. *Chemical reviews* **111**, 688–764 (2011).
7. Janiak, C. & Vieth, J. K. MOFs, MILs and more: concepts, properties and applications for porous coordination networks (PCNs). *New Journal of Chemistry* **34**, 2366 (2010).
8. Mislin, G. *et al.* Synthesis and structural analysis of an infinite linear coordination network formed by the self-assembly of tetracyanocalix [4] arene ligands and silver cations. 2545–2546 (1998).
9. Chakrabarty, R., Mukherjee, P. S. & Stang, P. J. Supramolecular Coordination: Self-Assembly of Finite Two- and Three-Dimensional Ensembles7. *Chemical Reviews* **111**, 6810–6918
10. Tăbăcaru, A. *et al.* Antibacterial action of 4,4'-bipyrazolyl-based silver(I) coordination polymers embedded in PE disks. *Inorganic chemistry* **51**, 9775–88 (2012).
11. Dang, D., Zheng, Y., Bai, Y., Guo, X. & Niu, J. Assembly of Polyoxometalate-Based Metal–Organic Frameworks with Silver(I)-Schiff Base Coordination Polymeric Chains as Building Blocks. **3**, (2012).

12. Ni, J., Wei, K.-J., Liu, Y., Huang, X.-C. & Li, D. Silver Coordination Polymers Based on Neutral Trinitrile Ligand: Topology and the Role of Anion. *Crystal Growth & Design* **10**, 3964–3976 (2010).
13. Eddaoudi, M. *et al.* Modular Chemistry: Secondary Building Units as a Basis for the Design of Highly Porous and Robust Metal–Organic Carboxylate Frameworks. *Accounts of Chemical Research* **34**, 319–330 (2001).
14. Batten, S. R. & Robson, R. Interpenetrating Nets: Ordered, Periodic Entanglement. *Angewandte Chemie International Edition* **37**, 1460–1494 (1998).
15. Blake, A. J. *et al.* Inorganic crystal engineering using self-assembly of tailored building-blocks. *Coordination Chemistry Reviews* **183**, 117–138 (1999).
16. Ma, S. *et al.* Framework-catenation isomerism in metal-organic frameworks and its impact on hydrogen uptake. *Journal of the American Chemical Society* **129**, 1858–9 (2007).
17. Murray, L. J., Dincă, M. & Long, J. R. Hydrogen storage in metal-organic frameworks. *Chemical Society reviews* **38**, 1294–314 (2009).
18. Rowsell, J. L. C. & Yaghi, O. M. Strategies for hydrogen storage in metal–organic frameworks. *Angewandte Chemie (International ed. in English)* **44**, 4670–9 (2005).
19. Jones, S. C. & Bauer, C. A. Diastereoselective heterogeneous bromination of stilbene in a porous metal-organic framework. *Journal of the American Chemical Society* **131**, 12516–7 (2009).
20. Evans, O. R. & Lin, W. Crystal Engineering of NLO Materials Based on Metal–Organic Coordination Networks. *Accounts of Chemical Research* **35**, 511–522 (2002).
21. Habib, H. A., Sanchiz, J. & Janiak, C. Mixed-ligand coordination polymers from 1,2-bis(1,2,4-triazol-4-yl)ethane and benzene-1,3,5-tricarboxylate: trinuclear nickel or zinc secondary building units for three-dimensional networks with crystal-to-crystal transformation upon dehydration. *Dalton transactions (Cambridge, England : 2003)* 1734–44 (2008).doi:10.1039/b715812b
22. Horcajada, P. *et al.* Metal-organic frameworks as efficient materials for drug delivery. *Angewandte Chemie (International ed. in English)* **45**, 5974–8 (2006).
23. Van Dongen, S. F. M. *et al.* Biohybrid polymer capsules. *Chemical reviews* **109**, 6212–74 (2009).

24. Bassanetti, I. & Marchio, L. Structural Variability in Ag(I) and Cu(I) Coordination Polymers with Thioether-Functionalized Bis(pyrazolyl)methane Ligands. *Inorganic Chemistry* **0**, 10786–97 (2011).
25. Uemura, T., Yanai, N. & Kitagawa, S. Polymerization reactions in porous coordination polymers. *Chemical Society reviews* **38**, 1228–36 (2009).
26. Rowsell, J. L. C., Spencer, E. C., Eckert, J., Howard, J. A. K. & Yaghi, O. M. Gas adsorption sites in a large-pore metal-organic framework. *Science (New York, N.Y.)* **309**, 1350–4 (2005).
27. Britt, D.; Yaghi, O. M. No Title. *Proc. Nat. Acad. Sci. USA* **2008**, 11623
28. Wu, H., Zhou, W. & Yildirim, T. High-capacity methane storage in metal-organic frameworks M2(dhtp): the important role of open metal sites. *Journal of the American Chemical Society* **131**, 4995–5000 (2009).
29. Kitagawa, S. Physical chemistry: gas in a straitjacket. *Nature* **441**, 584–5 (2006).
30. Kitagawa, S., Kitaura, R. & Noro, S. Functional porous coordination polymers. *Angewandte Chemie (International ed. in English)* **43**, 2334–75 (2004).
31. Seward, C., Jia, W.-L., Wang, R.-Y., Enright, G. D. & Wang, S. Luminescent 2D macrocyclic networks based on starburst molecules: [[Ag(CF₃SO₃)(1.5)(tdapb)] and [[Ag(NO₃)(3)(tdapb)]. *Angewandte Chemie (International ed. in English)* **43**, 2933–6 (2004).
32. Xie, Z., Ma, L., deKrafft, K. E., Jin, A. & Lin, W. Porous phosphorescent coordination polymers for oxygen sensing. *Journal of the American Chemical Society* **132**, 922–3 (2010).
33. Yuan, M., Zhao, F., Zhang, W., Wang, Z.-M. & Gao, S. Azide-bridged one-dimensional Mn(III) polymers: effects of side group of Schiff base ligands on structure and magnetism. *Inorganic chemistry* **46**, 11235–42 (2007).
34. Li, B. *et al.* [Ln₂(C₂O₄)₂(pyzc)₂(H₂O)₂]_n [Ln = Pr (1), Er (2)]: novel two-dimensional lanthanide coordination polymers with 2-pyrazinecarboxylate and oxalate. *Inorganic chemistry* **45**, 10425–7 (2006).
35. Imaz, I. *et al.* Coordination polymer particles as potential drug delivery systems. *Chemical communications (Cambridge, England)* **46**, 4737–9 (2010).

36. Comba, P. *et al.* Stable five- and six-coordinate cobalt(III) complexes with a pentadentate bispidine ligand. *Angewandte Chemie (International ed. in English)* **47**, 4740–3 (2008).
37. Chakraborty, B., Halder, P. & Paine, T. K. Conformational supramolecular isomerism in one-dimensional silver(I) coordination polymer of a flexible bis(bidentate) N,N-donor ligand with p-xylyl spacer. *Dalton transactions (Cambridge, England : 2003)* **40**, 3647–54 (2011).
38. Little, M. A., Halcrow, M. A., Harding, L. P. & Hardie, M. J. Ag(I) organometallic coordination polymers and capsule with tris-allyl cyclotriveratrylene derivatives. *Inorganic chemistry* **49**, 9486–96 (2010).
39. Libri, S. *et al.* Ligand Substitution within nonporous crystals of a coordination polymer: elimination from and insertion into Ag-O bonds by alcohol molecules in a solid-vapor reaction. *Angewandte Chemie (International ed. in English)* **47**, 1693–7 (2008).
40. Uemura, K. *et al.* Novel flexible frameworks of porous cobalt(III) coordination polymers that show selective guest adsorption based on the switching of hydrogen-bond pairs of amide groups. *Chemistry-A European Journal* **8**, 3586–3600
41. Zhang, J.-P., Horike, S. & Kitagawa, S. A flexible porous coordination polymer functionalized by unsaturated metal clusters. *Angewandte Chemie (International ed. in English)* **46**, 889–92 (2007).
42. Jouaiti, A., Hosseini, M. W., Kyritsakas, N., Grosshans, P. & Planeix, J.-M. Orthogonal packing of enantiomerically pure helical silver coordination networks. *Chemical communications (Cambridge, England)* 3078–80 (2006).doi:10.1039/b605166a
43. Nagarathinam, M. & Vittal, J. J. Anisotropic movements of coordination polymers upon desolvation: solid-state transformation of a linear 1D coordination polymer to a ladderlike structure. *Angewandte Chemie (International ed. in English)* **45**, 4337–41 (2006).
44. The, K.I.; Peterson, L. K. No Title. *Can. J. Chem.* **51**, 422–426 (1973).
45. The, K.I.; Peterson, L. K. No Title. *Can. J. Chem.* **51**, 2448–2451 (1973).
46. Peterson, L.K.; Kiehlmann, E. No Title. *Can. J. Chem.* **52**, 2367–2374 (1974).

47. SMART (control) and SAINT (integration) software for CCD systems, Bruker AXS, Madison, WI, U. No Title. (1994).
48. Area-Detector Absorption Correction, Siemens Industrial Automation Inc., Madison, W. No Title. (1996).
49. Burla, M. C.; Caliandro, R.; Camalli, M.; Carrozzini, B.; Cascarano, G. L.; De Caro, L.; Giacovazzo, C.; Polidori, G. . S. SIR2004: an improved tool for crystal structure determination and refinement. *Journal of Applied Crystallography* **38**, 381–388 (2005).
50. Sheldrick, G. M. SHELX97. Programs for Crystal Structure Analysis. (1997).
51. Farrugia, L. J. WinGX suite for small-molecule single-crystal crystallography. *Journal of Applied Crystallography* **32**, 837–838 (1999).
52. Macrae, C. F. *et al.* Mercury: visualization and analysis of crystal structures. *Journal of Applied Crystallography* **39**, 453–457 (2006).
53. Halper, S. R., Do, L., Stork, J. R. & Cohen, S. M. Topological control in heterometallic metal-organic frameworks by anion templating and metalloligand design. *Journal of the American Chemical Society* **128**, 15255–68 (2006).
54. Lehn, J. M. *Supramolecular Chemistry, Concepts and Perspectives*. (Weinheim, 1995).
55. Swiegers, G. F. & Malefetse, T. J. New Self-Assembled Structural Motifs in Coordination Chemistry. *Chemical Reviews* **100**, 3483–3538 (2000).
56. Fujita, M. *et al.* Molecular paneling via coordination. *Chemical Communications* 509–518 (2001).doi:10.1039/b008684n
57. Stang, P. J. & Olenyuk, B. Self-Assembly, Symmetry, and Molecular Architecture: Coordination as the Motif in the Rational Design of Supramolecular Metallacyclic Polygons and Polyhedra. *Accounts of Chemical Research* **30**, 502–518 (1997).
58. Reger, D. L., Semeniuc, R. F., Silaghi-Dumitrescu, I. & Smith, M. D. Influences of changes in multitopic tris(pyrazolyl)methane ligand topology on silver(I) supramolecular structures. *Inorganic chemistry* **42**, 3751–64 (2003).

59. Lü, X.-Q. *et al.* Triple-Stranded Helical and Plywood-Like Arrays: Two Uncommon Framework Isomers Based on the Common One-Dimensional Chain Structures. *Crystal Growth & Design* **6**, 1910–1914 (2006).
60. McMorran, D. A. Ag(I)-based tectons for the construction of helical and meso-helical hydrogen-bonded coordination networks. *Inorganic chemistry* **47**, 592–601 (2008).
61. Schultheiss, N., Powell, D. R. & Bosch, E. Anion control of the self-assembly of 2,3-diarylpirazines with silver(I) salts. *Inorganic chemistry* **42**, 8886–90 (2003).
62. Caradoc-Davies, P. L. & Hanton, L. R. Formation of a single-stranded silver(i) helical-coordination polymer containing π -stacked planar chiral N4S2 ligands. *Chemical Communications* 1098–1099 (2001).doi:10.1039/b101875m
63. Withersby, M. A. *et al.* Anion Control in Bipyridylsilver(I) Networks: A Helical Polymeric Array. *Angewandte Chemie International Edition in English* **36**, 2327–2329 (1997).
64. Biradha, K., Seward, C. & Zaworotko, M. J. Helical Coordination Polymers with Large Chiral Cavities. *Angewandte Chemie International Edition* **38**, 492–495 (1999).
65. Fitchett, C. M. & Steel, P. J. Chiral heterocyclic ligands. XIV. Control of directionality in silver coordination polymers through ligand design. *Dalton transactions (Cambridge, England : 2003)* 4886–8 (2006).doi:10.1039/b611622c
66. Burla, M. C. *et al.* SIR2004 : an improved tool for crystal structure determination and refinement. *Journal of Applied Crystallography* **38**, 381–388 (2005).
67. Becke, A. D. Density-functional exchange-energy approximation with correct asymptotic behavior. *Physical Review A* **38**, 3098–3100 (1988).
68. Becke, A. D. Density-functional thermochemistry. III. The role of exact exchange. *The Journal of Chemical Physics* **98**, 5648 (1993).
69. Dichtfield, R.; Hehre, W. J. ;Peopl. J. A. No Title. *Comp Chem* **22**, 976 (2001).
70. Fuentealba, P., Preuss, H., Stoll, H. & Von Szentpály, L. A proper account of core-polarization with pseudopotentials: single valence-electron alkali compounds. *Chemical Physics Letters* **89**, 418–422 (1982).

71. Schwerdtfeger, P., Dolg, M., Schwarz, W. H. E., Bowmaker, G. A. & Boyd, P. D. W. Relativistic effects in gold chemistry. I. Diatomic gold compounds. *The Journal of Chemical Physics* **91**, 1762 (1989).
72. Frisch, M. J.; Trucks, G. W.; Schlegel, H. B.; Scuseria, G. E.; Robb, M. A.; Cheeseman, J. R.; Montgomery, Jr., J. A.; Vreven, T.; Kudin, K. N.; Burant, J. C.; Millam, J. M.; Iyengar, S. S.; Tomasi, J.; Barone, V.; Mennucci, B.; Cossi, M.; Scalmani, G.; R, J. A. *Gaussian 03, Revision C.02*. (Wallingford CT, 2004).
73. Bassanetti, I. *et al.* Influence of anions in silver supramolecular frameworks: structural characteristics and sorption properties. *Journal of the American Chemical Society* **134**, 9142–5 (2012).
74. Iengo, E., Milani, B., Zangrando, E., Geremia, S. & Alessio, E. Novel Ruthenium Building Blocks for the Efficient Modular Construction of Heterobimetallic Molecular Squares of Porphyrins This work was supported by the Italian MURST. We thank Prof. L. G. Marzilli (Emory University, Atlanta, USA) for helpful discussions. *Angewandte Chemie (International ed. in English)* **39**, 1096–1099 (2000).
75. Iengo, E. *et al.* Pyridylporphyrin metallacycles with a slipped cofacial geometry: spectroscopic, X-ray, and photophysical characterization. *Inorganic chemistry* **44**, 9752–62 (2005).
76. Krämer, R., Lehn, J.-M., De Cian, A. & Fischer, J. Self-Assembly, Structure, and Spontaneous Resolution of a Trinuclear Triple Helix from an Oligobipyridine Ligand and NiII Ions. *Angewandte Chemie International Edition in English* **32**, 703–706 (1993).
77. Mezei, G., Zaleski, C. M. & Pecoraro, V. L. Structural and functional evolution of metallacrowns. *Chemical reviews* **107**, 4933–5003 (2007).
78. Stang, P. J., Cao, D. H., Saito, S. & Arif, A. M. Self-Assembly of Cationic, Tetranuclear, Pt(II) and Pd(II) Macrocyclic Squares. x-ray Crystal Structure of [Pt2+(dppp)(4,4'-bipyridyl).cntdot.2-OSO2CF3]4. *Journal of the American Chemical Society* **117**, 6273–6283 (1995).
79. Anderson, S., Anderson, H. L., Bashall, A., McPartlin, M. & Sanders, J. K. M. Assembly and Crystal Structure of a Photoactive Array of Five Porphyrins. *Angewandte Chemie International Edition in English* **34**, 1096–1099 (1995).
80. Cárdenas, D. J. *et al.* Synthesis, X-ray Structure, and Electrochemical and Excited-State Properties of Multicomponent Complexes Made of a [Ru(Tpy) 2] 2+ Unit

- Covalently Linked to a [2]-Catenate Moiety. Controlling the Energy-Transfer Direction by Changing the Catenate Metal Io. *Journal of the American Chemical Society* **121**, 5481–5488 (1999).
81. Cram, D. J. Preorganization? From Solvents to Spherands. *Angewandte Chemie International Edition in English* **25**, 1039–1057 (1986).
 82. Lehn, J.-M. Dynamic Combinatorial Chemistry and Virtual Combinatorial Libraries. *Chemistry - A European Journal* **5**, 2455–2463 (1999).
 83. Leung, D. H., Fiedler, D., Bergman, R. G. & Raymond, K. N. Selective C-H bond activation by a supramolecular host-guest assembly. *Angewandte Chemie (International ed. in English)* **43**, 963–6 (2004).
 84. Lützen, A. Self-assembled molecular capsules--even more than nano-sized reaction vessels. *Angewandte Chemie (International ed. in English)* **44**, 1000–2 (2005).
 85. Sozzani, P., Bracco, S., Comotti, A., Ferretti, L. & Simonutti, R. Methane and carbon dioxide storage in a porous van der Waals crystal. *Angewandte Chemie-International Edition* **44**, 1816–1820 (2005).
 86. Sozzani, P. *et al.* A Porous Crystalline Molecular Solid Explored by Hyperpolarized Xenon We thank the Italian Ministry of Universities and Scientific Research (PRIN program) for financial support. The research with laser-polarized xenon was supported by the Director, Office. *Angewandte Chemie (International ed. in English)* **39**, 2695–2699 (2000).
 87. Pinalli, R., Nachtigall, F., Ugozzoli, F. & Dalcanale, E. Supramolecular Sensors for the Detection of Alcohols. *Angewandte Chemie (International ed. in English)* **38**, 2377–2380 (1999).
 88. Anelli, P. L. *et al.* Molecular meccano. 1. [2]Rotaxanes and a [2]catenane made to order. *Journal of the American Chemical Society* **114**, 193–218 (1992).
 89. Jiménez, M., Dietrich-Buchecker, C. & Sauvage, J. Towards Synthetic Molecular Muscles: Contraction and Stretching of a Linear Rotaxane Dimer We are grateful to M. Jean-Daniel Sauer and Dr. Roland Graff for high-field NMR experiments, Hélène Nierengarten and Raymond Hubert for mass determinations. M.C.J. . *Angewandte Chemie (International ed. in English)* **39**, 3284–3287 (2000).
 90. Dalgarno, S. J., Power, N. P. & Atwood, J. L. Metallo-supramolecular capsules. *Coordination Chemistry Reviews* **252**, 825–841 (2008).

91. Brody, M. S., Schalley, C. A., Rudkevich, D. M. & Rebek, J. Synthesis and Characterization of a Unimolecular Capsule. *Angewandte Chemie International Edition* **38**, 1640–1644 (1999).
92. Hof, F., Craig, S. L., Nuckolls, C. & Rebek, J. Molecular Encapsulation. *Angewandte Chemie International Edition* **41**, 1488 (2002).
93. Johnson, D. W., Hof, F., Iovine, P. M., Nuckolls, C. & Rebek, J. Solid-state and solution studies of a tetrameric capsule and its guests. *Angewandte Chemie (International ed. in English)* **41**, 3793–6 (2002).
94. Pinalli, R. *et al.* Cavitand-based nanoscale coordination cages. *Journal of the American Chemical Society* **126**, 6516–7 (2004).
95. Olenyuk, B., Whiteford, J. A., Fechtenkötter, A. & Stang, P. J. Self-assembly of nanoscale cuboctahedra by coordination chemistry. *Nature* **398**, 796–9 (1999).
96. Rivera, J. M., Martín, T. & Rebek, J. Chiral Softballs: Synthesis and Molecular Recognition Properties. *Journal of the American Chemical Society* **123**, 5213–5220 (2001).
97. Macchioni, A., Ciancaleoni, G., Zuccaccia, C. & Zuccaccia, D. Determining accurate molecular sizes in solution through NMR diffusion spectroscopy. *Chemical Society Reviews* **37**, 479–489 (2008).
98. Zuccaccia, D. & Macchioni, A. An Accurate Methodology to Identify the Level of Aggregation in Solution by PGSE NMR Measurements: The Case of Half-Sandwich Diamino Ruthenium(II) Salts. *Organometallics* **24**, 3476–3486 (2005).
99. Pregosin, P. S. Ion pairing using PGSE diffusion methods. *Progress in Nuclear Magnetic Resonance Spectroscopy* **49**, 261–288 (2006).
100. Dinnebier, R. E. *et al.* Order–disorder phenomena determined by high-resolution powder diffraction: the structures of tetrakis(trimethylsilyl)methane $C[Si(CH_3)_3]_4$ and tetrakis(trimethylsilyl)silane $Si[Si(CH_3)_3]_4$. *Acta Crystallographica Section B Structural Science* **55**, 1014–1029 (1999).
101. Spek, A. L. Structure validation in chemical crystallography. *Acta crystallographica. Section D, Biological crystallography* **65**, 148–55 (2009).
102. Bassanetti, I. ; Mezzadri, F.; Comotti, A.; Sozzani, P. . M. L. *No Title*. (editing, 2012).

103. Gennari, M., Bassanetti, I. & Marchio, L. Metal-organic chains constructed from pre-organized N2S2 donor ligands. *Polyhedron* **29**, 361–371 (2010).
104. Altomare, A.; Burla, M. C.; Camalli, M.; Cascarano, G. L.; Giacovazzo, C.; Guagliardi, A.; Moliterni, A. G. G.; Polidori, G.; Spagna, R. No Title. *J. Appl. Cryst.* **32**, 115–119 (1999).
105. PIGUET, C., BORKOVEC, M., HAMACEK, J. & ZECKERT, K. Strict self-assembly of polymetallic helicates: the concepts behind the semantics. *Coordination Chemistry Reviews* **249**, 705–726 (2005).
106. Otero, A. *et al.* An unprecedented hybrid scorpionate/cyclopentadienyl ligand. *Journal of the American Chemical Society* **126**, 1330–1 (2004).
107. Otero, A. *et al.* Preparation of New Monoanionic “Scorpionate” Ligands: Synthesis and Structural Characterization of Titanium(IV) Complexes Bearing This Class of Ligand. *Inorganic Chemistry* **41**, 5193–5202 (2002).
108. Byers, P. K., Canty, A. J. & Honeyman, R. T. The synthesis of tripodal nitrogen donor ligands and their characterization as PdII_{Me}₂ and PdIII_{Me} derivatives. *Journal of Organometallic Chemistry* **385**, 417–427 (1990).
109. Higgs, T. C. & Carrano, C. J. A New Class of Biomimetically Relevant “Scorpionate” Ligands. 1. The (2-Hydroxyphenyl)bis(pyrazolyl)methanes: Synthesis and Structural Characterization of Some Cobalt(II) Complexes. *Inorganic Chemistry* **36**, 291–297 (1997).
110. Flack, H. D. & Bernardinelli, G. Absolute structure and absolute configuration. *Acta Crystallographica Section A Foundations of Crystallography* **55**, 908–915 (1999).
111. Flack, H. D. & Bernardinelli, G. Reporting and evaluating absolute-structure and absolute-configuration determinations. *Journal of Applied Crystallography* **33**, 1143–1148 (2000).
112. Erxleben, A. Synthesis and Structure of {[Ag(SalGly)]·0.33H₂O}_n: An Infinite Double Helical Coordination Polymer. *Inorganic Chemistry* **40**, 2928–2931 (2001).
113. Otero, A. *et al.* Versatile scorpionates and new developments in the denticity changes of NNCp hybrid scorpionate/cyclopentadienyl ligands in Sc and Y compounds: from kappa1-Neta5-Cp to kappa2-NNeta5-Cp. *Inorganic chemistry* **47**, 4996–5005 (2008).

114. Hammes, B. S. & Carrano, C. J. Synthesis and Characterization of Pseudotetrahedral N₂O and N₂S Zinc(II) Complexes of Two Heteroscorpionate Ligands: Models for the Binding Sites of Several Zinc Metalloproteins. *Inorganic Chemistry* **38**, 4593–4600 (1999).
115. Figuly, G. D., Loop, C. K. & Martin, J. C. Directed ortho-lithiation of lithium thiophenolate. New methodology for the preparation of ortho-substituted thiophenols and related compounds. *Journal of the American Chemical Society* **111**, 654–658 (1989).
116. Qin, L. *et al.* Redox-dependent conformational changes in cytochrome C oxidase suggest a gating mechanism for proton uptake. *Biochemistry* **48**, 5121–5130 (2009).
117. Linder, C. Copper biochemistry and molecular biology. *Am. J. Clin. Nutr.* **63**, 797 (1996).
118. Strange, R. W., Hough, M. a, Antonyuk, S. V & Hasnain, S. S. Structural evidence for a copper-bound carbonate intermediate in the peroxidase and dismutase activities of superoxide dismutase. *PloS one* **7**, e44811 (2012).
119. Linder, M. C. *et al.* Copper transport. *The American journal of clinical nutrition* **67**, 965S–971S (1998).
120. Bartnikas, T. B. & Gitlin, J. D. How to make a metalloprotein. *Nature structural biology* **8**, 733–734 (2001).
121. Hindo, S. S. *et al.* Metals in anticancer therapy: copper(II) complexes as inhibitors of the 20S proteasome. *European journal of medicinal chemistry* **44**, 4353–4361 (2009).
122. Zamble, D. B. & Lippard, S. J. Cisplatin and DNA repair in cancer chemotherapy. *Trends in Biochemical Sciences* **20**, 435 (1995).
123. Ding, W.-Q., Liu, B., Vaught, J. L., Yamauchi, H. & Lind, S. E. Anticancer activity of the antibiotic clioquinol. *Cancer research* **65**, 3389–95 (2005).
124. You, B. Y., Wang, Y. H. & Kuo, M. L. Role of reactive oxygen species in cupric 8-quinolinoxide-induced genotoxic effect. *Mutation research* **491**, 45–56 (2001).
125. Cherny, R. A. *et al.* Treatment with a Copper-Zinc Chelator Markedly and Rapidly Inhibits B-Amyloid Accumulation in Alzheimer ' s Disease Transgenic Mice. *Neuron* **30**, 665–676 (2001).

126. Basnyat, P. *et al.* Mechanical and tribological properties of CrAlN-Ag self-lubricating films. *Surface and Coatings Technology* **202**, 1011–1016 (2007).
127. Daniel, K. G., Gupta, P., Harbach, R. H., Guida, W. C. & Dou, Q. P. Organic copper complexes as a new class of proteasome inhibitors and apoptosis inducers in human cancer cells. *Biochemical pharmacology* **67**, 1139–1151 (2004).
128. Copper-dependent cytotoxicity of 8-Hydroxyquinoline derivatives correlates with their hydrophobicity and does not require caspase activation Saverio Tardito,.
129. Chang, F.-S., Chen, W., Wang, C., Tzeng, C.-C. & Chen, Y.-L. Synthesis and antiproliferative evaluations of certain 2-phenylvinylquinoline (2-styrylquinoline) and 2-furanylvinyquinoline derivatives. *Bioorganic & medicinal chemistry* **18**, 124–33 (2010).
130. Tardito, S. *et al.* Copper binding agents acting as copper ionophores lead to caspase inhibition and paraptotic cell death in human cancer cells. *Journal of the American Chemical Society* **133**, 6235–42 (2011).
131. Kelland, L. The resurgence of platinum-based cancer chemotherapy. *Nature reviews. Cancer* **7**, 573–84 (2007).
132. Antonarakis, E. S. & Emadi, A. Ruthenium-based chemotherapeutics: are they ready for prime time? *Cancer chemotherapy and pharmacology* **66**, 1–9 (2010).
133. Nobili, S. *et al.* Gold compounds as anticancer agents: chemistry, cellular pharmacology, and preclinical studies. *Medicinal research reviews* **30**, 550–80 (2010).
134. Kim, B.-E. *et al.* Cardiac Copper Deficiency Activates a Systemic Signaling Mechanism that Communicates with the Copper Acquisition and Storage Organs. *Cell Metabolism* **11**, 353–363 (2010).
135. Banci, L. *et al.* Affinity gradients drive copper to cellular destinations. *Nature* **465**, 645–8 (2010).
136. Collins, J. F., Prohaska, J. R. & Knutson, M. D. Metabolic crossroads of iron and copper. *Nutrition reviews* **68**, 133–47 (2010).
137. Finney, L., Vogt, S., Fukai, T. & Glesne, D. Copper and angiogenesis: unravelling a relationship key to cancer progression. *Clinical and experimental pharmacology & physiology* **36**, 88–94 (2009).

138. Tardito, S. & Marchiò, L. Copper compounds in anticancer strategies. *Current medicinal chemistry* **16**, 1325–1348 (2009).
139. Bröker, L. E., Kruyt, F. A. E. & Giaccone, G. Cell death independent of caspases: a review. *Clinical cancer research : an official journal of the American Association for Cancer Research* **11**, 3155–62 (2005).
140. Liu, J., Thallapally, P. K., McGrail, B. P. & Brown, D. R. Progress in adsorption-based CO₂ capture by metal-organic frameworks. *Chemical Society Reviews* **41**, 2308–2322 (2012).
141. Sperandio, S., De Belle, I. & Bredesen, D. E. An alternative, nonapoptotic form of programmed cell death. *Proceedings of the National Academy of Sciences of the United States of America* **97**, 14376–81 (2000).
142. Tardito, S. *et al.* Non-apoptotic programmed cell death induced by a copper(II) complex in human fibrosarcoma cells. *Histochemistry and cell biology* **126**, 473–482 (2006).
143. Marzano, C. *et al.* Synthesis, characterization, and in vitro antitumor properties of tris(hydroxymethyl)phosphine copper(I) complexes containing the new bis(1,2,4-triazol-1-yl)acetate ligand. *Journal of medicinal chemistry* **49**, 7317–24 (2006).
144. Tardito, S. *et al.* The thioxotriazole copper(II) complex A0 induces endoplasmic reticulum stress and paraptotic death in human cancer cells. *The Journal of biological chemistry* **284**, 24306–24319 (2009).
145. Heynderickx, A., Samat, A. & Guglielmetti, R. Synthesis of new benzylpyridines as potential photochromic compounds. *Journal of Heterocyclic Chemistry* **38**, 737–742 (2001).
146. Ozanne, A., Pouységu, L., Depernet, D., François, B. & Quideau, S. A stabilized formulation of IBX (SIBX) for safe oxidation reactions including a new oxidative demethylation of phenolic methyl aryl ethers. *Organic letters* **5**, 2903–6 (2003).
147. Gennari, M. *et al.* CuI complexes with N,N',S,S' scorpionate ligands: evidence for dimer-monomer equilibria. *Inorganic chemistry* **47**, 2223–32 (2008).
148. Gennari, M., Tegoni, M., Lanfranchi, M., Pellinghelli, M. A. & Marchio, L. A new chiral N,N',O-donor heteroscorpionate ligand. Structures of Ni²⁺, Cu²⁺, Zn²⁺ complexes and study of solution equilibria by means of ¹H NMR/UV-vis titrations and EXSY NMR spectroscopy. *Inorganic chemistry* **46**, 3367–77 (2007).

149. Field, L. D., Messerle, B. A., Rehr, M., Soler, L. P. & Hambley, T. W. Cationic Iridium(I) Complexes as Catalysts for the Alcoholysis of Silanes. *Organometallics* **22**, 2387–2395 (2003).
150. Gampp, H.; Maeder, M.; Meyer, C. J.; Zuberbühler, A. D. No Title. *Talanta* **32**, 265 (1985).
151. Binstead, R. A.; Jung, B.; Zuberbühler, A. D. No Title. *Specfit/32 Ver.3.0*, Marlborough, USA
152. Gans, P.; Sabatini, A. No Title. *Talanta* **43**, 1739 (1996).
153. Gazzola, G. C.; Dall'Asta, V.; Franchi-Gazzola, R.; White, M. F. No Title. *Anal. Biochem* **115**, 368 (1981).
154. *No Title*. (2005).
155. Tardito, S. *et al.* The thioxotriazole copper(II) complex A0 induces endoplasmic reticulum stress and paraptotic death in human cancer cells. *The Journal of biological chemistry* **284**, 24306–19 (2009).
156. Lee, C., Kim, J.-S. & Waldman, T. PTEN gene targeting reveals a radiation-induced size checkpoint in human cancer cells. *Cancer research* **64**, 6906–14 (2004).
157. Cen, D., Brayton, D., Shahandeh, B., Meyskens, F. L. & Farmer, P. J. Disulfiram facilitates intracellular Cu uptake and induces apoptosis in human melanoma cells. *Journal of medicinal chemistry* **47**, 6914–20 (2004).
158. Tardito, S. *et al.* Thioamido coordination in a thioxo-1,2,4-triazole copper(II) complex enhances nonapoptotic programmed cell death associated with copper accumulation and oxidative stress in human cancer cells. *Journal of medicinal chemistry* **50**, 1916–1924 (2007).
159. Galluzzi, L. *et al.* Molecular definitions of cell death subroutines: recommendations of the Nomenclature Committee on Cell Death 2012. *Cell death and differentiation* **19**, 107–20 (2012).
160. Cheng G.; Lai, P. B. S. *Apoptosis in carcinogenesis and chemotherapy*. (Dordrecht, the Netherland., 2009).
161. Pop, C. & Salvesen, G. S. Human caspases: activation, specificity, and regulation. *The Journal of biological chemistry* **284**, 21777–81 (2009).

162. Salvesen, G. S. & Ashkenazi, A. Snapshot: caspases. *Cell* **147**, 476–476.e1 (2011).
163. Candé, C., Vahsen, N., Garrido, C. & Kroemer, G. Apoptosis-inducing factor (AIF): caspase-independent after all. *Cell death and differentiation* **11**, 591–5 (2004).
164. Susin, S. A. *et al.* Molecular characterization of mitochondrial apoptosis-inducing factor. *Nature* **397**, 441–6 (1999).
165. Walter, P. & Ron, D. The unfolded protein response: from stress pathway to homeostatic regulation. *Science (New York, N.Y.)* **334**, 1081–6 (2011).
166. Hetz, C. The unfolded protein response: controlling cell fate decisions under ER stress and beyond. *Nature reviews. Molecular cell biology* **13**, 89–102 (2012).
167. Festa, R. A. & Thiele, D. J. Copper: an essential metal in biology. *Current biology : CB* **21**, R877–83 (2011).
168. Rosenzweig, A. Structure and chemistry of the copper chaperone proteins. *Current Opinion in Chemical Biology* **4**, 140–147 (2000).
169. Price, K. A. *et al.* Mechanisms controlling the cellular accumulation of copper bis(thiosemicarbazonato) complexes. *Inorganic chemistry* **50**, 9594–605 (2011).
170. Treiber, C. *et al.* Clioquinol mediates copper uptake and counteracts copper efflux activities of the amyloid precursor protein of Alzheimer's disease. *The Journal of biological chemistry* **279**, 51958–64 (2004).
171. Ritchie, C. W. *et al.* Metal-protein attenuation with iodochlorhydroxyquin (clioquinol) targeting Abeta amyloid deposition and toxicity in Alzheimer disease: a pilot phase 2 clinical trial. *Archives of neurology* **60**, 1685–91 (2003).
172. Adlard, P. A. *et al.* Rapid restoration of cognition in Alzheimer's transgenic mice with 8-hydroxy quinoline analogs is associated with decreased interstitial Abeta. *Neuron* **59**, 43–55 (2008).
173. Treatment Horizon.
174. Ding, W.-Q., Liu, B., Vaught, J. L., Yamauchi, H. & Lind, S. E. Anticancer activity of the antibiotic clioquinol. *Cancer research* **65**, 3389–95 (2005).
175. Dallavalle, F., Folesani, G., Marchelli, R. & Galaverna, G. Stereoselective Formation of Ternary Copper(II) Complexes of (S)-amino-acid amides and (R)- or (S)-amino acids in aqueous solution. *Helvetica Chimica Acta* **77**, 1623–1630 (1994).

176. Di Vaira, M. *et al.* Clotiquinol, a drug for Alzheimer's disease specifically interfering with brain metal metabolism: structural characterization of its zinc(II) and copper(II) complexes. *Inorganic chemistry* **43**, 3795–7 (2004).
177. Ahmed, I. T., Ahmed Boraei, A. A. & El-Roudi, O. M. Mixed-Ligand Complexes of Some Divalent Transition Metal Ions with Dicarboxylic Amino Acids and 8-Hydroxyquinoline. *Journal of Chemical & Engineering Data* **43**, 459–464 (1998).
178. Sawicka, J. *et al.* Synthesis and coordination ability of substituted imidazopyridines, structural analogues of oxine. Influence of copper(II) and nickel(II) ions on toxicity of the organic ligand. *Journal of Inorganic Biochemistry* **44**, 117–125 (1991).
179. Stary, J.; Zolotov, Y. A.; Petrukhin, O. M. Critical Evaluation of Equilibrium Constants Involving 8-Hydroxyquinoline and Its Metal Chelates. *Pergamon press, IUPAC Chemical Data Series 24* 18–55 (1979).
180. Pettit, L. D.; Powell, H. K. J. No Title. *The IUPAC Stability Constants Database* (2000).
181. Smith, R. M.; Martell, A. E.; Motekaitis, R. J. No Title. *NIST Critically Selected Stability Constants of Metal Complexes Database* (2007).
182. Aquilanti, G. *et al.* A study on the coordinative versatility of new N,S-donor macrocyclic ligands: XAFS, and Cu²⁺ complexation thermodynamics in solution. *Dalton transactions (Cambridge, England : 2003)* **40**, 2764–77 (2011).
183. Ruschak, A. M., Slassi, M., Kay, L. E. & Schimmer, A. D. Novel proteasome inhibitors to overcome bortezomib resistance. *Journal of the National Cancer Institute* **103**, 1007–17 (2011).
184. Kaiser, S. M. & Escher, B. I. The evaluation of liposome-water partitioning of 8-hydroxyquinolines and their copper complexes. *Environmental science & technology* **40**, 1784–1791 (2006).
185. Cherny, R. A. *et al.* Treatment with a Copper-Zinc Chelator Markedly and Rapidly Inhibits β -Amyloid Accumulation in Alzheimer's Disease Transgenic Mice. *Neuron* **30**, 665–676 (2001).
186. Zhai, S. *et al.* Tumor cellular proteasome inhibition and growth suppression by 8-hydroxyquinoline and clotiquinol requires their capabilities to bind copper and transport copper into cells. *Journal of biological inorganic chemistry* **15**, 259–269 (2010).

187. Avramovich-Tirosh, Y. *et al.* Therapeutic targets and potential of the novel brain-permeable multifunctional iron chelator-monoamine oxidase inhibitor drug, M-30, for the treatment of Alzheimer's disease. *Journal of neurochemistry* **100**, 490–502 (2007).
188. Deraeve, C. *et al.* Preparation and study of new poly-8-hydroxyquinoline chelators for an anti-Alzheimer strategy. *Chemistry (Weinheim an der Bergstrasse, Germany)* **14**, 682–96 (2008).
189. Mekouar, K. *et al.* Styrylquinoline derivatives: a new class of potent HIV-1 integrase inhibitors that block HIV-1 replication in CEM cells. *Journal of medicinal chemistry* **41**, 2846–2857 (1998).
190. Chang, F.-S., Chen, W., Wang, C., Tzeng, C.-C. & Chen, Y.-L. Synthesis and antiproliferative evaluations of certain 2-phenylvinylquinoline (2-styrylquinoline) and 2-furanylvinyquinoline derivatives. *Bioorganic & medicinal chemistry* **18**, 124–133 (2010).
191. Lescoat, G., Léonce, S., Pierré, A., Gouffier, L. & Gaboriau, F. Antiproliferative and iron chelating efficiency of the new bis-8-hydroxyquinoline benzylamine chelator S1 in hepatocyte cultures. *Chemico-biological interactions* **195**, 165–172 (2012).
192. Mouralian, C., Buss, J. L., Stranix, B., Chin, J. & Ponka, P. Mobilization of iron from cells by hydroxyquinoline-based chelators. *Biochemical pharmacology* **71**, 214–222 (2005).
193. Jiang, H. *et al.* Nitroxoline (8-hydroxy-5-nitroquinoline) is more a potent anti-cancer agent than clioquinol (5-chloro-7-iodo-8-quinoline). *Cancer letters* **312**, 11–17 (2011).
194. Kitamura, C., Maeda, N. & Kamada, N. Synthesis of 2-(substituted methyl) quinolin-8-ols and their complexation with Sn (II). *J. Chem. Soc., Perkin Transactions 1* 781–785 (2000).doi:10.1039/a908636f
195. Phillips, J. P., Breese, R. & Barrall, E. Styryl derivatives of 8-quinolinol. *The Journal of Organic Chemistry* **475**, 2–4 (1959).
196. Kashaev, a. G., Zimichev, a. V., Klimochkin, Y. N. & Zemtsova, M. N. Synthesis of 2-[2-(2-aminophenyl)ethyl]-6-R-quinoline-4-carboxylic acids from 2-[2-(2-nitrophenyl)ethenyl]-6-R-quinoline-4-carboxylic Acids. *Russian Journal of Organic Chemistry* **46**, 1425–1426 (2010).

197. Albrecht, M. *et al.* Di(8-hydroxyquinoline) Derivatives for Supramolecular Chemistry: Syntheses and Solid State Superstructures. *Synthesis* **1999**, 1819–1829 (1999).
198. Kashaev, a. G., Zimichev, a. V, Klimochkin, Y. N. & Zemtsova, M. N. Synthesis of 2-[2-(2-aminophenyl)ethyl]-6-R-quinoline-4-carboxylic acids from 2-[2-(2-nitrophenyl)ethenyl]-6-R-quinoline-4-carboxylic Acids. *Russian Journal of Organic Chemistry* **46**, 1425–1426 (2010).

12. Acknowledgement

Vorrei prima di tutto ringraziare il prof. Lanfranchi, anche se non c'è più, perché è stato il primo a credere in me e a propormi questo dottorato. Grazie anche a lui sono arrivata fin qui.

Grazie anche a tutti quelli che hanno collaborato con me in tutti i progetti intrapresi in questi 3 anni.

Come non ringraziare il mio Supervisor, penso il migliore di questa università, Luciano che è riuscito ad insegnarmi migliaia di cose, anche quelle inutili: non dimenticherò mai il termine "pedissequi". Lo ringrazio anche perché è riuscito a farmi sorridere tutti i giorni ed è riuscito a farmi capire le cose, anche quando sbagliavo, sempre con gentilezza e leggerezza. Grazie per avermi chiamato (urlando nei corridoi) PATATONA o a livello internazionale BIG POTATO. Ma non riuscirò mai abbastanza a ringraziarlo. E lui non avrà mai più un dottorando così bravo da vincere 3 premi poster di cui 2 internazionali.

Ringrazio il mio mentore Gennari per le perle che mi dà tutte le volte che andiamo a cena fuori e ringrazio anche il mio puccettone americano Pax e la sua dolce Christie per i momenti indimenticabili che mi ha fatto passare a Chicago. Devo poi ringraziare tutti gli amici dei chimica: tutti i prof che si sono rivelati ottimi amici, il Tego e la Domi con i loro fantastici racconti sugli esami agli studenti del primo anno, Mauro e il nostro amore per Federer e tutti gli altri. Ringrazio anche i miei due tecnici preferiti: Marco che riusciva a farmi ridere sempre anche quando gli rispondevo male e il dolcissimo Beppe, con le sue battute sottili, che non mi ha mai detto di no. Tutti i laureandi a cui ho insegnato qualcosa(spero di buono) in particolare Corrado a cui lascio lo scettro del potere e Dario che purtroppo devo lasciare sul più bello. Ringrazio anche gli altri dottorandi per le cene e le fantastiche serate: Gabry per tutto il cibo che ha ingurgitato e Domenico per le sue uscite inaspettate e meravigliose. Grazie anche a Tucci, l'Ellen, la Vero, Penna, il Milio, Fede, Dany, i polacchi e anche chi ho dimenticato. Un grazie anche alla Cri e alla sua meravigliosa pancia e quindi a Kevin. E poi in fondo i due amori della mia vita, le mie due bionde ricce: senza di loro non avrei saputo che fare...grazie Dany e grazie Bigna, grazie per esserci state sempre, grazie per le mille risate, grazie veramente di tutto.

Un grazie alla mia maestosissima squadra di calcetto..grazie PAPERRE..grazie a voi ho sfogato la mia ira sulle avversarie.

Grazie alle amiche di sempre: la Kerol e i frittoni, la dolcissima Sandry, la Pizzu e i suoi mille racconti, la Kim e cose che non si possono scrivere, la Giady, la Misc e la mia Gio ora anche testimone di nozze.

Grazie ai miei fratelloni sempre uguali e fuori di testa e alle mie dolci nonne.

Grazie alla Minni che mi ama sempre molto, allo stupido Roger, alla Foca Liz, al morbidissimo Henry e le vecchiette Beth e Fency. Grazie anche ai nuovi arrivati Mojito, Martini, Gin e Spritz.

Grazie ai miei meravigliosi suoceri che mi hanno sempre sostenuta.

Ma il grazie piu grande va ai miei genitori: sono loro che mi hanno insegnato tutto. Mi hanno insegnato ad affrontare il lavoro fino in fondo, mi hanno insegnato a non mollare mai, ad essere audace e ambiziosa. Mi hanno insegnato di dare sempre il massimo se si vuole ottenere il massimo. Grazie mamma e grazie papà, tutto questo è per voi.

Grazie Giamma che sei ancora qui al mio fianco, ancora piu vicino, ora che sei mio marito. Grazie per supportarmi e sopportarmi sempre anche nei periodi di stress. Grazie per sentire tutte le mie presentazioni anche capendo poco. Grazie per amarmi così tanto.

E brava Ire...

13. Appendix

Crystallographic data for [Ag(L^HCH₂S)]_n(BF₄)_n (1), [Cu(L^HCH₂S)]_n(BF₄)_n (2), [Ag(L^{Me}CH₂S)]_n(BF₄)_n (3), [Cu(L^{Me}CH₂S)]_n(BF₄)_n (4), [Ag(L^{Me}CH₂S)]_n(PF₆)_n (5).

	1	2	3	4	5
Empirical formula	C ₁₄ H ₁₂ AgBF ₄ N ₂ S	C ₁₄ H ₁₂ BCuF ₄ N ₂ S	C ₁₈ H ₁₂ AgBF ₄ N ₂ S	C ₁₈ H ₁₂ BCuF ₄ N ₂ S	C ₁₈ H ₁₂ AgF ₆ N ₂ PS
Formula weight	465.03	420.70	521.14	476.81	579.30
Colour, habit	Colorless, block	Colorless, block	Colorless, block	Colorless, block	Colorless, block
Crystal size, mm	0.33×0.24×0.14	0.27×0.15×0.12	0.31×0.08×0.06	0.22×0.12×0.10	0.24×0.17×0.09
Crystal system	Monoclinic	Monoclinic	Monoclinic	Monoclinic	Monoclinic
Space group	<i>P</i> 2 ₁ / <i>c</i>	<i>P</i> 2 ₁ / <i>c</i>	<i>P</i> 2 ₁ / <i>c</i>	<i>P</i> 2 ₁ / <i>c</i>	<i>P</i> 2 ₁ / <i>c</i>
<i>a</i> , Å	8.901(1)	9.056(1)	10.358(2)	10.460(1)	9.672(1)
<i>b</i> , Å	17.268(2)	17.253(1)	18.275(4)	17.394(1)	19.400(2)
<i>c</i> , Å	11.510(1)	11.107(1)	11.743(3)	11.542(1)	12.301(1)
α , deg.	90	90	90	90	90
β , deg.	102.979(1)	101.500(2)	91.791(4)	96.521(1)	100.521(2)
γ , deg.	90	90	90	90	90
<i>V</i> , Å ³	1723.9(3)	1700.6(3)	2221.8(9)	2086.4(3)	2269.3(4)
<i>Z</i>	4	4	4	4	4
<i>T</i> , K	293(2)	293(2)	293(2)	190(2)	293(2)
ρ (calc), Mg/m ³	1.792	1.643	1.558	1.518	1.696
μ , mm ⁻¹	1.335	1.452	1.045	1.193	1.112
θ range, deg.	2.17 to 30.51	2.21 to 28.36	1.97 to 27.07	1.96 to 28.02	1.98 to 27.69
No. of rflcn/unique	27964 / 5172	22633 / 4246	24947 / 4864	25185 / 4988	30119 / 5297
Goof	1.003	1.011	1.001	1.007	1.015
<i>R</i> 1	0.0380	0.0371	0.0523	0.0344	0.0390
<i>wR</i> 2	0.1094	0.0847	0.0555	0.0670	0.0920

$$R_1 = \sum ||F_o| - |F_c|| / \sum |F_o|, wR_2 = [\sum (w(F_o - F_c)^2) / \sum (w(F_o)^2)]^{1/2}, w = 1/[\sigma^2(F_o) + (aP)^2 + bP], \text{ where } P = [\max(F_o, 0) + 2F_c]/3$$

Crystallographic data for $[\text{Ag}(\text{L}^{10})\text{CH}_2\text{S}]_n(\text{PF}_6)_n(\text{CH}_3)_2\text{CO}$ (6), $[\text{Ag}(\text{L}^{10})\text{CH}_2\text{S}]_n(\text{CF}_3\text{SO}_3)_n$ (7) $[\text{Ag}(\text{L}^{10})\text{CH}_2\text{S}]_n(\text{CF}_3\text{SO}_3)_n \cdot 2\text{CH}_2\text{Cl}_2$ (8), $[\text{Cu}(\text{L}^{10})\text{CH}_2\text{S}]\text{PPh}_3\text{BF}_4$ (10).

	6	7	8	10
Empirical formula	$\text{C}_{55}\text{H}_{82}\text{Ag}_2\text{F}_{12}\text{N}_8\text{OP}_2\text{S}_2$	$\text{C}_{19}\text{H}_{22}\text{AgF}_3\text{N}_4\text{O}_3\text{S}_2$	$\text{C}_{29}\text{H}_{42}\text{AgCl}_4\text{F}_3\text{N}_4\text{O}_3\text{S}_2$	$\text{C}_{33}\text{H}_{32}\text{BCuF}_4\text{N}_4\text{O}_5\text{P}_5$
Formula weight	1441.09	583.40	865.46	712.01
Colour, habit	Colorless, block	Colorless, block	Colorless, block	Colorless, block
Crystal size, mm	0.26×0.17×0.11	0.45×0.16×0.05	0.21×0.17×0.09	0.17×0.10×0.08
Crystal system	Monoclinic	Monoclinic	Monoclinic	Triclinic
Space group	Cc	$P2_1/c$	$C2/c$	$P-1$
<i>a</i> , Å	19.316(1)	10.668(1)	23.477(2)	11.641(1)
<i>b</i> , Å	17.068(1)	17.659(1)	12.839(1)	11.854(1)
<i>c</i> , Å	21.141(2)	12.544(1)	26.057(2)	13.121(1)
α , deg.	90	90	90	79.685(1)
β , deg.	102.624(2)	95.56(1)	106.500(1)	77.861(1)
γ , deg.	90	90	90	70.546(1)
<i>V</i> , Å ³	6801.4(8)	2352.0(3)	7531(1)	1657.3(2)
<i>Z</i>	4	4	8	2
<i>T</i> , K	293(2)	293(2)	200(2)	200(2)
$\rho(\text{calc})$, Mg/m ³	1.407	1.684	1.527	1.427
μ , mm ⁻¹	0.758	1.086	0.980	0.825
θ range, deg.	1.61 to 26.86	1.92 to 27.10	1.63 to 26.75	1.60 to 23.26
No. of rflcn/unique	42584 / 14619	29952 / 5183	21169 / 7955	14162 / 4761
Goof	1.001	1.005	1.002	1.006
<i>R</i> 1	0.0387	0.0416	0.0493	0.0242
<i>wR</i> 2	0.0769	0.1127	0.0612	0.0627

$$R1 = \sum ||F_o| - |F_c|| / \sum |F_o|, wR2 = [\sum [w(F_o - F_c)^2] / \sum [w(F_o)^2]]^{1/2}, w = 1 / [\sigma^2(F_o) + (ap)^2 + bp], \text{ where } P = [\max(F_o, 0) + 2F_c] / 3$$

Crystallographic data for, $[\text{Ag}(\text{L}^{\text{Me}}\text{-CH}_2\text{S})\text{PPh}_3]\text{BF}_4$ (**11**), $[\text{Cu}(\text{L}^{\text{Me}}\text{-CH}_2\text{S})\text{PPh}_3]\text{BF}_4$ (**12**), $[\text{Ag}(\text{L}^{\text{Pr}}\text{-CH}_2\text{S})\text{PPh}_3]\text{BF}_4$ (**13**), $[\text{Cu}(\text{L}^{\text{Pr}}\text{-CH}_2\text{S})\text{PPh}_3]\text{BF}_4\cdot\text{THF}$ (**14**), $[\text{Ag}(\text{L}^{\text{Ph}}\text{PhS})]_n(\text{BF}_4)_n$ (**15**).

	11	12	13	14	15
Empirical formula	$\text{C}_{36}\text{H}_{37}\text{AgBF}_4\text{N}_4\text{P}_5\text{S}$	$\text{C}_{36}\text{H}_{37}\text{BCuF}_4\text{N}_4\text{P}_5\text{S}$	$\text{C}_{48}\text{H}_{61}\text{AgBF}_4\text{N}_4\text{P}_5\text{S}$	$\text{C}_{48}\text{H}_{61}\text{BCuF}_4\text{N}_4\text{OP}_5\text{S}$	$\text{C}_{38}\text{H}_{32}\text{Ag}_2\text{B}_2\text{F}_8\text{N}_8\text{S}_2$
Formula weight	783.41	739.08	895.61	923.39	1054.20
Colour, habit	Colorless, block	Colorless, block	Colorless, block	Colorless, block	Colorless, block
Crystal size, mm	0.34 x 0.21 x 0.21	0.45 x 0.33 x 0.15	0.16 x 0.11 x 0.08	0.27 x 0.15 x 0.15	0.47 x 0.32 x 0.13
Crystal system	Orthorhombic	Monoclinic	Monoclinic	Triclinic	Monoclinic
Space group	$Pbcn$	$P2_1/c$	$P2_1$	$P1$	$P2_1/a$
a , Å	21.741(2)	13.075(1)	9.860(1)	9.440(1)	21.368(1)
b , Å	20.335(2)	15.748(1)	16.751(2)	10.440(1)	10.170(1)
c , Å	16.420(1)	17.820(1)	13.817(1)	12.261(1)	21.555(2)
α , deg.	90	90	90	101.536(1)	90
β , deg.	90	95.372(5)	90.526(2)	90.687(1)	118.776(1)
γ , deg.	90	90	90	93.756(1)	90
V , Å ³	7259(1)	3653.1(4)	2282.0(4)	1181.0(2)	4105.7(6)
Z	8	4	2	1	4
T , K	293(2)	293(2)	293(2)	293(2)	293(2)
ρ (calc), Mg/m ³	1.434	1.344	1.303	1.198	1.705
μ , mm ⁻¹	0.709	0.750	0.572	0.596	1.132
θ range, deg.	1.37 to 26.49	1.56 to 26.42	1.47 to 25.72	1.70 to 26.50	2.16 to 28.37
No. of rflcn/unique	84181 / 7500	42281 / 7498	26604 / 8689	13340 / 9582	56570 / 10270
Goof	1.022	1.006	1.004	1.002	1.044
$R1$	-	-	0.00(2)	-0.019(8)	0.0554
$wR2$	0.0355	0.0423	0.0429	0.0403	0.1314
	0.0837	0.1011	0.0852	0.0604	

$$R1 = \sum ||F_o| - |F_c|| / \sum |F_o|, wR2 = [\sum [w(F_o2 - F_c2)^2] / \sum [w(F_o2)^2]]^{1/2}, w = 1 / [\sigma^2(F_o2) + (ap)^2 + bP], \text{ where } P = [\max(F_o2, 0) + 2F_c2] / 3$$

Crystallographic data for $[\text{Ag}(\text{L}^{\text{PhS}})]_2(\text{PF}_6)_2 \cdot \text{CH}_2\text{Cl}_2$ (**16**), $[\text{Cu}(\text{L}^{\text{PhS}})(\text{CH}_3\text{CN})_2](\text{BF}_4)_2$ (**17**), $[\text{Cu}(\text{L}^{\text{PhS}})\text{PPh}_3]\text{BF}_4$ (**18**) and $[\text{Cu}(\text{L}^{\text{MePhS}})\text{PPh}_3]\text{BF}_4$ (**21**).

	16	17	18	21
Empirical formula	$\text{C}_{40}\text{H}_{36}\text{Ag}_2\text{Cl}_2\text{F}_{12}\text{N}_8\text{P}_2\text{S}_2$	$\text{C}_{42}\text{H}_{38}\text{B}_2\text{Cu}_2\text{F}_8\text{N}_{10}\text{S}_2$	$\text{C}_{37}\text{H}_{31}\text{BCuF}_4\text{N}_4\text{P}_5\text{S}$	$\text{C}_{82}\text{H}_{78}\text{B}_2\text{Cu}_2\text{F}_8\text{N}_8\text{P}_2\text{S}_2$
Formula weight	1340.37	1047.64	745.04	1602.28
Colour, habit	Colorless, block	Colorless, block	Colorless, block	Colorless, Block
Crystal size, mm	0.19×0.17×0.12	0.20×0.12×0.05	0.10×0.08×0.05	0.45×0.30×0.30
Crystal system	Triclinic	Monoclinic	Monoclinic	Triclinic
Space group	<i>P</i> -1	<i>C</i> 2/c	<i>P</i> 2 ₁ /n	<i>P</i> -1
<i>a</i> , Å	10.160(2)	26.105(3)	13.953(4)	14.345(1)
<i>b</i> , Å	10.620(2)	8.080(1)	15.533(4)	14.540(1)
<i>c</i> , Å	12.736(2)	21.356(2)	16.860(5)	18.668(2)
α , deg.	78.688(3)	90	90	96.202(1)
β , deg.	73.156(3)	99.832(2)	106.95(1)	90.753(1)
γ , deg.	71.562(3)	90	90	91.947(1)
<i>V</i> , Å ³	1239.4(4)	4438.4(9)	3495(2)	3868.1(6)
<i>Z</i>	1	4	4	2
<i>T</i> , K	293(2)	190(2)	190(2)	293(2)
ρ (calc), Mg/m ³	1.796	1.568	1.416	1.376
μ , mm ⁻¹	1.240	1.131	0.785	0.714
θ range, deg.	1.68 to 27.10	1.58 to 27.05	1.67 to 26.00	1.10 to 28.02
No. of rflcn/unique	14504 / 5407	18698 / 4837	36407 / 6857	47135 / 18143
Goof	1.004	1.006	0.775	1.008
<i>R</i> 1	0.0391	0.0521	0.0490	-
<i>wR</i> 2	0.0813	0.0773	0.0509	0.0362
				0.0723

$$R1 = \sum ||F_o| - |F_c|| / \sum |F_o|, wR2 = [\sum [w(F_o^2 - F_c^2)^2] / \sum [w(F_o^2)^2]]^{1/2}, w = 1 / [\sigma^2(F_o^2) + (aP)^2 + bP], \text{ where } P = [\text{max}(F_o^2, 0) + 2F_c^2] / 3$$

Summary of X-ray crystallographic data for 23-BF₄, 24-PF₆, 25-CF₃SO₃, 26-NO₃ and 22.

	23-BF ₄	24-PF ₆	25-CF ₃ SO ₃	26-NO ₃	22
Empirical formula	C ₁₅₀ H ₁₆₈ Ag ₆ B ₆ Cl ₂₄ F ₂₄ N ₂₄ S ₆	C ₁₈₀ H ₂₄₀ Ag ₆ F ₃₆ N ₂ O ₁₂ P ₆ S ₆	C ₂₀₄ H ₂₆₈ Ag ₆ F ₁₈ N ₂₄ O ₃₀ S ₁₂	C ₁₆₂ H ₁₉₆ Ag ₆ Cl ₂₄ N ₃₀ O ₁₈ S ₆	C ₁₅₀ H ₁₆₈ Cu ₆ B ₆ Cl ₂₄ F ₂₄ N ₂₄ S ₆
Formula weight	4518.32	4641.36	4910.36	4541.87	4252.34
Colour, habit	Colorless, prism	Colorless, prism	Colorless, prism	Colorless, prism	Colorless, prism
Crystal size, mm	0.36x0.32x0.32	0.29x0.26x0.15	0.38x0.20x0.11	0.26x0.23x0.16	0.15x0.13x0.09
Crystal system	Cubic	Cubic	Rhombohedral	Rhombohedral	Cubic
Space group	Fd-3	Fd-3	R-3	R-3	Fd-3
a, Å	42.382(2)	42.990(9)	29.434(1)	29.821(5)	41.603(3)
b, Å	42.382(2)	42.990(9)	29.434(1)	29.821(5)	41.603(3)
c, Å	42.382(2)	42.990(9)	22.407(1)	20.416(3)	41.603(3)
α, deg.	90	90	90	90	90
β, deg.	90	90	90	90	90
γ, deg.	90	90	120	120	90
V, Å ³	76128(6)	79452(29)	16811.7(11)	15723(4)	72007(9)
Z	16	16	3	3	16
T, K	205(2)	205(2)	205(2)	190(2)	190(2)
ρ(calcd), Mg/m ³	1.577	1.552	1.455	1.439	1.569
μ, mm ⁻¹	1.084	0.788	0.711	0.977	1.203
θ range, deg.	1.36 to 27.02	0.82 to 23.99	1.21 to 27.03	1.27 to 27.07	1.23 to 23.00
No. of rflcn/unique	222427 / 6956	32151 / 5228	66483 / 8189	56680 / 7668	82253 / 4202
Goof	1.008	1.005	1.002	1.001	1.002
R1	0.0437	0.0428	0.0505	0.0464	0.0594
wR2	0.1046	0.1033	0.1291	0.1067	0.1142

$$R1 = \Sigma||F_o| - |F_c|| / \Sigma|F_o|, wR2 = [\Sigma[w(F_o2 - F_c2)^2] / \Sigma[w(F_o2)^2]]^{1/2}, w = 1/(\sigma^2(F_o2) + (ap)^2 + bp^2), \text{ where } P = [\max(F_o2, 0) + 2F_c2] / 3$$

V

Summary of X-ray crystallographic data for $[\text{Ag}(\text{L}^{\text{M}})]_n(\text{CF}_3\text{SO}_3)_n$ (**27-CF₃SO₃**), $[\text{Ag}(\text{L}^{\text{PMe}})]_n(\text{CF}_3\text{SO}_3)_n$ (**28-CF₃SO₃**), $[\text{Ag}(\text{L}^{\text{T}})]_n(\text{CF}_3\text{SO}_3)_n$ (**29-CF₃SO₃**), $[\text{Ag}(\text{L}^{\text{OMe}})]_n(\text{CF}_3\text{SO}_3)_n$ (**30-CF₃SO₃**), $[\text{Ag}(\text{L}^{\text{OMe}})]_n(\text{CF}_3\text{SO}_3)_n$ (**31-CF₃SO₃**).

	27-CF₃SO₃	28-CF₃SO₃	29-CF₃SO₃	30-CF₃SO₃	31-CF₃SO₃
Empirical formula	$\text{C}_{58}\text{H}_{56}\text{Ag}_2\text{Cl}_4\text{F}_6\text{N}_6\text{O}_{34}\text{S}_4$	$\text{C}_{51}\text{H}_{54}\text{Ag}_2\text{F}_6\text{N}_6\text{O}_{32}\text{S}_4$	$\text{C}_{25}\text{H}_{52}\text{AgCl}_2\text{F}_4\text{N}_4\text{O}_{32}\text{S}_2$	$\text{C}_{51}\text{H}_{54}\text{AgCl}_2\text{F}_6\text{N}_6\text{O}_{34}\text{S}_4$	$\text{C}_{56}\text{H}_{64}\text{Ag}_2\text{F}_6\text{N}_6\text{O}_{37}\text{S}_4$
Formula weight	1560.89	1337.51	748.38	1435.90	1427.13
Colour, habit	Colorless, block	Colorless, block	Colorless, prism	Colorless, plate	Colorless, block
Crystal size, mm	0.20×0.14×0.09	0.11×0.05×0.03	0.42×0.14×0.14	0.48×0.43×0.13	0.28×0.24×0.20
Crystal system	Orthorhombic	Orthorhombic	Orthorhombic	Orthorhombic	Monoclinic
Space group	<i>Pcab</i>	<i>Pbca</i>	<i>Pbca</i>	<i>Pc2₁b</i>	<i>C2/c</i>
<i>a</i> , Å	20.464(1)	21.775(1)	11.708(1)	13.108(5)	30.542(7)
<i>b</i> , Å	22.444(1)	21.080(1)	15.342(1)	20.763(7)	22.961(5)
<i>c</i> , Å	28.423(1)	27.323(2)	34.461(2)	22.726(9)	24.166(5)
α , deg.	90	90	90	90	90
β , deg.	90	90	90	90	131.839(3)
γ , deg.	90	90	90	90	90
<i>V</i> , Å ³	13055(1)	12541(1)	6190.0(8)	6185(4)	12626(5)
<i>Z</i>	8	8	8	4	8
<i>T</i> , K	293(2)	293(2)	293(2)	293(2)	293(2)
ρ (calc), Mg/m ³	1.588	1.417	1.606	1.542	1.502
μ , mm ⁻¹	0.964	0.825	1.016	0.928	0.826
θ range, deg.	1.81 to 25.03	1.49 to 25.06	2.10 to 25.73	1.55 to 26.55	1.23 to 26.00
No. of rflcn/unique	105327 / 11426	65160 / 11099	67712 / 5893	67327 / 12833	33267 / 12378
Goof	1.016	1.003	1.032	1.003	1.015
<i>R</i> 1	-	-	-	0.23(2)	-
<i>wR</i> 2	0.0512	0.0555	0.0462	0.0401	0.0532
	0.0856	0.1049	0.1288	0.0865	0.1217

$$R1 = \sum ||F_o| - |F_c|| / \sum |F_o|, wR2 = [\sum [w(F_o^2 - F_c^2)^2] / \sum [w(F_o^2)^2]]^{1/2}, w = 1/[\sigma^2(F_o^2) + (aP)^2 + bP], \text{ where } P = [\max(F_o, 0) + 2F_c^2]/3$$

Summary of X-ray crystallographic data for $[\text{Ag}(\text{L}^{\text{N}})]_6(\text{PF}_6)_6$ (**27-PF₆**), $[\text{Ag}(\text{L}^{\text{PMe}})]_n(\text{PF}_6)_n$ (**28-PF₆**), $[\text{Ag}(\text{L}^{\text{OMe}})]_6(\text{PF}_6)_6$ (**30-PF₆**), $[\text{Ag}(\text{L}^{\text{I}})]_6(\text{PF}_6)_6$ (**29-PF₆**), $[\text{Ag}(\text{L}^{\text{mMe}})]_6(\text{PF}_6)_6$ (**31-PF₆**).

	27-PF ₆	30-PF ₆	31-PF ₆	28-PF ₆	29-PF ₆
Empirical formula	C ₁₈₃ H ₂₀₄ Ag ₆ F ₃₆ N ₂₄ O ₆ P ₆ S ₆	C ₁₅₆ H ₁₈₀ Ag ₆ Cl ₂₄ F ₃₆ N ₂₄ O ₆ P ₆ S ₆	C ₁₅₀ H ₁₆₈ Ag ₆ Cl ₁₂ F ₃₆ N ₂₄ P ₆ S ₆	C ₂₆ S ₁₃ H ₁₅₀ Ag ₆ F ₆ N ₆ O ₇ P ₅	C ₁₈₀ H ₂₃₄ Ag ₆ F ₄₂ N ₂₄ O ₁₂ P ₆ S ₆
Formula weight	4545.10	5047.44	4441.88	702.96	4749.31
Colour, habit	Colorless, block	Colorless, prism	Colorless, prism	Colorless, needle	Colorless, block
Crystal size, mm	0.18×0.18×0.14	0.10×0.07×0.05	0.33×0.26×0.21	0.25×0.05×0.04	0.13×0.12×0.09
Crystal system	Cubic	Cubic	Cubic	Tetragonal	Cubic
Space group	Fd-3	Fd-3	Fd-3	I4 ₁ /a	Fd-3
a, Å	43.025(2)	42.950(3)	43.300(1)	23.758(2)	43.087(2)
b, Å	43.025(2)	42.950(3)	43.300(1)	23.758(2)	43.087(2)
c, Å	43.025(2)	42.950(3)	43.300(1)	22.318(2)	43.087(2)
α, deg.	90	90	90	90	90
β, deg.	90	90	90	90	90
γ, deg.	90	90	90	90	90
V, Å ³	79646(6)	79230(10)	81183(3)	12597(2)	79991(6)
Z	16	16	16	16	16
T, K	293(2)	293.2	293(2)	293(2)	293(2)
ρ(calcd), Mg/m ³	1.516	1.693	1.454	1.483	1.577
μ, mm ⁻¹	0.783	1.109	0.916	0.818	0.789
θ range, deg.	1.34 to 25.77	0.82 to 20.95	1.33 to 24.00	1.71 to 25.80	1.34 to 22.77
No. of reflections/unique	107924 / 6362	133557 / 3545	184803 / 5240	72145 / 6036	43789 / 4527
Goof	1.007	1.087	1.064	1.027	1.007
R1	0.0419	0.0773	0.0501	0.0420	0.0466
wR2	0.1063	0.2156	0.1163	0.1091	0.0903

$$R1 = \sum ||F_o| - |F_c|| / \sum |F_o|, wR2 = [\sum [w(F_o^2 - F_c^2)^2] / \sum [w(F_o^2)^2]]^{1/2}, w = 1 / [\sigma^2(F_o^2) + (ap)^2 + bP], \text{ where } P = [\max(F_o^2, 0) + 2Fc^2] / 3$$

Summary of X-ray crystallographic data for L^{Br} PhSPhSPH, **33**, **34** and **35**.

	L^{Br} PhSPhSPH	33	34	35
Empirical formula	$C_{37}H_{14}N_4S_2$	$C_{35}H_{20}AgBF_4N_4S_2$	$C_{35}H_{40}AgBF_4N_4O_2S_2$	$C_{40}H_{50}AgBF_4N_4O_5S_2$
Formula weight	608.88	635.25	807.51	861.64
Colour, habit	Colorless, prism	Colorless, block	Colorless, block	Colorless, block
Crystal size, mm	0.45x0.10x0.10	0.65x0.25x0.15	0.48x0.23x0.11	0.45x0.40x0.37
Crystal system	Monoclinic	Tetragonal	Orthorhombic	Orthorhombic
Space group	$P2_1/c$	$P4_1$	$Pca2_1$	$Pbca$
a , Å	20.758(2)	9.138(1)	27.664(2)	20.781(1)
b , Å	8.218(1)	9.138(1)	8.836(1)	18.131(1)
c , Å	21.153(2)	30.539(4)	15.110(1)	22.205(1)
α , deg.	90	90	90	90
β , deg.	100.57(1)	90	90	90
γ , deg.	90	90	90	90
V , Å ³	3547.2(6)	2550.1(5)	3693.5(6)	8366.4(7)
Z	4	4	4	8
T , K	293(2)	173(2)	200(2)	293(2)
ρ (calc), Mg/m ³	1.140	1.655	1.452	1.368
μ , mm ⁻¹	0.180	1.006	0.716	0.635
θ range, deg.	1.00 to 26.00	2.23 to 26.99	1.47 to 28.02	1.75 to 28.00
No. of rflcn/unique	36977 / 3814	26687 / 4742	42998 / 7522	96601 / 9977
Goof	-	0.05(4)	-0.01(1)	-
$R1$	1.009	1.036	1.007	1.004
$wR2$	0.0693	0.0691	0.0280	0.0597
	0.2052	0.1635	0.0517	0.1040

$$R1 = \frac{\sum ||F_o| - |F_c||}{\sum |F_o|}, wR2 = \frac{[\sum [w(F_o^2 - F_c^2)^2]]}{[\sum [w(F_o^2)^2]]}^{1/2}, w = 1/(\sigma^2(F_o^2) + (aP)^2 + bP), \text{ where } P = [\max(F_o^2, 0) + 2F_c^2]/3$$

Summary of X-ray crystallographic data for compounds 37-41.

	37	38	39	40	41
Empirical formula	C ₂₈ H ₃₈ Cl ₄ Cu ₂ N ₆ O ₂	C ₃₈ H ₃₈ Cl ₆ Cu ₂ N ₆ O ₂	C ₄₀ H ₆₂ Cl ₄ Cu ₂ N ₆ O ₂	C ₂₄ H ₂₃ Cl ₂ CuN ₃ O	C ₁₉ H ₂₁ Cl ₂ CuN ₃ OS
Formula weight	759.52	1041.58	927.84	503.89	473.89
Colour, habit	Green, block	Green, block	Green, block	Green, block	Green, needle
Crystal size, mm	0.19x0.16x0.14	0.26x0.13x0.10	0.27x0.16x0.13	0.27x0.25x0.13	0.31x0.08x0.08
Crystal system	Triclinic	Triclinic	Monoclinic	Monoclinic	Monoclinic
Space group	P-1	P-1	P2 ₁ /n	P2 ₁ /c	P2 ₁ /c
a, Å	10.542(1)	8.814(2)	16.047(1)	11.234(3)	8.082(1)
b, Å	10.549(1)	11.758(2)	10.655(1)	18.920(6)	12.312(1)
c, Å	17.058(2)	13.140(3)	28.388(1)	12.151(4)	21.242(2)
α, deg.	84.088(1)	99.094(4)	90	90	90
β, deg.	74.721(1)	101.834(4)	106.313(1)	109.295(5)	98.477(3)
γ, deg.	61.569(1)	109.287(4)	90	90	90
V, Å ³	1608.7(3)	1219.9(4)	4658.4(6)	2438(1)	2090.6(4)
Z	2	1	4	4	4
T, K	293(2)	293(2)	293(2)	293(2)	293(2)
ρ(calcd), Mg/m ³	1.568	1.418	1.323	1.373	1.506
μ, mm ⁻¹	1.691	1.384	1.181	1.135	1.414
θ range, deg.	1.24 to 27.02	1.63 to 27.02	1.32 to 24.80	1.92 to 26.99	1.92 to 27.53
No. of rflcn/unique	18936 / 7011	14283 / 5302	47722 / 8015	27842 / 5317	24703 / 4808
Goof	1.007	1.005	1.016	1.002	1.008
R1	0.0386	0.0390	0.0460	0.0312	0.0380
wR2	0.0670	0.0731	0.1104	0.0719	0.0615

$$R1 = \sum |F_o| - |F_c| / \sum |F_o|, wR2 = [\sum [w(F_o2 - F_c2)^2] / \sum [w(F_o2)^2]]^{1/2}, w = 1/(\sigma2(F_o2) + (ap)^2 + bP), \text{ where } P = [\max(F_o2, 0) + 2F_c2] / 3$$

Summary of X-ray crystallographic data for compounds **42-44**, **46** and **48**.

	42	43	44	46
Empirical formula	C ₂₈ H ₃₈ Cl ₄ Cu ₂ N ₆ O ₅ S ₂	C ₃₃ H ₄₀ Cl ₄ Cu ₂ N ₆ O ₅ S ₂	C ₄₀ H ₆₂ Cl ₄ Cu ₂ N ₆ O ₅ S ₂	C ₄₄ H ₁₆ Cl ₄ Cu ₂ N ₈
Formula weight	823.64	911.79	991.96	565.23
Colour, habit	Green, block	Green, block	Green, block	Green, block
Crystal size, mm	0.12x0.09x0.04	0.32x0.27x0.07	0.15x0.11x0.05	0.09x0.09x0.05
Crystal system	Triclinic	Triclinic	Triclinic	Monoclinic
Space group	<i>P</i> -1	<i>P</i> -1	<i>P</i> -1	<i>P</i> 2 ₁ / <i>c</i>
<i>a</i> , Å	8.576(1)	9.371(3)	9.304(6)	8.685(3)
<i>b</i> , Å	10.448(2)	10.681(4)	11.801(8)	15.198(6)
<i>c</i> , Å	11.856(2)	12.106(4)	12.441(9)	15.769(6)
α , deg.	93.069(3)	100.153(6)	73.951(9)	90
β , deg.	109.670(2)	108.798(6)	74.725(9)	93.87(1)
γ , deg.	110.080(2)	109.823(6)	68.733(9)	90
<i>V</i> , Å ³	922.2(3)	1022.1(6)	1203(1)	2077(1)
<i>Z</i>	1	1	1	4
<i>T</i> , K	293(2)	293(2)	293(2)	293(2)
ρ (calc), Mg/m ³	1.483	1.481	1.369	1.808
μ , mm ⁻¹	1.590	1.444	1.232	2.581
θ range, deg.	1.86 to 29.87	1.88 to 26.25	1.73 to 26.08	1.86 to 26.23
No. of rflcn/unique	14292 / 5266	12479 / 4123	11738 / 4636	11979 / 4078
Goof	1.003	1.018	1.007	0.876
<i>R</i> 1	0.0357	0.042	0.0679	0.0381
<i>wR</i> 2	0.0787	0.0918	0.0795	0.0503

$$R1 = \sum ||F_o| - |F_c|| / \sum |F_o|, wR2 = [\sum [w(F_o^2 - F_c^2)^2] / \sum [w(F_o^2)^2]]^{1/2}, w = 1/[\sigma^2(F_o^2) + (aP)^2 + bP], \text{ where } P = [\max(F_o^2, 0) + 2F_c^2]/3$$

X

Summary of X-ray crystallographic data for 50-52 and 54-55 complexes.

	48	50	51	52
Empirical formula	C ₁₉ H ₃₂ Cl ₂ CuN ₄	C ₃₈ H ₅₀ Cl ₄ Cu ₂ N ₈ S ₂	C ₄₆ H ₅₀ Cl ₄ Cu ₂ N ₈ O _{1.25} S ₂	C ₃₁ H ₄₀ Cl ₂ CuN ₄ S
Formula weight	450.93	933.72	1068.44	635.17
Colour, habit	Green, block	Green, block	Green, block	Green, block
Crystal size, mm	0.19x0.16x0.04	0.08x0.07x0.05	0.18x0.15x0.06	0.27x0.24x0.14
Crystal system	Triclinic	Monoclinic	Triclinic	Monoclinic
Space group	<i>P</i> -1	<i>P</i> ₂ / <i>c</i>	<i>P</i> -1	<i>P</i> ₂ / <i>n</i>
<i>a</i> , Å	9.337(3)	8.483(1)	8.990(4)	13.002(1)
<i>b</i> , Å	9.811(3)	20.248(3)	17.036(7)	16.610(2)
<i>c</i> , Å	13.137(4)	11.613(2)	17.751(8)	15.314(1)
α , deg.	84.748(6)	90	107.320(7)	90
β , deg.	74.118(5)	105.140(4)	93.791(7)	106.638(5)
γ , deg.	85.003(6)	90	98.286(7)	90
<i>V</i> , Å ³	1150.2(6)	1925.5(5)	2551(2)	3168.1(5)
<i>Z</i>	2	2	2	4
<i>T</i> , K	293(2)	293(2)	293(2)	293(2)
ρ (calc), Mg/m ³	1.302	1.610	1.391	1.332
μ , mm ⁻¹	1.192	1.532	1.168	0.950
θ range, deg.	1.62 to 25.00	2.08 to 26.02	2.01 to 24.76	1.82 to 27.03
No. of rflcn/unique	11422 / 4051	11526 / 3774	26216 / 8602	36271 / 6932
Goof	0.918	0.710	1.001	1.004
<i>R</i> 1	0.0521	0.0459	0.1056	0.0324
<i>wR</i> 2	0.0514	0.0604	0.2762	0.0543

$$R1 = \frac{\sum |F_o| - |F_c|}{\sum |F_o|}, wR2 = \frac{[\sum [w(F_o^2 - F_c^2)^2] / \sum [w(F_o^2)^2]]^{1/2}}{w}, w = 1/[\sigma^2(F_o^2) + (aP)^2 + bP], \text{ where } P = [\max(F_o^2, 0) + 2F_c^2]/3$$

Summary of X-ray crystallographic data for 50-52 and 54-55 complexes.

	54	55	60
Empirical formula	C ₁₈ H ₂₂ Cl ₂ CuN ₂ S	C ₂₆ H ₃₀ Cl ₂ CuN ₂ S	C ₆₆ H ₆₀ Cu ₃ N ₆ O ₆
Formula weight	460.90	573.10	1223.82
Colour, habit	Green, block	Green, block	Green, block
Crystal size, mm	0.23x0.22x0.14	0.25x0.13x0.06	0.13x0.12x0.07
Crystal system	Orthorhombic	Monoclinic	Triclinic
Space group	P2 ₁ 2 ₁ 2 ₁	P2 ₁ /c	P-1
a, Å	7.263(1)	10.011(1)	9.242(3)
b, Å	15.448(2)	17.382(2)	10.288(3)
c, Å	18.549(2)	17.323(2)	14.494(4)
α, deg.	90	90	77.219(5)
β, deg.	90	90.740(2)	84.291(4)
γ, deg.	90	90	80.289(5)
V, Å ³	2081.2(5)	3014.1(6)	1321.9(7)
Z	4	4	1
T, K	293(2)	293(2)	293(2)
ρ(calcd), Mg/m ³	1.471	1.263	1.537
μ, mm ⁻¹	1.416	0.991	1.259
θ range, deg.	1.72 to 26.43	1.66 to 27.03	1.44 to 25.72
No. of rflcn/unique	25537 / 4282	22963 / 6555	15119 / 5043
Goof	1.034	1.009	1.047
R1	-0.01(1)	-	0.0546
wR2	0.0336	0.0429	0.1273
	0.0755	0.0646	

	64	67	73	L72
Empirical formula	C ₃₄ H ₂₄ CuN ₂ O ₄	C ₃₆ H ₂₈ CuN ₂ O ₄	C ₃₂ H ₂₆ CuN ₄ O ₆	C ₂₆ H ₃₈ Cl ₂ CuN ₄ S
Formula weight	588.09	616.14	626.11	256.30
Colour, habit	Green, block	Green, block	Green, block	Colorless, block
Crystal size, mm	0.19x0.16x0.13	0.15x0.13x0.09	0.08x0.05x0.05	0.34x0.20x0.11
Crystal system	Monoclinic	Monoclinic	Monoclinic	Monoclinic
Space group	P2 ₁ /c	C2/c	P2 ₁ /c	P2 ₁ /n
a, Å	10.167(1)	24.782(7)	15.91(7)	9.952(1)
b, Å	21.499(1)	7.293(2)	4.73(1)	13.391(2)
c, Å	12.025(1)	15.647(4)	20.75(6)	10.197(1)
α, deg.	90	90	90	90
β, deg.	90.542(3)	92.667(4)	104.70(9)	99.739(2)
γ, deg.	90	90	90	90
V, Å ³	2623.4(4)	2824.9(13)	1515(9)	1339.3(3)
Z	4	4	2	4
T, K	293(2)	293(2)	293(2)	293(2)
ρ(calcd), Mg/m ³	1.489	1.449	1.372	1.316
μ, mm ⁻¹	0.878	0.186	0.771	0.86
θ range, deg.	1.89 to 26.40	1.65 to 24.54	2.03 to 20.70	2.53 to 26.53
No. of rflcn/unique	14334 / 5336	13715 / 2334	968 / 708	16184 / 2777
Goof	1.012	1.003	1.005	1.007
R1	0.0481	0.1171	0.1494	0.0560
wR2	0.1024	0.1475	0.2602	0.1146